Aus dem
Pathologischen Institut
der
Ludwig-Maximilians-Universität zu München

Direktor: Prof. Dr. med. Thomas Kirchner

Integrative characterization of the cooperation between EWSR1-FLI1 and regulatory germline variants in tumor progression of Ewing sarcoma

Dissertation
zum Erwerb des Doktorgrades der Medizin
an der Medizinischen Fakultät der
Ludwig-Maximilians-Universität zu München

Vorgelegt von
Julian Musa

aus
St. Wendel

Heidelberg
2021

Mit Genehmigung der Medizinischen Fakultät

der Universität München

Berichterstatter:	Prof. Dr. Dr. med. Thomas Grünewald
Mitberichterstatter:	Prof. Dr. rer. nat. Roland Kappler
	Prof. Dr. med. Joachim-Ulrich Walther
	Prof. Dr. med. Hans Roland Dürr
Dekan:	Prof. Dr. med. Thomas Gudermann
Tag der mündlichen Prüfung:	09.12.2021

This thesis is dedicated in love and gratitude
that can hardly be expressed in words to my family

It is especially dedicated to my father,
who sadly cannot witness my graduation anymore

TABLE OF CONTENTS

1. SUMMARY

1.1. English

Obtaining insights into mechanisms underlying inter-individual tumor heterogeneity is necessary in order to optimize diagnostic and therapeutic approaches in the context of precision oncology. As compared to adulthood cancers, pediatric malignancies, such as Ewing sarcoma, harbor a low frequency of recurrent somatic alterations with the exception of pathognomonic driver-mutations that cannot sufficiently explain the wide range of observed clinical outcomes. This may render current approaches of precision oncology as applied for adulthood cancers, mainly focusing on identification of somatic mutations in the protein-coding genome, to be less effective in pediatric malignancies.

The data presented in this thesis exemplify in the Ewing sarcoma model how an 'oncogenic cooperation' between somatic mutations (here *EWSR1-FLI1*) and regulatory germline variants (here a polymorphic enhancer-like GGAA-microsatellite) determines inter-individual heterogeneity regarding tumor growth, patient survival, and drug response. The present results show that binding of the pathognomonic fusion transcription factor EWSR1-FLI1 to a polymorphic enhancer-like GGAA-microsatellite regulates the expression of the oncogenic transcription factor MYBL2 and that high intra-tumoral *MYBL2* expression is associated with shorter overall survival of Ewing sarcoma patients. Consistently, Clustered Regularly Interspaced Short Palindromic Repeats interference (CRISPRi) with this polymorphic regulatory GGAA-microsatellite strongly reduces *MYBL2* expression in Ewing sarcoma cells, and furthermore, inter-individual genetic variability at this locus, which is inherited via the germline, is associated with inter-individual differences of intra-tumoral *MYBL2* expression in primary Ewing sarcoma. Functional experiments *in vitro* and *in vivo* demonstrate that knockdown of MYBL2 in Ewing sarcoma cells impairs cell proliferation, cell survival, as well as growth of cell line-derived xenografts. Integrative analysis of RNA sequencing (RNA-seq) data, chromatin immunoprecipitation and DNA sequencing (ChIP-seq) data, microarray gene expression data with matched clinical data, as well as further functional experiments reveals *CCNF*, *BIRC5*, and *AURKB* as the most functionally and clinically relevant MYBL2 target genes that predominantly mediate the phenotypic effects of MYBL2 in Ewing sarcoma. Moreover, the results show that high MYBL2 levels sensitize Ewing sarcoma cells for targeted inhibition of its upstream activating Cyclin-dependent kinase CDK2 *in vitro* and *in vivo*, suggesting MYBL2 as a putative predictive biomarker for targeted anti-CDK2 therapy.

In conclusion, the present data exemplify in the Ewing sarcoma model how the interaction between somatic mutations and regulatory germline variants determines inter-individual heterogeneity regarding tumor growth, patient survival, and drug response, and thus indicate the importance of integrating the non-protein-coding regulatory genome, next to the protein-coding genome, into future approaches of precision oncology.

Essential parts of this thesis have been published in the following articles:

Original article:

Musa, J., Cidre-Aranaz, F., Aynaud, M.-M., Orth, M.F., Knott, M.M.L., Mirabeau, O., Mazor, G., Varon, M., Hölting, T.L.B., Grossetête, S., Gartlgruber, M., Surdez, D., Gerke, J.S., Ohmura, S., Marchetto, A., Dallmayer, M., Baldauf, M.C., Stein, S., Sannino, G., Li, J., Romero-Pérez, L., Westermann, F., Hartmann, W., Dirksen, U., Gymrek, M., Anderson, N.D., Shlien, A., Rotblat, B., Kirchner, T., Delattre, O., Grünewald, T.G.P. Cooperation of cancer drivers with regulatory germline variants shapes clinical outcomes. **Nature Communications** 2019; 10, 4128.

Commentary and review articles:

Musa, J., and Grünewald, T.G.P. Interaction between somatic mutations and germline variants contributes to clinical heterogeneity in cancer. **Molecular & Cellular Oncology** 2019; 7, 1682924.

Musa, J., Aynaud, M.-M., Mirabeau, O., Delattre, O., Grünewald, T.G. MYBL2 (B-Myb): a central regulator of cell proliferation, cell survival and differentiation involved in tumorigenesis. **Cell Death & Disease** 2017; 8, e2895.

The original article was published as a preprint ahead of journal publication (DOI 10.1101/506659).

1.2. German

Um diagnostische und therapeutische Strategien im Rahmen der Präzisionsonkologie zu optimieren, ist es notwendig die der inter-individuellen Tumorheterogenität zugrundeliegenden Mechanismen aufzuklären. Verglichen mit malignen Tumoren des Erwachsenenalters sind maligne pädiatrische Tumore, wie etwa das Ewing Sarkom, mit Ausnahme von wenigen pathognomonischen Treibermutationen durch eine geringe Anzahl rekurrierender somatischer Alterationen charakterisiert, welche das breite Spektrum der beobachteten klinischen Verläufe nicht hinreichend erklären können. Aktuelle Ansätze der Präzisionsonkologie, wie sie bei malignen Tumoren des Erwachsenenalters Anwendung finden und welche sich im Wesentlichen auf die Identifikation von somatischen Mutationen innerhalb des proteinkodierenden Genoms fokussieren, erscheinen daher bei malignen pädiatrischen Tumoren weniger effektiv.

Die hier präsentierten Daten zeigen anhand des Ewing Sarkom Modells, wie eine „onkogene Kooperation“ zwischen somatischen Mutationen (hier *EWSR1-FLI1*) und regulatorischen Keimbahn-varianten (hier ein polymorpher Enhancer-artiger GGAA-Mikrosatellit) inter-individuelle Heterogenität hinsichtlich Tumorwachstum, Patientenüberleben und Therapieansprechen bedingen kann. Die vorliegenden Ergebnisse zeigen, dass die Bindung des pathognomonischen Fusions-Transkriptionsfaktors EWSR1-FLI1 an einen polymorphen Enhancer-artigen GGAA-Mikrosatelliten die Expression des onkogenen Transkriptionsfaktors MYBL2 reguliert und dass hohe intra-tumorale *MYBL2* Expression mit kürzerem Gesamtüberleben von Ewing Sarkom Patienten assoziiert ist. Entsprechend führt die Clustered Regularly Interspaced Short Palindromic Repeats Interferenz (CRISPRi) mit diesem polymorphen GGAA-Mikrosatelliten zu einer starken Reduktion der *MYBL2* Expression in Ewing Sarkom Zellen und darüber hinaus ist die über die Keimbahn vererbte inter-individuelle genetische Variabilität an diesem Locus mit inter-individuellen Unterschieden der intra-tumoralen *MYBL2* Expression von primären Ewing Sarkomen assoziiert. Funktionelle Experimente *in vitro* und *in vivo* zeigen, dass der Knockdown von MYBL2 in Ewing Sarkom Zellen die Zellproliferation, das Zellüberleben sowie das Wachstum von Zelllinien-Xenografts reduziert. Die integrative Analyse von RNA-Sequenzierungsdaten (RNA-seq), Chromatin Immunopräzipitation und DNA-Sequenzierungsdaten (ChIP-seq), Microarray-Genexpressionsdaten mit korrespondierenden klinischen Daten sowie weiteren funktionellen Experimenten zeigt *CCNF*, *BIRC5* und *AURKB* als funktionell und klinisch relevanteste MYBL2 Zielgene auf, welche den phänotypischen Effekt von MYBL2 im Ewing Sarkom insbesondere

vermitteln. Ferner belegen die Ergebnisse, dass hohe MYBL2-Spiegel Ewing Sarkom Zellen für die zielgerichtete Hemmung der MYBL2-aktivierenden Cyclin-abhängigen Kinase CDK2 *in vitro* und *in vivo* sensitivieren, was die Nutzbarkeit von MYBL2 als möglichen prädiktiven Biomarker für eine gezielt gegen CDK2 gerichtete Therapie nahelegt.

Zusammenfassend zeigen die präsentierten Daten beispielhaft wie die Interaktion zwischen somatischen Mutationen und regulatorischen Keimbahnvarianten inter-individuelle Heterogenität hinsichtlich Tumorwachstum, Patientenüberleben und Therapieansprechen bedingt und verdeutlichen die Wichtigkeit das nicht-proteinkodierende regulatorische Genom, neben dem proteinkodierenden Genom, in zukünftige Ansätze der Präzisionsonkologie miteinzubeziehen.

Essenzielle Teile dieser Dissertation wurden in folgenden Publikationen veröffentlicht:

Originalartikel:

Musa, J., Cidre-Aranaz, F., Aynaud, M.-M., Orth, M.F., Knott, M.M.L., Mirabeau, O., Mazor, G., Varon, M., Hölting, T.L.B., Grossetête, S., Gartlgruber, M., Surdez, D., Gerke, J.S., Ohmura, S., Marchetto, A., Dallmayer, M., Baldauf, M.C., Stein, S., Sannino, G., Li, J., Romero-Pérez, L., Westermann, F., Hartmann, W., Dirksen, U., Gymrek, M., Anderson, N.D., Shlien, A., Rotblat, B., Kirchner, T., Delattre, O., Grünewald, T.G.P. Cooperation of cancer drivers with regulatory germline variants shapes clinical outcomes. **Nature Communications** 2019; 10, 4128.

Kommentar- und Übersichtsartikel:

Musa, J., and Grünewald, T.G.P. Interaction between somatic mutations and germline variants contributes to clinical heterogeneity in cancer. **Molecular & Cellular Oncology** 2019; 7, 1682924.

Musa, J., Aynaud, M.-M., Mirabeau, O., Delattre, O., Grünewald, T.G. MYBL2 (B-Myb): a central regulator of cell proliferation, cell survival and differentiation involved in tumorigenesis. **Cell Death & Disease** 2017; 8, e2895.

Der Originalartikel wurde vorab der Journalpublikation als Preprint veröffentlicht (DOI 10.1101/506659).

2. INTRODUCTION AND BACKGROUND

2.1. Precision oncology in the age of ‘omics‘-data

Over the recent years, development and accessibility of technologies generating high-throughput ‘omics‘-data led to the possibility of individual diagnosis and potential stratification of patients to certain therapeutic strategies (Garraway et al., 2013; Senft et al., 2017). This approach is ofter referred to as ‘personalized medicine‘ or ‘precision medicine‘, within which oncology holds a pioneer position (Garraway et al., 2013; Senft et al., 2017). The initial idea behind precision oncology was to sequence protein-coding genes of an individual tumor genome and to characterize the tumor molecularly by its variety of mutations in oncogenes and tumor suppressors that may functionally cooperate in tumorigenesis, tumor maintenance, and tumor progression (Garraway et al., 2013). However, as in addition to the tumor genome, multiple additional functional regulatory levels such as the epigenome, the trancriptome, the proteome, and the metabolome define important parameters impacting on cancer phenotypes, the most coprehensive way to identify individual cancer vulnerabilities would be to include multi-‘omics‘ data regarding these regulatory levels, but such comprehensive strategies appear to not be feasable yet in clinical routine algorithms (Senft et al., 2017). Up until now, predominantly, inclusion of genomic data focusing on identification of mutations in protein-coding genomic regions has entered clinical routine (Garraway et al., 2013; Hyman et al., 2017; Senft et al., 2017). However, pediatric malignancies are, compared to adulthood cancers, characterized by a low frequency of recurrent somatic mutations/alterations, which alone cannot explain the highly variable clinical courses and outcomes being observed (Brohl et al., 2014; Crompton et al., 2014; Gröbner et al., 2018; Grünewald et al., 2018; Musa and Grünewald, 2019; Musa et al., 2019; Tirode et al., 2014; Vogelstein et al., 2013). Therefore, the current concept of precision oncology mainly based on identification of mutations in protein-coding genomic regions, that may be comparatively successful in adulthood cancers, may not be applied as successfully in pediatric oncology (Garraway et al., 2013; Hyman et al., 2017; Musa and Grünewald, 2019; Senft et al., 2017). The data presented in this thesis exemplifies in the EwS model, how the interaction between a somatic mutation (here *EWSR1-FLI1*) and a regulatory genetic variant which is inherited via the germline (here a polymorphic enhancer-like GGAA-mSat) may determine the expression of a functionally and clinically relevant druggable downstream target (here MYBL2), or in other words, exemplifies on a molecular level why patients harboring the same somatic driver mutations may show strong variations in tumor growth and clinical outcomes depending on the polymorphic

regulatory genetic background of the individual (Musa and Grünewald, 2019; Musa et al., 2019). These results indicate that, espacially in pediatric cancers in which the success of current approaches of precision oncology may be limited, it is important to not only include mutations of the protein-coding genome, but also variations in the regulatory germline-inherited genomic background into such approaches, in order to more specifically exploit the potential of precision oncology (Garraway et al., 2013; Hyman et al., 2017; Musa and Grünewald, 2019; Musa et al., 2019; Senft et al., 2017).

2.2. Ewing sarcoma (EwS)

2.2.1. Definition

Ewing sarcoma (EwS) is a malignant bone and soft-tissue tumor mainly affecting children, adolescents, and young adults (Gaspar et al., 2015; Grünewald et al., 2018). It has firstly been described by James Ewing as ‘diffuse endothelioma of bone‘ in 1921 (Ewing, 1921, 1972). It is typically occurring in the pelvis, femur, tibia, and ribs when bone-related, or in the thoracic wall, pleural cavities and gluteal as well as cervical muscles when soft-tissue-related (Grünewald et al., 2018). Histomorphologically, it belongs to the group of small round blue cell tumors (Grünewald et al., 2018; Watson et al., 2018), but genetically harbors pathognomonic balanced chromosomal translocations leading to fusions between members of the *FET* and *ETS* gene families, whereby *EWSR1-FLI1* is by far the most common fusion (85%) (Grünewald et al., 2018; Sankar and Lessnick, 2011; Watson et al., 2018). Several different former tumor entities were historically subsumed under the term ‘Ewing family of tumors‘, including EwS of the bone, extraosseous EwS, peripheral primitive neuroectodermal tumors (pPNET) and Askin tumors (PNET of the chest wall), according to their histomorphological similarities. However, as chromosomal translocations leading to fusions between members of the *FET* and *ETS* gene families occur in more than 95% of these former entities (Grünewald et al., 2018; Iwamoto, 2007), the term ‘Ewing family of tumors‘ was left in the current World Health Organization (WHO) classification of soft-tissue and bone tumors published in 2013 and these former entities were summarized under the term ‘Ewing sarcoma‘ (Fletcher et al., 2013; Grünewald et al., 2018). The WHO classification furthermore describes a group of tumors called ‘Ewing-like sarcomas‘, which are histomorphologically and clinically almost not distinguishable from EwS, but do not exhibit pathognomonic *FET-ETS* fusions, rather different recurrent gene fusions or genetic rearrangements, such as *CIC*-, *BCOR*-, or *NAFTC*-fusions/rearrangements (Fletcher et al., 2013; Grünewald et al., 2018). Despite its extensive genetic characterization, the cellular

origin of EwS is still under discussion and remains to be unclear (Grünewald et al., 2018). Mesenchymal stem cells (MSC) as well as neural crest-originated stem cells and osteochondrogenic progenitor cells can be immortalized by EWSR1-FLI1 and were proposed to be potential cells of EwS origin (Grünewald et al., 2018; von Levetzow et al., 2011; Riggi et al., 2005; Tanaka et al., 2014; Tirode et al., 2007). However, as fully conclusive data regarding the cell of EwS origin is lacking yet, future studies are required to clarify this matter of debate (Grünewald et al., 2018).

2.2.2. Epidemiology

EwS mainly affects children as well as adolescents and young adults (AYA), showing a peak of incidence at the age of 15 years, whereby males are more frequently affected than females (ratio 3:2) (Grünewald et al., 2018; Jawad et al., 2009). The age-adjusted annual incidence rate is ~1.4 cases per million individuals (Grünewald et al., 2018; Worch et al., 2011). Demographically, the incidence of EwS is inconsistently distributed throughout different human populations: in Caucasians, EwS occurs more frequently as compared to Asian/Native American or African-American populations (age-adjusted annual incidence rate ~1.6, 0.9, and 0.2 cases per million individuals, respectively) (Grünewald et al., 2018; Jawad et al., 2009; Worch et al., 2011). As the incidence of EwS in African-American populations is lower as compared to European-Americans, the variation of EwS occurrence is probably underlying inherited genetic factors rather than environmental factors (Grünewald et al., 2018). These observations are supported by rare reports of accumulated EwS occurrence in siblings of EwS patients (Grünewald et al., 2018; Hutter et al., 1964; Ji and Hemminki, 2006; Joyce et al., 1984).

2.2.3. Etiology and pathophysiology

2.2.3.1. Risk factors

Genetic risk factors / predispositions

In ~13% of EwS patients, mutations in the germline genome enriched for genes associated with DNA repair and tumor predisposition syndromes, such as *BRCA1*, can be detected (Brohl et al., 2017; Chang et al., 2016; Grünewald et al., 2018). However, as EwS is very rarely occurring in the context of any known cancer predisposition syndrome, the pathophysiological role of these aberrations as well as implications for genetic testing of patients and their relatives remains unclear (Garber and Offit, 2005;

Grünewald et al., 2018). In genome-wide association studies (GWAS) several risk loci were identified in which common variants are associated with EwS susceptibility and expression levels of nearby genes: 1p36.22 (*TARDBP*), 10q21 (*ADO* and *EGR2*), 15q15, 6p25.1 (*RREB1*), 20p11.22 (*NKX2-2*), and 20p11.23 (*KIZ*) (Grünewald et al., 2018; Lin et al., 2020; Machiela et al., 2018; Postel-Vinay et al., 2012). A mechanistic link between EwS susceptibility and a common single nucleotide polymorphism (SNP) in the respective risk locus has been described for the *EGR2*-associated locus (10q21): variations in the rs79965208 SNP modify the structure of an *EGR2*-associated EWSR1-FLI1-responsive enhancer-like GGAA-microsatellite (mSat) (see section 'Genetics' for details), leading to differential EWSR1-FLI1 binding at this locus and thereby to differential EGR2 expression (Grünewald et al., 2015, 2018). Interestingly, the major risk haplotypes identified in the first EwS GWAS were less prevalent in Africans than in Europeans, which may account for differences of EwS incidences across populations of different descent (see section 'Epidemiology' for details) (Grünewald et al., 2018; Postel-Vinay et al., 2012). Furthermore, genetic polymorphisms in *CD99*, encoding for a surface protein usually stained immunohistochemically during the (differential-)diagnostic work-up of suspected EwS and playing a role in EwS tumor formation and metastatic spread *in vivo*, has been shown to be associated with EwS susceptibility (Grünewald et al., 2018; Martinelli et al., 2016; Rocchi et al., 2010).

Environmental risk factors

In an Australian case-control study of 106 EwS cases and 344 control cases an association between EwS occurrence and farm exposure was described (Grünewald et al., 2018; Valery et al., 2002).

2.2.3.2. Genetics

Pathognomonic chromosomal translocations

EwS harbor pathognomonic balanced chromosomal translocations leading to fusions between members of the *FET* and *ETS* gene families (Delattre et al., 1992; Grünewald et al., 2018; Zucman et al., 1993). The most commonly found translocation is t(11;22)(q12;q24), leading to fusion of *EWSR1* (*FET* gene family) to *FLI1* (*ETS* gene family), which is detected in 85% of EwS cases (Delattre et al., 1992; Grünewald et al., 2018). Different subtypes of *EWSR1-FLI1* fusions are described, depending on the localization of the breakpoint (Grünewald et al., 2018; Zucman et al., 1993). However, alternative fusions may occur in the remaining 15% of cases (Grünewald et al., 2018; Zucman et al., 1993): the second

most common translocation t(21;22)(q22;q12), leading to the *EWSR1-ERG* fusion, can be detected in about 10% of EwS cases (Grünewald et al., 2018; Sorensen et al., 1994), and 5% of cases consist of several other fusions between *FET* and *ETS* family members (Grünewald et al., 2018; Jeon et al., 1995; Ng et al., 2007; Peter et al., 1997; Urano et al., 1998). An overview on chromosomal translocations described in EwS is given in **Figure 1**. All of these gene fusions result in chimeric fusion proteins which are steadily expressed as they are under control of the constantly active *FET* family gene promoters (Grünewald et al., 2018). EWSR1-FLI1 and EWSR1-ERG fusion proteins act as aberrant transcription factors regulating the expression of genes impacting on various cellular properties (Cidre-Aranaz and Alonso, 2015; Grünewald et al., 2018; Shi et al., 2020). Functionally, EWSR1-FLI1 and EWSR1-ERG are comparable as the DNA binding domain of FLI1 and ERG binds the same DNA motifs, and consistently, occurrence of the different fusions does not translate into differential clinical phenotypes (Ginsberg et al., 1999; Grünewald et al., 2018; Sorensen et al., 1994). Both bind to either polymorphic ETS binding motifs containing a core GGAA motif, less frequently a GGAT motif, which are not fusion oncoprotein-specific, or polymorphic GGAA-mSats harboring variable numbers of consecutive GGAA-repeats, which are specific binding motifs for these fusion oncoproteins (Gangwal et al., 2008; Grünewald et al., 2018; Guillon et al., 2009). However, EWSR1-FLI1 is able to activate or to repress the expression of genes (Grünewald et al., 2018), and in this regard, a model for binding motif-specific function of EWSR1-FLI1 has been proposed: in case of EWSR1-FLI1 polymer binding at GGAA-mSats, these repetitive former ‘junk DNA‘ elements are converted into *de novo* enhancers by inducing an open chromatin state, and thereby steering the expression of nearby genes (Riggi et al., 2014), whereby in case of EWSR1-FLI1 binding to ETS binding motifs, dislocation of wild-type ETS transcription factors leads to a reduction of wild-type ETS target gene expression (Riggi et al., 2014). These results are supported by previous data showing that GGAA-mSats are enriched nearby EWSR1-FLI1 upregulated, but not downregulated genes (Gangwal et al., 2008). Interestingly, GGAA-mSats appear to be evolutionary non-conserved and to lack functional relevance in other cellular contexts than EwS (that is without occurrence of a FET-ETS fusion oncoprotein), while evolutionary conserved enhancers containing ETS binding sites are, among other cell types, functionally relevant in cells of mesenchymal origin (such as MSC, which are discussed to constitute potential cells of EwS origin), suggesting that EWSR1-FLI1 may hijack oncogenes via converting GGAA-mSats into active enhancers and repress tumor suppressor genes and genes involved in cell differentiation by functionally inactivating ETS

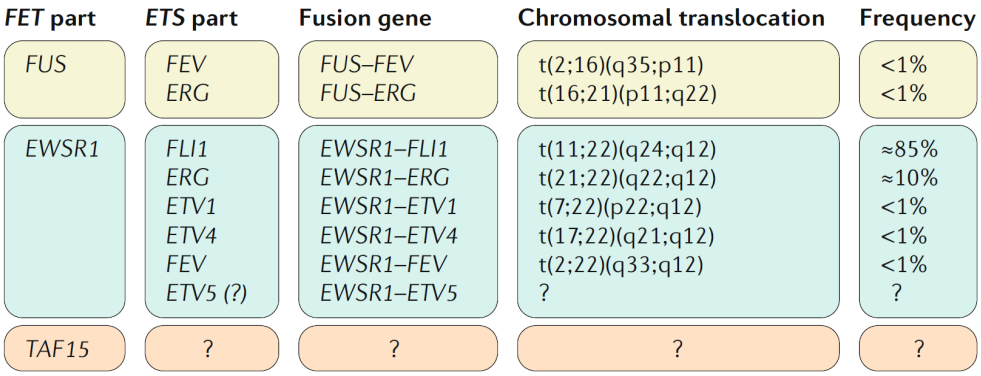

Figure 1: Chromosomal translocations in EwS fusing different members of the *FET* and *ETS* gene families. Figure from Grünewald et al., 2018.

binding site-containing enhancers via dislocation of wild-type ETS transcription factors (Riggi et al., 2014) (**Figure 2**). When converting GGAA-mSats into *de novo* enhancers, EWSR1-FLI1 was shown to act as a pioneer transcription factor: depending on the prion-like domain of EWSR1, EWSR1-FLI1 is able to recruit the BRG1- or HBRM-associated factors (BAF) chromatin remodeling complex to these enhancer sites and thereby locally modulate chromatin state (Boulay et al., 2017; Grünewald et al., 2018; Selvanathan et al., 2019; Sheffield et al., 2017). Interestingly, the number of consecutive GGAA-repeats at these loci determines the activity of the enhancer: peaks of activity have been described at around 20 and 50 consecutive GGAA-repeats, whereby the activity decreases in between 20 and 50 repeats and above 50 repeats (Monument et al., 2014). In case of transcriptional repression at ETS binding site containing enhancers, an additional potentially supportive mechanism next to dislocation of wild-type ETS transcription factor has been proposed: EWSR1-FLI1 can recruit the nucleosome remodeling and deacetylase (NuRD) repressor complex that promotes an inactive epigenetic state at these loci, and thereby further promotes repression of respective genes (Sankar et al., 2013). Moreover, EWSR1-FLI1 can indirectly repress genes by upregulating the expression of transcriptional repressors (Sankar et al., 2013).

Recurrent protein-coding mutations and copy-number alterations

As it is the case for most pediatric cancers, EwS show a low frequency of protein-coding mutations except for pathognomonic chromosomal translocations (Brohl et al., 2014; Crompton et al., 2014; Gröbner et al., 2018; Grünewald et al., 2018; Musa and Grünewald, 2019; Musa et al., 2019; Tirode et al., 2014; Vogelstein et al., 2013). Most frequently found recurrent protein-coding mutations are

mutations of *STAG2* (~15-22% of cases), which is a subunit of the cohesin complex involved in proper chromosome segregation during mitosis favoring aneuploidy when mutated (Brohl et al., 2014; Crompton et al., 2014; Grünewald et al., 2018; Romero-Pérez et al., 2019; Tirode et al., 2014), and *TP53* (~5-13% of cases), a central tumor suppressor regarded as 'the guardian of the genome' (Brohl et al., 2014; Brown et al., 2009; Crompton et al., 2014; Grünewald et al., 2018; Huang et al., 2005; Kovar et al., 1993; Tirode et al., 2014). *STAG2* and *TP53* mutations are both associated with adverse prognostic parameters (Brohl et al., 2014; Crompton et al., 2014; Grünewald et al., 2018; Huang et al., 2005; Tirode et al., 2014). Several other genes harboring recurrent somatic mutations have been identified in a lower frequency (such as *EZH2*, *BCOR*, and *ZMYM3* in each 2.7% of cases), but their clinical significance remains unclear (Grünewald et al., 2018; Tirode et al., 2014). The most common copy-number alterations (CNAs) in EwS are gains of chromosome 8 (~35-48% of cases), 12 (~11-38% of cases), 1q (~15-31% of cases), 20 (~13-18% of cases), and losses of chromosome 16q (~10-21% of cases) and 9p21(~13% of cases) (Crompton et al., 2014; Huang et al., 2005; Shukla et al., 2013; Tirode et al., 2014). Of these most frequent CNAs, gains of chromosome 12, 1q, and 20, as well as losses of chromosome 16q and 9p21 are associated with adverse prognosis (Hattinger et al., 2002; Huang et al., 2005; Shukla et al., 2013; Tirode et al., 2014). In case of chromosome 9p21 loss, the adverse prognostic effect may be explainable by loss of the tumor suppressor gene *CDKN2A*, encoding for a Cyclin-dependent kinase (CDK) inhibiting protein (Huang et al., 2005), and in case of chromosome 1q gain, amplification of *CDT2*, a gene involved in regulation of protein ubiquitinylation, was supposed to mediate the adverse prognostic effect (Mackintosh et al., 2012). For other loci, distinct relevant candidate genes mediating such effect remain to be elucidated (Crompton et al., 2014).

2.2.3.3. Epigenetics

EWSR1-FLI1 occurrence leads to a genome-wide rewiring of the cellular epigenomic landscape (Sheffield et al., 2017; Tomazou et al., 2015). This epigenetic remodeling affects promoters as well as enhancers and super-enhancers, and is associated with corresponding changes of the transcriptome (Tomazou et al., 2015). When comparing the DNA methylation signature of EwS to numerous different cell types, it appears to be highly specific (Sheffield et al., 2017). However, despite the fact that EwS are genetically homogeneous, assessment of inter-tumoral and intra-tumoral variations in methylation signatures revealed substantial epigenetic heterogeneity (Sheffield et al., 2017). Interestingly, inter-

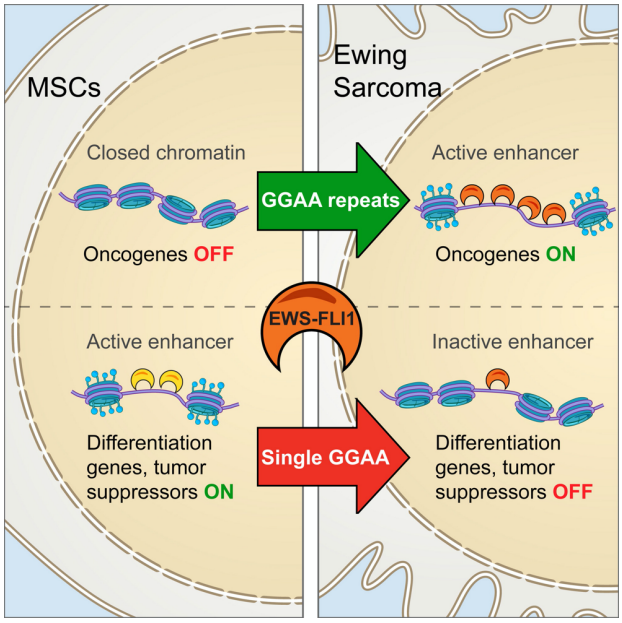

Figure 2: Model for a binding site-specific regulatory role of EWSR1-FLI1. EWSR1-FLI1 may either convert evolutionary non-conserved GGAA-microsatellites (mSats) into active enhancers steering the expression of oncogenes or functionally inactivate evolutionary conserved ETS binding site-containing enhancers of tumor suppressor genes and differentiation-associated genes by dislocation of wild-type ETS transcription factors. MSCs: Mesenchymal stem cells. Figure from Riggi et al., 2014.

individual heterogeneity reflects a continuous spectrum between two dimensions: one dimension reflecting the strongness of the regulatory EWSR1-FLI1 signature that defines the so-called 'Ewing-ness' of the tumor and a second dimension reflecting the differentiation of the tumor on a spectrum between 'stem-cell like' and 'mesenchymally differentiated' (Sheffield et al., 2017). It was proposed that the first dimension may represent the degree of EwS-specific enhancer reprogramming, and that the second dimension may represent the degree of differentiation of the respective EwS cell of origin (Sheffield et al., 2017). Additionally, higher epigenetic intra-tumoral heterogeneity has been observed in primary EwS from patients with metastatic disease at diagnosis as compared to EwS from patients with localized disease (Sheffield et al., 2017), which is consistent with the idea of intra-tumoral heterogeneity and clonal cancer evolution being a driving force for metastatic spread (Li et al., 2018; Sheffield et al., 2017), but whether this reflects a causality in EwS remains to be elucidated (Sheffield et al., 2017).

2.2.4. Diagnosis

Every patient with a radiologically suspected malignant bone tumor should be assigned to an interdisciplinary reference center for bone tumors or to an institute which is part of a specialized sarcoma network for further diagnostic work-up (Casali et al., 2018).

2.2.4.1. Signs and symptoms

In localized disease stage, the vast majority of patients present with local pain, which mostly occurs intermittently, can be related to strain, may also occur during the night, and worsens over the time (Grünewald et al., 2018; Widhe and Widhe, 2000). This pain is often misinterpreted by patients for ‘bone growth‘ or is thought to relate to minor traumata that happened at the time symptoms firstly appeared (Grünewald et al., 2018; Widhe and Widhe, 2000). Following pain, a locoregional swelling with a palpable tumor mass may occur, whereby the timepoint of manifestation largely depends on the localization of the tumor (Grünewald et al., 2018; Widhe and Widhe, 2000). The intermittent character of the pain can easily mislead physicians to attribute symptoms to a temporary cause, such as a minor trauma, and may delay diagnosis (Grünewald et al., 2018; Widhe and Widhe, 2000). Therefore, pain lasting more than one month and pain without adequate trauma should be subjected to fast diagnostic work-up (Grünewald et al., 2018). In metastatic stage, B-symptoms (fever, night sweats, or unintended weight loss greater that 10% over the last six or less months) may arise, which is not typical for localized disease stage (Grünewald et al., 2018).

2.2.4.2. Laboratory testing

Currently, specific blood markers for EwS are not in clinical routine use yet, but are under development (Casali et al., 2018; Grünewald et al., 2018; Samuel et al., 2020; Zhang et al., 2018). Routine parameters like blood count, erythrocyte sedimentation rate (ESR), blood serum chemistry, and coagulation test should be collected standardly (Grünewald et al., 2018). High serum levels of indirect markers for bone affection, such as alkaline phosphatase (AP), or markers associated with high cell turnover, such as lactate dehydrogenase (LDH), may be increased and have a prognostic value (Casali et al., 2018; Grünewald et al., 2018). Additionally, elevated levels of C-reactive protein (CRP), low levels of hemoglobin and albumin as well as several scores combining multiple parameters were also shown to have a prognostic value (Aggerholm-Pedersen et al., 2016; Biswas et al., 2014; Li et al., 2017). Non-routine markers, such as IGF-1, IGFBP-3, and detection of circulating tumor DNA have been shown to be associated with EwS prognosis, but are not standardly determined (Casali et al., 2018; Grünewald et al., 2018; Rutkowski et al., 2003; Shulman et al., 2018; Toretsky et al., 2001). Pregnancy test in female patients as well as virological testing (according to institutional/national guidelines) should be performed in respect of potential subsequent surgery, radio-, or chemotherapy (Grünewald et al., 2018).

2.2.4.3. Imaging of primary lesion and staging

Imaging of primary lesion

Initial imaging is crucial for evaluation of local disease extension and metastatic spread (Grünewald et al., 2018). Characteristic features of EwS in X-ray imaging include periosteal reactions (such as multilayered 'onion skin'-like or spiculated appearance and occurrence of a 'Codman triangle'), permeative/osteolytic and sclerotic components as well as soft-tissue involvement (Grünewald et al., 2018; Kuleta-Bosak et al., 2010; Niethard et al., 2009; Patnaik et al., 2018). To a lower extent, soft-tissue calcifications, saucerization, cortical thickening or destruction, bone expansion, pathological fractures or cystic components can be observed (Kuleta-Bosak et al., 2010; Patnaik et al., 2018). If X-ray imaging exhibits radiographic signs indicating malignancy, magnet resonance imaging (MRI) is regarded to be the leading modality to assess local disease progression and is especially valuable in evaluation of soft-tissue lesions (Casali et al., 2018; Grünewald et al., 2018; Kasalak et al., 2019). Generally, MRI should include the whole compartment as well as adjacent joints to identify potential 'skip-lesions' (Casali et al., 2018; Barnett et al., 2020) and measurement of tumor volume should be performed to assess therapy response at a later timepoint (Aghighi et al., 2016; Koshkin et al., 2016; Saleh et al., 2020). Additional computed tomography (CT) may be of use for better evaluation of calcifications, periosteal reactions, and cortical destructions (Casali et al., 2018). Representative X-ray and MRI images of primary EwS lesions are shown in **Figure 3**.

Staging

Tumor burden (volume) and detection of metastases are the major parameters considered during EwS staging (Casali et al., 2018) and should be re-evaluated during/after treatment to control therapy success or to identify relapses after treatment was finished (**Figure 4**) (Costelloe et al., 2017). EwS predominantly metastasize to the lungs, bone, and bone marrow via the bloodstream (Casali et al., 2018; Grünewald et al., 2018). About 20-25% of patients show metastatic disease at diagnosis, with ~10% exhibiting lung metastases, ~10% exhibiting bone/bone marrow metastases, and ~5% exhibiting combined or other metastases (Casali et al., 2018). Several imaging modalities may be included for proper staging: chest X-ray, CT, bone scintigraphy, ^{18}F-fluorodeoxyglucose positron-emission tomography (^{18}F-FDG-PET), combined ^{18}F-FDG-PET/CT, whole-body MRI or combined ^{18}F-FDG-PET/MRI (Casali et al., 2018; Grünewald et al., 2018). In the ESMO-PaedCan-EURACAN guidelines for

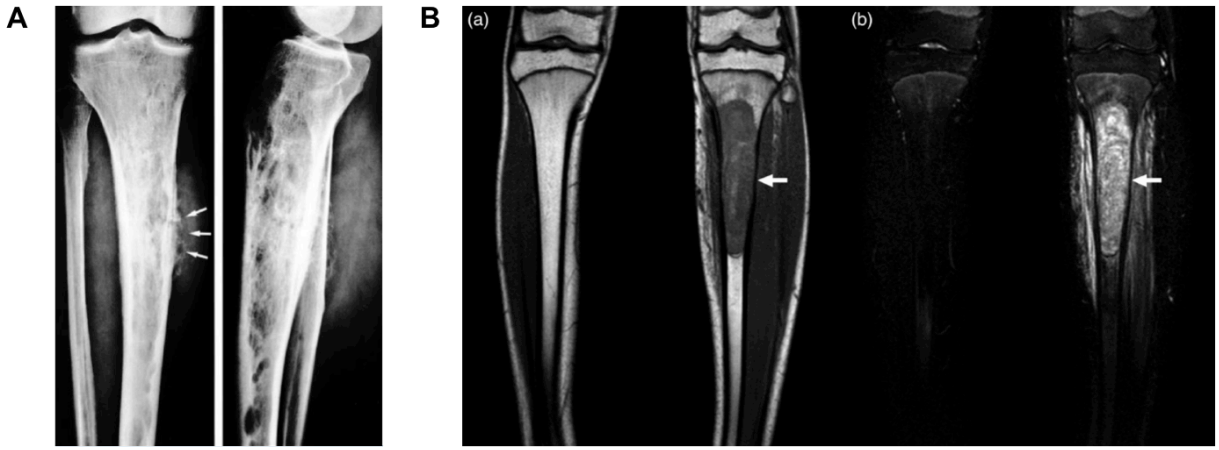

Figure 3: Imaging of primary EwS lesion. (A) Anterior-posterior (a.p.) (left) and lateral (right) X-ray of a primary EwS localized in the right proximal tibia. Typical permeative/osteolytic lesions as well as destruction of the corticalis are visible, arrows pointing toward spiculae and Codman triangle, multilayered 'onion skin'-like periosteal reaction appears nearby, and extensive soft-tissue involvement is displayed. (B) MRI of a different patient showing a primary EwS localized in the left proximal tibia. Coronary T1 weighted images (a) show a hypointense, inhomogeneous but clearly delineated lesion in the left proximal tibia. In fat-suppressed T2 weighted images (b) the lesion appears hyperintense. Arrows indicate the lesion. X-ray images from Niethard et al., 2009 and MRI images from Kasalak et al., 2019.

bone sarcomas, published in 2018, no specific advice for usage of certain modalities is given (Casali et al., 2018). However, it has been shown that spiral CT is superior to ^{18}F-FDG-PET in detection of lung metastases (Franzius et al., 2001; Völker et al., 2007), whereas ^{18}F-FDG-PET was superior compared to ultrasound, CT, MRI, and bone scintigraphy in detection of lymph node and secondary bone lesions (Tal et al., 2020; Völker et al., 2007). Expectedly, combined ^{18}F-FDG-PET/CT is superior in detection of new lesions compared to ^{18}F-FDG-PET alone (Gerth et al., 2007). In order to increasingly detect bone marrow metastases at diagnosis, bone marrow aspirates/biopsies have usually been performed in patients with localized EwS negative for bone marrow lesions by imaging, but several lines of evidence indicated that modern imaging techniques are sufficient for detection of bone marrow metastases during initial staging (Breitegger et al., 2020; Casali et al., 2018; Grünewald et al., 2018; Kopp et al., 2015; Newman et al., 2013). However, lesions in doubt should be biopsied (Casali et al., 2018).

2.2.4.4. Pathology

Macroscopy and histopathology

A biopsy of the suspected lesion is required for definitive diagnosis of EwS and should supply enough material for routine histology, immunohistochemistry (IHC), molecular pathology, and sample archiving

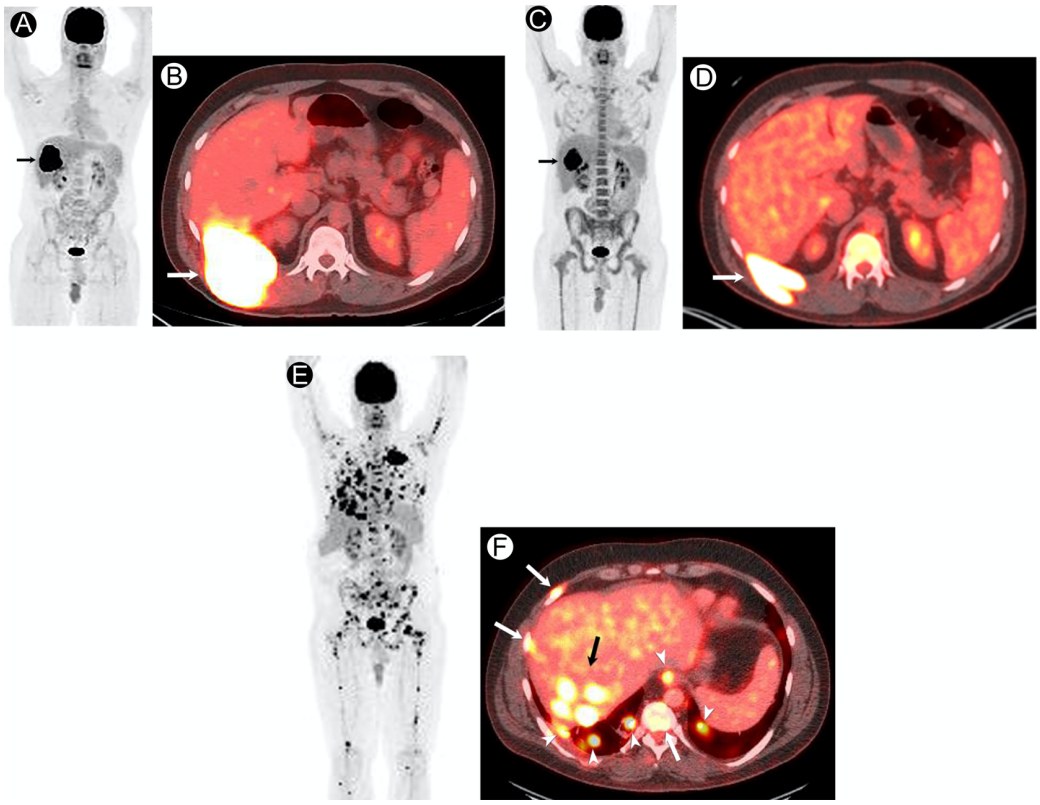

Figure 4: Staging and re-staging in EwS using ^{18}F-FDG-PET/CT. Maximum intensity projection of ^{18}F-FDG-PET (A,C,E) as well as fused axial ^{18}F-FDG-PET/CT images (B,D,F) are shown. A representative case is displayed. (A,B) Primary EwS in the right 11th rib with soft-tissue affection. No metastases were detectable at initial diagnosis. The black and the white arrow indicate the tumor. (C,D) After treatment with two cycles of vincristine, doxorubicin, and ifosfamide regression of soft-tissue extension of the tumor is visible. The black and the white arrow indicate the tumor. (E,F) Subsequent further chemotherapeutic treatment as well as tumor resection at first led to a disease-free interval, but two years after initial treatment, bone, liver, and lung metastases were evident. The long white arrows indicate bone metastases, the black arrow indicates liver metastases, and the short white arrowheads indicate lung metastases. Figure from Costelloe et al., 2017.

(**Figure 5**) (Casali et al., 2018; Grünewald et al., 2018; Kalus et al., 2020; Kim and Park, 2016). In most cases, imaging-guided core-needle biopsy is a possible alternative to open biopsy, whereby the biopsy tract and drain channels need to be clearly marked in order to entirely resect these potentially contaminated areas during definitive surgical procedure (Casali et al., 2018). Macroscopically, the cut surface of EwS appears grey/white, is soft and often exhibits hemorrhagic and necrotic areas (Grünewald et al., 2018). Histomorphologically, EwS belongs to the group of small round cell sarcomas and shows a solid growth pattern (Grünewald et al., 2018; Watson et al., 2018). The nuclei are round, nucleoli are usually not visible, and chromatin appears finely freckled (Fletcher et al., 2013; Grünewald et al., 2018). About 50% of EwS are positive for Periodic acid-Schiff (PAS) staining, revealing large glycogen deposits (Grünewald et al., 2018). Reticulin staining is usually negative as EwS lack interstitial matrix between tumor cells (Grünewald et al., 2018). Immunohistochemical staining of CD99 is positive

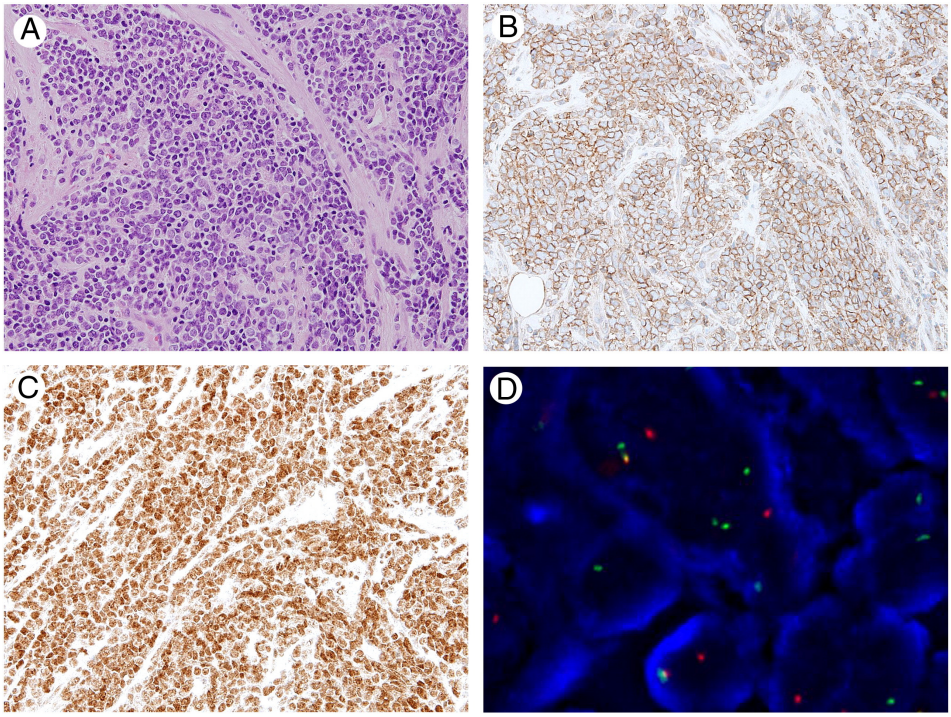

Figure 5: Pathological assessment of EwS. (A) Hematoxylin and eosin (HE) staining showing small round blue cells harboring round nuclei and freckled chromatin. (B) Immunohistochemical membranous staining for CD99. (C) Immunohistochemical nuclear staining for FLI1 (not routinely used for EwS diagnosis). (D) Fluorescence in-situ hybridization (FISH) for *EWSR1* break-apart showing distinct orange and green signals. (A)-(C) 200x magnification; (D) 1,000x magnification. Figure from Kim and Park, 2016.

in ~95% of EwS, but is not highly specific as several normal tissues and other tumor entities (such as other round cell sarcomas, leukemia, or lymphoblastic lymphoma) also display CD99 positivity (Grünewald et al., 2018). Alternatively, other markers, such as FLI1, have as well been suggested to be valuable in EwS diagnosis, but either lack high specificity or are not yet prospectively validated and are therefore not yet in clinical routine use (Baldauf et al., 2017; Hornick, 2014; Llombart-Bosch et al., 2009; Machado et al., 2018).

Molecular pathology

Although most EwS can be recognized by routine histology and IHC, confirmation of pathognomonic chromosomal translocations by usage of molecular methods is necessary for validation of initial diagnosis and classification of molecular subtypes (Casali et al., 2018). If fresh frozen tissue is available, detection of fusion transcripts using either reverse transcription polymerase chain reaction (PCR) or anchored multiplex PCR-based targeted next-generation sequencing (NGS) is the approach of choice (Casali et al., 2018). However, the latter technique is also applicable for formalin-fixed and paraffin-

embedded (FFPE) tissue which has either not been decalcified or was decalcified using EDTA (Casali et al., 2018). If frozen tissue is not available, fluorescence in-situ hybridization (FISH) may be used to detect an *EWSR1* break-apart (Casali et al., 2018; Grünewald et al., 2018). As FISH does not per se detect *EWSR1-ETS* fusions but *EWSR1* rearrangements, this method cannot distinguish between EwS and other *EWSR1* rearranged sarcomas and was shown to not be reliable in detection of *EWSR1-ERG* fusion (Casali et al., 2018; Chen et al., 2016; Grünewald et al., 2018). However, although not the diagnostic gold standard, FISH is considered to be a sufficient diagnostic tool in combination with proper integration of clinical and other pathological information when application of other molecular diagnostic techniques is not possible (Casali et al., 2018).

2.2.5. Treatment

Generally, EwS treatment should be conducted in a specialized reference center/network by a multidisciplinary team including pediatric oncologists, medical oncologists, radiation oncologists as well as general and orthopedic surgeons (Casali et al., 2018; Grünewald et al., 2018). In such reference centers/networks, therapy is conducted according to either established protocols or in context of prospective clinical studies (Casali et al., 2018).

2.2.5.1. Localized disease

Localized EwS are currently treated following a multimodal treatment protocol including 3-6 cycles of neoadjuvant multidrug chemotherapy, radical local therapy including surgery and/or radiation, and subsequent 6-10 cycles of adjuvant multidrug chemotherapy (Casali et al., 2018).

Systemic treatment .

Chemotherapy is conducted in 2-3 week intervals and total treatment period is 10-12 months (Casali et al., 2018). Neoadjuvant chemotherapy is applied before local tumor treatment in order to optimize conditions for surgical resection by decreasing tumor size and in order to reduce relapse due to micrometastases (Grünewald et al., 2018). Up to date protocols for neoadjuvant chemotherapy include multiple drugs, such as doxorubicin, cyclophosphamide, ifosfamide, vincristine, dactinomycin, and etoposide which are considered to be most effective (Casali et al., 2018). Currently used protocols usually consist of combinations of the latter drugs, whereby dose-densfication due to interval

compression was shown to be associated with better patient outcome (Casali et al., 2018; Lu et al., 2020). Extensive consolidation chemotherapy is a central element in EwS treatment to also eradicate cancer cells that proliferate slowly (Grünewald et al., 2018). For consolidation, mostly the same drugs as for induction are used (Casali et al., 2018; Grünewald et al., 2018). In patients with poor response to initial chemotherapy and/or initial tumor volume >200ml, high-dose treatment with the alkylating agents Busulfan and Melphalan following autologous hematopoietic stem cell transplantation was shown to be associated with a survival advantage (Casali et al., 2018; Ferrari et al., 2011; Grünewald et al., 2018; Whelan et al., 2016, 2018). However, several experimental therapy approaches are under development and agents/therapy regimens already shown to be pre-clinically effective are in clinical trials but did not reach clinical routine yet (Charan et al., 2020; Harlow et al., 2019; Italiano et al., 2020).

Local control

Surgery and/or radiation are used to achieve local control (Casali et al., 2018). Entire surgical resection of the tumor is the preferred method, as radiation alone is associated with an increased risk of local relapse (Casali et al., 2018). Exhaustive resection should include the whole tumor volume at diagnosis, not only the leftover volume after neoadjuvant chemotherapy (Casali et al., 2018). In case of inappropriate surgical margins or poor chemotherapy response as determined by histopathological examination (e.g. more than 10% of viable cancer cells), additional radiation should be considered (Casali et al., 2018). Radiotherapy alone should only be applied in case of impossible entire surgical resection (Casali et al., 2018). In each scenario (postoperatively or without operation), radiotherapy is applied in a dose of 45-60 Gy depending on the location, surgical margins, and/or histological response to chemotherapy (Casali et al., 2018). In case of extraskeletal EwS, general therapy regimens are the same as for bone-associated EwS with the exception that radiotherapy should be generally applied and may only be dispensible in superficial EwS which harbor a good prognosis (Casali et al., 2018).

2.2.5.2. Metastatic disease

About 20-25% of patients diagnosed with EwS show metastatic disease at diagnosis, whereby lungs (10% of cases) and bone/bone marrow (10% of cases) are the most frequent metastatic sites (Casali et al., 2018). Patients harboring metastases at diagnosis receive treatment according to the same regimens as patients showing localized disease or are subjected to randomized clinical trials that aim

for outcome improvement (Casali et al., 2018; Grünewald et al., 2018). However, in metastatic disease, responses are not as durable as in case of localized disease (Casali et al., 2018). Generally, also treatment of the primary lesion (as described in subsection 'Local control') was shown to be appropriate in metastatic disease (Casali et al., 2018; Haeusler et al., 2010). Whole-lung irradiation (WLI) is associated with slightly better overall survival in patients harboring only primary lung metastases (Bölling et al., 2008; Casali et al., 2018; Grewal et al., 2020). In this case, no benefit from high-dose chemotherapy without WLI compared to conventional chemotherapy with WLI was evident (Dirksen et al., 2019). Pulmonary metastasectomy can be discussed, but its prognostic role is not yet finally clear (Cariboni et al., 2019; Casali et al., 2018).

2.2.5.3. Relapse

Prognosis in case of local or metastatic EwS relapse is usually fatal (Casali et al., 2018). Resection of local recurrence may be benificial, but requires prospective evaluation (Xue et al., 2019). Accumulated dose limit of doxorubicin has often already been reached and no standardized chemotherapy protocols are established for relapsed EwS yet, but suggested regimens for example include cyclophosphamide with topotecan, irinotecan with temozolomide, or high-dose ifosfamide (Casali et al., 2018; Ferrari et al., 2009; Hunold et al., 2006; Salah et al., 2020; Wagner et al., 2007). Prospective evaluation of therapy regimens for relapsed EwS is still ongoing (Casali et al., 2018; Grünewald et al., 2018).

2.2.6. Prognosis

Using the current multimodal treatment regimens, in case of localized disease 5-year overall survival is ~60-80% and in case of metastatic disease 5-year overall survival is ~20-40% (Casali et al., 2018; Grünewald et al., 2018). Patients exhibiting multiple bone metastases show worse 5-year overall survival rates as compared to patients exhibiting lung metastases (<20% vs. ~20-40%, respectively) (Casali et al., 2018; Grünewald et al., 2018). Moreover, other prognostic factors associated with adverse outcome, such as large tumor volume/size, elevated levels of LDH in the serum, tumor localization at a non-extremity site, age older than 15 years, weak histological response after neo-adjuvant chemotherapy, and no/incomplete surgical treatment of the primary site, were identified (Casali et al., 2018). In case of relapse, only time to relapse was found to be a prognostic factor: relapse occurrence later than two years after initial diagnosis is associated with favorable outcome (Casali et al., 2018).

2.3. V-Myb avian myeloblastosis viral oncogene homolog-like 2 (MYBL2)

2.3.1. MYB family of transcription factors

The MYB transcription factor family encompasses three members: MYB (alias c-MYB or c-Myb), MYBL1 (alias A-MYB or A-Myb), and MYBL2 (alias B-MYB or B-Myb), of which MYB was first discovered as the mammalian homolog of the v-Myb retroviral oncogene that has been shown to cause leukemia in birds and to have transforming properties in hematopoietic cells (Musa et al., 2017; Ness, 2003; Roussel et al., 1979). The MYB family members differ in their expression patterns: MYB is mainly expressed in hematopoietic cells, colonic crypts, and brain (Musa et al., 2017; Shin et al., 2001; Zorbas et al., 1999), whereby MYBL1 expression is evident in certain regions of the developing central nervous system, germinal B-lymphocytes, and reproductive systems of both genders (Musa et al., 2017; Toscani et al., 1997; Trauth et al., 1994). As compared to specific tissue expression patterns of MYB and MYBL1, MYBL2 is expressed in almost all proliferating tissues (Musa et al., 2017; Ness, 2003). In line with this, deregulation of MYB and MYBL1 expression is described in specific cancer entities related to their tissue-specific expression, such as several leukemia subtypes (MYB and MYBL1), colon cancer (MYB), and Burkitt lymphoma (MYBL1), whereas MYBL2 deregulation is evident in a broad variety of cancer entities (Golay et al., 1996; Musa et al., 2017; Ramsay and Gonda, 2008).

2.3.2. Regulation of MYBL2 expression during cell cycle

On the transcriptional level, MYBL2 expression is regulated by the DREAM complex, composed of the **D**imerization partner (DP1, 2, or 3), the **R**B-like proteins p130 or p107, **E**2F 4 or 5, **a**nd the **M**ulti-vulval class B core (MuvB, which is itself a multiprotein complex consisting of LIN9, LIN37, LIN52, LIN54, and RBBP4) (Musa et al., 2017; Sadasivam and DeCaprio, 2013). The DREAM complex is central in coordination of gene expression during cell cycle and in repression of genes during cellular quiescence (Musa et al., 2017; Sadasivam and DeCaprio, 2013). Physiologically, when a cell enters the cell cycle, p130 or p107 dissociate from MuvB and from repressing E2Fs (4 or 5) as a result of a loss of DYRK1A-dependent LIN52 phosphorylation, which in turn allows activating E2Fs (1, 2, or 3) the transactivation of G1/S genes, such as MYBL2, which becomes consequently expressed in late G1 and S phase (Musa et al., 2017; Sadasivam and DeCaprio, 2013) (**Figure 6**). However, in cellular quiescence MYBL2 expression is suppressed by the DREAM complex and additionally, on a post-transcriptional level, by

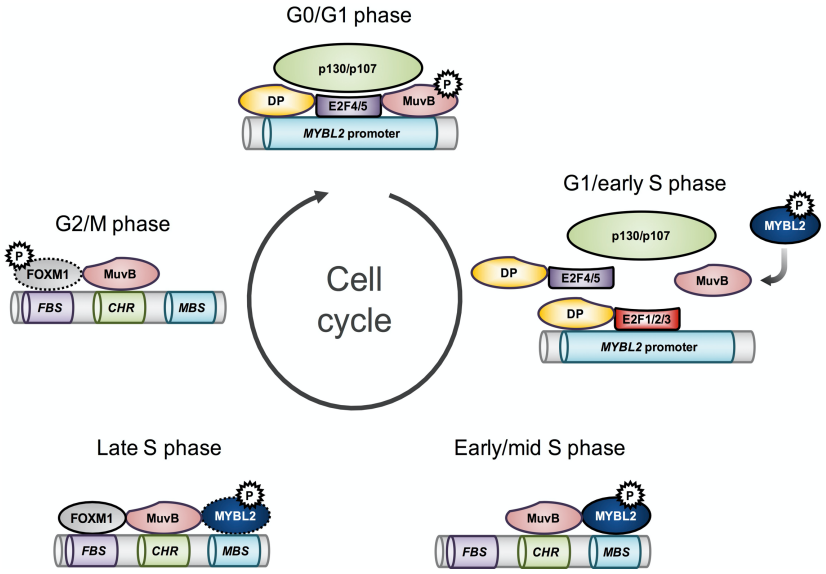

Figure 6: MYBL2 expression and sequential assembly with its cooperative binding partners MuvB and FOXM1 during cell cycle. MYBL2 expression is repressed by the DREAM complex in G0 and early G1 phase. Due to loss of LIN52 (part of the MuvB core) phosphorylation by DYRK1A, the DREAM complex dissociates in G1 and early S phase. Subsequently, MYBL2 is expressed and activated due to phosphorylation by Cyclin A/E-CDK2. Following its expression and activation, MYBL2 assembles with MuvB to functionally cooperate in transactivation of predominantly G2 and M phase genes in early and mid S phase. This functional cooperation is complemented by FOXM1 in late S phase, forming the MYBL2-MuvB-FOXM1 complex. Due to increasing contemporary proteasomal degradation of MYBL2, MuvB-FOXM1 complexes are predominant in G2 and M phase, which is accompanied by increasing FOXM1 activation through phosphorylation. Degradation of FOXM1 in an APC/C-CDH1-dependent manner in M phase leads to dissociation of remaining MuvB-FOXM1 complexes. Figure from Musa et al., 2017.

micro RNAs (miRNAs) (Martinez and Dimaio, 2011; Musa et al., 2017). Post-translational activation of MYBL2 is on the one hand regulated via post-translational modifications and on the other hand by direct protein-protein interactions (Morita et al., 2020; Musa et al., 2017; Werwein et al., 2019). In late G1 and S phase, MYBL2 is initially phosphorylated and thereby activated by CDK2-Cyclin A/E, which releases the nuclear receptor co-repressors N-CoR and SMRT from MYBL2, which keep MYBL2 inhibited when unphosphorylated (Johnson et al., 1999; Li and McDonnell, 2002; Musa et al., 2017; Sala et al., 1997). Recent evidence supports a model in which after the initial priming CDK2-Cyclin A/E-dependent phosphorylation of MYBL2 subsequent phosphorylation by PLK1 as well plays a role in MYBL2 activation (Werwein et al., 2019). Additionally, p300, a co-activating protein, may increase the transactivation capabilities of MYBL2 by direct interaction and acetylation, whereby the latter also seems to at least partly depend on prior phosphorylation by CDK2-Cyclin A (Musa et al., 2017; Schubert et al., 2004). However, Cyclin D1 in contrary was shown to reduce the transactivation capabilities of MYBL2 by directly interfering with the p300-MYBL2 interaction and thereby reducing its acetylation by p300

(Horstmann et al., 2000; Johnson et al., 2002; Musa et al., 2017; Schubert et al., 2004). However, a number of additional other co-activators (e.g. PARP1, ZPR9, or TAF(II)250) and co-repressors (e.g. p107, p57, or CDK9), have been shown to functionally converge in regulating the transactivational activity of MYBL2 (Musa et al., 2017).

2.3.3. MYBL2 in cell cycle regulation

2.3.3.1. Association and dissociation of the MYBL2-MuvB-FOXM1 complex

When expressed and activated in late G1 and S phase, MYBL2 directly binds the promoters of its target genes that are mainly expressed in G2 and M phase (Musa et al., 2017). MYBL2 targets include genes playing a key role in cell cycle regulation (such as *CCNB1* (Cyclin B1), *CDK1*, or *CCNA2* (Cyclin A2)), cell survival (such as *BCL2*, *CLU* (Clusterin), or *BIRC5* (Survivin)), cell differentiation (such as *NANOG*, *POU5F1* (OCT-4), or *SOX2*), and invasion/metastasis formation (such as *SNAI1* (SNAIL)) (Cervellera et al., 2000; Grassilli et al., 1999; Knight et al., 2009; Musa et al., 2017; Tao et al., 2015; Tarasov et al., 2008a; Zhan et al., 2012; Zhu et al., 2004). However, it has been shown that MuvB, a part of the DREAM complex that is dissociating upon cell cycle entry, and FOXM1 (see section 'Regulation of MYBL2 expression during cell cycle' for details) collaborate with MYBL2 in transactivation of these genes, which is supported by the fact that MYB binding sites (MBS), cell cycle genes homology region (CHR, binding motif for LIN54 that belongs to MuvB) elements, and FOXM1 binding sites (FBS) altogether can be found in the promoters of respective genes (Musa et al., 2017; Sadasivam and DeCaprio, 2013; Sadasivam et al., 2012). The following model has been proposed: as soon as the DREAM complex dissociates when a cell enters the cell cycle, MYBL2 is expressed and consequently activated (Musa et al., 2017; Sadasivam and DeCaprio, 2013; Sadasivam et al., 2012). In early and mid S phase it interacts with MuvB, a part of the former DREAM complex (Musa et al., 2017; Sadasivam and DeCaprio, 2013; Sadasivam et al., 2012). Knockdown of either MuvB components or MYBL2, as well as MBS or CHR motif depletion, reciprocally diminish target promoter binding of the respective other, indicating the interdependency of both partners in transactivation of their target genes (Knight et al., 2009; Müller et al., 2012; Musa et al., 2017; Sadasivam et al., 2012). In late S phase, FOXM1 is additionally recruited to the MYBL2-MuvB complex, whereby MYBL2 undergoes increasing proteasomal degradation (Charrasse et al., 2000; Musa et al., 2017; Sadasivam and DeCaprio, 2013; Sadasivam et al., 2012). As a result, in G2 and M phase MuvB-FOXM1 complexes are predominant, accompanied by increasing

phosphorylation/activation of FOXM1 (Fu et al., 2008; Musa et al., 2017; Sadasivam and DeCaprio, 2013; Sadasivam et al., 2012). However, FOXM1 suppression does not affect binding of MYBL2 to its target gene promoters, but *vice versa*, suppression of MYBL2 or LIN9 (part of the MuvB core) inhibits FOXM1 binding to its target gene promoters, suggesting that the MYBL2-MuvB complex is crucial for FOXM1 target gene promoter binding, but FOXM1 is not reciprocally necessary for MYBL2-MuvB target gene promoter binding (Musa et al., 2017; Sadasivam et al., 2012). Due to the low affinity of the DNA binding domain of FOXM1 to the FBS and the fact that FOXM1 promoter binding depends on MYBL2-MuvB and their respective MBS and CHR binding sites, MYBL2-MuvB is thought to be necessary to increase the target specificity of FOXM1 (Musa et al., 2017; Sadasivam and DeCaprio, 2013). In M phase, FOXM1 is increasingly degraded via an APC/C-CDH1-dependent mechanism, leading to dissociation of remaining MuvB-FOXM1 complexes (Musa et al., 2017; Park et al., 2008) (**Figure 6**).

2.3.3.2. Functional properties of MYBL2 in cell cycle progression

Early studies have already described an association between MYBL2 and cell proliferation (Arsura et al., 1992; Musa et al., 2017). Despite the fact that some of the early pioneer studies suggested a role for MYBL2 in G1/S progression (Iwai et al., 2001; Lin et al., 1994; Musa et al., 2017), over the years it became increasingly clear that MYBL2 plays a predominant role in G2/M progression: knockdown experiments in human cell lines, as well as knockout experiments of the *MYBL2* homolog *DMyb* in *Drosophila melanogaster*, showed a reduction in cell proliferation, a reduction of G2/M gene expression, and a reduced fraction of cells in G2/M phase (Katzen et al., 1998; Musa et al., 2017; Okada et al., 2002; Osterloh et al., 2007; Papetti and Augenlicht, 2011; Pilkinton et al., 2007; Santilli et al., 2005; Tarasov et al., 2008a). Although *DMyb* is the only homolog of the *MYB* gene family in *Drosophila*, it is phylogenetically as well as functionally equivalent to vertebrate *MYBL2*, which makes it a reasonable model for vertebrate *MYBL2* function (Davidson et al., 2005; Musa et al., 2017). These experiments in *Drosophila* furthermore remarkably showed that a loss-of-function mutation of *DMyb* leads to mitotic failure resulting in aneuploidy, indicating that MYBL2 is needed to sustain an adequate proliferation rate in order to preserve genomic stability (Fung et al., 2002; Manak et al., 2002; Musa et al., 2017; Shepard et al., 2005; Tarasov et al., 2008a). Consistently, further data in human cells showing that MYBL2 alterations are associated with various chromosomal aberrations converging in structural chromosomal instability support these finding in *Drosophila* (García and Frampton, 2006; Musa et al., 2017; Pfister et

al., 2018). Mechanistically, this may be at least in part mediated by complex formation of MYBL2, Clathrin, and Filamin, necessary for proper Clathrin localization at the mitotic spindle, leading to kinetochore fiber stabilization (Musa et al., 2017; Yamauchi et al., 2008), and furthermore, it may be mediated by MYBL2 transactivating *PRC1*, a gene encoding for a central protein in regulation of cytokinesis which was shown to be associated with chromosomal instability when deregulated (Li et al., 2018; Musa et al., 2017). However, apart from its role during mitosis, MYBL2 is additionally implicated in proper DNA replication and thus protection from DNA damage during S phase, which is, at least partly, mediated through adequate transactivation of *MYC* and *FOXM1* by MYBL2 (Bayley et al., 2018; García and Frampton, 2006; Lorvellec et al., 2010; Musa et al., 2017).

2.3.4. MYBL2 in regulation of cell survival

The association between MYBL2 and cell survival has been already described early on (Musa et al., 2017). This effect is to a major extent mediated by MYBL2 transactivating a specific set of genes important in regulation of cell survival, but may to a lower extent also be mediated by direct protein-protein interactions of MYBL2 (Musa et al., 2017). However, regulation of cell survival by MYBL2 via target gene transactivation appears to be cell type-dependent: in the majority of cell types MYBL2 has a survival-promoting function, but exhibits survival-impeding functions in cells derived from neural origin subjected to apoptotic stimulation (Musa et al., 2017) (**Figure 7**).

2.3.4.1. Survival-promoting function via transactivation of target genes

In murine T cells that depend on Interleukin 2 (IL-2), it has been shown that overexpression of MYBL2 leads to increased BCL-2 expression, which thereby decreases dependency on cytokines and promotes resistance toward apoptosis induced by doxorubicin, dexamethasone, and ceramide (Grassilli et al., 1999; Musa et al., 2017). Accordingly, overexpression of MYBL2 in a human B cell line not expressing BCL-2, leads to BCL-2 expression and conversely, MYBL2 depletion in an acute lymphoblastic leukemia cell line reduces BCL-2 expression and induces apoptosis (Lang et al., 2005; Musa et al., 2017). However, MYBL2 was shown to furthermore regulate the expression of *CLU* (Clusterin, alias Apolipoprotein J), that mediates resistance toward doxorubicin-induced apoptosis in neuroblastoma

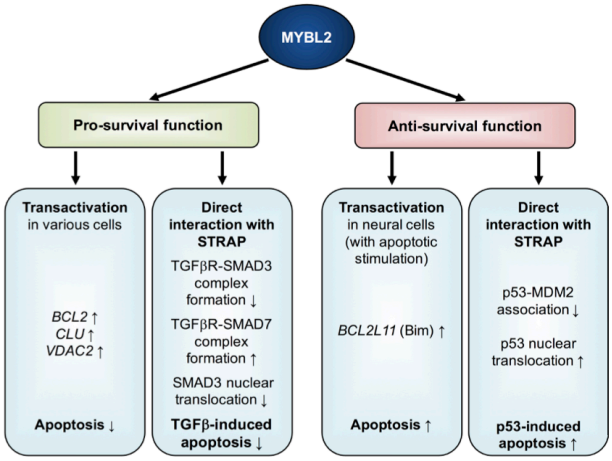

Figure 7: Regulation of cell survival by MYBL2. MYBL2 predominantly exerts pro-survival functions, which are described in numerous cell types, but can as well exert anti-survival functions, mainly reported in apoptotic stimuli-exposed cells of neural origin. Both of these functions may be regulated by direct transactivation of target genes implicated in cell survival (such as *BCL2*, *CLU*, *VDAC* (pro-survival), or *BCL2L11* (anti-survival)) or may be regulated by direct protein-protein interaction with STRAP. Interaction of MYBL2 with STRAP may on the one hand lead to an inhibition of TGF-β-induced apoptosis by impeding TGF-β receptor-SMAD3 complex formation and enhancing TGF-β receptor-SMAD7 complex formation which consequently prevents SMAD3-translocation into the nucleus after TGF-β1 stimulation (pro-survival), or on the other hand increase p53-induced apoptosis by reducing the association of p53 and MDM2 which leads to increased nuclear translocation of p53 (anti-survival). Figure from Musa et al., 2017.

(Cervellera et al., 2000; Musa et al., 2017). These results are confirmed by a study showing that *CLU* expression by MYBL2 is enhanced after exposure to thermal cell stress and may be seen as a protective mechanism to thermal injury (Musa et al., 2017; Santilli et al., 2005). Furthermore, MYBL2 was shown to enhance cell survival by suppressing autophagy in oocytes through transactivation of the autophagy-inhibitor VDAC2 (Musa et al., 2017; Yuan et al., 2015) (**Figure 7**).

2.3.4.2. Survival-impeding function via transactivation of target genes

In contrast to the survival-promoting function of MYBL2, it appears to have a contrary function regarding cell survival regulation mainly in cells derived from neural origin. In pheochromocytoma cells, as well as cortical and sympathetic neurons, knockdown of MYBL2 is protecting against nerve growth factor (NGF) withdrawal-induced or DNA damage-induced cell death (Liu et al., 2004; Musa et al., 2017). Moreover, MYBL2 was shown to transactivate the apoptosis-promoting gene *Bcl2l11* (BIM) in rat neurons (Greene et al., 2007; Musa et al., 2017) and is mandatory in β-Amyloid-induced BIM expression and cell death which is pathophysiologically implicated in Alzheimer´s disease (Biswas et al., 2007; Musa et al., 2017). In *Drosophila*, apoptosis of sensory organ precursor daughter cells is promoted by DMyb, indicating an

evolutionary conservation of this MYBL2 function (Musa et al., 2017; Rovani et al., 2012). The following model has been proposed for the role of MYBL2 in cell survival of murine neurons, which may as well be translatable to mammals: under basal conditions the *Mybl2* promoter is occupied by the repressive E2F4-p130 complex inhibiting MYBL2 expression and thereby protecting neurons from cell death, whereby cell stress leads to dissociation of this complex and activating E2F1 may promote MYBL2 expression and thus neuronal cell death, potentially via promotion of BIM expression by MYBL2 (Greene et al., 2007; Iyirhiaro et al., 2014; Musa et al., 2017). However, also in non-neural TGF-β1-treated M1 myeloid leukemia cell lines that overexpress MYBL2, apoptosis induced by TGF-β1 was found to be accelerated (Bies and Wolff, 1995; Musa et al., 2017) (**Figure 7**).

2.3.4.3. Protein-protein interactions

Independent of its function as a transcription factor, MYBL2 may regulate cell survival via direct protein-protein interaction with the serine-threonine kinase receptor-associated protein (STRAP) (Musa et al., 2017; Seong et al., 2011). MYBL2 appears to be a positive regulator of STRAP, which may on the one hand exert a survival-promoting, and on the other hand a survival-impeding function (Musa et al., 2017; Seong et al., 2011). MYBL2 supports STRAP-mediated association of the TGF-β receptor with SMAD7 and dissociation of the TGF-β receptor with SMAD3, causing inhibition of TGF-β-induced SMAD3 nuclear translocation, which subsequently results in blockage of TGF-β signaling pathways that mediate growth inhibition and apoptosis (pro-survival function) (Musa et al., 2017; Seong et al., 2011). On the contrary, MYBL2 co-expression can stimulate STRAP-mediated nuclear translocation of p53, apoptosis-induction by p53, and cell cycle arrest via decreased association of p53 with MDM2 (anti-survival function) (Musa et al., 2017; Seong et al., 2011) (**Figure 7**).

2.3.5. MYBL2 in regulation of cell differentiation and stem cell properties

Various studies indicate a role for MYBL2 in maintenance of a proliferative but undifferentiated, stem cell-like, cellular phenotype (Musa et al., 2017). Differentiation of human myeloid cell lines, as well as neural and glial retinoic acid-induced differentiation of murine neuroblastoma cells, is associated with decreasing MYBL2 levels, and furthermore, conversely, constitutive MYBL2 expression is able to prevent neural differentiation of murine neuroblastoma cells by retinoid acid (Arsura et al., 1994; Musa

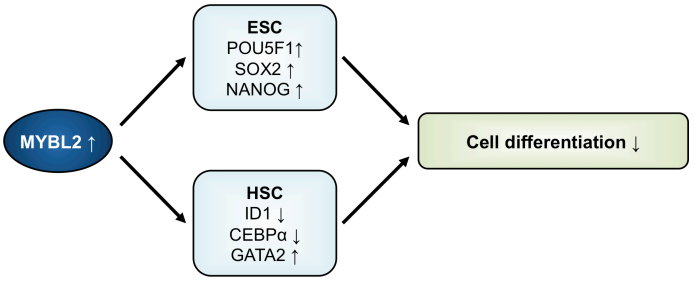

Figure 8: MYBL2 in regulation of cell differentiation and stem cell properties. High MYBL2 expression was shown to be associated with a low degree of cellular differentiation in numerous studies. Most mechanistic studies have been performed in embryonic stem cells (ESC) or hematopoietic stem cells (HSC), which have shown that MYBL2 may regulate the expression of important mediators of cellular differentiation, such as POU5F1, SOX2, NANOG, ID1, CEBPα, and GATA2, in a manner that MYBL2 promotes the cellular maintenance of an undifferentiated, proliferative, and pluripotent state. Figure from Musa et al., 2017.

et al., 2017; Raschellà et al., 1995). In line with this, p130, a protein of the DREAM complex suppressing the *Mybl2* promoter during cellular quiescence (see section 'Regulation of MYBL2 expression during cell cycle' for details), is upregulated during cellular differentiation, accompanied by reduced MYBL2 levels in murine neuroblastoma cells (Musa et al., 2017; Raschellà et al., 1998). In a number of different cell types, such as in leukemia cell lines, keratinocytes, male gonocytes, and intestinal epithelial cells, similar results associate MYBL2 with maintenance of an undifferentiated phenotype (Bies et al., 1996; Latham et al., 1996; Maruyama et al., 2014; Musa et al., 2017; Papetti and Augenlicht, 2011). Most mechanistic studies regarding the role of MYBL2 in cell differentiation were conducted in embryonic stem cells (ESC) and hematopoietic stem cells (HSC) (Musa et al., 2017) (**Figure 8**). In ESC, MYBL2 was proposed to guide a transcriptional network ensuring self-renewal and maintenance of pluripotency (Musa et al., 2017; Zhan et al., 2012). In this regard, MYBL2 was shown to upregulate the expression of *POU5F1*, *SOX2*, and *NANOG*, which are genes encoding for key regulators of differentiation and pluripotency (Musa et al., 2017; Tarasov et al., 2008a, 2008b; Zhan et al., 2012) (**Figure 8**). Consistently, in HSC, MYBL2 impairs the expression of *ID1* and *CEBPα*, genes involved in promotion of cell differentiation, and to upregulate *GATA2*, encoding for a transcription factor promoting cell proliferation and inhibiting cell differentiation (Baker et al., 2014; Briegel et al., 1993; Musa et al., 2017) (**Figure 8**). Taken together, these studies demonstrate that MYBL2 supports the maintenance of an undifferentiated, pluripotent, but proliferative condition (Musa et al., 2017). In contrary to the majority of previous studies, a recent study described a role for MYBL2 in prohibiting somatic reprogramming of cells by blocking factors inducing pluripotency (Ward et al., 2018), indicating that future studies are needed to clarify a potential dual role of MYBL2 in regulation of cellular differentiation.

2.3.6. MYBL2 in cancer

Given the physiological role of MYBL2 in regulation of cell cycle progression, cell survival, and cell differentiation, its deregulation can contribute to tumor initiation and/or progression, predominantly by driving uncontrolled cell proliferation, as well as therapy resistance and metastatic spread (Musa et al., 2017) (**Figure 9**). In line with this, MYBL2 overexpression is associated with unfavorable patient outcome in various cancer entities, such as breast cancer, colorectal cancer, acute myeloid leukemia, as well as neuroblastoma, and thus may serve as a prognostic biomarker (Fuster et al., 2013; Inoue and Fry, 2016; Musa et al., 2017; Raschellà et al., 1999; Ren et al., 2015).

2.3.6.1. Mechanisms driving deregulation of MYBL2 expression in cancer

Deregulation of MYBL2 in cancer is mainly driven via three mechanisms. First, copy number variations of the chr20q13 locus may alter MYBL2 expression (Lassmann et al., 2007; Musa et al., 2017; Shi et al., 2011; Tanner et al., 2000). Amplification of the respective locus leading to MYBL2 overexpression is occurring in numerous cancer entities, such as breast cancer, colorectal cancer, and ovarian cancer (Lassmann et al., 2007; Musa et al., 2017; Shi et al., 2011; Tanner et al., 2000). Second, deregulations in expression of specific miRNAs that are able to suppress MYBL2 on a post-transcriptional level are frequently found in cancer, and can thereby contribute to MYBL2 level alterations (Deng et al., 2008; Fuster et al., 2013; Martinez and Dimaio, 2011; Musa et al., 2017; Papetti and Augenlicht, 2011; Wu et al., 2013; Yu et al., 2014; Zauli et al., 2011). Third, deregulations of transcriptional MYBL2 repression by the DREAM complex may lead to alterations in MYBL2 expression (Musa et al., 2017). This may occur for example by aberrant p53 signaling or by transformation through the human papillomavirus (HPV) 16 E7 oncoprotein (Musa et al., 2017). Aberrations in p53 signaling are frequently observed in cancers (Stracquadanio et al., 2016). Under physiological conditions, p53 activates p21, preventing phosphorylation of p130 by CDKs, which thereby promotes DREAM complex assembly and suppresses *MYBL2* on a transcriptional level (Fischer et al., 2016a; Musa et al., 2017; Quaas et al., 2012). This p53-p21-DREAM complex axis is especially active when cells are exposed to stress, as for example DNA damage (Fischer et al., 2015; Musa et al., 2017). Accordingly, MYBL2 upregulation is frequent in p53-mutant cancers (Musa et al., 2017; Parikh et al., 2014). Constitutive MYBL2 expression can bypass G1 checkpoint arrest induced by p53 and G2 checkpoint arrest induced by DNA damage in p53-mutated cells (Lin et al., 1994; Mannefeld et al., 2009; Musa et al., 2017). The HPV16 E7 oncoprotein can

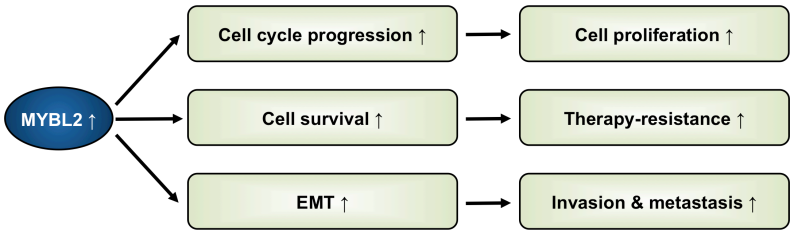

Figure 9: The role of MYBL2 in cancer progression and/or initiation. MYBL2 upregulation drives cell cycle progression, cell survival, and epithelial-to-mesenchymal transition (EMT), consequently promoting cell proliferation, therapy-resistance, and invasion/metastasis formation, respectively. Figure from Musa et al., 2017.

mechanistically lead to DREAM complex disassembly by binding to p130 and thus promoting its proteasomal degradation (Musa et al., 2017; Nor Rashid et al., 2011; Pang et al., 2014; Zhang et al., 2006), and consistently, MYBL2 levels are found to be upregulated in HPV16-immortalized cells (Musa et al., 2017; Yang et al., 1997). Furthermore, apart from its role in DREAM complex disassembly, E7 can bind the MYBL2-MuvB-FOXM1 complex, and thereby cooperate in transactivation of cell cycle genes (Musa et al., 2017; Pang et al., 2014), and interestingly, in E7-transformed cells, MYBL2 can bypass G1 checkpoint arrest induced by DNA-damage via CDK1 upregulation and can rescue oncogene-induced senescence most likely through $p16^{INK4A}$ suppression (Fan and Chen, 2014; Huang et al., 2011; Martinez and Dimaio, 2011; Mowla et al., 2014; Musa et al., 2017). In conclusion, MYBL2 expression can be deregulated on a genomic level by CNAs, on a transcriptional level by alterations in DREAM complex assembly, and on a post-transcriptional level by alterations in expression of certain miRNAs (Musa et al., 2017).

2.3.6.2. Deregulation of proliferation

As MYBL2 physiologically drives proliferation in non-malignant proliferative tissues, but is found to be deregulated in numerous cancer entities (see sections ‘MYBL2 in cell cycle regulation‘ and ‘MYBL2 in cancer‘ for details), it appears that altered MYBL2 levels contribute to aberrations of cell cycle progression and cell proliferation in cancer, as for example described in cervical cancer, colorectal cancer, hepatocellular carcinoma, leukemia, lung adenocarcinoma, and neuroblastoma (MYCN-amplified) (Calvisi et al., 2011; Gualdrini et al., 2010; Iltzsche et al., 2017; Musa et al., 2017; Nor Rashid et al., 2011; Ren et al., 2015; Zauli et al., 2011).

2.3.6.3. Mediation of therapy resistance

Resistance to radiation and/or systemic therapy is a major challenge in cancer treatment (Holohan et al., 2013; Kim et al., 2015). As described above (see section ‘MYBL2 in regulation of cell survival‘ details), overexpression of MYBL2 in murine T cells that depend on IL-2 leads to increased BCL-2 expression, and thereby promotes resistance toward apoptosis induced by doxorubicin, dexamethasone, and ceramide (Grassilli et al., 1999; Musa et al., 2017). In neuroblastoma, MYBL2 furthermore regulates the expression of *CLU* (Clusterin, alias Apolipoprotein J), mediating resistance toward doxorubicin-induced apoptosis (Cervellera et al., 2000; Musa et al., 2017). These studies are in accordance with the findings that genetic suppressor element (GSE)-induced resistance to cytostatic drugs, such as aphidicolin, hydroxyurea, cytarabine, etoposide, doxorubicin, and mafosfamide, leads to upregulation of MYBL2 in fibrosarcoma cells (Levenson et al., 2000; Musa et al., 2017). However, MYBL2 not exclusively mediates chemotherapy resistance, but also confers resistance to DNA damage-induced apoptosis as for example caused by irradiation: in p53-wildtype cancers, DNA damage induces DREAM complex assembly via the p53-p21 axis and blockage of MYBL2 expression through DREAM, whereas in p53-mutated cancers, proper activation of respective axis and DREAM complex assembly fails, leading to continuous MYBL2 expression that may overcome G2 checkpoint arrest induced by DNA-damage (see section ‘Mechanisms driving deregulation of MYBL2 expression in cancer‘ for details) (Fischer et al., 2015, 2016a; Mannefeld et al., 2009; Musa et al., 2017; Quaas et al., 2012). Consistently, chicken B cells that lack MYBL2 were shown to be more sensitive to DNA damage elicited by alkylation and UV irradiation (Ahlbory et al., 2005; Musa et al., 2017), and similarly, EwS cells in which MYBL2 can quickly be degraded upon UV irradiation soon go into apoptosis, whereas in neuroblastoma cells MYBL2 levels do not change upon UV irradiation and the cells exhibit apoptosis resistance (Musa et al., 2017; Schwab et al., 2007). As in neuroblastoma MYBL2 appears to be hypophosphorylated and as overexpression of a MYBL2 mutant that is not phosphorylatable protects HEK293 cells from apoptosis induced by UV irradiation, it was proposed that a decrease of CDK2-Cyclin A-dependent phosphorylation of MYBL2, leading on the one hand to less MYBL2 activation but on the other hand also to less proteasomal degradation, may facilitate cell survival as mediated by MYBL2 (Musa et al., 2017; Schwab et al., 2007). In line with these results, cell survival promoting functions of MYBL2 has been described for several further cancer entities, as for example colorectal cancer, hepatocellular carcinoma, and leukemia (Calvisi et al., 2011; Musa et al., 2017; Ren et al., 2015; Vrana et al., 1999).

2.3.6.4. Mediation of invasion and metastatic spread

Suppression of MYBL2 in mouse ESC was shown to be associated with dispersion of cell colonies into single cells and with decreased cell adhesion to the cell culture dish (Iwai et al., 2001; Musa et al., 2017). Mechanistically, it has been proposed that MYBL2 suppression leads to reduced expression of Integrin β-1 on the cell surface, which then leads to reduced adhesion of the cell to proteins of the extracellular matrix, as for example Laminin, Collagen, and Fibronectin (Iwai et al., 2001; Musa et al., 2017). However, in contrast to this early study, MYBL2 has been shown to mediate epithelial-to-mesenchymal transition (EMT) in breast cancer: knockdown of MYBL2 was shown to restore epithelial marker (E-cadherin) expression, cell-cell junctions, and to inhibit cell invasion as well as anchorage-independent growth, and *vice versa*, MYBL2 overexpression decreased epithelial marker expression but promoted mesenchymal marker expression (Musa et al., 2017; Tao et al., 2015). This effect of MYBL2 on EMT mechanistically may be mediated by upregulation of the key EMT regulating protein SNAIL (Musa et al., 2017; Tao et al., 2015). In support of these findings, *MYBL2* transcripts were shown to be overexpressed in metastases derived from prostate cancer xenografts as compared to locally growing xenografts (Bar-Shira et al., 2002; Musa et al., 2017), and *MYBL2* expression was detectable in matched metastases from *MYBL2*-negative primary renal cell carcinomas (Musa et al., 2017; Sakai et al., 1993).

2.4. The concept of ‘oncogenic cooperation‘

Recently, several studies from research fields beyond oncology showed that polymorphisms of regulatory elements located in the non-protein-coding genome can modify the impact of a certain somatic mutations/events on disease phenotypes and treatment effectiveness (Genetic Modifiers of Huntington’s Disease (GeM-HD) Consortium, 2015; Musa and Grünewald, 2019; Soccio et al., 2015; Vu et al., 2015). Indeed, as such disease modifying polymorphisms may constitute a key source of inter-tumoral heterogeneity, their characterization may be a useful tool to predict disease course, patient outcome, as well as treatment effectiveness, in order to adapt diagnosis and therapy to individual risk profiles in the context of precision medicine (Musa and Grünewald, 2019). However, although regulatory variants in the non-protein-coding genome impacting on disease phenotypes might constitute a general mechanism, they may be especially of relevance in pediatric oncology, as pediatric cancers harbor a low frequency of somatic mutations in the protein-coding genome as compared to adulthood cancers,

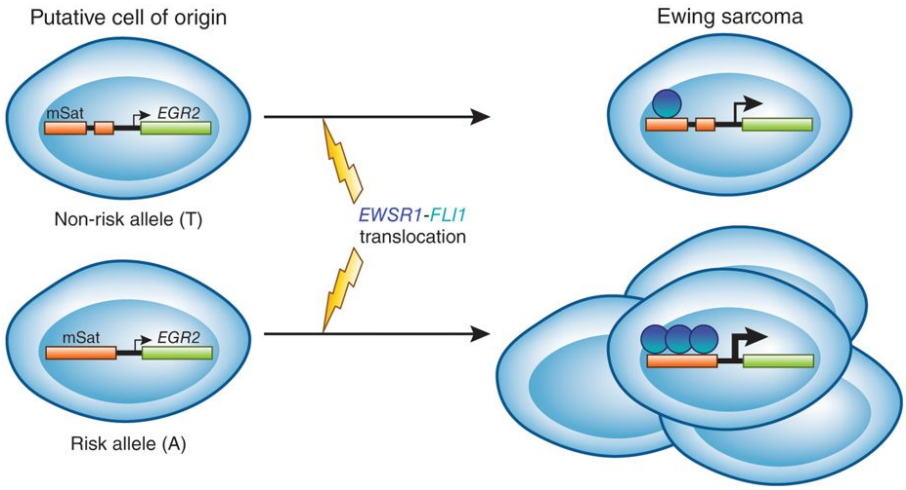

Figure 10: 'Oncogenic cooperation' impacting on EwS susceptibility. A single nucleotide polymorphism (SNP) in an enhancer-like GGAA-microsatellite (mSat) via which EWSR1-FLI1 steers the expression of the pro-proliferative gene *EGR2* may modify the number of consecutive GGAA-repeats at this respective locus and thereby modifies its enhancer activity and the extent of *EGR2* expression. The frequency of the risk allele varies between ethnic populations harboring different EwS incidences, whereby a high allele frequency of the risk allele is associated with higher EwS incidence, which indicates a role for the interaction between EWSR1-FLI1 and regulatory germline variants in EwS susceptibility. Figure from Gomez et al., 2015, commenting on Grünewald et al., 2015.

which cannot solely explain the wide range of clinical courses and outcomes that are observed (Brohl et al., 2014; Crompton et al., 2014; Gröbner et al., 2018; Musa and Grünewald, 2019; Musa et al., 2019; Tirode et al., 2014). In EwS, it has been shown that the interaction between a somatic mutation, leading to the expression of the pathognomonic fusion transcription factor EWSR1-FLI1, and a regulatory variant, a SNP (rs79965208) in an enhancer-like GGAA-mSat via which EWSR1-FLI1 drives the expression of the pro-proliferative gene *EGR2*, can influence susceptibility to EwS (Grünewald et al., 2015) (**Figure 10**). This SNP modifies the number of consecutive repeats of the respective GGAA-mSat and thereby its enhancer activity as well as *EGR2* expression levels (Grünewald et al., 2015). Notably, the risk allele A connects adjacent GGAA-repeats to a longer non-disrupted stretch of consecutive GGAA-repeats with preferential EWSR1-FLI1 binding, whereby the protective T allele disrupts the consecutive stretch (Grünewald et al., 2015), and consistently, the risk allele A shows a significantly higher allele frequency in non-African populations as compared to African populations, which may at least partly explain the higher EwS incidence in non-Africans as compared to Africans and implies a role of *EGR2* and the respective SNP in the associated GGAA-mSat in EwS susceptibility (Grünewald et al., 2015). However, whether such so-called 'oncogenic cooperation' between somatic mutations and regulatory germline variants only influences cancer susceptibility/initiation or may also determine cancer progression remained largely unclear (Musa and Grünewald, 2019). For this reason, the recently

published study that is mainly underlying this thesis was specifically designed to clarify the potential impact of ‘oncogenic cooperation‘ as a major source of inter-tumoral heterogeneity on tumor progression, patient survival, and drug response, in order to evaluate the implication of such mechanism for future diagnostic and therapeutic strategies in the context of precision oncology (Musa et al., 2019).

3. AIMS AND OBJECTIVES

1. **Aim:** Identification of functionally and clinically relevant genes regulated via an ‘oncogenic cooperation‘ between EWSR1-FLI1 and polymorphic GGAA-microsatellites (mSats) in EwS.

   Objectives:

   1. Identification of genes strongly regulated by EWSR1-FLI1 via analysis of a published microarray gene expression dataset generated from a EwS cell line containing a doxycycline (DOX)-inducible shRNA directed against *EWSR1-FLI1* profiled with and without previous DOX treatment.
   2. Identification of genes whose high intra-tumoral expression is associated with poor overall EwS patient survival via analysis of microarray gene expression data from 166 primary EwS with matched clinical annotations using the custom code software GenEx.
   3. Definition of the top candidate gene most strongly regulated by EWSR1-FLI1 whose high intra-tumoral expression is at the same time most significantly associated with poor overall EwS patient survival using datasets as described in objectives 1 and 2 (of aim 1).
   4. Identification of a potential regulatory GGAA-mSat bound by EWSR1-FLI1 nearby the candidate gene (identified as described in objective 3 of aim 1) showing epigenetic signs of an active enhancer, using published EWSR1-FLI1, H3K4me1, and H3K27ac chromatin immunoprecipitation and DNA sequencing (ChIP-seq) data as well as DNase I hypersensitive sites sequencing (DNAse-seq) data of one to two EwS cell lines.
   5. Validation of the EWSR1-FLI1-dependent enhancer activity of the candidate GGAA-mSat identified as described in objective 4 (of aim 1) via cloning of respective mSat haplotypes from genomic cell line DNA into a luciferase reporter vector and subsequent performance of luciferase reporter assays in a EwS cell line containing a DOX-inducible shRNA directed against *EWSR1-FLI1* treated with or without DOX.
   6. Validation of the regulatory capacity of the GGAA-mSat identified as described in objective 4 (of aim 1) regarding candidate gene expression *in vitro* using Clustered Regularly Interspaced Short Palindromic Repeats interference (CRISPRi) with the respective GGAA-mSat and subsequent determination of candidate gene expression via quantitative real-time polymerase chain reaction (qRT-PCR) in a EwS cell line.
   7. Validation of the association between the number of consecutive GGAA-repeats of the GGAA-mSat identified as described in objective 4 (of aim 1) and intra-tumoral candidate gene

expression as well as evaluation of the inheritance of the GGAA-mSat alleles via the germline in primary EwS by analysis of whole genome sequenced (WGS) matched germline/tumor DNA pairs with corresponding tumor gene expression data (e.g. by expression quantitative trait loci (eQTL) analysis).

8. Evaluation of the distinctness of the candidate gene as a mediator of ‘oncogenic cooperation‘ via identification of the top five additional genes fulfilling the criteria as described in objectives 1-3 (of aim 1), and subsequent identification of potential regulatory GGAA-mSats nearby these genes as described in objective 4 (of aim 1), as well as performance of eQTL analyses for such potential loci as described in objective 7 (of aim 1) if applicable.

2. Aim: Functional characterization of the identified candidate gene (see aim 1) in EwS.

Objectives:

1. Characterization of the functional role of the candidate gene regarding cell proliferation, cell cycle progression, cell survival, and clonogenic growth *in vitro* by RNA interference (RNAi) using non-targeting negative control siRNAs and non-targeting DOX-inducible negative control shRNAs as well as siRNAs and DOX-inducible shRNAs directed against the candidate gene in two to three EwS cell lines.
2. Characterization of the functional role of the candidate gene regarding tumor growth *in vivo* using subcutaneous (s.c.) xenografts of two EwS cell lines containing either a DOX-inducible non-targeting control shRNA or a DOX-inducible specific shRNA directed against the candidate gene, each treated with or without DOX in NSG mice.

3. Aim: Obtaining mechanistic insights into the mode of action of the identified candidate gene in EwS.

Objectives:

1. Identification of potential functionally relevant mediators acting downstream of the candidate gene using ‘omics‘-based profiling of three EwS cell lines with and without candidate gene knockdown. The choice of method depends on the functional role of the candidate gene.
2. Validation of the clinical relevance of the downstream mediators identified as described in objective 1 (of aim 3) via analysis of microarray gene expression data from 166 primary EwS with matched clinical annotations using the custom code software GenEx.

3. Validation of the functional relevance of identified downstream mediators using siRNA-mediated knockdown of those mediators in order to investigate their ability to phenocopy the effect of the candidate gene knockdown in two EwS cell lines.

4. Aim: Evaluation of the upregulation of the identified candidate gene via ‘oncogenic cooperation‘ as a potential therapeutic vulnerability in EwS.

Objectives:

1. Evaluation of targeted therapy effectiveness depending on the expression of the candidate gene *in vitro*, using two small molecule inhibitors directed against either the candidate gene itself (if possible) or relevant mediators of its up- or downstream regulatory network in cell viability assays of a EwS cell line containing either a DOX-inducible non-targeting negative control shRNA or a DOX-inducible specific shRNA directed against the candidate gene, each treated with or without DOX.
2. Evaluation of targeted therapy effectiveness depending on candidate gene expression *in vivo*, using intraperitoneal (i.p.) injection of a small molecule inhibitor directed against either the candidate gene itself (if possible) or relevant players of its up- or downstream regulatory network in mice subcutaneously xenografted with a EwS cell line containing a DOX-inducible shRNA directed against the candidate gene treated with or without DOX.

4. MATERIALS AND METHODS

4.1. Materials

4.1.1. Manufacturers

Manufacturer	City and country
Abcam	Cambridge, UK
Accuri	Ann Arbor, USA
Addgene	Cambridge, USA
Agilent	Santa Clara, USA
Air Liquide Medical	Düsseldorf, Germany
Alpha Innotech	Miami, USA
American Type Culture Collection (ATCC)	Manassas, USA
Applied Biosystems	Foster City, USA
B. Braun	Melsungen, Germany
Becton Dickinson (BD)	Franklin Lakes, USA
Bela-pharm	Vechta, Germany
Bemis	Neenah, USA
Bio-Rad	Hercules, USA
Bio-Techne	Minneapolis, USA
Biochrom	Berlin, Germany
Biosan	Riga, Latvia
Biozym	Hessisch Oldendorf, Germany
Bosch	Gerlingen, Germany
Brand	Wertheim, Germany
Broad Institute	Cambridge, USA
Brooks Life Sciences	Chelmsford, USA
Campingaz	Hattersheim, Germany
Carl Roth	Karlsruhe, Germany
Cell Signaling	Danvers, USA
Charles River Laboratories	Wilmington, USA
Children's Oncology Group (COG)	Monrovia, USA
Corning	Corning, USA
DeNovix	Wilmington, USA
Diagenode	Seraing (Ougrée), Belgium
Eppendorf	Munich, Germany
Epson	Suwa, Japan
Eurofins	Ebersberg, Germany
Fiji	Madison, USA
GE Healthcare	Chicago, USA
German Collection of Microorganisms and Cell lines (DSMZ)	Brunswick, Germany
Gilson	Middleton, USA
GraphPad Software	San Diego, USA
Greiner	Kremsmünster, Austria

H. Kerndl	Weißenfeld, Germany
Hartenstein	Würzburg, Germany
Hettich	Tuttlingen, Germany
Illumina	San Diego, USA
Integra	Zizers, Switzerland
Invivogen	San Diego, USA
Kern & Sohn	Balingen-Frommern, Germany
Kimberly-Clark	Irving, USA
Köttermann	Uetze, Germany
Leica	Wetzlar, Germany
Machery-Nagel	Düren, Germany
Matsunami Glass	Bellingham, USA
Meditrade	Kiefersfelden, Germany
Memmert	Schwabach, Germany
Merck	Darmstadt, Germany
Microsoft	Redmond, USA
Miele	Gütersloh, Germany
NanoEnTek	Seoul, Korea
Neolab	Heidelberg, Germany
New England Bio Labs	Ipswich, USA
Nordcap	Bremen, Germany
Peqlab	Erlangen, Germany
PJK Biotech	Kleinblittersdorf, Germany
Promega	Madison, USA
Qiagen	Hilden, Germany
Quartett	Berlin, Germany
Santa Cruz	Dallas, USA
Sartorius	Göttingen, Germany
Schott	Mainz, Germany
Scientific Industries	Bohemia, USA
Siemens	Munich, Germany
Sigma	Osterode am Harz, Germany
Sigma-Aldrich	St. Louis, USA
Takara	Kusatsu, Japan
Thermo Fisher Scientific	Waltham, USA
Titertek-Berthold	Pforzheim, Germany
Tocris	Bristol, UK
TPP	Trasadingen, Switzerland
Vector Laboratories	Burlingame, USA
Welch	Monroe, USA
Zeiss	Oberkochen, Germany

4.1.2. Technical equipment and instruments

Device / Equipment	Model specification	Manufacturer
Aspirators	Vacusafe FTA-1	Integra Biosan
Automatic ice maker	SPR-80	Nordcap
Bunsen burners	Labogaz 206 C 206 GLS	Campingaz Campingaz
Calipers	Analog (S14) Digital (S15D)	Hartenstein Hartenstein
Cell counter	Countess II	Invitrogen
Centrifuges	Heraeus Megafuge 40R Heraeus Megafuge 8R 5415R Universal 320 Rotina 320R 4K15C	Thermo Fisher Scientific Thermo Fisher Scientific Eppendorf Hettich Hettich Sigma
Drigalski spatula	Glass	Hartenstein
Electrophoresis gel chambers	Sub-cell GT 40-0911 40-1410 40-0708	Bio-Rad Peqlab Peqlab Peqlab
Electrophoresis gel imager	Multiimage Light Cabinet	Alpha Innotech
Electrophoresis power suppliers	PowerPac 300 Model 200	Bio-Rad Bio-Rad
Flasks and bottles	Erlenmeyer flask (Duran 500ml) Laboratory flask (Duran 1000ml, 500ml, 250ml, 100ml)	Schott
Flow cytometer	Accuri C6	Accuri
Forceps	Anatomical, 200mm Anatomical, 160mm Anatomical, 145mm Anatomical, 130mm Surgical,160mm Surgical, 140mm	Hartenstein
Photo (plate) scanner	Epson Perfection V370 Photo	Epson
Fridges and freezers	4°C, -20°C -80°C	Bosch, Siemens Thermo Fisher Scientific
Hemocytometers	Neubauer Improved	Hartenstein
Incubators	HERAcell 240i Forma 3111 CB-170	Thermo Fisher Scientific Thermo Fisher Scientific Binder
Inoculation loops	2.5mm diameter	Hartenstein
Laminar flow cabinets	Safe 2020 Maxisafe 2020 Herasafe	Thermo Fisher Scientific Thermo Fisher Scientific Thermo Fisher Scientific
Liquid nitrogen tank	Arpege 70	Air Liquide Medical
Manual counter	Analog	Hartenstein

Microscopes	Axiovert 200 Axiovert 25 Axioplan 2 imaging Primovert	Zeiss Zeiss Zeiss Zeiss
Microwave	8201-1	Miele
Multistep pipet	Handy Step	Brand
PCR cyclers	T100 Thermal Cycler Mastercycler pro	Bio-Rad Eppendorf
Pipets	Pipetman 1000µl, 200µl, 100µl, 20µl, 10µl, 2µl	Gilson
Pipetting assistants	Pipetboy 2 Accu-jet pro	Integra Brand
Plate readers	Orion II microplate luminometer Varioskan	Titertek-Berthold Thermo Fisher Scientific
qRT-PCR cycler	CFX Connect	Bio-Rad
Racks	For 15ml and 50ml tubes For 1.5ml and 2ml tubes For cryotubes For PCR tubes	Hartenstein Hartenstein Hartenstein Hartenstein
Scales	GE1302 KB1000-2	Sartorius Kern & Sohn
Scissors	Surgical, 160mm	Hartenstein
Sequencing system	Illumina HiSeq2500	Illumina
Sonication device	Bioruptor Plus	Diagenode
Spectrophotometers	DS-11 Nanodrop ND-1000	DeNovix Peqlab
Table centrifuges	PerfectSpin mini Sprout LSE Spectrafuge 3-180 Qualitron DW-41	Peqlab Biozym Corning Neolab Thermo Fisher Scientific
Thermoblocks and Thermoshakers	Thermomixer comfort Thermomixer compact ThermoStat plus TS-100	Eppendorf Eppendorf Eppendorf Biosan
Transilluminator	Fisherbrand FT-20E/365	Thermo Fisher Scientific
Vacuum manifold	Vac-Man	Promega
Vacuum pump	2522Z-02	Welch
Vortexers	Vortex Genie 2 LSE 7-2020	Scientific Industries Corning Neolab
Water baths	WNB 7 3042	Memmert Köttermann

4.1.3. Consumables

Consumable	Specification	Manufacturer
Cell culture flasks	T150 (150cm^2), T75 (75cm^2), T25 (25cm^2) T175 (175cm^2), T75 (75cm^2), T25 (25cm^2)	TPP Corning
Cell culture plates	96-well, 12-well, 6-well	TPP
Filters	Rotilabo, sterile, 0.45 µm pore size	Carl Roth
Freezing containers	Mr. Frosty	Thermo Fisher Scientific
Gloves	Kimtech, Purple Nitrile Nitril NextGen	Kimberly-Clark Meditrade
Hemocytometers (single use)	C-Chip Neubauer Improved	NanoEnTek
Laboratory film	Parafilm	Bemis
Micropestle	Steel	Hartenstein
Microscope slides	TOMO adhesive glass slide	Matsunami Glass
Needles	Sterican 30G, 23G, 18G	B. Braun
PCR tube strips	4titude	Brooks Life Sciences
Petri dishes	10cm GBO 10cm Nunclon	Greiner Thermo Fisher Scientific
Pipet tips	1250µl, 200µl, 100µl, 20µl, 10µl SurPhob SafeSeal	Biozym
qRT-PCR plate seals	4ti-0560	Brooks Life Sciences
qRT-PCR plates	Framestar, 96-well, semi-skirted	Brooks Life Sciences
Reaction tubes	50ml, 15ml 2ml, 1.5ml TPX Polymethylpentene (PMP) tubes for DNA sonication	Greiner, Falcon Diagenode
Scalpels	Surgical Disposable Scalpels	B. Braun
Serological pipets	25ml, 10ml, 5ml, 2ml Costar	Corning
Syringes	Micro-Fine 30G 0.5ml Injekt 5ml	Becton Dickinson (BD) B. Braun

4.1.4. Chemicals, reagents, and drugs

Chemical / reagent	Specification	Manufacturer
Acetic acid	100%, Rotipuran, 1l	Carl Roth
Agarose	1kg	Carl Roth
Ampicillin	100mg/ml solution	Sigma-Aldrich
Aqua bidestillata (Aqua bidest.)	NA	H. Kerndl
Crystal violet	NA	Sigma-Aldrich
CutSmart buffer	10x	New England Bio Labs

CVT-313	10mg 1mg	Tocris Merck
DAB+ chromogen	NA	Agilent
Dimethyl sulfoxide (DMSO)	Sterile-filtered	Sigma-Aldrich
DNA ladders	GeneRuler 1kb Plus GeneRuler 100bp Plus	Thermo Fisher Scientific
dNTPs	10mM	Sigma-Aldrich
Doxycycline (DOX) (*in vitro*)	Doxycycline hyclate 5mg	Sigma-Aldrich
Doxycycline (DOX) (*in vivo*)	Beladox 1kg	Bela-pharm
Ethanol	≥99.8%, denatured	Carl Roth
Ethidium bromide (EtBr)	500µg/ml solution	Sigma-Aldrich
Ethylenediaminetetraacetic acid (EDTA)	≥99%, 1kg	Carl Roth
Fetal calf serum (FCS)	NA	Sigma-Aldrich
Formaldehyde	Pierce, 16% methanol-free	Thermo Fisher Scientific
G418	100mg/ml	Invivogen
Geltrex	LDEV-Free Reduced Growth Factor Basement Membrane Matrix	Thermo Fisher Scientific
Glycerol	1l	Carl Roth
GoTaq colorless buffer	NA	Promega
GoTaq Hot Start polymerase	NA	Promega
Hydrochloric acid (HCl)	0.1N solution, endotoxin-free	Merck
Hematoxylin counterstain	Based on Gill‘s formulation	Vector Laboratories
Isopropanol	2-Propanol Rotipuran ≥99.8%	Carl Roth
LB powder	LB-Medium (Luria/Miller)	Carl Roth
$MgCl_2$	25mM	Promega
NU6140	50mg 10mg 5mg	Biotechne Tocris Merck
Nuclease-free H_2O	NA	Carl Roth
Opti-MEM	Reduced Serum Medium	Thermo Fisher Scientific
Penicillin/Streptomycin	Penicillin: 10,000U/ml; Streptomycin: 10,000µg/ml	Biochrom
Phosphate-buffered saline (PBS)	Dulbecco, 500ml	Biochrom
Plasmocure	100mg/ml	Invivogen
Propidium iodide (PI)	≥94.0% (HPLC)	Sigma-Aldrich
ProTaqs I Antigen-Enhancer	Main component: citric acid, pH=6.0	Quartett
Puromycin	10mg/ml	Invivogen
Radioimmunoprecipitation assay (RIPA) buffer	Pierce	Thermo Fisher Scientific
RNAse A	Invitrogen PureLink RNase A 20mg/ml	Thermo Fisher Scientific

Roswell Park Memorial Institute (RPMI) 1640 medium	Supplemented with stable glutamine	Biochrom
Sodium acetate	≥99%	Sigma-Aldrich
Sucrose	≥99.5%	Sigma-Aldrich
Super Optimal broth with Catabolite repression (SOC) medium	NA	Takara
SYBR safe	400µl solution	Thermo Fisher Scientific
SYBR Select Mastermix	Contains SYBR GreenER dye, AmpliTaq DNA polymerase UP, dNTPs with dUTP/dTTP-mixture, heat-labile UDG and optimized buffer components	Applied Biosystems
Target Retrieval Solution	Main component: citrate, pH=6.1	Agilent
Transfection reagents	HiPerfect Lipofectamine LTX and Plus Reagent	Qiagen Thermo Fisher Scientific
Trichloroacetic acid	≥99%, 1kg	Sigma-Aldrich
Tris(hydroxymethyl)aminomethane (TRIS)	≥99%, Cryst., 1kg	Carl Roth
Trypan blue	0.4%	Sigma-Aldrich, Thermo Fisher Scientific
Trypsin	(10x) Trypsin (1:250)/EDTA-Solution (0,5%/0,2 %)	Biochrom

4.1.5. Commercial kits

Usage	Kit	Components	Manufacturer
Cloning of pGL3-Promoter-Fluc vector	In-Fusion HD Cloning Kit	5x In-Fusion HD Enzyme Premix, linearized pUC19 Control Vector (50ng/µl), 2kb Control Insert (40ng/µl)	Takara
DNA extraction from agarose electrophoresis gel	NucleoSpin Gel and PCR Clean-up	Binding Buffer NTI, Wash Buffer NT3 (concentrate), Elution Buffer NE, NucleoSpin Gel and PCR Clean-up Columns (yellow rings), Collection Tubes (2ml)	Machery-Nagel
Firefly luciferase detection	Beetle-Juice Luciferase Assay Firefly	Lysis-Juice (2x), Beetle-Juice fluid, D-Luciferine substrate for Firefly luciferase, ATP Cofactor	PJK Biotech
Fluorescein isothiocyanate (FITC)-Annexin V/ PI staining	BD Pharmingen FITC Annexin V Apoptosis Detection Kit II	Annexin V Binding Buffer (10x), purified recombinant Annexin V, FITC-Annexin V, propidium iodide (PI) staining solution	Becton Dickinson (BD)

Genomic DNA extraction	NucleoSpin Tissue	Lysis Buffer T1, Lysis Buffer B3, Wash Buffer BW, Wash Buffer B5 (concentrate), Elution Buffer BE, Proteinase K (lyophilized), Proteinase Buffer PB, NucleoSpin Tissue Columns (light green rings), Collection Tubes (2ml)	Machery-Nagel
Plasmid DNA extraction	PureYield Plasmid Midiprep	Neutralization Solution (NSB), PureYield Binding Columns, PureYield Clearing Columns, Endotoxin Removal Wash, Column Wash, Cell Resuspension Solution (CRA), Cell Lysis Solution (CLA), Nuclease-Free Water	Promega
Renilla luciferase detection	Renilla-Juice Luciferase Assay	Lysis-Juice (2x), Renilla-Juice fluid, Coelenterazine substrate for Renilla luciferase, Reconstruction Buffer for Coelenterazine; pH value adjustment was performed using 1.8ml of 25% HCl (not included in kit) per provided Renilla-Juice in order to adapt pH for dual luciferase measurement	PJK Biotech
Reverse transcription	High-Capacity cDNA Reverse Transcription Kit	10x RT Buffer, 10x RT Random Primers, 25x dNTP Mix (100mM), MultiScribe Reverse Transcriptase (50U/µl)	Applied Biosystems
RNA extraction	NucleoSpin RNA	Lysis Buffer RA1, Wash Buffer RAW2, Wash Buffer RA3 (concentrate), Membrane Desalting Buffer MDB, Reaction Buffer for rDNase, rDNase (RNase-free, lyophilized), RNase-free H_2O, NucleoSpin Filters (violet rings), NucleoSpin RNA Columns (light blue rings - plus Collection Tubes), Collection Tubes (2ml), Collection Tubes (1.5ml)	Machery-Nagel
ChIP-seq	iDeal ChIP-seq Kit for Transcription Factors	Protease inhibitor cocktail, 5% BSA (DNA-free), Rabbit IgG, ChIP-seq grade CTCF antibody, ChIP-seq grade H19 imprinting control region primer pair (human), ChIP-seq grade Myoglobin exon 2 primer pair (human), Carrier, Glycine, Shearing Buffer iS1b, DiaMag protein A-coated magnetic beads, Wash Buffer iW1-4, ChIP-seq grade water, Elution Buffer iE2, Fixation buffer, Wash Buffer 1 and 2, Buffer C, IPure Beads v2, Elution Buffer iE1, 5x ChIP Buffer iC1b, Lysis Buffer iL1b, Lysis Buffer iL2	Diagenode

4.1.6. Media, buffers, and solutions

Name	Usage	Composition
Cell culture medium	Culturing of human cell lines	RPMI 1640 (500ml), FCS (10%), Penicillin (100U/ml), Streptomycin (100µg/ml)
Electrophoresis gel (agarose)	Agarose gel for DNA electrophoresis	1x TAE buffer (100-200ml), agarose (0.8-1.5%), EtBr (5-10µl) or SYBR Safe (5-10µl)
Flow cytometry buffer	Suspending of cells for flow cytometry	PBS, FCS (2%)
Formalin	Fixation of tissues	4% aqueous formaldehyde solution
Lysogeny broth (LB) medium	Culturing of bacteria	LB (Luria/Miller): 25g diluted in 1l of Aqua bidest., then autoclave sterilization
Propidium iodide (PI) solution	Cell cycle analysis by flow cytometry	Flow cytometry buffer, PI (50µg/ml), RNAse A (20µg/ml)
TRIS, acetic acid, and EDTA (TAE) buffer	Running buffer for DNA gel electrophoresis	10x TAE buffer: 48.4g trishydroxymethylaminomethane (TRIS), 11.4ml acetic acid (17.4M), 3.7g EDTA, 1000ml of deionized water

4.1.7. Human cell lines, bacteria, and mouse model

4.1.7.1. Human cell lines

Cell line	Origin	Provenience
A673	EwS, primary, muscle, 15-year-old female	American Type Culture Collection (ATCC)
A673/TR/shEF1 (alias Asp114)	See A673	Provided by Dr. Javier Alonso (Insituto de Salud Carlos III, Madrid, Spain)
CHLA-10	EwS, metastasis post-chemotherapy, thoracic lymph node, 14-year-old caucasian female, 1987	Children’s Oncology Group (COG)
EW1	EwS, metastasis, pleural effusion, 19-year-old male	Provided by Dr. Olivier Delattre (Institut Curie, Paris, France)
EW16	EwS, male	Provided by Dr. Olivier Delattre (Institut Curie, Paris, France)
EW17	EwS	Provided by Dr. Olivier Delattre (Institut Curie, Paris, France)
EW18	EwS	Provided by Dr. Olivier Delattre (Institut Curie, Paris, France)
EW22	EwS	Provided by Dr. Olivier Delattre (Institut Curie, Paris, France)

EW23	EwS	Provided by Dr. Olivier Delattre (Institut Curie, Paris, France)
EW24	EwS	Provided by Dr. Olivier Delattre (Institut Curie, Paris, France)
EW3	EwS, metastasis, pleural effusion, 14-year-old male	Provided by Dr. Olivier Delattre (Institut Curie, Paris, France)
EW7	EwS, metastasis, pleural effusion, 20-year-old female	Provided by Dr. Olivier Delattre (Institut Curie, Paris, France)
HEK293T	Human embryonic kidney, transformed, fetus, female	American Type Culture Collection (ATCC)
LAP35	EwS, 12-year-old female	Provided by Dr. Olivier Delattre (Institut Curie, Paris, France)
MHH-ES1	EwS, metastasis, ascites, 12-year-old male	German Collection of Microorganisms and Cell lines (DSMZ)
MIC	EwS	Provided by Dr. Olivier Delattre (Institut Curie, Paris, France)
ORS	EwS	Provided by Dr. Olivier Delattre (Institut Curie, Paris, France)
POE	EwS	Provided by Dr. Olivier Delattre (Institut Curie, Paris, France)
RDES	EwS, primary, humerus, 19-year-old male, 1984	German Collection of Microorganisms and Cell lines (DSMZ)
RH1	EwS, metastasis, bone marrow, male	German Collection of Microorganisms and Cell lines (DSMZ)
SK-ES1	EwS, primary, 18-year-old male, 1971	German Collection of Microorganisms and Cell lines (DSMZ)
SK-N-MC	EwS, metastasis, supraorbital, 14-year-old female, 1971	German Collection of Microorganisms and Cell lines (DSMZ)
STA-ET1	EwS, 13-year-old female	Provided by Dr. Olivier Delattre (Institut Curie, Paris, France)
STA-ET8	EwS	Provided by Dr. Olivier Delattre (Institut Curie, Paris, France)
TC-32	EwS, primary, 31-months-old female	Children’s Oncology Group (COG)
TC-71	EwS, primary post-chemotherapy, humerus, 22-year-old male, 1981	Children’s Oncology Group (COG)

4.1.7.2. Bacteria

Name	Bacteria of origin	Manufacturer
Stellar competent cells	E. coli	Takara
SURE2 supercompetent cells	E. coli	Agilent

4.1.7.3. Mouse model

Name	Genetic deficiencies	Manufacturer
NOD scid gamma (NSG) mice	NOD/ShiLtJ background (several deficiencies in innate immunity); severe combined immune deficiency mutation (scid); IL-2 receptor gamma chain deficiency (disabling cytokine signaling)	Charles River Laboratories

4.1.8. Plasmids and oligonucleotides

4.1.8.1. Plasmids

Name	Decription	Manufacturer
pGL3-Promoter-Fluc	Luciferase reporter vector (Firefly luciferase)	Promega
pGL3-Rluc (pRL)	Luciferase control reporter vector (Renilla luciferase)	Promega
pHAGE TRE dCas9-KRAB	Lentiviral vector for DOX-inducible expression of dCas9 fused to the Krüppel associated box (KRAB) domain	Addgene
pLKO Tet-On	Lentiviral vector for DOX-inducible expression of shRNAs	Addgene
pLKO.1-puro U6 sgRNA BfuAI large stuffer	Lentiviral vector for expression of gRNAs	Addgene
pCMV-VSV-G	Lentiviral envelope vector	Addgene
pCMV-dR8.91	Lentiviral packaging vector	Provided by Dr. Olivier Delattre (Institut Curie, Paris, France)

4.1.8.2. Small interfering RNAs (siRNAs)

Target gene	siRNA number	Sense sequence (5‘-3‘)	Antisense sequence (5‘-3‘)	Manufacturer
Negative control	Mission Universal Negative Control #1	No sequence available	No sequence available	Sigma Aldrich
MYBL2	siRNA #1	GCAGAGGACAGUAUCAACAtt	CGUCUCCUGUCAUAGUUGUtt	Eurofins
	siRNA #2	GAUCUGGAUGAGCUGCACUtt	CUAGACCUACUCGACGUGAtt	Eurofins
	siRNA #4	CGAGCUGGUUAAGAAGUAUtt	GCUCGACCAAUUCUUCAUAat	Eurofins

	siRNA #6	AGAAGUACUCCAU GGACAAtt	UCUUCAUGAGGUAC CUGUUga	Eurofins
CCNF	siRNA #1	GGAGGACAGAUGU GUCAGAtt	UCUGACACAUCUGU CCUCCtt	Eurofins
	siRNA #2	UAGCCUACCUCUA CAAUGAtt	UCAUUGUAGAGGUA GGCUAtt	Eurofins
BIRC5	siRNA #1	GCAUUCGUCCGG UUGCGCUtt	AGCGCAACCGGACG AAUGCtt	Eurofins
	siRNA #2	GAAUUUGAGGAAA CUGCGAtt	UCGCAGUUUCCUCA AAUUCtt	Eurofins
AURKB	siRNA #1	CGCGGCACUUCAC AAUUGAtt	UCAAUUGUGAAGUG CCGCGtt	Eurofins
	siRNA #2	GGUGAUGGAGAAU AGCAGUtt	ACUGCUAUUCUCCA UCACCtt	Eurofins

4.1.8.3. Short hairpin RNAs (shRNAs)

Target gene	**shRNA number**	**Top sequence (5‘-3‘)**	**Bottom sequence (5‘-3‘)**	**Manufacturer**
Negative control	shRNA #1	CCGGCAACAAGATG AAGAGCACCAACTC GAGTTGGTGCTCTT CATCTTGTTGTTTTT	AATTAAAAACAACAA GATGAAGAGCACCA ACTCGAGTTGGTGC TCTTCATCTTGTTG	Eurofins
MYBL2	shRNA #4	CCGGCTCGAGCTGG TTAAGAAGTATCTCG AGATACTTCTTAACC AGCTCGAGTTTTT	AATTAAAAACTCGAG CTGGTTAAGAAGTAT CTCGAGATACTTCTT AACCAGCTCGAG	Eurofins
	shRNA #6	CCGGCCAGAAGTAC TCCATGGACAACTC GAGTTGTCCATGGA GTACTTCTGGTTTTT	AATTAAAAACCAGAA GTACTCCATGGACA ACTCGAGTTGTCCA TGGAGTACTTCTGG	Eurofins
EWSR1-FLI1	shRNA #1	CCGGGCAGCAGAAC CCTTCTTATGACTCG AGTCATAAGAAGGG TTCTGCTGCTTTTTG	AATTCAAAAAGCAGC AGAACCCTTCTTATG ACTCGAGTCATAAGA AGGGTTCTGCTGC	Eurofins

4.1.8.4. Guide RNAs (gRNAs)

Target	**gRNA number**	**Sequence (5‘-3‘)**	**Manufacturer**
Control	gRNA #1	ACCGCGCCAAACGTGCCCTGACGG	Eurofins
MYBL2 mSat	gRNA #1	ATGTCTTGAAGTCGTGGGC	Eurofins
	gRNA #2	CTCTGTTGCTGGAGTACAG	Eurofins

4.1.8.5. Primers

Target gene	Forward (5‘-3‘)	Reverse (5‘-3‘)	Manufacturer
AURKB	ACCCTTTGAGAGTG CATCAC	CTTGAGCAGTTTGG AGATGAG	Eurofins
BIRC5	CCACCGCATCTCTA CATTCAAG	CAAGTCTGGCTCGT TCTCAG	Eurofins
CCNF	CCCCGAAGATGTGC TCTTTCA	GCCTTCATTGTAGA GGTAGGCT	Eurofins
EWSR1-FLI1	GCCAAGCTCCAAGT CAATATAGC	GAGGCCAGAATTCA TGTTATTGC	Eurofins
KIF20A	GTTGTGTCCGTATT GAGAATGTG	GATGCCTGTCCCAC TTCTG	Eurofins
MKI67	AAAAGAATTGAACCT GCGGAAG	AGTCTTATTTTGGCG TCTGGAG	Eurofins
MYBL2	GTCCCCTGTCACTG AGAATAG	GCTCCAATGTGTCC TGTTTG	Eurofins
MYBL2 mSat primer with In-Fusion overhang	CTAGCCCGGGCTCG AGCAACCAGGTTTC TGGCTCTAA	GATCGCAGATCTCG AGTATAGTCCACCT CTGGGTAAGG	Eurofins
MYBL2 mSat primer without In-Fusion overhang	CAACCAGGTTTCTG GCTCTAA	TATAGTCCACCTCTG GGTAAGG	Eurofins
PIF1	GGTAAGGTACACAG ATTTGAGGC	CCCGAGACACCGAT AAGTTTT	Eurofins
RPLP0	GAAACTCTGCATTCT CGCTCC	GGTGTAATCCGTCT CCACAG	Eurofins
GL primer 2 (sequencing primer)	CTTTATGTTTTTGGC GTCTTCCA	NA	Promega
pLKO Tet-On (insert amplification)	GGCAGGGATATTCA CCATTAT	CTATTCTTTCCCCTG CACTG	Eurofins
pLKO-Tet-On (sequencing primer)	GGCAGGGATATTCAC CATTATCGTTTCAGA	NA	Eurofins

4.1.9. Restriction enzymes

Name	Manufacturer
AgeI-HF (20U)	New England Bio Labs
EcoRI-HF (20U)	New England Bio Labs
EcoRV-HF (20U)	New England Bio Labs
HindIII-HF (20U)	New England Bio Labs
XhoI (20U)	New England Bio Labs

4.1.10. Antibodies

4.1.10.1. Western blot

Target	Antibody type	Species / Clonality	Identification	Manufacturer
MYBL2	Primary	Rabbit / polyclonal	sc-725	Santa Cruz
FLI1	Primary	Rabbit / monoclonal	ab133485	Abcam
β-actin	Primary	Mouse / monoclonal	A-5316	Sigma-Aldrich
Anti-Rabbit IgG	Secondary (HRP-coupled)	Donkey	Amersham ECL NA9340	GE Healthcare
Anti-Mouse IgG	Secondary (HRP-coupled)	Sheep	Amersham ECL NA9310	GE Healthcare

4.1.10.2. Immunohistochemistry (IHC)

Target	Antibody type	Species / Clonality	Identification	Manufacturer
p-MYBL2	Primary	Rabbit / monoclonal	ab76009	Abcam
Cleaved caspase 3 (CC3)	Primary	Rabbit / polyclonal	ab133485	Cell Signaling
Anti-Rabbit IgG	Secondary (HRP-coupled)	Horse	MP-7401	Vector Laboratories

4.1.10.3. Chromatin immunoprecipitation and DNA sequencing (ChIP-seq)

Target	Antibody type	Species / Clonality	Identification	Manufacturer
p-MYBL2	Primary	Rabbit / monoclonal	ab76009	Abcam
FLI1	Primary	Rabbit / polyclonal	ab15289	Abcam

4.1.11. Software and interfaces

Name	Version	Usage	Provider
Accuri C6 software	NA	Flow cytometry data collection and analysis	Accuri
Bowtie2	NA	Alignment of ChiP-seq reads to the human reference genome	Freely available, Johns Hopkins University
Brainarray chip description files (CDF)	v20	RMA-based normalization of Affymetrix microarray gene expression data	Freely available, University of Michigan

BWA-MEM	v0.7.8	Alignment of WGS reads on reference genome	Freely available, Wellcome Trust Sanger Institute
ComBat	NA	Removal of batch effects in microarray data analysis	Freely available, Dana-Farber Cancer Institute
DESeq2	v1.18.0	Sample-to-sample normalization and differential expression analyses of RNA-seq data	Freely available, European Molecular Biology Laboratory (EMBL)
Fiji / ImageJ	NA	Analysis of histological images	Freely available, University of Wisconsin at Madison
GenEx	v2015 v2016.5 v2017.10	Automated Kaplan-Meier analyses using microarray gene expression and matched survival data	Custom code (provided by Julia S. Gerke; Grünewald laboratory, Munich, Germany)
Genome Analysis Toolkit	v.2.8.1	Indel realignment and base quality score recalibration of WGS data	Freely available, Broad Institute
GraphPad PRISM	v5	Data collection, analysis, and visualization	GraphPad Software
GSEA tool	NA	Gene set enrichment analysis	Freely available, Broad Institute
HipSTR	v.0.6.2	Haplotype calling of repetitive sequences in WGS data	Freely available, New York Genome Center
HTSeq-count	vHTSeq-0.5.3p9	Counting of RNA-seq reads on annotated genes from the GRCh37 gene build	Freely available, European Molecular Biology Laboratory (EMBL)
IGV genome browser	v2.4.10	Visualization of ChIP-seq data	Freely available, Broad Institute
Aperio ImageScope	v12.4	Visualization of scanned histological slides	Leica
MACS2	NA	ChIP-seq peak calling	Freely available, Dana-Farber Cancer Institute
Microsoft Excel	v14.7.6	Data collection, analysis, and visualization	Microsoft

PAVIS	v1.8	ChIP-seq peak annotation	Freely available, National Institutes of Health (NIH)
R	NA	Environment for statistical computing and graphics	Freely available, The R Foundation
SAMtools	NA	Spanning read extraction and haplotype mapping of EWSR1-FLI1 ChIP-seq data	Freely available, Wellcome Trust Sanger Institute
TopHat	v2.0.6	Alignment of RNA-seq reads to the reference genome	Freely available, Johns Hopkins University
UCSC genome browser	NA	Broad usage in displaying genomic information and visualization of ChIP-seq data	Freely available, University of California Santa Cruz (UCSC)

4.2. Methods

4.2.1. Cell culture conditions

Human cell lines (see section ‘Human cell lines, bacteria, and mouse model‘ for details) were cultured in RPMI 1640 growth medium containing stable glutamine, 10% fetal calf serum (FCS), 100U/ml penicillin, and 100µg/ml streptomycin. Cells were incubated in humidified atmosphere at 37°C with 5% CO_2. Routine culturing of cells was performed in T175, T150, T75, or T25 cell culture flasks, experimental *in vitro* procedures were carried out in either 96-, 12-, or 6-well plates. Cell line identity was verified by short tandem repeat (STR) profiling and cell lines were regularly tested for mycoplasma infection by nested polymerase chain reaction (PCR).

4.2.2. Transient transfection

For transient transfection of plasmids, 2 x 10^5 cells were seeded in 1.8 ml of growth medium in a 6-well plate and transfected 24 hours after seeding. Per well of a 6-well plate, plasmid DNA was transfected using a mixture of 1µg plasmid DNA, 200µl Opti-MEM, 2µl of Plus Reagent, and 2.5µl of Lipofectamine LTX (regarding plasmid transfection for lentivirus production see section ‘Production of lentiviruses, cell transduction, and single cell cloning‘) (**Table 1**).

Reagent	Volume
Plasmid DNA (1µg)	Depending on DNA concentration
Opti-MEM	200µl
Plus Reagent	2µl
Lipofectamine LTX	2.5µl

Table 1: Reaction for transfection of plasmid DNA. Volumes relate to transfection of one well of a 6-well plate.

After mixing of plasmid DNA, Opti-MEM, and Plus Reagent, the mixture was incubated for 10 minutes at room temperature, and after subsequent addition of Lipofectamine LTX, the mixture was incubated for further 25 minutes. Following incubation, the mixture was given on top of 1.8ml of growth medium in which the cells were seeded per well of a 6-well plate. Growth medium containing the components for transfection was exchanged for fresh medium 4 hours after transfection. For siRNA transfection, 1.5 x 10^5 cells were seeded in a 6-well plate in 1.6ml of growth medium and transfected with a siRNA concentration of 25-65nM (depending on the cell line and the siRNA) using HiPerfect immediately after seeding. To achieve this, per 6-well plate, 324-337µl of RPMI 1640 growth medium was mixed with 2.6-6.7µl of siRNA (20µM stock siRNA concentration), and 5.2-13.5µl of HiPerfect, prior to transfection in order to get final concentrations of 25-65nM in the well (exemplified in **Table 2**).

Reagent	Volume (25nM)	Volume (65nM)
RPMI 1640	337µl	324µl
siRNA (20µM)	2.6µl	6.7µl
HiPerfect	5.2µl	13.5µl

Table 2: Reaction for transfection of siRNAs. Volumes relate to transfection of one well of a 6-well plate. Reactions for achieving final siRNA concentrations of 25nM and 65nM are exemplified here.

After mixing the components, the mixture was incubated for 12 minutes at room temperature and subsequently given on top of 1.6ml of growth medium in which the cells were seeded per well of a 6-well plate immediately before transfection. 4 hours after transfection, 6ml of growth medium was added per well to reduce HiPerfect toxicity. 48 hours after siRNA transfection, medium was changed and a re-transfection was performed. 4 hours after re-transfection, the transfection medium was exchanged for fresh medium (1.4ml per well of a 6-well plate). For details of the experimental assay design see sections ‘Luciferase reporter assays‘ and ‘Proliferation assays‘. Plasmids and siRNAs used are described in section ‘Plasmids and oligonucleotides‘. In case of siRNA transfection, if necessary, RNA was extracted

from the samples at the end of the experimental procedure as described in section ‘Extraction of RNA‘, reverse transcription of respective RNA was performed as described in section ‘Reverse transcription‘, and knockdown evaluation by quantitative real-time polymerase chain reaction (qRT-PCR) was performed as described in section ‘Quantitative real-time polymerase chain reaction (qRT-PCR)‘ (see section ‘Plasmids and oligonucleotides‘ for primer sequences).

4.2.3. Production of lentiviruses, cell transduction, and single cell cloning

Per produced lentivirus, HEK293T cells (2 x 10^6 per flask) were seeded with 10ml of growth medium in a T75 cell culture flask. 24 hours after seeding, the cells were transfected using a mixture of 10µg of the pLKO Tet-On vector (lentiviral transfer plasmid) containing the cloned shRNA (see section ‘Cloning of pLKO Tet-On constructs‘ for details), 10µg of the lentiviral packaging plasmid pCMV-dR8.91, 3µg of the lentiviral envelope plasmid pCMV-VSV-G, 4.6ml of Opti-MEM, 46µl of Plus reagent, and 60µl of Lipofectamine LTX (**Table 3**).

Reagent	Volume
pLKO Tet-On vector containing cloned shRNA (transfer plasmid) (10µg)	Depending on DNA concentration
pCMV-dR8.91 (packaging plasmid) (10µg)	Depending on DNA concentration
pCMV-VSV-G (envelope plasmid) (3µg)	Depending on DNA concentration
Opti-MEM	4.6ml
Plus Reagent	46µl
Lipofectamine LTX	60µl

Table 3: Reaction for transfection of plasmids required for lentivirus production. Volumes relate to transfection of one T75 flask.

After mixing of plasmid DNA, Opti-MEM, and Plus Reagent, the mixture was incubated for 10 minutes at room temperature, and after subsequent addition of Lipofectamine LTX, the mixture was incubated for further 25 minutes at room temperature. 4.4ml of this reaction was applied on the seeded HEK293T cells. The medium containing all transfection components was removed after 4 hours of incubation and exchanged for fresh growth medium. 48 hours thereafter, the supernatant was filtered using a 0.45µm filter and collected in a 15ml reaction tube. 24 hours before lentiviral transduction, 5 x 10^5 of the required EwS cells (A673 and SK-N-MC) were seeded per lentivirus transduction in 4.5ml of growth medium in a T25 flask and were transduced with 500µl of lentivirus-containing supernatant. The cells were incubated with respective lentiviruses for 3 days and then selected with 1.5µg/ml puromycin in three selection sweeps of each 3 days with a break of 2 days between each sweep. For single cell cloning,

the harvested cells were either seeded at a very low density (1 x 10^3 cells per petri dish) in 10ml of growth medium in a petri dish or in 100µl of growth medium per well in a 96-well plate (1 cell per well). Seeded cells were monitored daily, picked using trypsin as soon as they were detectable as a single cell colony by eye, and afterwards expanded. To evaluate the presence of a *MYBL2* knockdown, each single cell clone was seeded in two wells of a 6-well plate (1.5 x 10^5 cells per well) in 2ml of growth medium per well treated either with or without doxycycline (DOX) (1µg/ml) for 48 hours. Afterwards, cells were lysed, RNA was extracted (see section 'Extraction of RNA' for details), RNA was reversely transcribed (see section 'Reverse transcription' for details), and the presence and quantity of a *MYBL2* knockdown was validated by qRT-PCR (see section 'Quantitative real-time polymerase chain reaction (qRT-PCR)' for details) for each single cell clone. Single cell clones showing no significant *MYBL2* knockdown upon DOX-treatment in case of non-targeting negative control shRNAs, or single cell clones with optimum knockdown efficiency upon DOX-treatment (knockdown onto ~5-50% remaining *MYBL2* expression) in case of cells transduced with pLKO Tet-On vectors containing specific shRNAs directed against *MYBL2*, were used for functional experiments.

4.2.4. Proliferation assays

A673, SK-N-MC, and RDES EwS cells (1.5 x 10^5 per well) were seeded in 1.6ml of growth medium per well of a 6-well plate and transfected/re-transfected with either a non-targeting negative control siRNA or specific siRNAs (see section 'Transient transfection' for details, see section 'Plasmids and oligonucleotides' for siRNA sequences). 96 hours after first transfection, supernatant of each well was separately collected and cells were detached from the wells using trypsin. The detached cells in trypsin of each well were mixed with respective supernatant, stained with Trypan blue (TB) (10µl cell suspension of each well was mixed with 10µl of TB), and counted manually in a standardized hemocytometer (10µl of cell suspension-TB mix per cell count of a well). Viable (TB negative) and dead (TB positive) cells of each well were counted in two technical replicates. Cell counts of wells treated with specific siRNAs were normalized to cell counts of control wells treated with a non-targeting negative control siRNA.

4.2.5. Analysis of cell cycle by flow cytometry

A673, SK-N-MC, and RDES EwS cells (1.5 x 10^5 per well) were seeded in 1.6ml of growth medium per well of a 6-well plate and transfected/re-transfected with either a non-targeting negative control siRNA

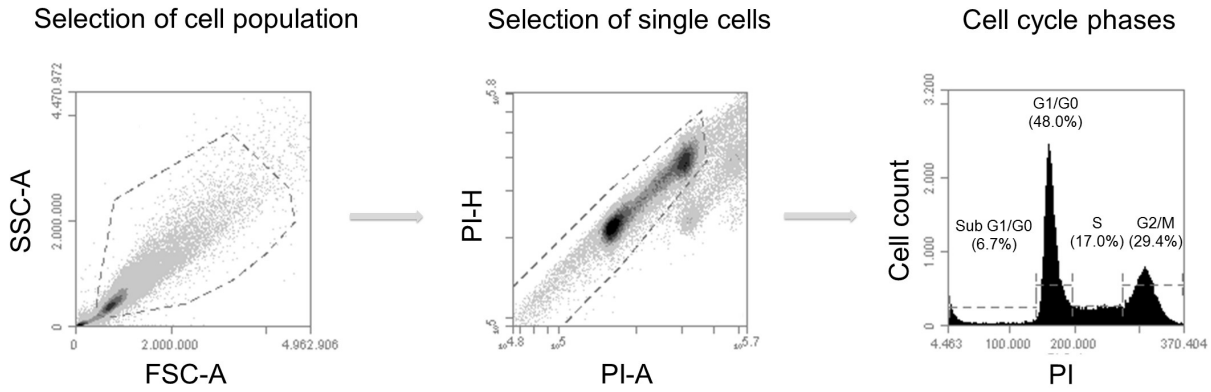

Figure 11: Gating strategy for analysis of cell cycle by flow cytometry. SSC-A: Side scatter area, FSC-A: Forward scatter area, PI-A: Propidium iodide area, PI-H: Propidium iodide height, PI: Propidium iodide.

or four different specific siRNAs directed against *MYBL2* (see section 'Transient transfection' for details). 96 hours after initial transfection the supernatant of each well was separately collected, cells were harvested by trypsination, suspended cells in trypsin of each well were mixed with respective supernatant, cells were spun down, washed with cold PBS twice, and fixed at 4°C with 1ml of 70% ethanol per sample for 24-48 hours. Cells were then spun down, washed with PBS twice, incubated with 500µl of propidium iodide (PI) solution (see section 'Media, buffers, and solutions' for details) per sample for 1 hour in the dark and afterwards assayed with the Accuri C6 flow cytometer. 30,000-100,000 events were recorded per sample. Data collection and analysis was performed using the Accuri C6 CFlow Plus software. Gating included selection of the cell population (exclusion of debris) and selection of single cells (exclusion of doublets) (**Figure 11**). Percentage of cells in each cell cycle phase (sub G1/G0, G1/G0, S, and G2/M) was determined for each sample (**Figure 11**).

4.2.6. Analysis of apoptosis by flow cytometry

A673, SK-N-MC, and RDES EwS cells (1.5 x 10^5 per well) were seeded in 1.6ml of growth medium per well of a 6-well plate and transfected/re-transfected with either a non-targeting negative control siRNA or four different specific siRNAs directed against *MYBL2* (see section 'Transient transfection' for details). 96 hours after initial transfection the supernatant of each well was separately collected, cells were harvested by trypsination, suspended cells in trypsin of each well were mixed with respective supernatant, cells were spun down and washed with cold PBS twice. Analysis of apoptosis was performed by combined fluorescein isothiocyanate (FITC)-AnnexinV/PI staining using the BD Pharmingen FITC Annexin V Apoptosis Detection Kit II (see section 'Commercial kits' for details). The

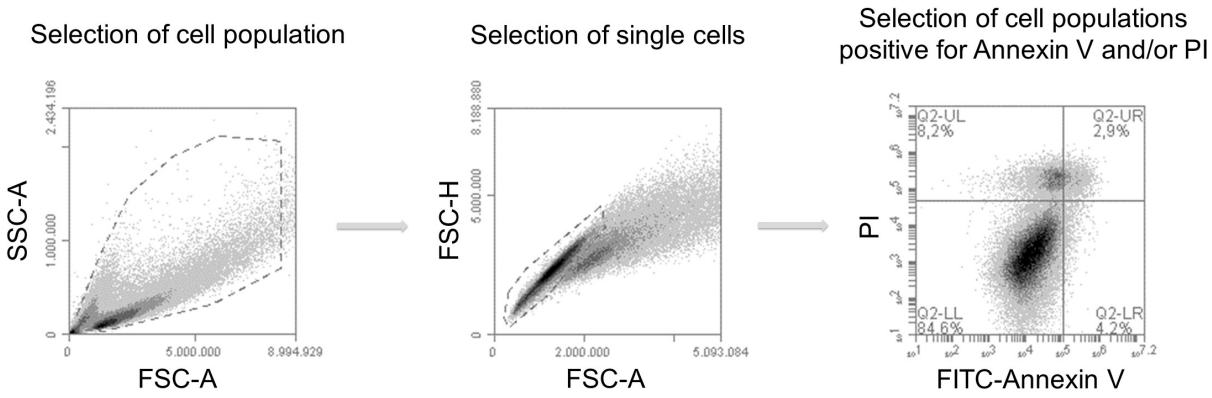

Figure 12: Gating strategy for analysis of cell death by flow cytometry. SSC-A: Side scatter area, FSC-A: Forward scatter area, FSC-H: Forward scatter height, PI: Propidium iodide, FITC: Fluorescein isothiocyanate. Figure from Musa et al., 2019.

cells of each sample were resuspended in 300µl of Annexin V binding buffer (1x; 1 part of the 10x Annexin V binding buffer diluted with 9 parts of Aqua bidest.) and 100µl of the resuspension was transferred in a 1.5ml reaction tube. 5µl of FITC-Annexin V and 5µl of PI (in provided concentrations) were added per sample. After gentle vortexing, the cells were incubated for 15 minutes at room temperature in the dark. 400µl of 1x Annexin V binding buffer was added on top per sample and samples were analyzed with the Accuri C6 flow cytometer. 30,000-100,000 events were recorded per sample. Data collection and analysis was performed using the Accuri C6 CFlow Plus software. Gating included selection of the cell population (exclusion of debris) and selection of single cells (exclusion of doublets) (**Figure 12**). Percentages of cells being either FITC-Annexin V and PI positive, FITC-Annexin V positive and PI negative, FITC-Annexin V negative and PI positive, or FITC-Annexin V and PI negative were determined for each sample (**Figure 12**).

4.2.7. Luciferase reporter assays

A673/TR/shEF1 EwS cells (2×10^5 per well) were seeded into 1.8ml of growth medium per well of a 6-well plate and were transfected with the cloned Firefly pGL3-Promoter-Fluc vector containing haplotypes of the *MYBL2*-associated microsatellite (mSat) with variable numbers of consecutive GGAA-repeats (see section ‘Cloning of pGL3-Promoter-Fluc constructs‘ for details) and the Renilla pGL3-Rluc vector (Firefly:Renilla ratio 100:1) (see section ‘Transient transfection‘ for details). As a transfection control, the pGL3-Promoter-Fluc vector containing *YFP* (provided by the Delattre laboratory, Paris, France) was transfected together with the pGL3-Rluc vector in additional wells and checked for yellow fluorescence 24 hours after transfection. When transfection of plasmids was performed as detailed in section

'Transient transfection', medium was refreshed and cells were treated with or without DOX (1µg/ml) for 72 hours. Afterwards, growth medium was discarded and the cells were lysed using 200µl of lysis buffer (2x Lysis Juice diluted 1:1 with PBS) per well. Cell lysates were transferred into a 1.5ml reaction tube, centrifuged (5,000 x g for 2 minutes), the supernatant was transferred into a new 1.5ml reaction tube, and pelleted cellular debris was discarded. Firefly and Renilla signals of the lysates were then measured in technical triplicates of each sample in an opaque 96-well plate using the Beetle and Renilla Juice (5µl of cell lysate with 50µl of each Beetle and Renilla Juice per well) with the Orion II microplate luminometer (dual luciferase assay system). Firefly luciferase signals were normalized to Renilla luciferase signals.

4.2.8. Colony formation assays (CFA)

A673 and SK-N-MC EwS cells that contain either a DOX-inducible non-targeting negative control shRNA or DOX-inducible specific shRNAs directed against *MYBL2* were seeded in a 12-well plate (in case of A673 500 cells per well, in case of SK-N-MC 1,000 cells per well) and were treated either with or without DOX (1µg/ml). Every condition was plated in triplicate wells. The cells were cultured for 10-14 days depending on the cell line and the shRNA, whereby DOX was refreshed every 72 hours. At the end of the observation period, growth medium was removed, cells were stained in the wells using crystal violet for 45 minutes and washed with PBS three times. After drying the plates by placing the plate with the wells upside down at room temperature for 12 hours, the plates were scanned using a photo scanner. The colony number for each well was determined using the scanned plates by counting of the colonies with the help of Fiji / Image J (see 'Software and interfaces' for details) (Schindelin et al., 2012; Schneider et al., 2012).

4.2.9. Clustered Regularly Interspaced Short Palindromic Repeats interference (CRISPRi)

The CRISPRi experiments were conducted by Gal Mazor and Mor Varon (Rotblat laboratory, Beer-Sheva, Israel). For reasons of coherence, consistency, and completeness, the results are described and displayed in this thesis, as they are a part of the published study underlying this thesis (Musa et al., 2019). A DNAse-dead Cas9 (dCas9) fused to the Krüppel associated box (KRAB) effector domain was targeted to the *MYBL2*-associated GGAA-mSat by specific gRNAs (see section 'Plasmids and oligonucleotides' for gRNA sequences) (Gilbert et al., 2014; Thakore et al., 2015). As no functional DNAse is involved, CRISPRi does not lead to a knockout of the targeted DNA sequence, as compared

to conventional CRISPR approaches, but can block protein binding to the respective sequence and cause an inhibitory chromatin state (Gilbert et al., 2014; Thakore et al., 2015). The pHAGE TRE dCas9-KRAB vector and the pLKO.1-puro U6 sgRNA BfuAI large stuffer vector, the latter one containing either a negative control gRNA or two gRNAs targeting the *MYBL2*-associated GGAA-mSat, were used for lentivirus production, followed by consecutive infection of RDES EwS cells with respective lentiviruses. General principles of lentivirus production are described in section 'Production of lentiviruses, cell transduction, and single cell cloning'. Selection of infected cells was performed using 1µg/ml puromycin and 1.5µg/ml G418 for 5 days, followed by measurement of *MYBL2* and *EWSR1-FLI1* expression levels by qRT-PCR after induction of dCas9-KRAB using DOX treatment (1µg/ml) for 5 days. Measurement of cell growth of the respective cells was performed by crystal violet staining and subsequent spectrophotometric analysis. The cells were pre-incubated with selection antibiotics (as described above) and DOX (2µg/ml) for 14 days, and afterwards seeded at a density of 8 x 10^4 cells per well in a 24-well plate. Every condition was plated in quadruplicate wells with growth medium containing DOX (2µg/ml). After 4 days the cells were washed and fixed for 1 hour at 4°C with trichloroacetic acid. Afterwards, the cells were washed with PBS and stained with crystal violet for 30 minutes after drying the plates. Subsequently, rinsing of the plate with PBS was performed to remove surplus crystal violet, followed by dissolvement of crystal violet bound by the cells using 10% acetic acid. Optical density of dissolved crystal violet was determined for each sample at 595nm using a DS-11 spectrophotometer.

4.2.10. CDK2 inhibitor assays (*in vitro*)

A673 cells containing a DOX-inducible specific shRNA directed against *MYBL2* (shMYBL2_4) or wildtype EwS cell lines harboring different constitutive *MYBL2* expression levels (RDES, SK-N-MC, and EW16) were seeded in a 96-well plate (5 x 10^3 per well). A673 cells containing a DOX-inducible specific shRNA directed against *MYBL2* were treated either with or without DOX-addition to the growth medium (1µg/ml). 24 hours after seeding (and DOX treatment in case of A673 cells containing a DOX-inducible specific shRNA directed against *MYBL2*), the CDK2 inhibitors NU6140 or CVT-313 were added in concentration ranging from 0.001µM to 100µM (80µl total volume per well). Each condition was plated in triplicate wells and each well contained an equal DMSO concentration (0.5%). As a control, wells only treated with 0.5% of DMSO were used. After 72 hours of treatment, 20µl of resazurin was added (20µg/ml) per well and plates were incubated for further 6 hours, followed by measurement of fluorescence per well using the Varioskan plate reader.

4.2.11. Cloning of pGL3-Promoter-Fluc constructs

Haplotypes of the *MYBL2*-associated GGAA-mSat including ~440bp of 5‘ and 3‘ flanking region were PCR-cloned from three EwS cell lines (RDES, A673, and SK-N-MC) each into the pGL3-Promoter-Fluc vector. For cloning, the In-Fusion HD Cloning Kit was used (see section ‘Commercial kits‘ for details). The pGL3-Promoter-Fluc vector was linearized using 1µg of the pGL3-Promoter-Fluc vector, 1µl of XhoI restriction enzyme, and 10µl of 10x CutSmart buffer, filled up with nuclease-free H_2O to a total volume of 50µl (**Table 4**), following incubation at 37°C overnight (12-24 hours).

Reagent	Volume
pGL3-Promoter-Fluc vector (1µg)	Depending on DNA concentration
Restriction enzyme (XhoI)	1µl
CutSmart buffer (10x)	10µl
Nuclease-free H_2O	Up to a total volume of 50µl

Table 4: Reaction for linearization of the pGL3-Promoter-Fluc vector.

For digestion of genomic EwS cell line DNA, 5µg of respective DNA (extracted as described in ‘Extraction of genomic DNA‘) was mixed with 1µl of each EcoRV-HD and HindIII-HD restriction enzymes, 10µl of 10x CutSmart buffer, and filled up with nuclease-free H_2O to a total volume of 50µl (**Table 5**), following incubation for 15 minutes at 37°C and inactivation of the reaction for 20 minutes at 80°C.

Reagent	Volume
Genomic DNA (5µg)	Depending on DNA concentration
Restriction enzyme 1 (EcoRV-HF)	1µl
Restriction enzyme 2 (HindIII-HF)	1µl
CutSmart buffer (10x)	10µl
Nuclease-free H_2O	Up to a total volume of 50µl

Table 5: Reaction for digestion of genomic EwS cell line DNA.

The DNA was applied on a 0.8% agarose gel, a gel electrophoresis was performed, the band including the desired fragment length (~1,000bp) was cut out, and DNA was extracted from the respective piece of gel (see sections ‘Agarose gel electrophoresis‘ and ‘Extraction of DNA from agarose electrophoresis gel‘ for details). Haplotypes of the *MYBL2*-associated GGAA-mSat with ~440bp of 5‘ and 3‘ flanking region were PCR-amplified from the digested genomic DNA (see section ‘Plasmids and oligonucleotides‘ for primer sequences). Per cell line, 200ng of digested DNA was mixed with each 2.5µl of 10µM respective primers, 10µl of 5x GoTaq colorless buffer, 6µl of 25mM $MgCl_2$, 1µl of 10mM dNTPs, 0.25µl of GoTaq DNA polymerase, and filled up with nuclease-free H_2O to 50µl total volume (**Table 6**).

Reagent	Volume
Digested genomic DNA (200ng)	Depending on DNA concentration
MYBL2 mSat primer with IF overhang F (10µM)	2.5µl
MYBL2 mSat primer with IF overhang R (10µM)	2.5µl
GoTaq colorless buffer (5x)	10µl
$MgCl_2$ (25mM)	6µl
dNTPs (10mM)	1µl
GoTaq DNA polymerase	0.25µl
Nuclease-free H_2O	Up to a total volume of 50µl

Table 6: Reaction for PCR-amplification of the *MYBL2*-associated GGAA-mSat with ~440bp of 5‘ and 3‘ flanking region from digested genomic EwS cell line DNA.

A PCR was run using the protocol specified in **Table 7**: initialization at 95°C for 2 minutes (1 cycle); denaturation at 98°C for 10 seconds, annealing at 65-55°C for 30 seconds (whereby temperature decreases about 0.5°C per cycle), extension at 72°C for 1 minute (20 cycles); denaturation at 98°C for 10 seconds, annealing at 60°C for 30 seconds, extension at 72°C for 1 minute (20 cycles); final extension at 72°C for 5 minutes (1 cycle).

PCR step	Temperature	Time	Cycles
Initialization	95°C	2 minutes	1 cycle
Denaturation	98°C	10 seconds	
Annealing	65-55°C*	30 seconds	20 cycles
Extension	72°C	1 minute	
Denaturation	98°C	10 seconds	
Annealing	60°C	30 seconds	20 cycles
Extension	72°C	1 minute	
Final extension	72°C	5 minutes	1 cycle
Infinite hold	4°C	Infinite	Infinite

Table 7: PCR protocol for amplification of the *MYBL2*-associated GGAA-mSat with ~440bp of 5‘ and 3‘ flanking region from digested genomic EwS cell line DNA. *Temperature decreases about 0.5°C per cycle.

The PCR products were applied on a 0.8% agarose gel, a gel electrophoresis was performed, from each cell line the band with the expected amplicon size (~1,000bp) was cut out from the gel, and DNA was extracted from the respective pieces of gel (see sections ‘Agarose gel electrophoresis‘ and ‘Extraction of DNA from agarose electrophoresis gel‘ for details). Afterwards, per cell line, ligation was performed using 20ng of amplicon DNA (mSat with 5‘ and 3‘ flanking region), 10ng of linearized pGL3-Promoter-Fluc vector, and 2µl of In-Fusion HD Enzyme Premix, filled up with nuclease-free H_2O to a total volume of 10µl (**Table 8**).

Reagent	Volume
Insert (amplified mSat / flanking region) (20ng)	Depending on DNA concentration
Linearized pGL3-Promoter-Fluc vector (10ng)	Depending on DNA concentration
In-Fusion HD Enzyme Premix	2µl
Nuclease-free H_2O	Up to a total volume of 10µl

Table 8: Reaction for ligation of the *MYBL2*-associated GGAA-mSat with ~440bp of 5‘ and 3‘ flanking region into the pGL3-Promoter-Fluc vector.

The reaction was incubated for 15 minutes at 50°C, followed by 5 minutes of incubation on ice. Per construct, on 50µl of competent bacteria (Stellar) 2.5µl of the ligation mix was applied, bacteria were incubated for 30 minutes on ice, heat-shocked for 45 seconds at 42°C, and then incubated for further 2 minutes on ice. 500µl of pre-warmed Super Optimal broth with Catabolite repression (SOC) medium was added per aliquot of bacteria and the bacteria were incubated for 1 hour at 37°C while shaking at 300rpm. Afterwards, bacteria were pelleted by centrifugation with 3.3 x g for 5 minutes, supernatant was removed, bacteria were resuspended in 100µl of fresh SOC medium per aliquot, and 10-50µl (depending on the opaqueness) of each aliquot was plated on an agar plate containing 100µg/ml of ampicillin. After overnight incubation (12-24 hours), bacteria colonies were picked from each plate with sterile 10µl tips and incubated for 1.5 hours in 100µl LB medium containing 100µg/ml ampicillin per colony. A colony PCR was performed for each colony using 2µl of respective bacteria colony solution, 2.5µl of 10µM primer mix, 10µl of 5x GoTaq colorless buffer, 6µl of 25mM $MgCl_2$, 1µl of 10mM dNTPs, and 0.25µl of GoTaq DNA polymerase, filled up with 28.25µl nuclease-free H_2O to a total volume of 50µl (**Table 9**).

Reagent	Volume
Bacteria colony solution	2µl
MYBL2 mSat primer with IF overhang F and R primer mix (10µM)	2.5µl
GoTaq colorless buffer (5x)	10µl
$MgCl_2$ (25mM)	6µl
dNTPs (10mM)	1µl
GoTaq DNA polymerase	0.25µl
Nuclease-free H_2O	Up to a total volume of 50µl

Table 9: Reaction for colony PCR performed after cloning of the *MYBL2*-associated GGAA-mSat with ~440bp of 5‘ and 3‘ flanking region into the pGL3-Promoter-Fluc vector and subsequent bacterial transformation.

Colony PCR was subsequently run as specified in **Table 10**: initialization at 95°C for 2 minutes (1 cycle); denaturation at 98°C for 10 seconds, annealing at 65-55°C for 30 seconds (whereby temperature

decreases about 0.5°C per cycle), extension at 72°C for 1 minute (20 cycles); denaturation at 98°C for 10 seconds, annealing at 60°C for 30 seconds, extension at 72°C for 1 minute (20 cycles); final extension at 72°C for 5 minutes (1 cycle).

PCR step	Temperature	Time	Cycles
Initialization	95°C	2 minutes	1 cycle
Denaturation	98°C	10 seconds	20 cycles
Annealing	65-55°C*	30 seconds	
Extension	72°C	1 minute	
Denaturation	98°C	10 seconds	20 cycles
Annealing	60°C	30 seconds	
Extension	72°C	1 minute	
Final extension	72°C	5 minutes	1 cycle
Infinite hold	4°C	Infinite	Infinite

Table 10: Protocol for colony PCR performed after cloning of the *MYBL2*-associated GGAA-mSat with ~440bp of 5‘ and 3‘ flanking region into the pGL3-Promoter-Fluc vector and subsequent bacterial transformation. *Temperature decreases about 0.5°C per cycle.

Colony PCR products were stained with a loading dye, applied on a 0.8% agarose gel with a corresponding DNA ladder, a gel electrophoresis was performed (see section ‘Agarose gel electrophoresis‘ for details), positive colonies transformed with the pGL3-Promoter-Fluc vector containing the correct insert were identified by gel imaging, respective positive colonies were separately expanded in each 50ml LB medium containing 100µg/ml ampicillin overnight (12-24 hours), and plasmid DNA of expanded positive colonies was extracted (see section ‘Extraction of plasmid DNA‘ for details). The plasmids were sanger sequenced using the GL primer 2 (sequencing primer; see section ‘Plasmids and oligonucleotides‘ for primer sequence) to evaluate correct cloning of the desired fragment.

4.2.12. Cloning of pLKO Tet-On constructs

A non-targeting negative control shRNA and two specific shRNAs directed against *MYBL2* were each cloned into the pLKO Tet-On vector in order to produce lentiviruses stably transducing EwS cells with DOX-inducible shRNAs (see section ‘Production of lentiviruses, cell transduction, and single cell cloning‘ for details). Native pLKO Tet-On vector was digested using 4µg of pLKO Tet-On vector, 1µl of AgeI-HF, 2µl of EcoRI-HF, and 2µl of 10x CutSmart buffer, filled up with nuclease-free H_2O to a total volume of 20µl (**Table 11**), following incubation for 15 minutes at 37°C and inactivation of the reaction for 20 minutes at 65°C.

Reagent	Volume
pLKO Tet-On vector (4µg)	Depending on DNA concentration
Restriction enzyme 1 (AgeI-HF)	1µl
Restriction enzyme 2 (EcoRI-HF)	2µl
CutSmart buffer (10x)	2µl
Nuclease-free H_2O	Up to a total volume of 20µl

Table 11: Reaction for digestion of the pLKO Tet-On vector.

Afterwards, DNA precipitation was performed using the digested pLKO Tet-On vector in a volume of 20µl (of the reaction described in **Table 11**), filled up with 180µl of nuclease-free H_2O to a total volume of 200µl, mixed with 20µl of 3M sodium acetate, and 440µl of 100% ethanol. These reagents were incubated for 45 minutes at -80°C and centrifuged for 30 minutes at 4°C and 15.7 x g. The supernatant was discarded, the pellet was washed with 70% ethanol and centrifuged for 15 minutes at 15.7 x g and 4°C. The supernatant was discarded, the pellet was dried for 2 minutes at 37°C, and afterwards reconstituted in 10µl of nuclease-free H_2O. The digested pLKO Tet-On plasmid DNA was applied on a 0.8% agarose gel and a gel electrophoresis was performed (see section ‘Agarose gel electrophoresis‘ for details), whereby visible bands at ~8800bp (vector backbone) and 1800bp (stuffer) indicated a successful digestion. The band at ~8800bp was cut out and DNA was extracted from the respective piece of gel (see section ‘Extraction of DNA from agarose electrophoresis gel‘ for details). The bottom and top strands of each shRNA (see section ‘Plasmids and oligonucleotides‘ for shRNA sequences) were separately reconstituted in nuclease-free H_2O (100µM each). 11.25µl of each matching bottom and top strand were mixed with 2.5µl of 10x annealing buffer and annealed in the thermocycler starting at 95°C for 1 minute, decreasing by 1°C per minute until 14°C was reached. Per construct, ligation of annealed shRNAs with the digested pLKO Tet-On vector was performed using 30ng of digested pLKO Tet-On vector, 200ng of annealed shRNA diluted in the annealing buffer, 1µl of T4 DNA Ligase, and 1.5µl of 10x T4 DNA Ligase Reaction Buffer, filled up with nuclease-free H_2O to a total volume of 15µl (**Table 12**), following incubation at 16°C overnight (12-24 hours).

Reagent	Volume
Digested pLKO Tet-On vector (30ng)	Depending on DNA concentration
Annealed shRNA (200ng)	Depending on DNA concentration
T4 DNA Ligase	1µl
10x T4 DNA Ligase Reaction Buffer	1.5µl
Nuclease-free H_2O	Up to a total volume of 15µl

Table 12: Reaction for ligation of annealed shRNAs with the digested pLKO Tet-On vector.

After ligation, competent bacteria were transformed with the pLKO Tet-On vectors containing the cloned shRNAs. Therefore, per construct, 100µl aliquots of competent bacteria (SURE2) were thawed on ice and incubated for 10 minutes with 2µl of 1.22M β-Mercaptoethanol on ice while shaking at 250rpm. Afterwards, 50ng of a cloned pLKO Tet-On construct (pooling of multiple ligation reactions per construct was performed to achieve this amount of DNA) was added per aliquot of competent bacteria and incubated for further 10 minutes on ice. Then, each aliquot was heat-shocked for 30 seconds at 42°C and afterwards incubated on ice for 2 minutes. 900µl of SOC medium was added per aliquot and bacteria were incubated for 1 hour at 37°C shaking at 250rpm. 10-50µl (depending on the opaqueness) of each bacteria aliquot was plated on an agar plate containing 100µg/ml ampicillin. The agar plates were incubated overnight (12-24 hours). Bacteria colonies from each plate were picked with sterile 10µl tips and incubated for 1.5 hour in 100µl LB medium containing 100µg/ml ampicillin per colony. A colony PCR was performed for each picked colony using 2µl of the respective bacteria colony solution, 2.5µl of 10µM pLKO Tet-on F and R primer mix (see section ‘Plasmids and oligonucleotides‘ for primer sequences), 10µl of 5x GoTaq colorless buffer, 6µl of 25mM $MgCl_2$, 1µl of 10mM dNTPs, 0.25µl of GoTaq DNA polymerase, filled up with 28.25µl of nuclease-free H_2O up to a total volume of 50µl (**Table 13**).

Reagent	**Volume**
Bacteria colony solution	2µl
pLKO Tet-On F and R primer mix (10µM)	2.5µl
GoTaq colorless buffer (5x)	10µl
$MgCl_2$ (25mM)	6µl
dNTPs (10mM)	1µl
GoTaq DNA polymerase	0.25µl
Nuclease-free H_2O	Up to a total volume of 50µl

Table 13: Reaction for colony PCR performed after cloning of shRNAs into the pLKO-Tet-On vector and subsequent bacterial transformation.

Colony PCR was subsequently run as specified in **Table 14**: initialization at 95°C for 10 minutes (1 cycle); denaturation at 98°C for 10 seconds, annealing at 59-49°C for 30 seconds (temperature decreases about 0.5°C per cycle), extension at 72°C for 1 minute (20 cycles); denaturation at 98°C for 10 seconds, annealing at 54°C for 30 seconds, extension at 72°C for 1 minute (20 cycles); final extension at 72°C for 10 minutes (1 cycle).

PCR step	Temperature	Time	Cycles
Initialization	95°C	10 minutes	1 cycle
Denaturation	98°C	10 seconds	20 cycles
Annealing	59-49°C*	30 seconds	
Extension	72°C	1 minute	
Denaturation	98°C	10 seconds	20 cycles
Annealing	54°C	30 seconds	
Extension	72°C	1 minute	
Final extension	72°C	10 minutes	1 cycle
Infinite hold	4°C	Infinite	Infinite

Table 14: Protocol for colony PCR performed after cloning of shRNAs into the pLKO-Tet-On vector and subsequent bacterial transformation. *Temperature decreases about 0.5°C per cycle.

Colony PCR products were stained with a loading dye, applied on a 1.5% agarose gel with a corresponding DNA ladder, a gel electrophoresis was performed (see section ‘Agarose gel electrophoresis‘ for details), and positive colonies of competent bacteria containing the correctly cloned pLKO Tet-On plasmid were identified by visualization of a 420bp (shRNA insert) amplicon by gel imaging. Positive colonies were then separately expanded in each 50ml LB medium containing 100µg/ml ampicillin and plasmid DNA from expanded positive colonies was extracted (see section ‘Extraction of plasmid DNA‘ for details). The plasmids were sanger sequenced using the pLKO Tet-On sequencing primer (see section ‘Plasmids and oligonucleotides‘ for primer sequence) to evaluate correct cloning of the desired shRNAs.

4.2.13. Agarose gel electrophoresis

For production of an agarose gel, 0.8g or 1.5g (for a 0.8% or a 1.5% gel, respectively) of agarose was mixed with 100ml of 1x TAE buffer (see section ‘Media, buffers, and solutions‘ for details) in an Erlenmeyer flask and heated in a microwave for 1-3 minutes until the agarose solution started boiling and the agarose was completely dissolved. Afterwards, the agarose solution was cooled down for 5 minutes, then poured into a gel tray containing a well comb, and 5µl of either ethidium bromide (EtBr) or SYBR Safe was added and mixed with the agarose solution. After 30 minutes of letting the gel cool down at room temperature, the set gel with the gel tray was transferred into the gel chamber, which was filled with 1x TAE buffer until the gel was completely covered. The well comb was removed and the DNA samples were stained with a 6x loading dye in a sample:dye ratio of 5:1. The comb wells were loaded with the DNA ladder and the DNA samples, the power supply was connected, and the electrophoresis

was performed using 130V for 20-30 minutes. Afterwards, the gel was imaged and, if necessary, processed for a PCR gel clean-up (see section ‘Extraction of DNA from agarose electrophoresis gel‘ for details).

4.2.14. Transformation of bacteria

Handling of bacteria was performed in proximity of the flame of a Bunsen burner to induce a nearly sterile field. Aliquots (50µl or 100µl) of competent bacteria (Stellar or SURE2, respectively) were thawed on ice (in case of transformation with pLKO Tet-On vectors SURE2 bacteria aliquots were additionally incubated for 10 minutes with 2µl of 1.22M β-Mercaptoethanol per aliquot on ice while shaking at 250rpm, in order to increase transformation efficiency) and at least 5ng of plasmid DNA per aliquot was added. Bacteria were incubated on ice for 30 or 10 minutes, then heated for 45 or 30 seconds in a thermoblock with 42°C (‘heat shock‘), and afterwards returned on ice for 2 minutes (Stellar or SURE2, respectively). 500µl or 900µl SOC medium was added afterwards per aliquot of bacteria and bacteria were incubated in a thermoshaker at 37°C and 300 or 250rpm for 1 hour (Stellar or SURE2, respectively). When medium turned opaque, 10-50µl (depending on the opaqueness of the aliquot) of the bacterial solution of each aliquot was transferred to each an agar plate containing 100µg/ml ampicillin in order to select for transformed bacteria. In case of Stellar competent cells, before plating, the bacteria were pelleted by centrifugation with 3.3 x g for 5 minutes, supernatant was removed, and bacteria were resuspended in 100µl of fresh SOC medium. The agar plates were afterwards incubated overnight for 12-24 hours. Single bacterial colonies were picked from each agar plate using sterile 10µl pipet tips and transferred into each either a 1.5ml reaction tube containing 100µl LB medium with 100µg/ml ampicillin and incubated for 1.5 hours prior to performance of a colony PCR, or an Erlenmeyer flask containing 50ml of LB medium with 100µg/ml ampicillin and incubated for 12-24 hours for immediate expansion of transformed bacteria mainly when a retransformation of an already successfully cloned plasmid was performed. Colonies subjected to colony PCR were only further expanded in an Erlenmeyer flask in case of successful cloning of the plasmid that was transformed. After expansion, bacteria were centrifuged at 5,000 x g for 10 minutes and the pellet was used for plasmid DNA extraction as described in section ‘Extraction of plasmid DNA‘. For details of bacterial transformation regarding the pGL3-Promoter-Fluc and the pLKO Tet-On vectors see sections ‘Cloning of pGL3-Promoter-Fluc constructs‘ and ‘Cloning of pLKO Tet-On constructs‘.

4.2.15. Extraction of plasmid DNA

Extraction of plasmid DNA was performed using the PureYield Plasmid Midiprep kit (see section ‘Commercial kits‘ for details). Pelleted bacteria (50ml bacteria culture) were resuspended in 3ml of Cell Resuspension Solution and 3ml Cell Lysis Solution was added per pellet. The mixtures were inverted 3-5 times and incubated for 3 minutes at room temperature. Afterwards, 5ml of Neutralization Solution was added per sample and the tubes were inverted 5-10 times, following centrifugation at 15,000 x g for 15 minutes to spin down and remove cellular debris. Blue Clearing Columns were stacked into white Binding Columns, the stacks were placed into a vacuum manifold, and the cell lysates (without the pelleted debris) were separately transferred each into one column stack. Vacuum was applied, leading to the cell lysates passing both columns, and thereby plasmid DNA was bound by the white Binding Columns. The vacuum was released afterwards and the blue Clearing Columns were discarded. The membranes of the white Binding Columns were washed with 5ml of Endotoxin Removal Wash and 20ml of Column Wash Solution per sample, each washing step followed by vacuum application to pull the respective washing buffer through the membranes. The membranes were dried afterwards for 1 minute by vacuum application. The white Binding Columns were transferred each into a 50ml reaction tube, 600µl of Nuclease-Free Water was added per sample to the membrane, and the tubes were centrifuged at 2,000 x g for 5 minutes. The flowthroughs containing the eluted plasmid DNA were then transferred each into a 1.5ml reaction tube. If needed, plasmid DNA concentration and purity was determined using the Nanodrop ND-1000 spectrophotometer.

4.2.16. Extraction of genomic DNA

Extraction of genomic DNA was performed using the NucleoSpin Tissue kit (see section ‘Commercial kits‘ for details). Cells (up to 10^7 per sample) were lysed with 200µl of Buffer T1 per sample. 25µl of Proteinase K solution and 200µl of Buffer B3 were added per sample and samples were incubated at 70°C for 10-15 minutes after vortexing. Subsequently, 210µl of 96-100% ethanol were added per sample and the samples were vortexed. The mixtures were transferred each into a NucleoSpin Tissue Column and centrifuged at 11,000 x g for 1 minute. The silica membranes of the columns were washed in two steps using 500µl of Buffer BW in the first step and 600µl of Buffer B5 in the second step per sample, each step followed by centrifugation at 11,000 x g for 1 minute. The DNA was afterwards eluted by addition of 100µl Buffer BE per sample to the silica membrane, followed by incubation for 1 minute and

centrifugation at 11,000 x g for 1 minute. If needed, DNA concentration and purity was determined using the Nanodrop ND-1000 spectrophotometer.

4.2.17. Extraction of DNA from agarose electrophoresis gel

Extraction of DNA that was run on an agarose electrophoresis gel was performed using the NucleoSpin Gel and PCR Clean-up kit (see section ‘Commercial kits‘ for details). Required bands of the agarose gel were visualized using an UV light transilluminator, cut out with a scalpel (using a new scalpel for each band), and transferred each into a 1.5ml or 2ml reaction tube. Respective pieces of gel were weighted and 200µl of Buffer NTI was added per 100mg of agarose gel per sample to the reaction tube containing the piece of gel. The samples were then incubated for 5-10 minutes at 50°C in a thermoblock and vortexed every 2-3 minutes until the gel was dissolved. Up to 700µl of dissolved gel per sample was transferred into a NucleoSpin Gel and PCR Clean-up Column and centrifuged at 11,000 x g for 30 seconds. Afterwards, the column silica membranes were washed with 700µl of Buffer NT3 per sample, centrifuged at 11,000 x g for 30 seconds, and subsequently centrifuged at 11,000 x g for 1 minute to dry the membranes. The DNA was eluted by addition of 20µl Buffer NE per sample to the silica membranes, followed by incubation for 1 minute at room temperature and centrifugation at 11,000 x g for 1 minute. If needed, DNA concentration and purity was determined using the Nanodrop ND-1000 spectrophotometer.

4.2.18. Extraction of RNA

Extraction of RNA from cells and tissues was performed using the NucleoSpin RNA kit (see section ‘Commercial kits‘ for details). Harvested cells (up to 5 x 10^6 per sample) or small pieces of frozen tumor tissue (up to 20mg per sample) were lysed using 350µl of RA1 lysis buffer (in case of frozen tumor tissue, disruption of the tissue with a mortar was performed in the presence of the RA1 lysis buffer) and mixed with 350µl of ethanol (70%) per sample. The lysates were then transferred each to a NucleoSpin RNA Column containing a silica membrane and the columns were centrifuged for 30 seconds at 11,000 x g. Afterwards, 350µl of the membrane desalting buffer (MDB) was applied per sample followed by centrifugation for 1 minute at 11,000 x g. To digest DNA that was also bound by the silica membranes, 95µl of rDNAse reaction mixture (10µl of reconstituted rDNAse and 90µl of reaction buffer for rDNAse) was applied on the column membranes per sample and incubated for 15 minutes at room temperature.

To wash and dry the membranes, several steps were performed sequentially: 200µl of RAW2 buffer was applied per sample to inactivate rDNAse and the columns were centrifuged for 30 seconds at 11,000 x g, then 600µl and 250 µl of RA3 buffer were applied per sample consecutively in two steps, with centrifugation at 11,000 x g for 30 seconds and 2 minutes, respectively. The RNA was eluted by application of 40µl of RNAse-free H_2O per sample to each of the membranes and centrifugation for 1 minute at 11,000 x g. The eluted RNA of each sample was collected in a 1.5ml reaction tube. If needed, RNA concentration and purity was determined using the Nanodrop ND-1000 spectrophotometer.

4.2.19. Reverse transcription

Reverse transcription of RNA was performed using the High-Capacity cDNA Reverse Transcription Kit (see section ‘Commercial kits‘ for details). For each reaction/sample, 2µl of 10x RT buffer, 2µl of 10x RT random primers, 0.7µl of 25x 100mM dNTP mix, and 0.7µl of MultiScribe reverse transcriptase were mixed with 14.6µl of RNA eluted in RNAse-free H_2O to achieve a total volume of 20µl. In case of necessity to determine the exact amount of applied RNA per sample, the concentration of RNA was determined using the Nanodrop ND-1000 spectrophotometer prior to reverse transcription, the volume of used eluted RNA was reduced according to the desired RNA concentration, and the reaction mixture was filled up with RNAse-free H_2O to a total volume of 20µl. Reverse transcription was performed using a PCR cycler using the following protocol: 25°C for 10 minutes, 37°C for 2 hours, 85°C for 10 seconds, 16°C infinite hold.

4.2.20. Quantitative real-time polymerase chain reaction (qRT-PCR)

qRT-PCRs were run on a Bio-Rad CFX Connect instrument. Data collection was performed using the Bio-Rad CFX Manager 3.1 software. Gene expression levels were calculated using Microsoft Excel according to the 2(-Delta Delta C(T)) method (Livak and Schmittgen, 2001). Per sample, cDNA of 20µl final volume was diluted with 180µl of nuclease-free H_2O (1:10 dilution). 20µl of each forward and reverse primers (0.5µM stock concentration) were mixed with 160µl H_2O in order to prepare the respective primer mix (see section ‘Plasmids and oligonucleotides‘ for primer sequences). Per reaction, 0.75µl of the primer mix was mixed with 7.5µl of the SYBR Select Master Mix. 8.25µl of this final mixture and 6.75µl of diluted cDNA were then applied per well of a 96-well qRT-PCR plate. After sealing and spinning down the qRT-PCR plate, the qRT-PCR was run with a final volume of 15µl per well as specified

in **Table 15**: initialization at 95 °C for 2 minutes (1 cycle); denaturation at 95 °C for 10 seconds, annealing and extension at 60 °C for 10 seconds each (49 cycles); denaturation at 95°C for 30 seconds, annealing at 65°C for 30 seconds, extension with melting curve starting at 65 °C and increasing by 0.5 °C per 5 seconds until 95 °C was reached (1 cycle).

PCR step	Temperature	Time	Cycles
Initialization	95°C	2 minutes	1 cycle
Denaturation	95°C	10 seconds	49 cycles
Annealing	60°C	10 seconds	
Extension	60°C	10 seconds	
Denaturation	95°C	30 seconds	1 cycle
Annealing	65°C	30 seconds	
Extension	65°C-95°C*	5 minutes	

Table 15: qRT-PCR protocol used for quantification of gene expression on mRNA level. *Temperature increases about 0.5°C per 5 seconds.

4.2.21. Western blot

Western blots were conducted by Dr. Marie-Ming Aynaud (Delattre laboratory, Paris, France). For reasons of coherence, consistency, and completeness, the results are described and displayed in this thesis, as they are a part of the published study underlying this thesis (Musa et al., 2019). Western blots were performed by Dr. Marie-Ming Aynaud according to routine protocols of the Delattre laboratory (Aynaud et al., 2020; Grünewald et al., 2015). EWSR1-FLI1 was suppressed in A673/TR/shEF1 EwS cells treated with DOX (1µg/ml) for 7 days, and re-expressed by removal of DOX from the growth medium for further 10 days. Protein extraction was performed at day 0, day 7, day 11, day 14, and day 17. Detection of specific bands was accomplished by usage of the following primary antibodies (see section ‘Antibodies‘ for details): rabbit monoclonal anti-FLI1 antibody (1:1,000), rabbit polyclonal anti-MYBL2 antibody (1:500), and mouse monoclonal anti-ß-actin (1:10,000). The following antibodies were used as secondary antibodies: anti-rabbit IgG horseradish peroxidase (HRP)-coupled antibody (1:3,000) and anti-mouse IgG HRP-coupled antibody (1:3,000). Chemiluminescence was used for protein visualization.

4.2.22. RNA sequencing (RNA-seq)

A673, SK-N-MC, and RDES EwS cells were transfected as described in sections 'Transient transfection' and 'Proliferation assays' with either a non-targeting negative control siRNA or a specific siRNA directed against *MYBL2* (siMYBL2_1) in triplicate wells (see section 'Plasmids and oligonucleotides' for siRNA sequences). RNA of each sample was extracted as described in 'Extraction of RNA'. RNA concentration of each sample was determined using the Nanodrop ND-1000 spectrophotometer. Sequencing of RNA and processing of raw data was performed at the Institut Curie Genomics of Excellence (ICGex) center (Paris, France) and was supervised by Dr. Marie-Ming Aynaud, Dr. Olivier Mirabeau, and Dr. Sandrine Grossetête (Delattre laboratory, Paris, France). For reasons of coherence, consistency, and completeness, the results are described and displayed in this thesis, as they are a part of the published study underlying this thesis (Musa et al., 2019). Sequencing of cDNA libraries was performed using an Illumina HiSeq2500 instrument (150bp paired-end sequencing). Alignment of reads on the human genome (hg19) was performed using TopHat (Trapnell et al., 2009). For read counting on annotated genes from the GRCh37 genebuild HTSeq-count was used (Anders et al., 2015) with following parameters: htseq-count -a 10 -q -s no -m union. Sample-to-sample normalization and analysis of differential expression was done using DESeq2 (R package) (Love et al., 2014). Raw RNA-seq data is deposited at the Gene Expression Omnibus (GEO) with the accession code GSE119972.

4.2.23. Chromatin immunoprecipitation and DNA sequencing (ChIP-seq)

p-MYBL2 ChIP-seq and processing of raw data in A673 EwS cells was performed by Dr. Marie-Ming Aynaud, Dr. Olivier Mirabeau, and Dr. Sandrine Grossetête (Delattre laboratory, Paris, France). EWSR1-FLI1 ChIP-seq and processing of raw data in RDES EwS cells was performed by Dr. Martin Orth (Grünewald laboratory, Munich, Germany). For reasons of coherence, consistency, and completeness, the results are described and displayed in this thesis, as they are a part of the published study underlying this thesis (Musa et al., 2019). Cross-linking of protein and DNA was performed using 1% paraformaldehyde for 10 minutes on 12 x 10^6 A673 cells and 4 x 10^6 RDES cells. The iDeal ChIP-seq Kit for Transcription Factors (see section 'Commercial kits' for details) was used to perform cell lysis, shearing of chromatin, immunoprecipitation, and purification of DNA. For chromatin shearing, a Bioruptor conducting 20 sonication cycles (30 seconds high, 30 seconds off) in TPX tubes was used. p-MYBL2 immunoprecipitation was performed using 2µg of monoclonal rabbit ChIP-grade anti-p-MYBL2 antibody and EWSR1-FLI1 immunoprecipitation was performed using 2µg of polyclonal rabbit ChIP-

grade anti-FLI1 antibody (see section ‘Antibodies‘ for details). MYBL2 and EWSR1-FLI1 ChIPs were both sequenced on an Illumina HiSeq2500 instrument (100bp and 150bp single-end, respectively). Alignment of ChIP-seq reads to the human genome (hg19) was performed using Bowtie2 (Langmead and Salzberg, 2012) and peak calling was performed using MACS2 with option narrow (Zhang et al., 2008). The input dataset of the same cell line was used for normalization. For peak annotation and visualization of p-MYBL2 ChIP-seq PAVIS was used (Huang et al., 2013). Analysis of EWSR1-FLI1 ChIP-seq reads spanning the different *MYBL2*-associated GGAA-mSat haplotypes in RDES was performed by extraction of exclusively the spanning reads from the BAM file using SAMtools mapped to the corresponding haplotype in accordance to CIGAR scores (Li et al., 2009). Significance levels for this analysis were calculated with a binomial test (p=0.5). p-MYBL2 ChIP-seq data is deposited at the GEO with the accession code GSE119972.

4.2.24. Xenotransplantation

All mouse experiments reported in this thesis were conducted with the approval of the government of Upper Bavaria and in accordance with the ARRIVE and UKCCCR guidelines as well as the recommendations of the European Community (86/609/EEC). Sample size calculation was done assuming β=0.8 and α=0.05 in compliance with the 3R model (replacement, reduction, refinement). 3 x 10^6 A673 or SK-N-MC cells containing either a non-targeting negative control shRNA or specific shRNAs directed against *MYBL2* or *EWSR1-FLI1* were suspended in a 1:1 mix of PBS and Geltrex (100µl total volume per injection) and subcutaneously injected into the right flanks of 3-9 months old NSG mice (see section ‘Plasmids and oligonucleotides‘ for shRNA sequences). As soon as tumors were palpable, randomization of mice to either the control group receiving drinking water containing sucrose (17.5mg/ml) or the treatment group receiving drinking water containing sucrose (50mg/ml) and DOX (2mg/ml) was performed. Sucrose concentration in the treatment group was adapted according to the average water intake of mice in different groups: as mice receiving DOX via their drinking water have a lower water intake in average due to the bitter taste of DOX, a higher concentration of sucrose is necessary to ensure equal sucrose intake of mice across the different groups. Every two days, the tumor size was measured using a caliper and tumor volumes were calculated according to the formula $V = a \times b^2 / 2$, whereby ‘a‘ corresponds to the largest and ‘b‘ corresponds to the smallest diameter. As soon as a tumor reached a tumor volume of 1500mm^3 or the mean diameter was equal or exceeding 15mm, the respective mouse was sacrificed by cervical dislocation. Other humane endpoints have

further been defined as follows: tumor ulceration, invasive tumor growth without movability of the tumor, apathy and self-isolation, defensive reaction while tumor palpation, strongly reduced food or water consumption, breathing abnormality, motoric neurological deficits, abnormal unphysiological body posture, bloody diarrhea or rectal prolapse, severe dehydration, visible abdominal distension, signs for severe pain according to the Mouse Grimace Scale, loss of 20% or more of body weight, and obese Body Condition Scores (BCS). After sacrification of mice, the respective tumors were extracted, a small piece of each tumor was frozen for RNA extraction (see section 'Extraction of RNA' for details), and the remaining tumors were formalin-fixed (4% formalin) for subjection to routine histology and immunohistochemistry (IHC) (see section 'Histology and immunohistochemistry (IHC)' for details).

4.2.25. CDK2 inhibitor treatment (*in vivo*)

All mouse experiments reported in this thesis were conducted with the approval of the government of Upper Bavaria and in accordance with the ARRIVE and UKCCCR guidelines as well as the recommendations of the European Community (86/609/EEC). A673 cells containing a DOX-inducible shRNA directed against *MYBL2* (shMYBL2_4) were subcutaneously injected in NSG mice as described in section 'Xenotransplantation'. As soon as tumors were palpable, the mice were randomized to either the vehicle control group (DMSO) or a CDK2 inhibitor (NU6140) treatment group (either 20mg/kg or 40mg/kg of NU6140). Within each group the mice either received only sucrose (17.5mg/ml) or sucrose and DOX (50mg/ml and 2mg/ml, respectively) via the drinking water. Sucrose concentration in the DOX-treated groups was adapted according to the average water intake of mice in different groups: as mice receiving DOX via their drinking water have a lower water intake in average due to the bitter taste of DOX, a higher concentration of sucrose is necessary to ensure equal sucrose intake of mice across the different groups. The CDK2 inhibitor NU6140 was applied via intraperitoneal (i.p.) injection for 12 days. The endpoint of the experiment at which the mice were sacrificed by cervical dislocation was pre-determined as 14 days after start of inhibitor treatment, including a break of 1 day after every 4 treatment days. In case that humane endpoints as described in 'Xenotransplantation' would have been reached before attaining the experimental endpoint, respective mice would have been sacrificed as soon as a humane endpoint was reached. After sacrification of the mice, the respective tumors were extracted, a small piece of each tumor was frozen for RNA extraction (see section 'Extraction of RNA' for details), and the remaining tumors were formalin-fixed (4% formalin) for subjection to routine histology and IHC (see section 'Histology and immunohistochemistry (IHC)' for details). Furthermore, heart, lungs, liver,

pancreas, spleen, stomach, intestines, kidneys, adrenal glands, and bone marrow of each mouse were subjected to routine histology (see section 'Histology and immunohistochemistry (IHC)' for details).

4.2.26. Analysis of microarray gene expression data and overall patient survival

Published Affymetrix microarray gene expression data of 166 primary EwS tumors with matched clinical annotations were obtained from the GEO and used for overall patient survival analyses (accession numbers: GSE63157 (Volchenboum et al., 2015), GSE34620 (Postel-Vinay et al., 2012), GSE12102 (Scotlandi et al., 2009), GSE17618 (Savola et al., 2011); for generation of the data Affymetrix HG U133 Plus 2.0 or Affymetrix HuEx-1.0-st chips were used). To analyze EWSR1-FLI1 dependent transcriptomic changes, gene expression microarray data from A673/TR/shEF1 EwS cells in which a time course EWSR1-FLI1 knockdown was performed was used (accession number: GSE27524 (Bilke et al., 2013); 53 hours of DOX treatment condition was analyzed; for generation of the data an Affymetrix HG U133A 2.0 chip was used). Pre-processed datasets were available at the Grünewald laboratory (Munich, Germany). Pre-processing included normalization by RMA with usage of custom brainarray chip description files (CDF) and removal of batch effects using ComBat (Dai et al., 2005; Irizarry et al., 2003; Johnson et al., 2007; Stein et al., 2015). Patient stratification was performed either by quintile or median intra-tumoral gene expression levels of the respective gene. Significance levels for overall survival analyses were calculated using the Mantel-Haenszel test, either using GraphPad PRISM for single gene queries or GenEx for batch queries. *P* values < 0.05 were regarded as statistically significant.

4.2.27. Gene set enrichment analysis (GSEA)

To identify gene sets co-expressed with *MYBL2* in primary EwS, we used a microarray gene expression dataset including 166 primary EwS tumors (see section 'Analysis of microarray gene expression data and overall patient survival' for dataset details). For every gene represented in this dataset, the Pearson's correlation coefficient of its respective expression with that of *MYBL2* was calculated, genes were ranked according to the Pearson's correlation coefficient, and a pre-ranked GSEA with 1,000 permutations was performed (Subramanian et al., 2005). To identify gene sets co-expressed with *MYBL2* in our cell line model, we used the RNA-seq dataset generated in A673, SK-N-MC, and RDES EwS cells treated either with a non-targeting negative control siRNA or a specific siRNA directed against *MYBL2* (siMYBL2_4) (see section 'RNA sequencing (RNA-seq)' for dataset details). For every gene

represented in this dataset, the mean log2 fold change (FC) of technical triplicates in three EwS cell lines upon MYBL2 knockdown was calculated, genes were ranked according to the mean log2 FC, and a pre-ranked GSEA with 1,000 permutations was performed (Subramanian et al., 2005).

4.2.28. Analysis of publicly available ChIP- and DNAse-seq data

Pre-processed ChIP-seq data of A673 and SK-N-MC EwS cells (GSE61944) (Riggi et al., 2014) and ENCODE SK-N-MC DNAse-seq data (GSM736570) were retrieved from the GEO and visualized in the UCSC genome browser. The following samples were used: GSM1517544 SK-N-MC_shGFP_48h_FLI1; GSM1517553 SK-N-MC_shFLI1_48h_FLI1; GSM1517569 A673_shGFP_48h_FLI1; GSM1517572 A673_shFLI1_48h_FLI1; GSM1517548 SK-N-MC_shGFP_96h_H3K4me1; GSM1517557 SK-N-MC_shFLI1_96h_H3K4me1; GSM1517545 SK-N-MC_shGFP_48h_H3K27ac; GSM1517554 SK-N-MC_shFLI1_48h_H3K27ac; GSM1517568 A673 whole-cell extract (WCE).

4.2.29. Calling of microsatellite haplotypes from whole genome sequencing (WGS) data

WGS data of 58 primary EwS for some of which matched germline WGS data were available either from EwS patients treated in the Hospital for Sick Children (SickKids) in Toronto (Canada; in compliance with the Research Ethics Board (REB) guidelines, approval number 1000053452) (Anderson et al., 2018), or were publicly available from the International Cancer Genome Consortium (ICGC) (Tirode et al., 2014). WGS was performed on Illumina instruments using established protocols (150/150bp paired-end for Toronto samples, 100/100bp paired-end for ICGC samples). Raw WGS data analysis and calling of GGAA-mSat haplotypes was performed by Dr. Nathaniel D. Anderson (Shlien laboratory, Toronto, Canada). For reasons of coherence, consistency, and completeness, the results are described and displayed in this thesis, as they are a part of the published study underlying this thesis (Musa et al., 2019). Alignment of paired-end FASTQ files to the human genome (hg19) was performed using BWA-MEM (Li and Durbin, 2009), indel realignment and base quality scores were recalibrated with the Genome Analysis Toolkit (McKenna et al., 2010). For genotype calling of the *MYBL2*-associated GGAA-mSat, the Haplotype inference and phasing for Short Tandem Repeats (HipSTR) algorithm was applied (Willems et al., 2017) on the WGS data with a 10 reads minimum threshold. The following HipSTR default filters were passed by all genotypes: --min-call-qual 0.9;--max-call-flank-indel 0.15;--max-call-stutter 0.15;--min-call-allele-bias -2;--min-call-strand-bias -2.

4.2.30. Analysis of expression quantitative trait loci (eQTL)

For a subset of patients of the WGS cohort (see section ‘Calling of microsatellite haplotypes from whole genome sequencing (WGS) data‘ for details), matched published tumor gene expression data were available: RNA-seq data corresponding to the Toronto cohort is deposited at the European Genome-phenome Archive (EGA) with the accession number EGAS00001003062, and gene expression microarrays (Affymetrix HG U133A or HG U133 Plus 2.0 chips) (GSE37371; GSE7007 (Tirode et al., 2007); GSE34620 (Postel-Vinay et al., 2012)) corresponding to the ICGC cohort are deposited at the Gene Expression Omnibus (GEO). Separate normalization for each chip type was done by RMA with usage of custom brainarray chip description files (CDF) and removal of batch effects was performed using ComBat (Dai et al., 2005; Irizarry et al., 2003; Johnson et al., 2007; Stein et al., 2015). According to The Cancer Genome Atlas (TCGA) standard tissue requirements (http://cancergenome.nih.gov/cancersselected/biospeccriteria), only tumor samples with a tumor purity of >60% were considered for eQTL analyses. Estimation of tumor purity was done using the AscatNGS algorithm (for the Toronto cohort) (Raine et al., 2016) and the ESTIMATE algorithm (for the ICGC cohort) (Yoshihara et al., 2013). The number of samples included for each analysis of GGAA-mSat and ETS motif variance as well as for each eQTL analysis depended on the amount of samples for which both haplotypes of the respective investigated locus were possible to call from WGS data by application of the HipSTR algorithm (see section ‘Calling of microsatellite haplotypes from whole genome sequencing (WGS) data‘ for details). Called haplotypes of the *MYBL2*-associated mSat were classified as either ‘Short‘ (≤13 GGAA-repeats) or ‘Long‘ (>13 GGAA-repeats), in agreement with previously published data indicating that a GGAA-repeat number >13 represents a critical number of repeats above which a particularly strong EWSR1-FLI1 signal can be detected (Grünewald et al., 2015; Guillon et al., 2009; Johnson et al., 2017), and EWSR1-FLI1 ChIP-seq data reported here showing that, within the RDES EwS cell line, EWSR1-FLI1 preferentially binds to the 14-repeat allele than to the 12-repeat allele of the *MYBL2*-associated GGAA-mSat. Every tumor sample was consequently classified into either the ‘Short / Short‘, the ‘Short / Long‘, or the ‘Long / Long‘ group, according to the GGAA-repeat numbers of both alleles, and a classical eQTL analysis was performed comparing these groups regarding their *MYBL2* expression levels.

4.2.31. Human tissue samples and tissue microarrays (TMA)

The EwS TMAs used have been described before (Baldauf et al., 2018). Formalin-fixed and paraffin-embedded (FFPE) EwS samples were retrieved from the Institute of Pathology of the LMU Munich

(Germany) and the Gerhard-Domagk Institute of Pathology of the University Hospital of Münster (Germany). Written informed consent was obtained from all patients. Anonymized samples were analyzed retrospectively and blinded with approval of the LMU Munich ethics committee (approval number: 550-16 UE). For every sample, at least two cores with a diameter of each 1mm were used to construct TMAs. The samples were examined by a reference pathologist and all samples either showed an *EWSR1* break-apart as determined by fluorescence in-situ hybridization (FISH) or detectable transcripts of pathognomonic fusion oncogenes as determined by qRT-PCR.

4.2.32. Histology and immunohistochemistry (IHC)

Hematoxylin and eosin (HE) stainings were performed according to routine protocols of the facility for histopathological diagnostic at the Institute of Pathology of the LMU Munich. IHC was performed at the IHC core facility at the Institute of Pathology of the LMU Munich by the technical assistants Andrea Sendelhofert and Anja Heier. For IHC, 4µm sections were cut followed by antigen retrieval with microwave heating using the ProTaqs I Antigen-Enhancer for p-MYBL2 IHC or the Target Retrieval Solution for cleaved caspase 3 (CC3) IHC. Endogenous peroxidase was blocked using aqueous H_2O_2 solution (7.5%) and blocking serum for 20 minutes. Afterwards, incubation of the slides with the primary antibodies was performed for 60 minutes: anti-p-MYBL2 (1:100) or anti-CC3 (1:100) (see section ‘Antibodies‘ for details). Slides were then incubated with a secondary anti-rabbit IgG antibody (see section ‘Antibodies‘ for details) and target detection was performed using DAB+ chromogen. For counterstaining, hematoxylin Gill’s Formula was used.

4.2.33. Quantification of immunoreactivity and mitoses

Quantification of p-MYBL2 immunoreactivity has been carried out in a semi-quantitative manner by a blinded observer (Dr. Maximilian M. L. Knott, Grünewald laboratory, Munich, Germany). Scoring was performed according to the Immune Reactive Score (IRS), which is in pathological routine use for scoring of hormone receptor expression in breast cancer (Remmele and Stegner, 1987). Intensity of immunoreactivity (score 0 = none, score 1 = low, score 2 = intermediate, and score 3 = strong) and percentage of cells stained with a respective intensity (score 0 = 0%, score 1 = 0–9%, score 2 = 10–50%, score 3 = 51–80%, and score 4 = 81–100%) was evaluated per representative high-power field (x40 objective). The IRS was defined as the product of the predominant intensity score and the corresponding

percentage score for each technical replicate of a sample. The median of IRS scores from the technical replicates of a sample define the final IRS score of a sample. CC3 immunoreactivity was automatically quantified on scanned slides by determination of the percentage of positive high-power field area, using Fiji (ImageJ) (Schindelin et al., 2012; Schneider et al., 2012). For this, a histological image of a representative high-power field was loaded in Fiji in JPEG data format. The image type was converted into a red-green-blue (RGB) stack, whereby for the blue stack image a threshold was applied with the pre-defined ‘intermode‘ setting. In case of images for which the ‘intermode‘ setting was not applicable, the pre-defined ‘default‘ setting was used instead. After setting the threshold, the CC3 positive picture area was displayed red and the percentage of red picture area was automatically quantified by Fiji. Quantification of mitoses has been performed by manual counting of mitoses in HE-stained slides per representative high-power field. For each sample, the final score/quantification was determined by evaluation of 4-16 representative high-power fields.

4.2.34. Statistics

Statistical analysis of the raw data of functional *in vitro* and *in vivo* experiments, as well as analysis of *in situ* and *in silico* data was done using GraphPad PRISM if not otherwise indicated (see section ‘Software and interfaces‘ for details). In case of patient survival analysis, *P* values were calculated either using GenEx (custom code by Julia S. Gerke, Grünewald laboratory, Munich, Germany) in case of batch queries, or GraphPad PRISM for single gene queries, stratifying patients either according to their quintile or median gene expression levels. *P* values regarding GSEA were calculated by the GSEA interface tool (see section ‘Software and interfaces‘ for details). For functional *in vitro* experiments, a two-tailed Mann-Whitney test was used, if not otherwise specified in the corresponding figure legend, whereby a P value < 0.05 was regarded as statistically significant (***P < 0.001, **P < 0.01, *P < 0.05, ns = not significant). For analysis of survival in functional *in vivo* experiments, the Mantel-Haenszel test was used, whereby a P value < 0.05 was regarded as statistically significant. In case of three-group comparison of ordinal-scale data, a Kruskal-Wallis test was used, whereby a P value < 0.05 was regarded as statistically significant. If applicable, correction for multiple testing was performed using the Bonferroni method. Sample size of functional *in vitro* experiments was chosen empirically, and sample size for *in vivo* experiments was pre-determined assuming $\beta=0.8$ and $\alpha=0.05$ in compliance with the 3R model (replacement, reduction, refinement).

5. RESULTS

5.1. *MYBL2* is a patient outcome-associated EWSR1-FLI1 target gene in EwS

In order to screen for genes that may mediate the effect of an 'oncogenic cooperation' between a dominant driver-oncogene (here *EWSR1-FLI1*) and regulatory germline variants (here a polymorphic enhancer-like GGAA-microsatellite (mSat)) on tumor progression of EwS, two datasets were used, whereby only genes represented in both datasets were considered. First, to identify genes strongly regulated by EWSR1-FLI1, a publicly available time course gene expression microarray dataset of A673/TR/shEF1 EwS cells containing a doxycycline (DOX)-inducible shRNA construct directed against *EWSR1-FLI1* treated with DOX for maximum 96 hours was used, whereby RNA expression was arrayed at six different timepoints (0, 18, 36, 53, 72, and 96 hours). Herein, the log2 fold change (FC) for the 53 hours of DOX-treatment condition was calculated for each gene compared to the 0 hours of DOX-treatment condition (**Table 16**).

Entrez ID	Gene Symbol	FC (log2)
797	*CALCB*	-4.048
5100	*PCDH8*	-4.045
5502	*PPP1R1A*	-3.754
55388	*MCM10*	-3.696
4998	*ORC1*	-3.514
990	*CDC6*	-3.426
79723	*SUV39H2*	-3.352
4602	*MYB*	-3.330
8318	*CDC45*	-3.293
9319	*TRIP13*	-3.233
9156	*EXO1*	-3.086
4886	*NPY1R*	-3.059
11339	*OIP5*	-3.050
29028	*ATAD2*	-3.048
51659	*GINS2*	-3.045
4605	*MYBL2*	-3.037
5427	*POLE2*	-3.029
51514	*DTL*	-2.943
55872	*PBK*	-2.915
641	*BLM*	-2.912
5449	*POU1F1*	-2.909
57405	*SPC25*	-2.907
5579	*PRKCB*	-2.903
79733	*E2F8*	-2.901
220134	*SKA1*	-2.900

Table 16: Top 25 downregulated genes upon 53 hours of EWSR1-FLI1 knockdown as determined by microarray gene expression profiling in A673/TR/shEF1 EwS cells. Data from Musa et al., 2019.

The 53 hours timepoint in the middle of the time course was chosen to ensure a sufficient EWSR1-FLI1 knockdown, while at the same time reflecting early transcriptomic alterations due to the EWSR1-FLI1 knockdown (see section 'Analysis of microarray gene expression data and overall patient survival' for microarray details and references). Second, to identify genes significantly associated with overall EwS patient survival, a publicly available gene expression microarray dataset of 166 primary EwS, for which matched clinical annotations were available, was used (see **Table 17** for patient characteristics).

Characteristic	Patients (%) (n=166)
Gender	
Female	72 (43%)
Male	94 (57%)
Age	
< 15 years	83 (50%)
≥ 15 years	83 (50%)
Disease time	
< 40 months	50 (30%)
40 months – 79 months	63 (38%)
≥ 80 months – 192 months	53 (32%)
Survival	
Alive	95 (57%)
Dead	71 (43%)
***MYBL2* expression level**	
Low	80 (48%)
Intermediate	58 (35%)
High	25 (15%)
Very high	3 (2%)

Table 17: Patient characteristics of the cohort comprising 166 primary EwS for which microarray gene expression data and matched clinical annotations were available.

Kaplan-Meier analysis for overall survival (OS) was performed in a batch-analysis for every gene that was represented on the microarray using GenEx (custom code software, developed by Julia S. Gerke, Grünewald laboratory, Munich, Germany), stratifying patients according to their quintile intra-tumoral expression levels of the respective gene (see section 'Analysis of microarray gene expression data and overall patient survival' for microarray details and references). Automated *P* value calculation for overall survival with GenEx was performed using the Mantel-Haenszel test comparing the group of highest vs. lowest intra-tumoral expression of the respective gene, including Bonferroni correction for multiple comparisons (**Table 18**).

Entrez ID	Gene symbol	*P* value	Bonferroni
9666	*DZIP3*	2.263E-08	4.365E-04
51473	*DCDC2*	3.908E-08	7.536E-04
284440	*LINC00663*	4.115E-08	7.936E-04
80208	*SPG11*	6.145E-08	0.001
79800	*CARF*	1.255E-07	0.002
252995	*FNDC5*	1.264E-07	0.002
494513	*dfnb59*	9.766E-08	0.002
727	*C5*	1.702E-07	0.003
4077	*NBR1*	1.411E-07	0.003
55650	*PIGV*	1.991E-07	0.004
83700	*JAM3*	1.818E-07	0.004
162427	*FAM134C*	2.901E-07	0.006
4636	*MYL5*	3.601E-07	0.007
92565	*fank1*	4.337E-07	0.008
54681	*P4HTM*	5.557E-07	0.011
1657	*DMXL1*	6.677E-07	0.013
401264	*TRAM2-AS1*	6.938E-07	0.013
10826	*FAXDC2*	8.493E-07	0.016
11279	*KLF8*	8.783E-07	0.017
4605	*MYBL2*	9.573E-07	0.018
54494	*C11orf71*	1.009E-06	0.019
375287	*RBM43*	9.958E-07	0.019
254295	*PHYHD1*	1.393E-06	0.027
152098	*ZCWPW2*	1.492E-06	0.029
55732	*c1orf112*	1.536E-06	0.030

Table 18: Top 25 genes whose high intra-tumoral expression levels are associated with poor overall EwS patient survival in a cohort comprising 166 primary EwS. Data from Musa et al., 2019.

Integration of both datasets reveals *MYBL2*, a gene encoding for a transcription factor regulating cell cycle progression, cell survival, and cell differentiation (Musa et al., 2017), as the top gene that is on the one hand strongly regulated by EWSR1-FLI1 (log2 FC = -3.037) and whose high intra-tumoral expression is on the other hand concurrently associated with unfavorable OS of EwS patients (nominal *P* value = 9.573 x 10^{-7}; Bonferroni-corrected *P* value = 0.018) (**Figure 13A,B**). The EWSR1-FLI1-dependent regulation of MYBL2 expression was validated on protein level in A673/TR/shEF1 cells by time course western blot, in which EWSR1-FLI1 knockdown was performed for seven days via DOX addition to the medium followed by EWSR1-FLI1 re-expression for further ten days via removal of DOX from the medium, whereby protein was harvested at day 0, 7, 11, 14, and 17 (**Figure 13C**). The results show that MYBL2 levels follow closely those of EWSR1-FLI1 on protein level *in vitro* (**Figure 13C**). In order to exclude that the observed regulatory effect of EWSR1-FLI1 is cell line specific, nine additional

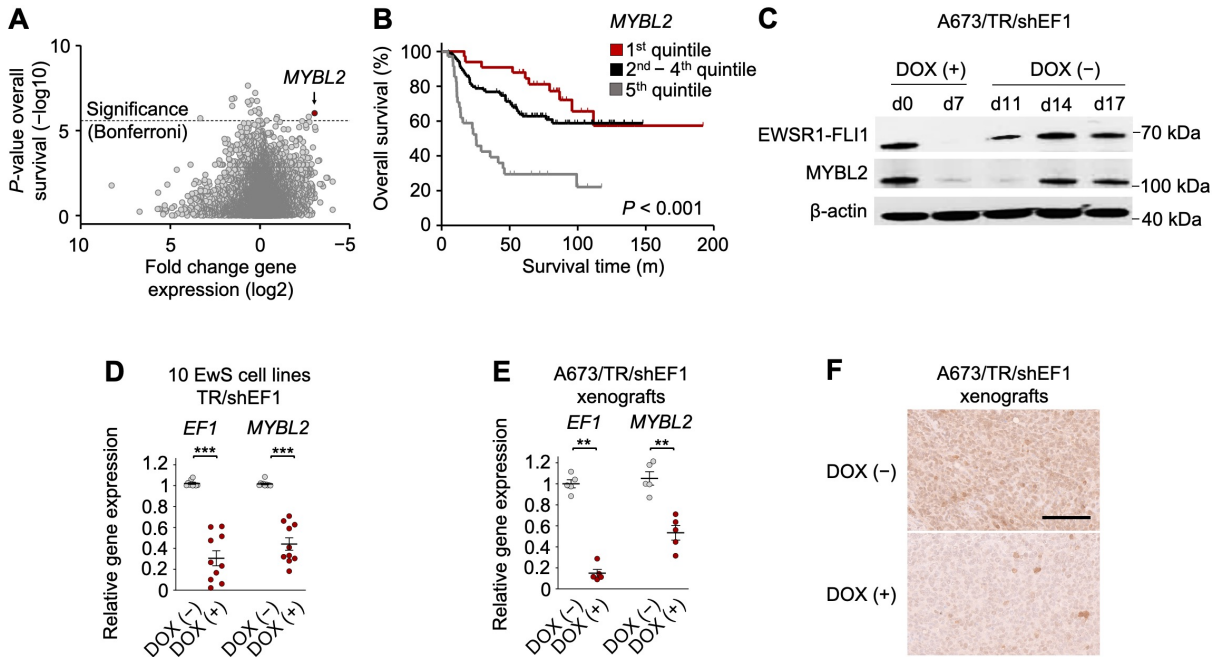

Figure 13: *MYBL2* is a patient outcome-associated EWSR1-FLI1 target gene in EwS. (A) Crossing of a microarray gene expression dataset of A673/TR/shEF1 cells profiled with or without doxycycline (DOX)-treatment for 53 hours and another microarray gene expression dataset of 166 primary EwS for which matched clinical annotations were available. For the first dataset, the log2 fold change (FC) for every gene represented on both microarrays was calculated, for the latter dataset, Bonferroni-corrected *P* values for association with overall patient survival were calculated for every gene represented on the microarray using the Mantel-Haenszel-test. Each dot indicates a gene represented on both microarrays. The dashed line indicates the significance threshold for Bonferroni-corrected *P* values ($P < 0.05$). (B) Kaplan-Meier plot showing overall survival analysis of 166 EwS patients stratified according to their intra-tumoral *MYBL2* expression quintiles. *P* value was determined by using the Mantel-Haenszel-test. (C) Time course western blot in A673/TR/shEF1 cells using anti-EWSR1-FLI1 and anti-MYBL2 antibodies. Knockdown of EWSR1-FLI1 was performed for seven days by DOX addition to the medium and EWSR1-FLI1 was re-expressed by removal of DOX from the medium for ten further days. Protein was extracted at indicated days. β-actin served as a loading control. (D) Relative *EWSR1-FLI1 (EF1)* and *MYBL2* expression as determined by qRT-PCR in ten different EwS cell lines containing a DOX-inducible shRNA directed against *EWSR1-FLI1* treated with or without DOX for 96 hours. n=1 biologically independent experiment for each of the ten cell lines. (E) Relative *EWSR1-FLI1 (EF1)* and *MYBL2* expression of A673/TR/shEF1 cell line xenografts, treated with or without DOX for 96 hours as determined by qRT-PCR. n=5 samples per condition. (F) Representative p-MYBL2 immunohisto-chemistry (IHC) micrographs of xenografts described in '(E)'. Scale bar represents 100µm. Larger scale image is displayed in **Supplementary Figure 1** (Appendix). ***$P < 0.001$, **$P < 0.01$. Horizontal bars represent means, whiskers represent the SEM, if not otherwise specified. *P* values were determined via two-tailed Mann-Whitney test, if not otherwise specified. Figures A-C and E from Musa et al., 2019. Figure F modified from Musa et al., 2019.

EwS cell lines harboring a DOX-inducible shRNA construct directed against *EWSR1-FLI1*, were treated with or without DOX and *EWSR1-FLI1* and *MYBL2* expression levels were determined by quantitative real-time polymerase chain reaction (qRT-PCR) (**Figure 13D**). In all tested cell lines, knockdown of EWSR1-FLI1 leads to a reduction of *MYBL2* expression (**Figure 13D**). However, to evaluate this association *in vivo*, A673/TR/shEF1 cells were xenografted subcutaneously in NOD scid gamma (NSG) mice and treated with or without DOX via the drinking water of the mice for 96 hours. After sacrification of the mice, tumors were excised, RNA was extracted from a piece of the tumor, followed by subsequent

reverse transcription and qRT-PCR to determine *EWSR1-FLI1* and *MYBL2* expression levels, and slides of formalin-fixed and paraffin-embedded (FFPE) tumors were subjected to immunohistochemistry (IHC) for p-MYBL2. The results consistently show a downregulation of *MYBL2* as determined by qRT-PCR and a reduction of p-MYBL2 immunoreactivity upon EWSR1-FLI1 suppression (**Figure 13E,F**), which is in accordance with the observed *in vitro* findings and shows that MYBL2 expression is as well reduced upon EWSR1-FLI1 suppression on mRNA and protein level *in vivo*. In summary, these data show that MYBL2 expression is regulated by EWSR1-FLI1 *in vitro* and *in vivo* and that high levels of intra-tumoral *MYBL2* expression are associated with unfavorable OS of EwS patients (**Figure 13**).

5.2. EWSR1-FLI1 regulates MYBL2 expression via a polymorphic GGAA-microsatellite in EwS

EWSR1-FLI1 binds polymorphic enhancer-like GGAA-microsatellites (mSats) in order to steer the expression of nearby genes, whereby polymorphisms in such regulatory elements determine inter-individual differences in intra-tumoral gene expression and susceptibility to EwS (Gangwal et al., 2008; Grünewald et al., 2015; Riggi et al., 2014) (see sections ‘Etiology and pathophysiology‘ and ‘The concept of ‘oncogenic cooperation‘‘ for details). Therefore, a screen for such GGAA-mSats in proximity to *MYBL2* (~150kb upstream and downstream of the gene body) was performed. Published chromatin immunoprecipitation and DNA sequencing (ChIP-seq) data for EWSR1-FLI1, H3K4me1, and H3K27ac in A673 and SK-N-MC EwS cells either expressing a shRNA directed against *GFP* (control) or *EWSR1-FLI1*, as well as DNase I hypersensitive sites sequencing (DNAse-seq) data in SK-N-MC cells were analyzed, revealing a strong EWSR1-FLI1 signal ~150kb downstream of *MYBL2* in A673 and SK-N-MC cells, mapping to a GGAA-mSat **(Figure 14A)**. Strikingly, this signal is diminished upon EWSR1-FLI1 knockdown in both cell lines (**Figure 14A**). The respective locus exhibits high DNAse I hypersensitivity, indicative for open chromatin, and strong H3K4me1 and H3K27ac ChIP-seq peaks, indicative for active enhancers, whereby both H3K4me1 and H3K27ac signals are as well strongly reduced upon EWSR1-FLI1 repression (**Figure 14A**). In order to validate the enhancer activity of this *MYBL2*-associated GGAA-mSat *in vitro*, haplotypes of the respective mSat with diverse numbers of consecutive GGAA-repeats were PCR-cloned from three different EwS cell lines (RDES, A673, and SK-N-MC) into a pGL3-Promoter-Fluc vector. The cloned haplotypes included ~440bp of upstream and downstream flanking region encompassing the GGAA-mSat. Luciferase reporter assays conducted in A673/TR/shEF1 cells with and without DOX-induced EWSR1-FLI1 knockdown confirm EWSR1-FLI1-dependent

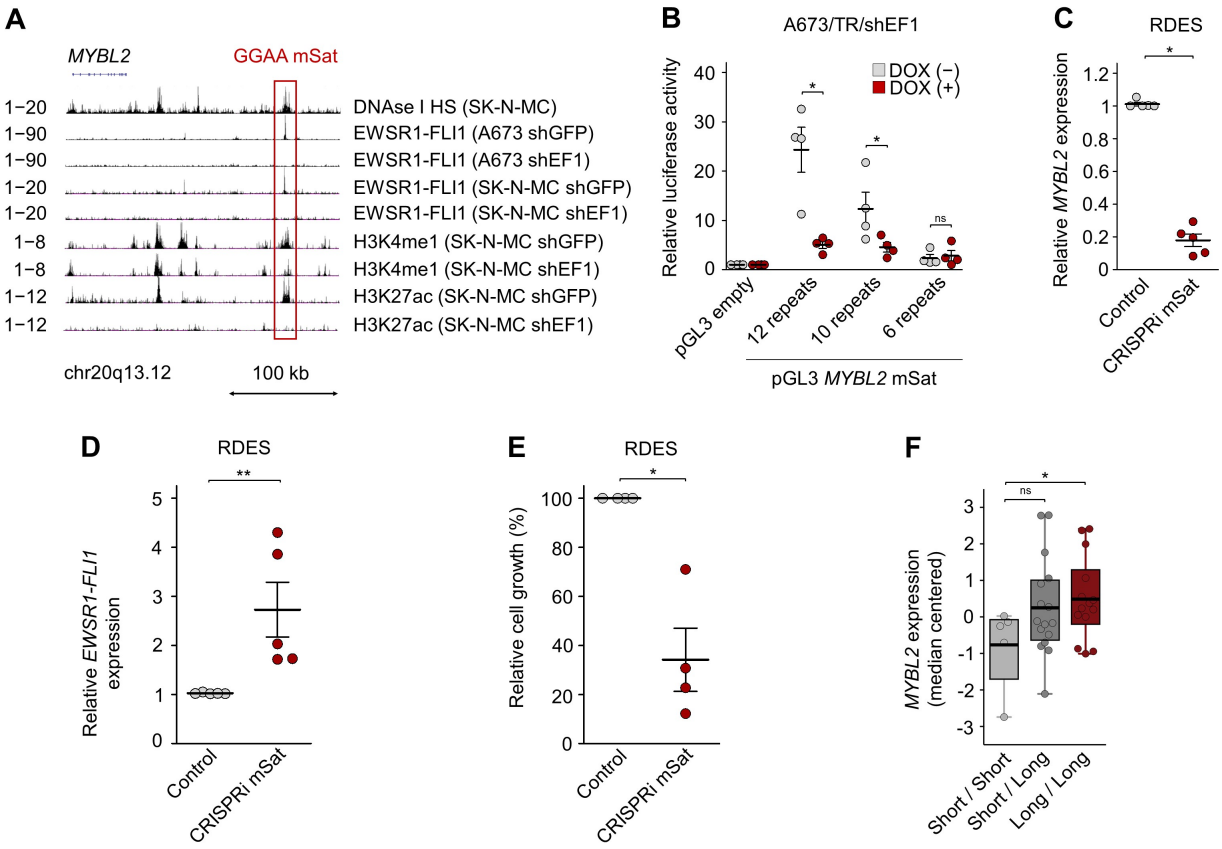

Figure 14: EWSR1-FLI1 regulates MYBL2 expression via a polymorphic GGAA-mSat in EwS. (A) Analysis of publicly available EWSR1-FLI1, H3K4me1, and H3K27ac chromatin immunoprecipitation and DNA sequencing (ChIP-seq) data in A673 and SK-N-MC EwS cells, each containing either a shRNA construct directed against *GFP* (shGFP, serving as a control) or *EWSR1-FLI1* (shEF1), as well as published DNAse I hypersensitivity sites sequencing (DNAse-seq) data in SK-N-MC cells. Displayed is the epigenetic profile at the *MYBL2* locus. (B) Luciferase reporter assays conducted in A673/TR/shEF1 cells that were transfected with pGL3-Promoter-Fluc vectors containing cloned haplotypes with variant consecutive GGAA-repeat numbers of the *MYBL2*-associated microsatellite (mSat) from three different EwS cell lines and treated with or without doxycycline (DOX). n=4 biologically independent experiments. *P* values were determined via one-tailed Mann-Whitney test. (C) Relative *MYBL2* expression as determined by quantitative real-time polymerase chain reaction (qRT-PCR) in RDES EwS cells with or without Clustered Regularly Interspaced Short Palindromic Repeats interference (CRISPRi) with the *MYBL2*-associated GGAA-mSat by using either a non-targeting gRNA (Control) or specific gRNAs targeting the *MYBL2*-associated mSat. n=5 biologically independent experiments. (D) Relative *EWSR1-FLI1* expression as determined by qRT-PCR in RDES EwS cells with or without CRISPR interference with the *MYBL2*-associated GGAA-mSat using either a non-targeting gRNA (Control) or specific gRNAs targeting the *MYBL2*-associated mSat. (E) Relative cell growth of RDES EwS cells as determined by colorimetry with or without CRISPRi with the *MYBL2*-associated GGAA-mSat using either a non-targeting gRNA (Control) or specific gRNAs targeting the *MYBL2*-associated mSat. (F) Expression quantitative trait loci (eQTL) analysis in 35 whole genome sequenced (WGS) primary EwS with matched tumor RNA-sequencing (RNA-seq) gene expression data, showing the intra-tumoral *MYBL2* expression in dependency of the number of consecutive GGAA-repeats of the *MYBL2*-associated GGAA-mSat. 'Short' refers to haplotypes harboring ≤13 consecutive GGAA-repeats, whereas 'Long' refers to haplotypes harboring >13 consecutive GGAA-repeats, allowing a subsequent classification of every patient into either the 'Short / Short', the 'Short / Long', or the 'Long / Long' group. Horizontal bars represent means, upper and lower hinges represent the 75th and 25th percentile (interquartile range), and whiskers minimum and maximum expression values. n≥5 samples per group. Not significant, ns; $^{**}P < 0.01$, $^{*}P < 0.05$. Horizontal bars represent means, whiskers represent the SEM, if not otherwise specified. *P* values were determined via two-tailed Mann-Whitney test, if not otherwise specified. Figures from Musa et al., 2019.

enhancer activity of the *MYBL2*-associated GGAA-mSat and show that the number of consecutive GGAA-repeats at this locus is positively correlated with the GGAA-mSat enhancer activity within the observed range of repeat numbers (**Figure 14B**). To test whether interference with this GGAA-mSat regulates *MYBL2* expression levels, Clustered Regularly Interspaced Short Palindromic Repeats interference (CRISPRi) with the respective mSat was performed. CRISPRi promotes an inhibiting chromatin state of the targeted genomic region and thereby blocks protein binding to it without induction of a knockout (as compared to classical CRISPR approaches; see section 'Clustered Regularly Interspaced Short Palindromic Repeats interference (CRISPRi) ' for details) (Boulay et al., 2018; Gilbert et al., 2014; Thakore et al., 2015). Using specific gRNAs targeting the *MYBL2*-associated GGAA-mSat, CRISPRi-mediated epigenetic inhibition of the respective mSat leads to strong *MYBL2* downregulation as compared to non-targeting negative control gRNAs, confirming the regulatory role of the GGAA-mSat regarding EWSR1-FLI1-driven *MYBL2* expression (**Figure 14C**). Interestingly, CRISPRi with the *MYBL2*-associated mSat is also associated with a potentially counter-regulatory increase of *EWSR1-FLI1* levels (**Figure 14D**) and a reduction of cell growth (**Figure 14E**). To evaluate the association between the number of consecutive GGAA-repeats of the *MYBL2*-associated mSat and *MYBL2* expression levels in primary EwS patient samples, expression quantitative trait loci (eQTL) analysis for this locus was performed in 35 whole genome sequenced (WGS) primary EwS for which matched tumor RNA sequencing (RNA-seq) gene expression data was available (see section 'Analysis of expression quantitative trait loci (eQTL)' for details). Haplotypes for both alleles of each patient sample were called using the Haplotype inference and phasing for Short Tandem Repeats (HipSTR) algorithm (see section 'Calling of microsatellite haplotypes from whole genome sequencing (WGS) data' for details and corresponding references). As described previously in the literature, 13 GGAA-repeats delineate a repeat number beyond which the EWSR1-FLI1-dependent enhancer activity of a GGAA-mSat strongly increases (Grünewald et al., 2015; Guillon et al., 2009; Johnson et al., 2017), which is in accordance with EWSR1-FLI1 ChIP-seq data in RDES EwS cells (heterozygous for the *MYBL2*-associated mSat, harboring 12 and 14 repeats) that show preferential EWSR1-FLI1 binding to the longer allele (71% of obtained reads spanning the mSat mapped to the longer haplotype vs. 29% mapping to the shorter haplotype). In this regard, a stratification of every haplotype as either 'Short' (≤13 GGAA-repeats) or 'Long' (>13 GGAA-repeats) was performed, allowing the classification of each sample into either the 'Short / Short', the 'Short / Long', or the 'Long / Long' group (**Table 19**).

Sample number	Tumor purity	Allele A (tumor)	Allele B (tumor)	Genotype	*MYBL2* expression (median centered)
1	0.76	6	13	Short / Short	-2.742
2	0.75	13	13	Short / Short	-0.702
3	0.96	6	12	Short / Short	-0.139
4	0.76	6	9	Short / Short	-0.249
5	0.76	13	13	Short / Short	0.026
6	0.69	6	15	Short / Long	-2.106
7	0.76	13	15	Short / Long	-0.913
8	0.76	6	16	Short / Long	-0.799
9	0.75	6	16	Short / Long	-0.701
10	0.77	6	15	Short / Long	-0.485
11	0.76	6	16	Short / Long	-0.333
12	0.76	6	15	Short / Long	-0.203
13	0.75	12	15	Short / Long	-0.168
14	0.75	6	16	Short / Long	-0.115
15	0.75	6	15	Short / Long	0.272
16	0.77	6	14	Short / Long	0.353
17	0.89	6	16	Short / Long	0.911
18	0.76	9	15	Short / Long	1.058
19	0.77	13	15	Short / Long	1.764
20	0.99	6	17	Short / Long	2.776
21	0.77	6	15	Short / Long	2.786
22	1.00	14	16	Long / Long	-0.946
23	0.76	15	16	Long / Long	-1.009
24	1.00	14	15	Long / Long	-0.874
25	0.96	15	16	Long / Long	0.050
26	0.75	14	16	Long / Long	0.000
27	1.00	16	16	Long / Long	0.200
28	1.00	14	16	Long / Long	0.232
29	0.77	15	15	Long / Long	0.375
30	0.76	15	16	Long / Long	0.461
31	0.78	16	16	Long / Long	0.549
32	0.76	14	16	Long / Long	1.064
33	0.76	14	14	Long / Long	1.994
34	0.82	14	16	Long / Long	2.366
35	0.76	15	16	Long / Long	2.407

Table 19: Called haplotypes of the *MYBL2*-associated GGAA-microsatellite (mSat) from 35 whole genome sequenced primary EwS with matched *MYBL2* gene expression data as determined by RNA sequencing (RNA-seq). Data from Musa et al., 2019.

Comparison of intra-tumoral *MYBL2* expression levels between these groups reveals that the ‘Long / Long‘ group exhibits significantly higher *MYBL2* levels as compared to the ‘Short / Short‘ group, whereby the ‘Short / Long‘ group ranges in between (**Figure 14F**). Importantly, to exclude somatic alterations as a source for variations in the number of consecutive GGAA-repeats of the *MYBL2*-associated mSat and

to evaluate inheritance of the inter-individually variable number of GGAA-repeats at the respective locus via the germline, haplotypes of 38 whole genome sequenced primary EwS tumor samples (to a large extent overlapping with the cohort used for eQTL analysis, see section 'Calling of microsatellite haplotypes from whole genome sequencing (WGS) data' for details and corresponding references; for merged patient characteristics see **Table 20**) were compared with the haplotypes of matched whole genome sequenced germline tissue samples, showing that in every individual the number of consecutive GGAA-repeats of both haplotypes is entirely conserved between the germline DNA and the tumor DNA, strongly suggesting the inheritance of the GGAA-repeat number of the *MYBL2*-associated mSat via the germline (**Table 21**).

Characteristic	Cohort (n=58)
Gender	
Female	26 (45%)
Male	32 (55%)
Age	
< 15 years	27 (47%)
≥ 15 years	31 (53%)
Primary tumor localization	
Axial	33 (57%)
Extremity (proximal)	15 (26%)
Extremity (distal)	9 (15%)
Information not available	1 (2%)
Tissue	
Bone	49 (84%)
Soft-tissue	8 (14%)
Information not available	1 (2%)

Table 20: Patient characteristics of 58 whole genome sequenced primary EwS, for some of which matched germline whole genome sequencing data and/or tumor RNA sequencing (RNA-seq) gene expression data were available.

In conclusion, the data reveals that EWSR1-FLI1 regulates the expression of MYBL2 via a polymorphic enhancer-like GGAA-mSat, whose number of consecutive GGAA-repeats is positively correlated with intra-tumoral *MYBL2* expression and is entirely conserved between germline DNA and tumor DNA, indicating the inheritance of the polymorphic features at this genomic locus via the germline (**Figure 14**, **Table 19,21**).

Sample number	Tumor purity	Allele A (germline)	Allele B (germline)	Allele A (tumor)	Allele B (tumor)
1	0.76	6	13	6	13
2	0.75	13	13	13	13
3	0.96	6	12	6	12
4	0.76	6	9	6	9
5	0.76	13	13	13	13
6	0.69	6	15	6	15
8	0.76	6	16	6	16
9	0.75	6	16	6	16
10	0.77	6	15	6	15
11	0.76	6	16	6	16
12	0.76	6	15	6	15
13	0.75	12	15	12	15
16	0.77	6	14	6	14
17	0.89	6	16	6	16
19	0.77	13	15	13	15
20	0.99	6	17	6	17
22	1.00	14	16	14	16
23	0.76	15	16	15	16
25	0.96	15	16	15	16
27	1.00	16	16	16	16
28	1.00	14	16	14	16
29	0.77	15	15	15	15
32	0.76	14	16	14	16
33	0.76	14	14	14	14
34	0.82	14	16	14	16
36	0.60	6	13	6	13
37	0.87	6	13	6	13
38	0.90	12	14	12	14
39	0.49	6	15	6	15
40	0.67	6	15	6	15
41	1.00	13	15	13	15
42	1.00	6	15	6	15
43	0.93	14	16	14	16
54	0.85	14	15	14	15
55	0.93	13	15	13	15
56	0.95	14	16	14	16
57	0.95	16	16	16	16
58	1.00	15	17	15	17

Table 21: Called haplotypes of the *MYBL2*-associated mSat from 38 whole genome sequenced matched germline and tumor (primary EwS) DNA pairs. Data from Musa et al., 2019.

5.3. MYBL2 is heterogeneously expressed in EwS

Given the regulation of MYBL2 expression by EWSR1-FLI1 via a polymorphic enhancer-like GGAA-mSat, it is expected that intra-tumoral MYBL2 expression levels vary between cell lines and patients. Indeed, *MYBL2* expression levels as measured by qRT-PCR in 22 EwS cell lines show strong variability between the cell lines (**Figure 15A**). Such variability was as well observed in a microarray gene expression dataset of 166 primary EwS patient samples, in which patients can be classified in four groups according to their log2 *MYBL2* expression levels (low: ≤6 - <7, 48%; intermediate: 7 - <8, 35%; high: 8 - <9, 15%; very high: ≥9, 2%) (**Figure 15B**). However, to rule out that the variability of *MYBL2* expression is caused by variability in EWSR1-FLI1 expression, a subset of the microarray dataset for which information about the present fusion oncogene type of the samples was available ('ICGC reference cohort') (Postel-Vinay et al., 2012), and in which samples harboring fusion types other than *EWSR1-FLI1* were excluded, was analyzed using linear regression of (*EWSR1-*)*FLI1* expression onto *MYBL2* expression. *MYBL2* expression levels do not correlate with expression levels of *FLI1* (which may serve as a surrogate marker for *EWSR1-FLI1* expression, as wildtype *FLI1* is almost not expressed in EwS) (**Figure 15C**), which indicates that inter-individual variations of *MYBL2* expression levels are not due to minor variations of *EWSR1-FLI1* expression between individual tumors, and may be caused by a different mechanism, such as regulation via a polymorphic enhancer-like GGAA-mSat (see section 'EWSR1-FLI1 regulates MYBL2 expression via a polymorphic GGAA-microsatellite in EwS' for details). To validate the inter-individual variability observed on mRNA level as well on protein level, a EwS tissue microarray (TMA) comprising an independent cohort of 208 primary EwS was immunohistochemically stained for p-MYBL2 (**Figure 15D**). Herein, compared to inter-individual variations in *MYBL2* mRNA expression (**Figure 15B**), p-MYBL2 protein expression shows a similar inter-individual variability as determined by semi-quantitative assessment of immunoreactivity using the Immune Reactive Score (IRS) (low: IRS 0 - <3, 44%; intermediate: IRS 3 - <6, 40%; high: IRS 6 - <9, 13%; very high: IRS 9-12, 3%) (**Figure 15D**). These data show that MYBL2 is heterogeneously expressed in EwS (**Figure 15**).

5.4. MYBL2 promotes proliferation, survival, and clonogenicity of EwS cells *in vitro*

In order to obtain first insights into the functional role of MYBL2 in EwS, a gene set enrichment analysis (GSEA) using the microarray gene expression dataset comprising 166 primary EwS patient samples was performed. Genes co-expressed with *MYBL2* were enriched in gene sets including human orthologs of known MYBL2 targets in zebrafish (Shepard et al., 2005), proliferation / cell cycle progression

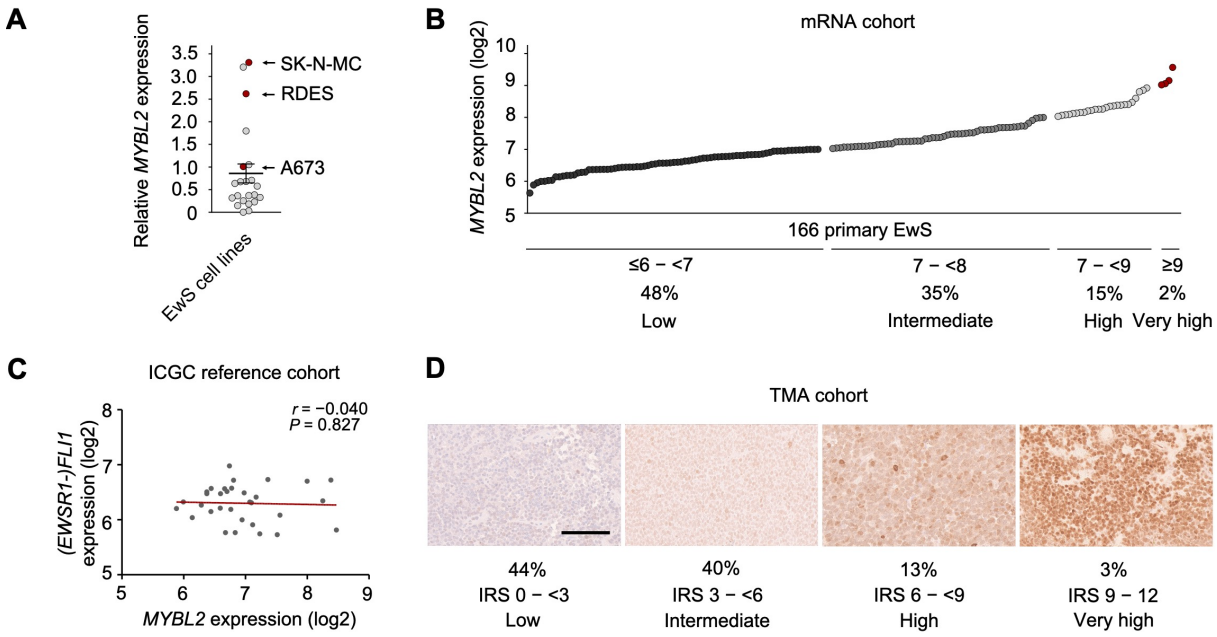

Figure 15: MYBL2 is heterogeneously expressed in EwS. (A) *MYBL2* expression of 22 EwS cell lines as determined by quantitative real-time polymerase chain reaction (qRT-PCR). *MYBL2* expression of each cell line is normalized to that of A673. Horizontal bars represent means, whiskers represent the SEM. n=1 biologically independent experiment per cell line. (B) Ranked log2 *MYBL2* expression of 166 primary EwS as determined by microarray profiling. Percentages of samples in expression groups are given. (C) Linear regression of (*EWSR1*-)*FLI1* expression onto *MYBL2* expression as determined by microarray profiling using 32 primary EwS samples of the 'ICGC reference cohort'. (D) Representative micrographs of p-MYBL2 immunohistochemistry (IHC) performed on a tissue microarray (TMA) including 208 primary EwS. Percentages of samples in expression groups are given. IRS: Immune Reactive Score. Scale bar represents 100µm. Larger scale image is displayed in **Supplementary Figure 2** (Appendix). Figure C from Musa et al., 2019. Figures B and D modified from Musa et al., 2019.

signatures (Ben-Porath et al., 2008; Fischer et al., 2016b), and sensitization to apoptosis through CDK inhibition (Wu et al., 2002) (**Figure 16A**), suggesting that MYBL2 is a central EWSR1-FLI1 downstream player promoting evolutionary conserved pro-proliferative programs. Knockdown of MYBL2 in three EwS cell lines (A673, SK-N-MC, and RDES) with high to moderate *MYBL2* expression using four different specific siRNAs directed against *MYBL2* (**Figure 16B,C**), leads to a reduction of viable cell number and an increase in trypan blue positive dead cells as measured by trypan blue exclusion (**Figure 16D,E**), alongside with a G2/M blockage and increased apoptotic cell death as measured by flow cytometry (**Figure 16F,G**), as compared to a non-targeting control siRNA. In order to assess clonogenic growth and growth of EwS cell line xenografts in dependency of their MYBL2 expression, A673 and SK-N-MC EwS cells containing either a DOX-inducible control shRNA or DOX-inducible specific shRNAs directed against *MYBL2* were generated using lentiviral transduction (**Figure 16H**). Colony formation assays (CFA) revealed that DOX-inducible *MYBL2* knockdown impairs clonogenic growth of EwS cells, which was not observed using cells containing a non-targeting control shRNA (**Figure 16I,J**). These results show that MYBL2 promotes proliferation, survival, and clonogenicity of EwS cells *in vitro* (**Figure 16**).

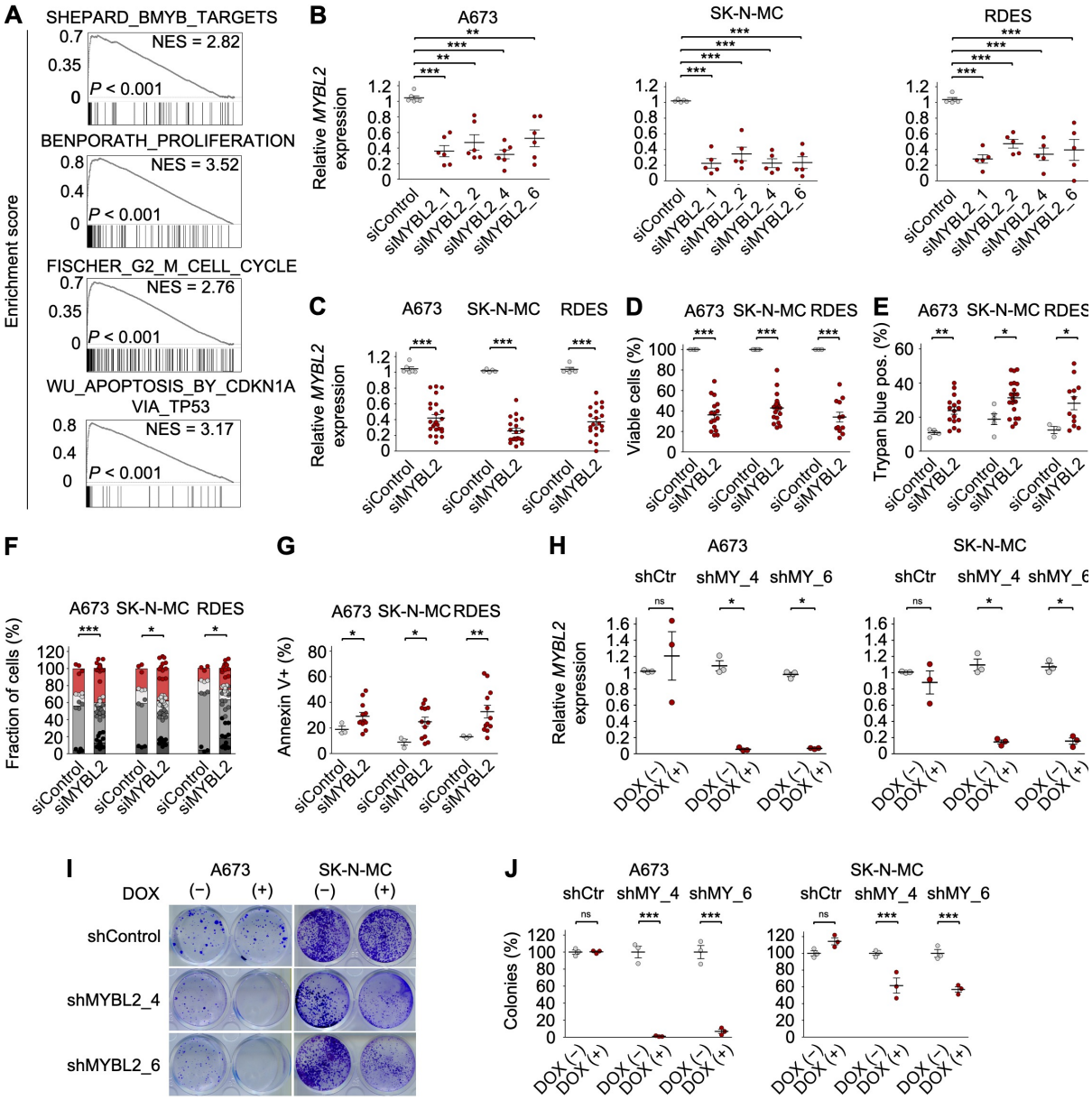

Figure 16: MYBL2 promotes cell proliferation, cell survival, and clonogenic growth of EwS cells. (A) Selected gene sets positively enriched with *MYBL2* in 166 primary EwS (pre-ranked GSEA). (B) Relative *MYBL2* expression as determined by qRT-PCR in A673, SK-N-MC, and RDES EwS cells after transfection with either a non-targeting control siRNA or four different *MYBL2*-targeting siRNAs. n≥5 biologically independent experiments. (C) Experiments described in '(B)' displayed as a summary of four different *MYBL2*-targeting siRNAs. n≥5 biologically independent experiments. (D) Relative amount of viable cells in A673, SK-N-MC, and RDES EwS cells transfected as described in '(B)'. Summary of four different *MYBL2*-targeting siRNAs. n≥3 biologically independent experiments. (E) Relative amount of trypan blue positive cells in experiments described in '(D)'. (F) Analysis of cell cycle using the experimental setup described in '(D)' as determined by PI staining and flow cytometry. Summary of four different *MYBL2*-targeting siRNAs. n≥3 biologically independent experiments. Black=subG1/G0; dark-grey=G1/G0; light-grey=S; red=G2/M. (G) Analysis of apoptosis using the experimental setup described in '(D)' as determined by combined AnnexinV/PI staining and flow cytometry. Summary of four different *MYBL2*-targeting siRNAs. n=3 biologically independent experiments. (H) Relative *MYBL2* expression as determined by qRT-PCR in A673 and SK-N-MC EwS cells containing either a DOX-inducible control shRNA or DOX-inducible *MYBL2*-targeting shRNAs. Cells were treated either with or without DOX. *P* values were determined by one-tailed Mann-Whitney test. n=3 biologically independent experiments. (I) Representative CFAs using cell lines described in '(H)' treated either with or without DOX. (J) Relative colony numbers of experiments described in '(I)'. n=3 biologically independent experiments. ***$P < 0.001$, **$P < 0.01$, *$P < 0.05$. Horizontal bars represent means, whiskers represent the SEM, if not otherwise specified. *P* values were determined via two-tailed Mann-Whitney test, if not otherwise specified. Figures A-D, F-H, and J from Musa et al., 2019. Figure I modified from Musa et al., 2019.

5.5. MYBL2 promotes EwS growth *in vivo*

A673 and SK-N-MC EwS cells, containing either a DOX-inducible non-targeting negative control shRNA or DOX-inducible specific shRNAs directed against *MYBL2*, were xenografted subcutaneously into the right flanks of NSG mice. As soon as tumors were palpable, mice were randomized to either the DOX-treatment group (DOX and sucrose), or the control group (sucrose), and tumor diameters were measured every two days. The mice were sacrificed as soon as the pre-defined experimental endpoint regarding tumor size, or other humane endpoints, were reached, and Kaplan-Meier curves were calculated for overall survival of respective mice (**Figure 17A,B**). Knockdown of MYBL2 using two different specific shRNAs significantly reduced growth of A673 and SK-N-MC xenografts (**Figure 17A,B**). Such effect was not observed in A673 and SK-N-MC xenografts containing a non-targeting negative control shRNA (**Figure 17A,B**). Knockdown of MYBL2 was verified on protein level by p-MYBL2 IHC (**Figure 17 C,D**). Consistent with functional *in vitro* experiments (**Figure 16**), histological analyses of the respective xenografts showed that MYBL2 knockdown leads to a significant increase of stalled mitoses that reflect G2/M blockage as assessed by hematoxylin and eosin (HE) staining, and a significant increase of apoptosis as assessed by cleaved caspase 3 (CC3) IHC (**Figure 17 E,F**). Taken together, these data indicate that MYBL2 promotes EwS growth *in vivo* (**Figure 17**).

5.6. *CCNF*, *BIRC5*, and *AURKB* are major MYBL2 downstream target genes in EwS

In order to identify the most functionally and clinically relevant downstream target genes of MYBL2, a multistep algorithm combining RNA-seq data, ChIP-seq data, microarray gene expression data, clinical data, as well as functional experiments, was used (**Figure 18A**). As MYBL2 is a transcription factor, RNA-seq of three EwS cell lines (A673, SK-N-MC, and RDES) either treated with a non-targeting negative control siRNA (siControl) or a specific siRNA directed against *MYBL2* (siMYBL2_1) was performed in technical triplicates to receive insights into the transcriptomic network signaling downstream of MYBL2. Using this RNA-seq dataset, the mean log2 FC upon MYBL2 suppression in three cell lines was calculated for each gene represented in the dataset in order to identify differentially expressed genes (DEG) (**Figure 18B**, **Supplementary Table 1**). Focusing on the strongest and most significantly differentially expressed genes (n=76) as defined by a mean log2 FC $|\geq 1.5|$ and a *P* value < 0.05 (Bonferroni-adjusted) (**Figure 18B, Supplementary Table 1**), a selection of these genes was validated for their regulation by MYBL2 as measured by qRT-PCR (**Figure 18C**). Of those 76 strongest and most significantly differentially expressed genes (**Supplementary Table 1**), only 50 (66%)

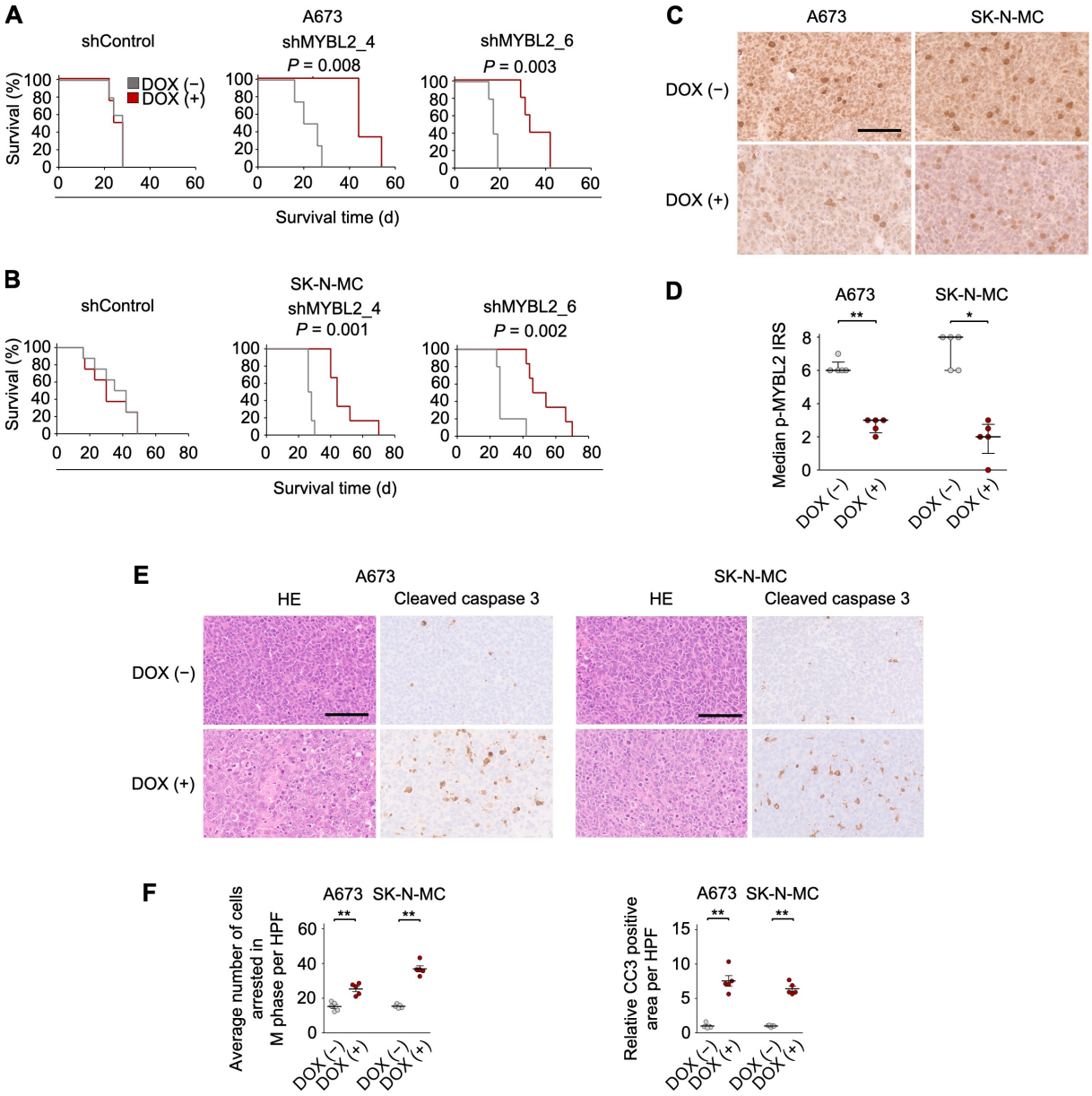

Figure 17: MYBL2 promotes EwS growth *in vivo*. (A,B) Kaplan-Meier curves of NOD scid gamma (NSG) mice subcutaneously xenografted with A673 (A) or SK-N-MC (B) EwS cell lines containing either a DOX-inducible non-targeting negative control shRNA or doxycycline (DOX)-inducible *MYBL2*-targeting shRNAs. When tumors were palpable, mice were randomized and treated either with or without DOX addition to the drinking water until the pre-defined experimental endpoint regarding tumor size was reached. n≥4 mice per condition. *P* values were determined by Mantel-Haenszel test. (C) Representative p-MYBL2 immunohistochemistry (IHC) micrographs of A673 and SK-N-MC xenografts containing a DOX-inducible *MYBL2*-targeting shRNA, whereby mice were treated either with or without DOX-addition to the drinking water. Scale bar represents 100µm. Larger scale image is displayed in **Supplementary Figure 3** (Appendix). (D) Semi-quantitative assessment of p-MYBL2 immunoreactivity of IHC micrographs described in '(C)' using the Immune Reactive Score (IRS). Horizontal bars represent medians, whiskers represent the interquartile range. n=5 samples were analyzed per condition. (E) Representative micrographs of hematoxylin and eosin (HE) staining and cleaved caspase 3 (CC3) IHC of cell line xenografts as described in '(C)'. Scale bar represents 100µm. Larger scale image is displayed in **Supplementary Figure 4** (Appendix). (F) Quantitative assessment of cells in M phase per high-power field (HPF) in HE stainings and quantification of CC3 positivity (percentage of positive HPF picture area) in CC3 IHC stainings, using micrographs described in '(E)'. n=5 analyzed samples per condition. $^{**}P < 0.01$, $^{*}P < 0.05$. Horizontal bars represent means, whiskers represent the SEM, if not otherwise specified. *P* values were determined via two-tailed Mann-Whitney test, if not otherwise specified. Figures A, B, D, F from Musa et al., 2019. Figures C and E modified from Musa et al., 2019.

show evidence for binding of MYBL2 to their promoters, as identified by ChIP-seq using a specific primary antibody directed against p-MYBL2 (**Figure 18D**). 46 of those 50 genes (92%) were represented in the microarray gene expression dataset of 166 primary EwS with matched clinical annotations. Expression levels of each of these 46 genes were correlated with that of *MYBL2* (**Figure 18E**, **Supplementary Table 2**) and analysis of overall EwS patient survival was performed stratifying patients according to their median intra-tumoral expression levels of the respective gene (**Figure 18F, Supplementary Table 3**). Only expression levels of three genes stood out to be strongly correlated with that of *MYBL2* ($r_{Pearson} \geq 0.7$; Bonferroni-adjusted $P < 0.05$) (**Supplementary Table 2**) and associated with unfavorable overall EwS patient survival when highly expressed ($P < 0.05$) (**Supplementary Table 3**): *CCNF* (alias Cyclin F, a CDK-independent Cyclin important in cell cycle progression and maintenance of genome stability) (D'Angiolella et al., 2013), *BIRC5* (alias Survivin, a member of the apoptosis inhibiting and cell proliferation promoting inhibitor of apoptosis proteins (IAP) family) (Mita et al., 2008), and *AURKB* (alias Aurora kinase B, a member of the Aurora kinase family of proteins that are crucial for proper mitosis/cytokinesis) (Carmena and Earnshaw, 2003) (**Figure 18D-F**). To functionally validate these findings, at first a pre-ranked gene set enrichment analysis (GSEA) using the RNA-seq data of three EwS cell lines (A673, SK-N-MC, and RDES) either treated with a non-targeting negative control siRNA (siControl) or a specific siRNA directed against *MYBL2* (siMYBL2_1) was performed, finding similar gene sets enriched with *MYBL2* expression as compared to the GSEA performed in 166 primary EwS (**Figure 19A,B**, see **Figure 16A** for comparison), indicating validity of the used cell line model and suggesting that the initial screen for differentially expressed genes most probably captures the main functionally relevant targets of MYBL2 that mediate its phenotype. Knockdown experiments in A673 and SK-N-MC EwS cells, using either a non-targeting negative control siRNA or two different specific siRNAs directed against each *CCNF*, *BIRC5*, and *AURKB* (**Figure 19C**), show that siRNA-mediated suppression of each CCNF, BIRC5, and AURKB leads to a significant decrease of viable cell number (**Figure 19D**). Knockdown of CCNF additionally increases cell death significantly in both cell lines, whereby BIRC5 knockdown only increases cell death significantly in A673 cells (**Figure 19E**). However, AURKB suppression did not significantly influence the amount of cell death in the investigated cell lines (**Figure 19E**). These functional experiments show that knockdown of respective MYBL2 target genes can phenocopy the effect of a MYBL2 knockdown *in vitro* (**Figure 19**). Collectively, application of an integrative multistep algorithm identifies *CCNF*, *BIRC5*, and *AURKB* as the most clinically and functionally relevant MYBL2 target genes in EwS (**Figure 18,19**).

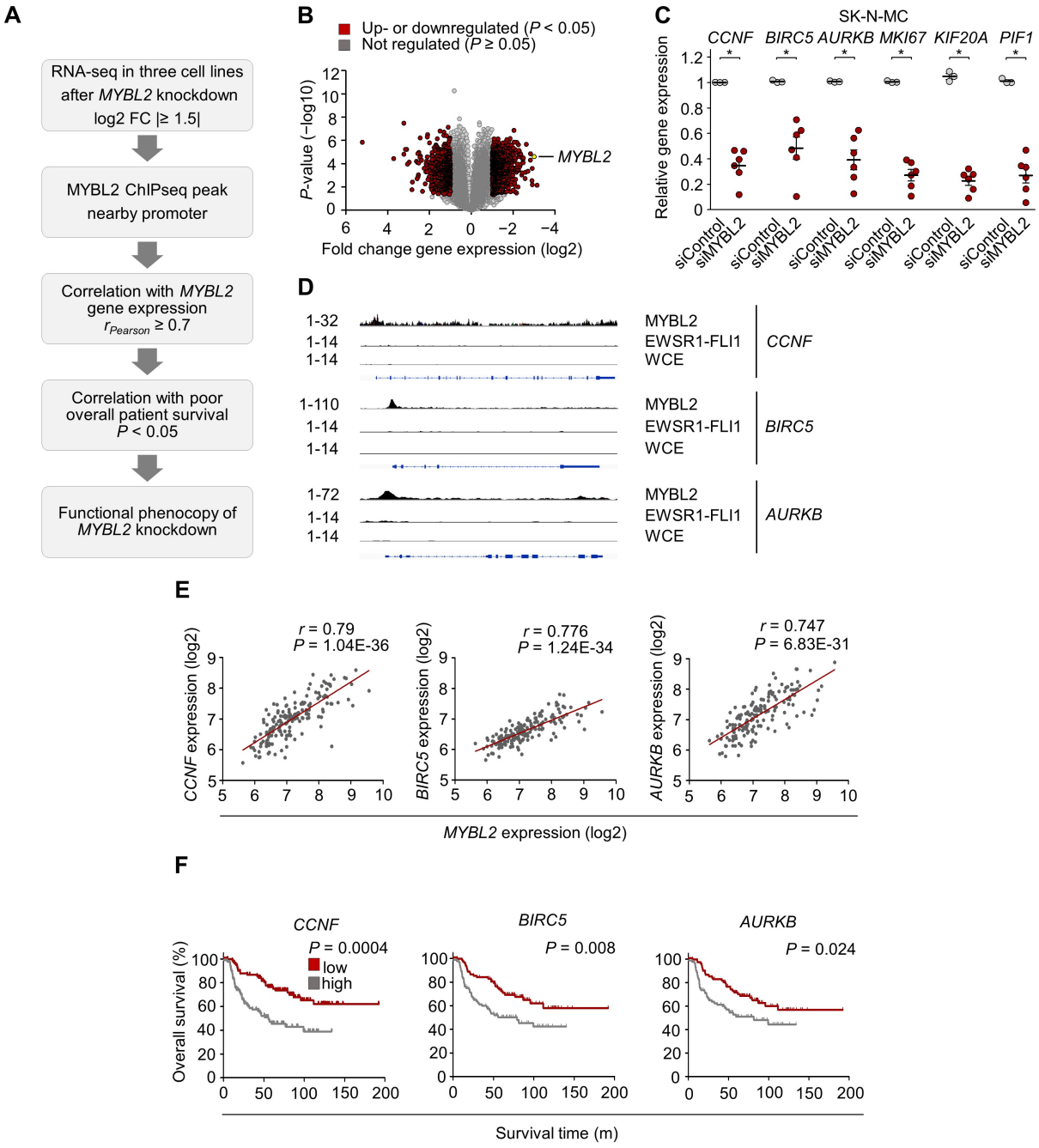

Figure 18: *CCNF*, *BIRC5*, and *AURKB* are clinically relevant MYBL2 target genes in EwS. (A) Algorithm used to identify the most clinically and functionally important direct MYBL2 target genes. (B) Volcano plot showing differential gene expression upon MYBL2 knockdown as compared to a non-targeting control siRNA (mean log2 fold change of three EwS cell lines) as determined by RNA-seq. Significantly up- or downregulated genes are displayed as red dots, not significantly regulated genes are displayed as grey dots. n=3 technical replicates per condition. (C) Validation of selected significantly downregulated genes as identified in '(B)' in SK-N-MC EwS cells by qRT-PCR. Summary of two different *MYBL2*-targeting siRNAs. n=3 biologically independent experiments. (D) p-MYBL2 ChIP-seq data analysis in A673 EwS cells. Peaks in promoters of *CCNF*, *BIRC5*, and *AURKB* are shown. Additionally, publicly available EWSR1-FLI1 ChIP-seq data in A673 EwS cells is displayed for the respective loci. Whole-cell extract (WCE) of A673 cells was displayed as a control. (E) Linear regression of *CCNF*, *BIRC5*, and *AURKB* expression levels onto *MYBL2* expression levels in a microarray gene expression dataset comprising 166 primary EwS. (F) Kaplan-Meier plots showing overall survival analysis of 166 EwS patients stratified according to their median intra-tumoral expression levels of the indicated gene. *P* values were determined by using the Mantel-Haenszel test. **P* < 0.05. Horizontal bars represent means, whiskers represent the SEM, if not otherwise specified. *P* values were determined via two-tailed Mann-Whitney test, if not otherwise specified. Figures from Musa et al., 2019.

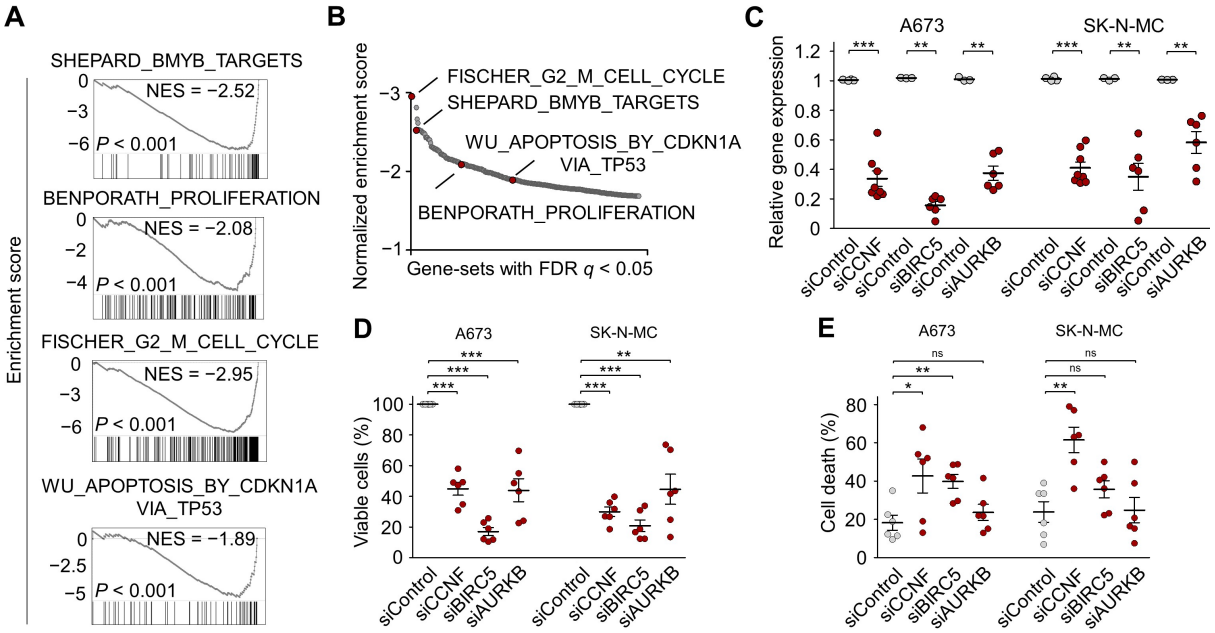

Figure 19: Suppression of CCNF, BIRC5, and AURKB can functionally phenocopy suppression of MYBL2 in EwS. (A,B) Pre-ranked gene set enrichment analysis (GSEA) (mean log2 fold change (FC) of genes represented in the RNA sequencing (RNA-seq) dataset described in 'Figure 18 (B)'). In '(B)', 275 gene sets that are downregulated upon MYBL2 knockdown and exhibited a false discovery rate (FDR) q < 0.05 are displayed. NES: Normalized Enrichment Score. (C) Relative gene expression of *CCNF*, *BIRC5*, and *AURKB* in A673 and SK-N-MC EwS cells treated either with a non-targeting negative control siRNA, or siRNAs directed against *CCNF*, *BIRC5*, or *AURKB* (summary of two different siRNAs is displayed per target). n≥3 biologically independent experiments. (D) Relative amount of viable cells in A673 and SK-N-MC EwS cells after transfection with either a non-targeting negative control siRNA or siRNAs directed against *CCNF*, *BIRC5*, or *AURKB* (summary of two different siRNAs is displayed per target). n≥3 biologically independent experiments. (E) Relative amount of trypan blue positive cells in the experiments described in '(D)' (summary of two different siRNAs is displayed per target). Not significant, ns; ***$P < 0.001$, **$P < 0.01$, *$P < 0.05$. Horizontal bars represent means, whiskers represent the SEM, if not otherwise specified. *P* values were determined via two-tailed Mann-Whitney test, if not otherwise specified. Figures from Musa et al., 2019.

5.7. High MYBL2 levels sensitize EwS cells for CDK2 inhibition *in vitro*

To exploit the functionally and clinically relevant role of MYBL2 in EwS therapeutically, targeting the upstream phosphorylating and activating Cyclin-dependent kinase (CDK2) of MYBL2 was hypothesized to be especially effective in EwS highly expressing MYBL2, as specific MYBL2 inhibitors are not yet available. To test this hypothesis, A673 cells containing either a DOX-inducible non-targeting negative control shRNA or a DOX-inducible specific shRNA directed against *MYBL2* (shMYBL2_4) were treated with small molecule inhibitors targeting CDK2 (CVT-313 and NU6140) in dilutions ranging from 100µM to 0.001µM with or without addition of DOX to the media (**Figure 20A**). Each inhibitor was able to strongly diminish growth of A673 cells at lower micromolar concentrations, whereby MYBL2 knockdown significantly decreased sensitivity toward CDK2 inhibition (**Figure 20A**). Such differential sensitivity

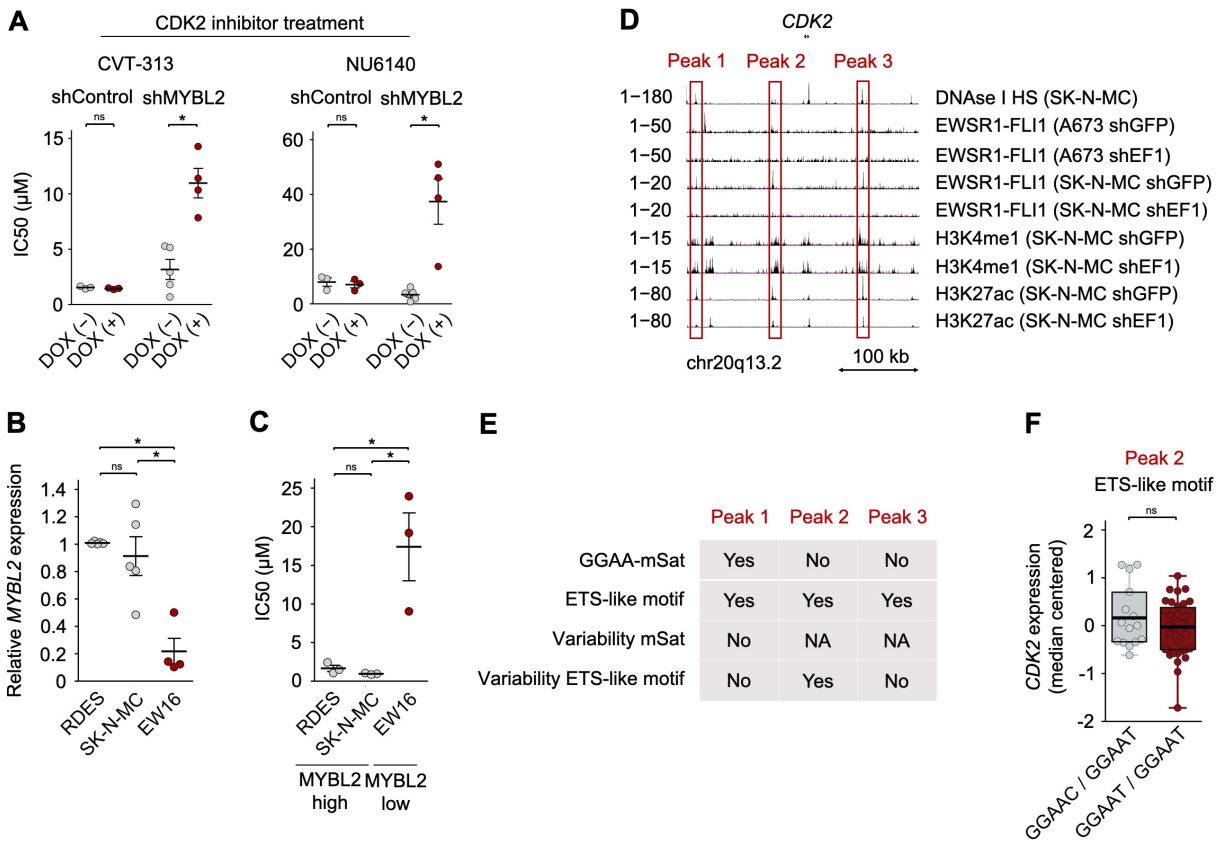

Figure 20: MYBL2 sensitizes EwS cells for CDK2 inhibition *in vitro*. (A) Analysis of half maximal inhibitory concentration (IC50) as measured by resazurin cell viability assays in A673 EwS cells containing either a DOX-inducible non-targeting negative control shRNA or a *MYBL2*-targeting shRNA, treated with the CDK2 inhibitors CVT-313 and NU6140 either with or without addition of DOX to the media. Horizontal bars represent means, whiskers represent the SEM. n≥3 biologically independent experiments. *P* values determined via two-tailed Mann-Whitney test. (B) *MYBL2* expression of three wildtype EwS cell lines as determined by qRT-PCR. Expression values were normalized to that of RDES. Horizontal bars represent means, whiskers represent the SEM. n≥4 biologically independent experiments. (C) IC50 analysis as measured by resazurin cell viability assays in *MYBL2* high (RDES and SK-N-MC) and *MYBL2* low (EW16) expressing EwS cell lines treated with the CDK2 inhibitor NU6140. Horizontal bars represent means, whiskers represent the SEM. n=3 biologically independent experiments. (D) Analysis of published EWSR1-FLI1, H3K4me1, and H3K27ac chromatin immunoprecipitation and DNA sequencing (ChIP-seq) data in A673 and SK-N-MC EwS cells, each containing either a shRNA construct directed against *GFP* (shGFP (control)) or *EWSR1-FLI1* (shEF1), as well as published DNAse-seq data in SK-N-MC cells. Here, the genomic region approximately 150kb up- and downstream of the *CDK2* locus is shown and EWSR1-FLI1 peaks with epigenetic signs of active enhancers were highlighted. (E) Binding motifs mapping to the peaks shown in ‘(D)‘ and variability of those motif haplotypes that were called from a cohort of whole genome sequenced primary EwS. (F) For motifs described in ‘(E)‘, in which variability between patient haplotypes was observed, expression quantitative trait loci (eQTL) analysis was performed in 51 primary EwS for which respective haplotypes could be called and matched gene expression data for *CDK2* was available. Horizontal bars represent means, upper and lower hinges represent the 75th and 25th percentile (interquartile range), and whiskers minimum and maximum expression values, n≥15 samples per condition. Not significant, ns; *$P < 0.05$. *P* values were determined via two-tailed Mann-Whitney test, if not otherwise specified. Figures A, B, D, E from Musa et al., 2019. Figures C and F modified from Musa et al., 2019.

upon DOX-addition to the media was not observed in A673 cells containing a DOX-inducible non-targeting control shRNA (**Figure 20A**). As NU6140 preferentially inhibits CDK2 as compared to other CDKs, but also inhibits the major MYBL2 downstream target AURKB, it enables up- and downstream targeting of MYBL2 and was therefore further validated in two additional EwS cell lines with constitutively

high *MYBL2* expression (SK-N-MC and RDES) and one EwS cell line with constitutively low *MYBL2* expression (EW16) in dilutions ranging from 100µM to 0.001µM (**Figure 20B,C**). Consistently, SK-N-MC and RDES cells harboring high *MYBL2* expression levels were more sensitive to CDK2 inhibition than EW16 cells harboring low *MYBL2* expression levels (**Figure 20B,C**). To evaluate whether EWSR1-FLI1 regulates CDK2 expression similarly to that of MYBL2, and thereby as well may influence sensitivity toward CDK2 inhibition via regulation of CDK2 expression levels independently of MYBL2, a time course microarray gene expression dataset generated in A673/TR/shEF1 EwS cells containing a DOX-inducible shRNA construct directed against *EWSR1-FLI1* treated with DOX for maximum 96 hours was used. RNA expression was arrayed at six different timepoints (0, 18, 36, 53, 72, and 96 hours). Herein, the log2 FC for the 53 hours of DOX-treatment condition was calculated for each gene compared to the 0 hours of DOX-treatment condition, revealing a downregulation of CDK2 after 53 hours of EWSR1-FLI1 suppression (log2 FC = -1.52). Analysis of published and freely available ChIP-seq data for EWSR1-FLI1, H3K4me1, and H3K27ac in A673 and SK-N-MC cells either expressing a shRNA directed against *GFP* (control) or *EWSR1-FLI1*, as well as DNAse-seq data in SK-N-MC cells reveals three EWSR1-FLI1 signals in between 150kb up- and downstream of *CDK2* in A673 and SK-N-MC cells (**Figure 20D**). One of those EWSR1-FLI1 peaks mapped to a GGAA-mSat and all peaks mapped to an ETS binding motif (**Figure 20E**). Analysis of respective loci in whole genome sequenced primary EwS using the HipSTR algorithm for haplotype calling reveals that only one of the ETS motifs (‘Peak 2‘) exhibits inter-individual variability, whereas the GGAA-mSat (‘Peak 1‘) and the other ETS motifs (‘Peak 1‘ and ‘Peak 3‘) were identical in all examined individuals (**Figure 20E**). However, using matched tumor RNA-seq gene expression data, eQTL analysis for the ETS motif at the ‘Peak 2‘ locus was performed, which showed no eQTL properties (**Figure 20F**). Thus, high MYBL2 expression levels sensitize EwS cells for CDK2 inhibition and although there is evidence for direct CDK2 regulation by EWSR1-FLI1, no inter-individually variant EWSR1-FLI1 binding motifs that harbor eQTL properties were found nearby the CDK2 locus, indicating that inter-individual variability of sensitivity toward CDK2 inhibition is more likely mediated by EWSR1-FLI1 regulating MYBL2 expression rather than regulating CDK2 (**Figure 20**).

5.8. High MYBL2 levels sensitize EwS cells for CDK2 inhibition *in vivo*

To see whether the effect of CDK2 inhibition on EwS growth and its dependency on MYBL2 can be as well observed *in vivo*, A673 cells containing a DOX-inducible specific shRNA directed against *MYBL2*

(shMYBL2_4) were injected subcutaneously into the right flanks of NSG mice, and as soon as tumors were palpable, mice were randomized and treated with either vehicle (DMSO), or NU6140 (20mg/kg or 40mg/kg) intraperitoneally (i.p.) for 14 days including a break of one day per four days of treatment (**Figure 21A**). Additionally, each group was treated with or without addition of DOX to the drinking water (**Figure 21A**). Treatment with each concentration of NU6140 significantly reduces growth of respective xenografts as compared to the vehicle condition and, when MYBL2 was suppressed, no additional effect of CDK2 inhibition was observed as compared to the vehicle group (**Figure 21B**). NU6140 treatment is associated with a decrease of p-MYBL2 immunoreactivity, confirming that CDK2 inhibition leads to reduced phosphorylation of MYBL2, and with an increase of immunoreactivity for CC3, showing that NU6140 treatment increases apoptosis *in vivo* which is in consistence with functional MYBL2 knockdown experiments conducted *in vitro* and *in vivo* (**Figure 21C,D**, see **Figure 16,17** for comparison). Neither significant weight loss of treated mice, nor histological alterations of inner organs (including heart, lungs, liver, pancreas, spleen, stomach, intestines, kidneys, and adrenal glands) or bone marrow was observed in mice treated for maximum 14 days (including a break of one day per four days of treatment) with NU6140. In conclusion, these data show that CDK2 inhibitors can safely diminish EwS growth *in vivo*, that their effectivity depends on MYBL2 expression levels, and suggest that MYBL2 may constitute a valuable predictive biomarker for effectivity of anti-CDK2 treatment (**Figure 21**).

5.9. The role of MYBL2 as an interface of ‘oncogenic cooperation‘ in EwS is distinct

To evaluate whether MYBL2 contains a distinct role as an interface of ‘oncogenic cooperation‘-mediated inter-individual heterogeneity of EwS phenotypes, the top five hits (*EXO1*, *C1ORF112*, *ESPL1*, *HJURP*, and *RAD54L*) of the initial screen of genes that are significantly downregulated upon EWSR1-FLI1 knockdown and whose high intra-tumoral expression is associated with unfavorable overall EwS patient survival (**Table 22**) were screened for EWSR1-FLI1 ChIP-seq peaks with epigenetic signs of active enhancers in close proximity (~150kb up- or downstream) to the respective gene bodies (**Figure 22A-E**). In case of EWSR1-FLI1 peaks mapping to a GGAA-mSat or an ETS binding motif with epigenetic marks indicative for active enhancers, the HipSTR algorithm was applied on the WGS dataset of primary EwS in order to call the haplotypes and thereby to screen for genetic variability at the respective loci (**Figure 22A-E**). Using matched tumor RNA-seq data, eQTL analyses were performed for every locus

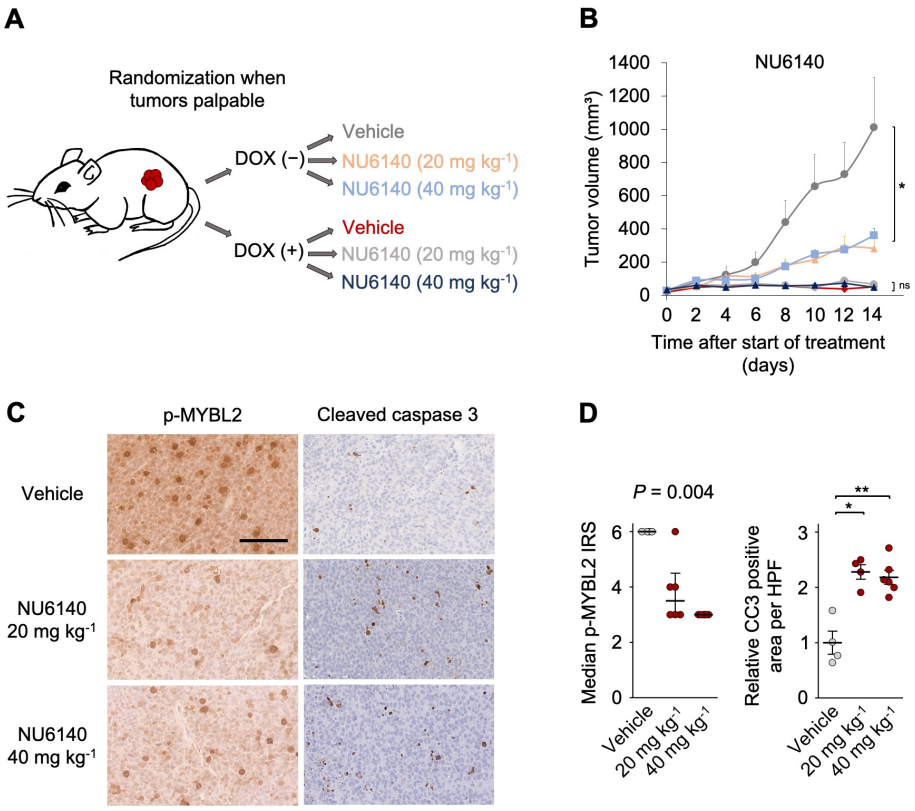

Figure 21: MYBL2 sensitizes EwS cells for CDK2 inhibition *in vivo*. (A) Schematic illustrating the experimental design for evaluation of CDK2 inhibitor (NU6140) treatment effectiveness and its MYBL2-dependency in subcutaneous EwS cell line xenografts. A673 cells containing a doxycycline (DOX)-inducible *MYBL2*-targeting shRNA were xenografted subcutaneously into the right flanks of NSG mice. As soon as tumors were palpable, the mice were randomized and treated with or without DOX-addition to the drinking water and either vehicle (DMSO) or NU6140 (in a dose of either 20 mg/kg or 40 mg/kg). (B) Mean tumor volume and SEM of 4–6 mice is shown over the time of the experiment for every treatment condition as described in '(A)'. (C) Representative micrographs of p-MYBL2 and cleaved caspase 3 (CC3) immunohistochemistry (IHC) for each treatment group as described in '(A)'. Scale bar represents 100µm. Larger scale image is displayed in **Supplementary Figure 5** (Appendix). (D) Left: Semi-quantitative assessment of p-MYBL2 immunoreactivity in IHC stainings of xenografts as described in '(A)' and representatively displayed in '(C)'. Horizontal bars represent medians, whiskers represent the interquartile range. n≥4 samples were analyzed per condition. *P* value was determined using the Kruskal-Wallis test. IRS: Immune Reactive Score. Right: Quantification of CC3 positivity (percentage of positive high-power field (HPF) picture area) in CC3 IHC stainings of xenografts as described in '(A)' and representatively displayed in '(C)'. Horizontal bars represent means, whiskers represent the SEM. n≥4 samples were analyzed per condition. Scale bar is 100µm. Not significant, ns; $^{**}P < 0.01$, $^{*}P < 0.05$. *P* values were determined via two-tailed Mann-Whitney test, if not otherwise specified. Figures A, B, D from Musa et al., 2019. Figure C modified from Musa et al., 2019.

that exhibited genetic variability (**Figure 22A-E**). Of the top five genes that are significantly downregulated upon EWSR1-FLI1 knockdown and whose high intra-tumoral expression is associated with unfavorable overall EwS patient survival (**Table 22**), only four genes exhibit EWSR1-FLI1 peaks in close proximity to their gene bodies (*EXO1*, *C1ORF112*, *HJURP*, and *RAD54L*), whereby peaks nearby all four genes map to ETS binding motifs, and peaks nearby two of the four genes (*EXO1* and *HJURP*) additionally map to GGAA-mSats (one GGAA-mSat nearby *EXO1* and three GGAA-mSats nearby *HJURP*) (**Figure 22A-E**). No genetic variability has been observed regarding the ETS-binding motifs of

all four genes (**Figure 22A-E**). However, the GGAA-mSat nearby *EXO1* and one of the GGAA-mSats nearby *HJURP* exhibited genetic variability and subsequent eQTL analysis has been performed for these loci (**Figure 22A-E**). The *EXO1*-associated GGAA-mSat did not exhibit eQTL properties, and for the polymorphic *HJURP*-associated GGAA-mSat, eQTL analysis could not be performed due to low sample size of certain groups (**Figure 22A-E**). These results indicate that MYBL2 has a distinct role as an interface of 'oncogenic cooperation'-mediated inter-individual heterogeneity of EwS phenotypes (**Figure 22**, **Table 22**). This is not the case for other clinically relevant EWSR1-FLI1-regulated genes, which suggests that the phenotype-shaping interfaces between regulatory genetic variants and dominant driver-mutations may be constituted by important distinct mediators (**Figure 22**, **Table 22**).

Entrez ID	Gene symbol	Rank sum	Log2 FC EF1 KD	*P* value	Bonferroni	Overall survival	GGAA-mSat	ETS motif
4605	*MYBL2*	30	-3.037	9.573E-07	0.018	Worse survival	Yes	No
4886	*NPY1R*	46	-3.059	6.125E-06	0.118	Better survival	Yes	Yes
9156	*EXO1*	55	-3.086	9.109E-06	0.176	Worse survival	Yes	Yes
55732	*C1orf112*	64	-2.709	1.536E-06	0.030	Worse survival	No	Yes
10149	*GPR64*	67	-2.742	3.172E-06	0.061	Better survival	NA	NA
9700	*ESPL1*	103	-2.579	6.860E-06	0.132	Worse survival	No	No
55355	*HJURP*	106	-2.551	4.685E-06	0.090	Worse survival	Yes	Yes
8438	*RAD54L*	141	-2.343	2.808E-06	0.054	Worse survival	No	Yes
51514	*DTL*	167	-2.943	9.760E-05	1.000	Worse survival	No	No
4751	*NEK2*	185	-2.182	6.268E-06	0.121	Worse survival	Yes	No
993	*CDC25A*	200	-2.394	4.582E-05	0.884	Worse survival	Yes	No

Table 22: Top ten genes strongly regulated by EWSR1-FLI1 in EwS and associated with overall EwS patient survival following *MYBL2*. Crossing of a microarray gene expression dataset of A673/TR/shEF1 cells profiled with and without DOX treatment for 53 hours and another microarray gene expression dataset of 166 primary EwS samples for which matched clinical annotations were available. For the first dataset, the log2 fold change (FC) for every gene represented on both microarrays was calculated, for the latter dataset, nominal and Bonferroni-corrected *P* values for association with overall EwS patient survival (OS) were calculated for every gene represented on the microarray using the Mantel-Haenszel-test. The top EWSR1-FLI1-regulated and survival associated genes were identified by rank sum calculation. These genes were screened for EWSR1-FLI1 signals with epigenetic signs for active enhancers in between 150kb up- and downstream of the gene body mapping to either a GGAA-microsatellite (mSat) or an ETS motif (see Figure 22 for details). Data from Musa et al., 2019.

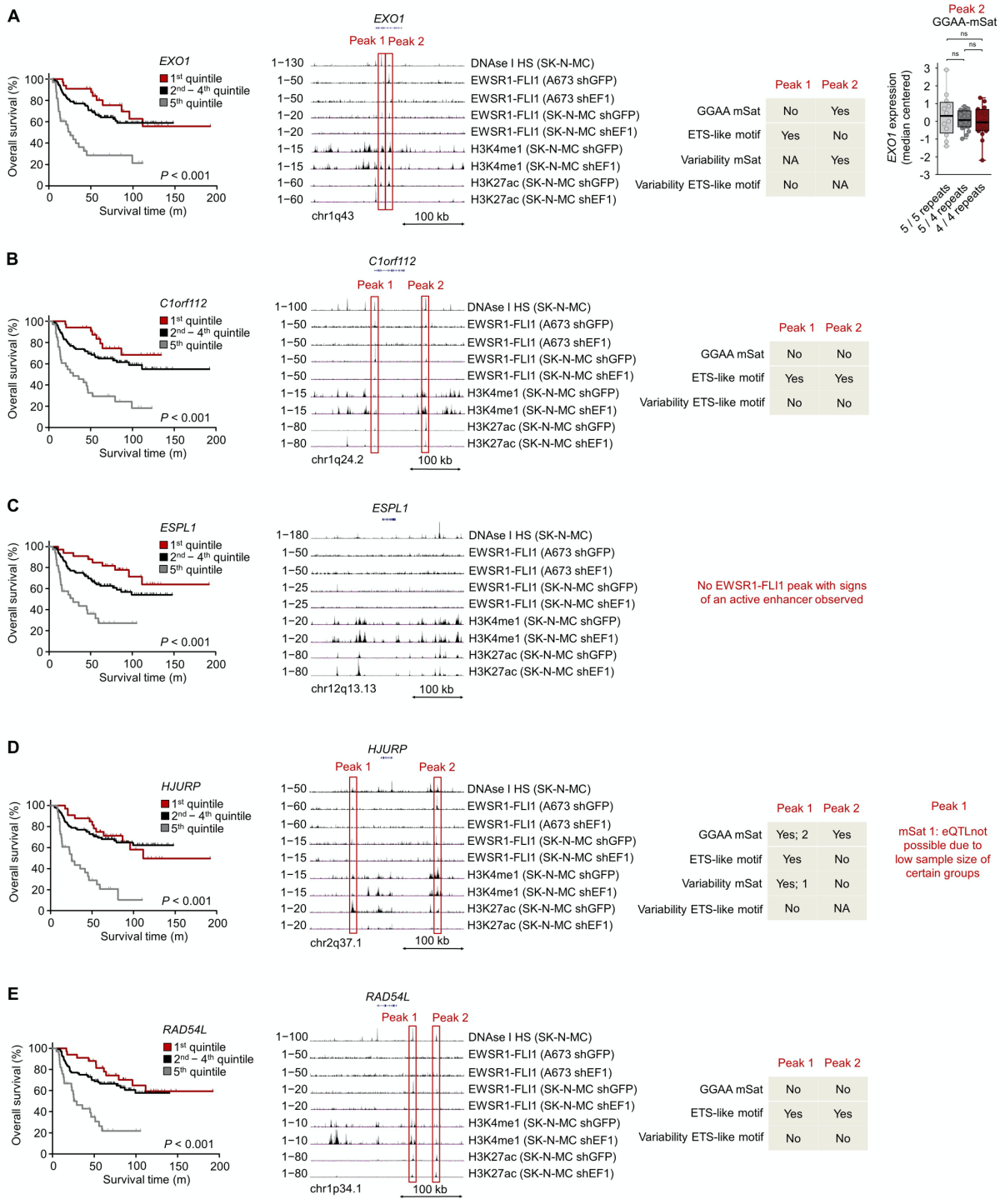

Figure 22: Epigenetic profiling and evaluation of expression quantitative trait loci (eQTL) properties of top five EWSR1-FLI1-regulated genes in EwS associated with unfavorable overall EwS patient survival. Kaplan-Meier plots showing overall survival analysis of 166 EwS patients stratified according to their intra-tumoral expression quintiles of the indicated gene, as well as analysis of published ChIP-seq data as described in 'Figure 14(A)'. *P* values of survival analyses were determined by using the Mantel-Haenszel test. Both analyses were performed for (A) *EXO1*, (B) *C1orf112*, (C) *ESPL1*, (D) *HJURP*, and (E) *RAD54L*. EWSR1-FLI1 peaks with epigenetic signs of active enhancers within ~150kb up- and downstream of the respective gene were highlighted. For motifs in which variability between patient haplotypes was observed in a cohort of whole genome sequenced primary EwS, eQTL analysis was performed using matched tumor RNA-seq data (n=47 samples for *EXO1* locus). Horizontal bars represent means, upper and lower hinges represent the 75th and 25th percentile (interquartile range), and whiskers minimum and maximum expression values. n≥12 samples per group. Not significant, ns; *P* values were determined via two-tailed Mann-Whitney test, if not otherwise specified. Figure A modified from Musa et al., 2019. Figures B-E from Musa et al., 2019.

5.10. ‘Oncogenic cooperation‘ determines clinical outcome and drug response in EwS

Collectively, the results presented in this thesis show that in EwS, an ‘oncogenic cooperation‘ between the fusion transcription factor EWSR1-FLI1 and a polymorphic enhancer-like GGAA-mSat, whose natural variability is inherited via the germline, regulates the expression of the pro-proliferative gene *MYBL2* (**Figure 23**). High *MYBL2* expression is associated with poor overall EwS patient survival, but also sensitizes EwS cells for targeted CDK2 inhibition, offering a therapeutic vulnerability (**Figure 23**). This mechanism exemplifies in the EwS model, how the interaction between a somatic mutation (here *EWSR1-FLI1*) and a regulatory genetic variant which is inherited via the germline (here a polymorphic enhancer-like GGAA-mSat) may determine the expression of a functionally and clinically relevant druggable downstream target (here MYBL2) (**Figure 24**). Such interplay may represent a general mechanism, determining inter-individual heterogeneity in phenotypes of diseases that are characterized by specific dominant disease-driving mutations/events, which may alone not explain the observed variability in clinical courses these diseases (see section ‘‘Oncogenic cooperation‘ beyond the EwS model‘ for details) (**Figure 24**). In this regard, future approaches of precision oncology could aim to not only identify alteration in the protein-coding genome, but also to identify variants in the non-protein-coding regulatory genome in order to refine individualized diagnosis and to accordingly adapt therapeutic strategies. Such future approaches may harbor the potential to optimize procedures and to more exhaustively exploit the potential of ‘omics‘-based precision medicine.

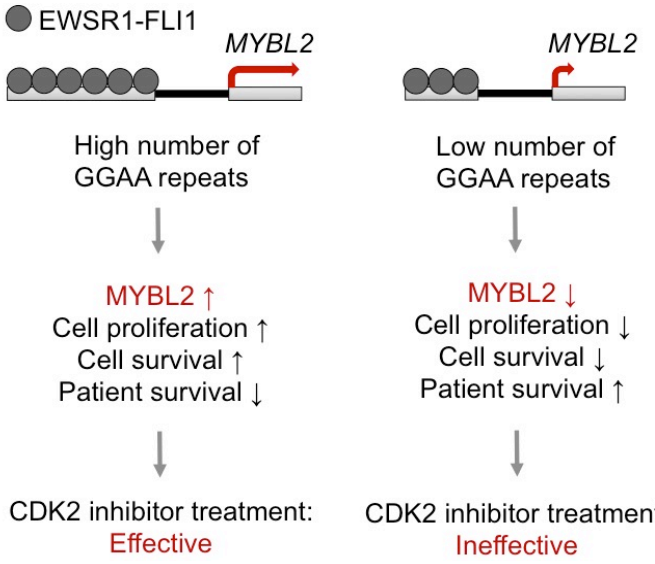

Figure 23: EWSR1-FLI1 regulating MYBL2 expression via a polymorphic enhancer-like GGAA-microsatellite (mSat) determining tumor growth, patient survival, and drug response in EwS. Figure from Musa et al., 2019.

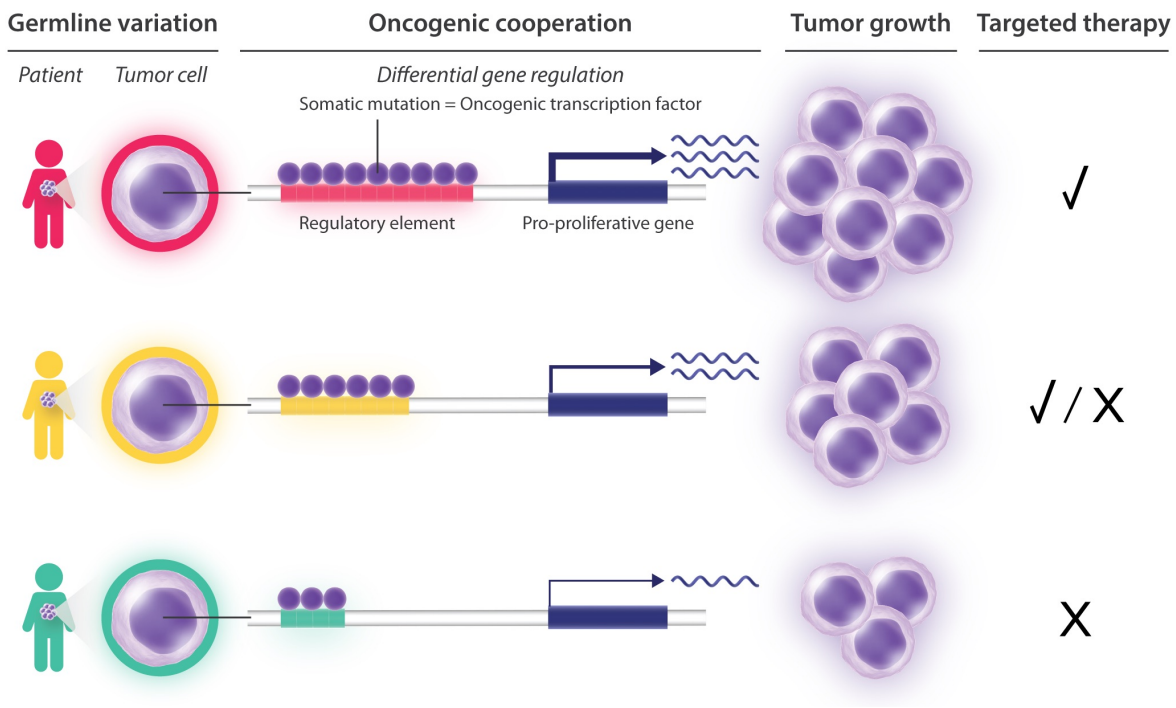

Figure 24: 'Oncogenic cooperation': general model of the interaction between somatic driver-mutations and inter-individually variable regulatory germline variants impacting on cancer phenotypes and targeted therapy effectivity. Figure from Musa and Grünewald, 2019.

6. DISCUSSION

6.1. ‘Oncogenic cooperation‘ impacting on EwS progression and susceptibility

The data presented in this thesis exemplifies in the EwS model that ‘oncogenic cooperation‘, defined here as the interaction between dominant driver-oncogenes and regulatory germline variants, is a key determinant of tumor growth, patient survival, and drug response (Musa and Grünewald, 2019; Musa et al., 2019). Such interplay constitutes a major source of inter-individual tumor heterogeneity, especially in oligomutated cancers, as it leads to inter-individual variations in gene expression that translate into diverse tumor behavior, diverse clinical courses, and differential treatment effectiveness (Musa and Grünewald, 2019; Musa et al., 2019). The impact of such ‘oncogenic cooperation‘ on tumor progression indicates that understanding of this interplay may be helpful to develop new strategies in order to stratify patients into risk-groups and accordingly subject them to specific therapies in the context of precision oncology (Musa and Grünewald, 2019; Musa et al., 2019). Specifically, the data presented here show that EWSR1-FLI1, a fusion transcription factor resulting from a chromosomal translocation which is pathognomonic for EwS, regulates the expression of the pro-proliferative and patient survival-associated gene *MYBL2* via a polymorphic enhancer-like GGAA-microsatellite (mSat) (Musa et al., 2019). Identification of MYBL2 as the top EWSR1-FLI1-regulated gene whose high expression is at the same time most strongly associated with overall EwS patient survival was performed by crossing of two datasets: first, a publicly available time course gene expression microarray dataset of A673/TR/shEF1 EwS cells containing a doxycycline (DOX)-inducible shRNA construct directed against *EWSR1-FLI1* treated with DOX for maximum 96 hours was used, whereby RNA expression was arrayed at six different timepoints (0, 18, 36, 53, 72, and 96 hours), and second, a publicly available gene expression microarray dataset of 166 primary EwS, for which matched clinical annotations were available, allowing the identification of genes significantly associated with overall EwS patient survival (Musa et al., 2019). In this regard, the timepoint chosen during the time course EWSR1-FLI1 knockdown microarray dataset (53 hours of DOX treatment) was chosen in the middle of the time course to ensure a sufficient EWSR1-FLI1 knockdown, while at the same time reflecting early transcriptomic alterations due to the EWSR1-FLI1 knockdown, but may nevertheless be regarded as to some extent arbitrarily chosen, and integrative analysis using a different timepoint may have led to slight, but most probably not biologically relevant, differences in mathematical gene ranking. However, resuming all presented data regarding this aspect, the regulation of MYBL2 expression levels by EWSR1-FLI1 has been robustly shown via a multi-method approach *in vitro* and *in vivo* on mRNA (using microarray gene expression data and quantitative real-

time polymerase chain reaction (qRT-PCR)) and protein level (using western blot and immunohistochemistry (IHC)) (Musa et al., 2019). The association of high *MYBL2* expression with unfavorable overall EwS patient survival was evaluated on mRNA level in a cohort of 166 therapy-naive primary EwS with matched microarray gene expression and clinical data. It needs to be considered that the underlying gene expression data was generated from therapy-naive tumor samples, but the matched clinical data reflect clinical courses of subsequently treated patients, which may confound the association of high *MYBL2* levels and overall EwS patient survival for example due to alterations in *MYBL2* expression induced by treatment application. However, as investigation of this association was only possible on mRNA level, further supportive validation on protein level in a second cohort may be helpful to be fully conclusive regarding the value of MYBL2 as a prognostic biomarker. Following interpretation of these results, the mechanism of MYBL2 regulation by EWSR1-FLI1 was investigated: after identification of a potentially regulatory GGAA-mSat nearby *MYBL2* in publicly available chromatin immunoprecipitation and DNA sequencing (ChIP-seq) data for EWSR1-FLI1, H3K4me1, and H3K27ac in A673 and SK-N-MC EwS cells, as well as DNAse-seq data in SK-N-MC, this GGAA-mSat was PCR-cloned into a luciferase reporter vector and its GGAA-repeat number dependent enhancer activity that relies on EWSR1-FLI1 was proven in reporter assays (Musa et al., 2019). However, as not every GGAA-mSat in the genome shows evidence for EWSR1-FLI1 binding, it is conceivable that the regions flanking the GGAA-mSat are additionally important for its binding specificity. As to this time point, detailed information about the functional role of such flanking regions is lacking, ~440bp up- and downstream of the *MYBL2*-associated GGAA-mSat were included into the GGAA-mSat-containing fragment that was cloned into the pGL3-Promoter-Fluc vector for performance of luciferase reporter assays, in analogy to previous studies using similar flanking region sizes (Grünewald et al., 2015). However, future studies are required to further investigate the extent of flanking region needed and its mechanistic role for mediation of EWSR1-FLI1 binding specificity. To validate the regulatory potential of the respective GGAA-mSat regarding *MYBL2* expression, Clustered Regularly Interspaced Short Palindromic Repeats interference (CRISPRi) was used (Boulay et al., 2018; Gilbert et al., 2014; Musa et al., 2019; Thakore et al., 2015). In contrary to conventional CRISPR approaches that lead to a knockout of the targeted genomic region, CRISPRi only confers an inhibitory epigenetic state of the targeted region by using a KRAB effector domain-coupled DNAse-dead Cas9 (Boulay et al., 2018; Gilbert et al., 2014; Musa et al., 2019; Thakore et al., 2015). This approach was chosen to not permanently and irreversibly knockout the genomic region of interest, but more dynamically regulate epigenetic inhibition of the genomic region

by DOX-induced expression of dCas9-KRAB, in order to avoid potential undesired effects of a permanent knockout, such as compensatory MYBL2 upregulation via alternative mechanisms. CRISPRi has already been applied successfully for targeting of GGAA-mSat loci in EwS before (Boulay et al., 2018). Also, as EWSR1-FLI1 was shown to act as a pioneer transcription factor by recruiting the BRG1- or HBRM-associated factors (BAF) chromatin remodeling complex to enhancer sites and thereby locally modulate chromatin state (Boulay et al., 2017; Grünewald et al., 2018; Sheffield et al., 2017) (see section 'Etiology and pathophysiology' for details), CRISPRi, leading to an inhibitory epigenetic state at the targeted locus, can be regarded as a valid model for diminishing EWSR1-FLI1 function at the respective locus. Subsequently, in 35 whole genome sequenced primary EwS with matched tumor RNA sequencing (RNA-seq) gene expression data, the stratification of every sample according to the GGAA-repeat number of both haplotypes of the *MYBL2*-associated GGAA-mSat into either the 'Short / Short', 'Short / Long', or 'Long / Long' group has been performed. Analysis of expression quantitative trait loci (eQTL) properties of the respective locus showed that the 'Long / Long' group exhibited significantly higher *MYBL2* expression levels as compared to the 'Short / Short' group. However, the 'Short / Long' group ranged in between both other groups, but did not reach statistical significance when comparing its *MYBL2* expression to the any of the other groups, which may be due to the relatively low sample size of 35 used samples. The stratification of every sample into either the 'Short / Short', 'Short / Long', or 'Long / Long' group according to the GGAA-repeat numbers of both haplotypes of a sample was based on the one hand on evidence from published studies showing that 13 GGAA-repeats delineate a critical GGAA-repeat number beyond which EWSR1-FLI1-dependent enhancer activity of a GGAA-mSat strongly increases (Grünewald et al., 2015; Guillon et al., 2009; Johnson et al., 2017), and on the other hand on EWSR1-FLI1 ChIP-seq data from RDES EwS cells (heterozygous for the *MYBL2*-associated GGAA-mSat, haplotypes harboring 14 and 12 repeats) that was available in the Grünewald laboratory, showing preferential EWSR1-FLI1 binding to the longer allele harboring 14 consecutive GGAA-repeats as compared to the shorter allele harboring 12 consecutive GGAA-repeats (71% of obtained reads spanning the GGAA-mSat mapped to the longer allele vs. 29% mapping to the shorter allele). However, it cannot be excluded that alternative stratification of samples into respective groups would have resulted in different conclusions regarding eQTL properties of this locus. The general existence of such interplay between the dominant fusion oncogene *EWSR1-FLI1* and GGAA-mSats in regulation of gene expression has already been described early on in EwS (Gangwal et al., 2008), but in 2015, a pioneering study by Grünewald *et al.* firstly showed that 'oncogenic cooperation' indeed influences inter-individual

heterogeneity toward susceptibility to EwS tumorigenesis (Grünewald et al., 2015). In the respective study, a single nucleotide polymorphism (SNP) (rs79965208) in a GGAA-mSat associated with the pro-proliferative gene *EGR2* was shown to modify the number of consecutive repeats of this respective GGAA-mSat and thereby its enhancer activity as well as *EGR2* expression levels (Grünewald et al., 2015). The risk allele 'A' connects adjacent GGAA-repeats to a longer non-disrupted stretch of consecutive GGAA-repeats, leading to preferential EWSR1-FLI1 binding as compared to the protective 'T' allele which disrupts the consecutive stretch (Grünewald et al., 2015). Notably, the risk allele 'A' shows a significantly higher allele frequency in non-African populations as compared to African populations, which may at least partly explain the higher EwS incidence in non-Africans as compared to Africans (Grünewald et al., 2015). The data presented here extends this knowledge about 'oncogenic cooperation' impacting on EwS initiation/susceptibility by showing that the interplay between somatic mutations and regulatory germline variants also determines tumor progression, patient outcome, and drug response (Musa et al., 2019). However, future studies are needed to further clarify the variety of pathways and/or mediators that are potentially regulated by such mechanism (possibly beyond EwS) in order to identify potential novel prognostic biomarkers or drug targets. Using routine methods of precision oncology, the expression of such disease-specific markers or targets could be determined (e.g. by IHC and/or qRT-PCR) and patients could be stratified to certain risk- or treatment-groups according their marker/target expression. However, given the interaction between regulatory germline variants in non-protein-coding genomic regions and somatic driver-mutations, future approaches of 'omics'-based precision oncology could additionally include sequencing of such polymorphic non-protein-coding regulatory regions in order to characterize the inter-individually variable genetic background of dominant driving alterations (Musa and Grünewald, 2019; Musa et al., 2019). Thereby, after disease-specific regulatory variants interacting with dominant oncogenes have been identified, the pattern of regulatory variants may enable or refine stratification of patients to certain risk- or treatment-groups, which may help to more exhaustively exploit the potential of precision oncology (Musa and Grünewald, 2019; Musa et al., 2019).

6.2. 'Oncogenic cooperation' beyond the EwS model

EwS constitutes a valuable model to investigate the influence of 'oncogenic cooperation' on clinical heterogeneity in cancer, as it is characterized by a nearly diploid genome and is mainly driven by a single dominant ETS-fusion oncogene (*EWSR1-FLI1* in ~85% of EwS cases) which regulates ~40% of

its downstream target genes via enhancer-like GGAA-mSats that show high inter-individual variability (Delattre et al., 1992, 1994; Gangwal et al., 2008; Gröbner et al., 2018; Grünewald et al., 2015, 2018; Guillon et al., 2009; Monument et al., 2012, 2014; Musa et al., 2019; Patel et al., 2012). However, such ETS-fusion oncogenes not only occur in EwS but also in other cancer entities, such as *TMPRSS2-ERG* in prostate cancer or *FUS-ERG* in myeloid leukemia (Shimizu et al., 1993; Sizemore et al., 2017; Tomlins et al., 2005, 2007). Similarly to what is mechanistically known about EWSR1-FLI1 function in EwS (see section 'Etiology and pathophysiology' for details), ERG overexpression resulting from *TMPRSS2-ERG* rearrangement in prostate cancer (~50% of prostate cancer cases) was shown to be associated with the occurrence of a distinct cis-regulatory epigenetic landscape and a distinct transcriptomic profile as compared to prostate cancers negative for *TMPRSS2-ERG* rearrangement (Kron et al., 2017). Mechanistically, ERG was shown to act as a pioneer transcription factor recruiting chromatin remodelers and further transcription factors leading to chromatin modification and increased transcription of genes that are related to cis-regulatory elements which exhibit epigenetic super-enhancer marks (H3K27ac) (Baumgart et al., 2019; Chen et al., 2013; Kron et al., 2017; Rickman et al., 2012; Stone, 2017; Yu et al., 2010). Interestingly, by induction of such distinct regulatory signature, *TMPRSS2-ERG* rearrangement with resulting ERG overexpression confers a vulnerability toward specific therapeutic targeting of the Notch signaling pathway (Kron et al., 2017). However, *TMPRSS2-ERG* status was shown to not be per se a strong prognostic biomarker in prostate cancer, although the prognostic impact of other biomarkers depends on the *TMPRSS2-ERG* status (Gerke et al., 2019). As compared to *TMPRSS2-ERG* rearrangement in prostate cancer, less is known about regulatory alterations induced by the *FUS-ERG* fusion in myeloid leukemia (present in ~1% of acute myeloid leukemia (AML) cases), but it has been shown that FUS-ERG has transforming properties, that it co-occupies genomic regions with transcription factors associated with regulation of stem cell programs, and consistently, that occurrence of *FUS-ERG* rearrangement is associated with unfavorable outcome in pediatric AML patients (Ichikawa et al., 1999; Noort et al., 2018; Sotoca et al., 2016; Yang et al., 2000; Zerkalenkova et al., 2018). Nevertheless, *FUS-ERG* rearrangement in AML was shown to sensitize for all-trans retinoic acid (ATRA) treatment, which leads to myeloid differentiation upon short-term treatment and apoptosis upon long-term treatment, constituting a vulnerability of *FUS-ERG*-driven AML, whereby interestingly, such sensitivity toward ATRA treatment has been mainly described before in acute promyelocytic leukemia (M3 AML subtype according to the French-American-British (FAB) classification) (Cicconi and Lo-Coco, 2016; Sotoca et al., 2016; Zerkalenkova et al., 2018). As *EWSR1-FLI1* is a member of the

ETS-fusion family and shares its DNA binding domain with other ETS family members (Fry et al., 2018; Grünewald et al., 2018), it is conceivable that our findings made for the cooperation of EWSR1-FLI1 with regulatory germline variants in EwS are translatable to other malignancies exhibiting *ETS* rearrangements, although a specific interaction between other fusion oncoproteins and regulatory genetic variants has not been shown yet. However, similar mechanisms representing an interplay between somatic mutations/events and (inherited) polymorphisms in regulatory elements that mediate diversity of disease phenotypes have been demonstrated in recent studies from other biomedical disciplines (Genetic Modifiers of Huntington's Disease (GeM-HD) Consortium, 2015; Soccio et al., 2015; Vu et al., 2015). As for example, in *Caenorhabditis elegans* (*C. elegans*), it has been shown that the severity of RNA interference (RNAi) phenotypes, which were used as a model for loss-of-function mutations, varies depending on the different genetic backgrounds of two natural *C. elegans* isolates (Vu et al., 2015). However, these findings in *C. elegans* are in consistence with other exemplary studies reporting similar mechanisms in mammals (Genetic Modifiers of Huntington's Disease (GeM-HD) Consortium, 2015; Soccio et al., 2015). In mouse and human adipose tissue, SNPs in PPARγ transcription factor binding sites were shown to modulate PPARγ function and response to anti-diabetic drugs targeting PPARγ, and in Huntington´s disease patients, a genome-wide association study (GWAS) identified genetic polymorphisms associated with variant onset of Huntington's disease that are not located within the disease-causing mutated *HTT* gene, although risk of Huntington´s disease development is entirely, and onset and course of Huntington´s disease are majorly, determined by mutations leading to CAG-repeat expansions within the *HTT* gene (Genetic Modifiers of Huntington's Disease (GeM-HD) Consortium, 2015; Soccio et al., 2015). Collectively, these studies suggest that an interaction between somatic mutations/events and (inherited) genetic variants may constitute a broad principle underlying inter-individual diversity in cancer phenotypes, and may be even translatable to non-malignant diseases as a generalized concept of genetic regulation (Musa and Grünewald, 2019; Musa et al., 2019).

6.3. MYBL2 as a key mediator of an EWSR1-FLI1-directed proliferation program in EwS

Generally, it has been shown that high EWSR1-FLI1 levels are associated with a high proliferative capacity and blockage of differentiation in EwS cells (Franzetti et al., 2017; Grünewald et al., 2018; Kovar, 2010). Indeed, EWSR1-FLI1 regulates the expression of numerous proliferation-associated genes (Cidre-Aranaz and Alonso, 2015), but whether this EWSR1-FLI1-mediated proliferative capacity

is mediated via key mediators/hubs is not yet clear. *MYBL2* is an evolutionary conserved gene, physiologically expressed in nearly all proliferating tissues, and deregulated in numerous different cancer entities (Musa et al., 2017). As *MYBL2* encodes for a transcription factor regulating the expression of crucial genes associated with cell cycle progression, cell survival, and cell differentiation (Musa et al., 2017), it has the potential to act as such key hub of proliferation control downstream of EWSR1-FLI1. The data presented in this thesis indicate in several aspects that this might be the case: first, the data show that *MYBL2* is the gene most strongly regulated by EWSR1-FLI1, whose high expression is at the same time most strongly associated with unfavorable overall EwS patient survival (Musa et al., 2019). Second, *MYBL2* is co-expressed with a gene set reflecting orthologs of MYBL2 target genes in zebrafish, and gene sets associated with cell cycle progression, proliferation, and sensitization to apoptosis through Cyclin-dependent kinase (CDK) inhibition, pointing toward an evolutionary conserved role for MYBL2 in proliferation of EwS (Musa et al., 2019). Third, functional experiments show that MYBL2 knockdown leads to a decrease of EwS cell proliferation *in vitro*, a decrease of EwS tumor growth *in vivo*, as well as induction of a cell cycle blockage in G2/M phase and an increase of apoptotic cell death *in vitro* and *in vivo* (Musa et al., 2019). Regarding the used cell line model for investigation of MYBL2 function in EwS, notably, similar gene sets are enriched with *MYBL2* when performing a GSEA using microarray gene expression data of 166 primary EwS as when performing a GSEA using RNA-seq gene expression data of three EwS cell lines with and without MYBL2 knockdown, indicating that the cell line model used for functional *in vitro* and *in vivo* experiments is a valid model for primary EwS (Musa et al., 2019). In those functional *in vitro* and *in vivo* experiments, consistent MYBL2 knockdown phenotypes regarding EwS proliferation/growth were observed in 2-3 EwS cell lines using four different specific *MYBL2*-targeting siRNAs or two different specific *MYBL2*-targeting shRNAs (depending on the experiment) (Musa et al., 2019), which is why the probability of cell line- or oligonucleotide-dependent off-target effects appears to be acceptably low. However, the influence of MYBL2 knockdown on other EwS cells properties, as for example the capability for migration, invasion, or anchorage-independent growth, was not investigated here and needs to be subject of future studies. For functional *in vivo* experiments investigating MYBL2-dependent EwS xenograft growth, exclusively subcutaneous cell line-derived xenograft models were used (Musa et al., 2019). As EwS more frequently occur bone-associated than soft tissue-associated (Grünewald et al., 2018), an intraosseous xenograft model could be regarded as more appropriate, but also goes along with the necessity of mouse anesthesia for cell injection, a much higher pain burden for the mice

throughout the experiment, and consequently the need for analgetic treatment of the mice. As *in vitro* models for mimicking of bone microenvironment exist (Bersini et al., 2014; Bongio et al., 2016; Qiao and Tang, 2018), the added scientific value of using intraosseous xenografts over subcutaneous xenografts is debatable, when considering the much higher burden of pain for the xenografted mice and potential interfering effects of necessarily applied hypnotic or analgetic drugs on xenograft growth. Additionally, patient-derived xenografts (PDX) could have been used to further improve model validity (Nanni et al., 2019), but as EwS is a rare disease, such patient-derived samples were unfortunately not available, and just as importantly, endogenous mouse models for EwS do not exist up until now (Grünewald et al., 2018; Kondo, 2020; Minas et al., 2017). For identification of the most functionally and clinical relevant mediators signaling downstream of the EWSR1-FLI1-MYBL2 axis and being the main effectors of the MYBL2 proliferation hub, a multistep algorithm was applied (Musa et al., 2019). By using this algorithm, genes were selected according to their extent of regulation by MYBL2, evidence for MYBL2 binding to their promoters, correlation of their respective expression with that of *MYBL2* in primary EwS samples, association of their high expression with unfavorable overall EwS patient survival, and their ability to phenocopy MYBL2 function *in vitro* (Musa et al., 2019). Following this algorithm, three major candidate target genes downstream of MYBL2 were identified that are most relevant in mediation of MYBL2 function: *CCNF*, *BIRC5*, and *AURKB* (Musa et al., 2019). All three downstream target genes encode for known physiological regulators of cell division and/or cell death, frequently found to be deregulated in cancer (Carmena and Earnshaw, 2003; Galper et al., 2017; Mita et al., 2008; Wang et al., 2014), which is consistent with the potential role of MYBL2 as a key evolutionary conserved mediator of an EWSR1-FLI1-driven proliferation program in EwS. To validate the findings presented in this thesis, the regulation of CCNF, BIRC5, and AURKB by MYBL2 in EwS could be additionally investigated on protein level by western blot or IHC in future studies. However, the effect of MYBL2 in EwS may to a large extent, but not exclusively, be mediated by these three downstream targets, as the expression of several other proliferation-associated genes, such as *MKI67*, *KIF20A*, or *PIF1*, is as well significantly reduced upon MYBL2 knockdown, but these genes did not match other criteria or passed other thresholds applied within the selection algorithm (Musa et al., 2019). In summary, the results presented in this thesis point toward a role for MYBL2 as an evolutionary conserved major key hub for EwS cell proliferation downstream of EWSR1-FLI1 (Musa et al., 2019).

6.4. Potential of targeting major MYBL2 downstream targets in EwS and other cancer entities

The data shown in this thesis identify *CCNF*, *BIRC5* and *AURKB* as the most functionally and clinically relevant target genes of MYBL2 in EwS (Musa et al., 2019). This implies the potential effectivity of targeted therapeutic strategies directed against these major MYBL2 downstream targets in MYBL2 high-expressing EwS. Especially targeted therapies directed against Aurora kinases and BIRC5 (alias Survivin) received increasing attention as effective anti-cancer agents throughout the recent years (Bavetsias and Linardopoulos, 2015; Borisa and Bhatt, 2017; Falchook et al., 2015; Keen and Taylor, 2004; Li et al., 2019; Mobahat et al., 2014; Tang et al., 2017; Xiao and Li, 2015). On the contrary, as far as described in the literature, no commercially available targeted anti-CCNF (alias Cyclin F) agents have been developed yet. Aurora kinases represent a group of proteins crucial for proper mitosis/cytokinesis that are frequently deregulated in cancer (Keen and Taylor, 2004; Tang et al., 2017) and can be directly blocked by several small-molecule inhibitors (Bavetsias and Linardopoulos, 2015; Tang et al., 2017). Pan-Aurora kinase inhibitors targeting all known Aurora kinase family members (Aurora A, B, and C kinases, alias AURKA, AURKB, and AURKC, respectively) as well as inhibitors preferentially blocking certain specific members of the Aurora kinase family were pre-clinically shown to be effective anti-cancer agents in several tumor entities *in vitro* and *in vivo* (Ditchfield et al., 2003; Harrington et al., 2004; Hauf et al., 2003; Keen and Taylor, 2004) and are consequently tested in clinical trials (Bavetsias and Linardopoulos, 2015; Tang et al., 2017). Focusing on the identified major MYBL2 downstream target AURKB, agents preferentially inhibiting AURKB (e.g. Barasertib, alias AZD1152), as well as pan-Aurora kinase inhibitors including, but not limited to, AURKB inhibition (e.g. Danusertib, alias PHA-739358), have been tested up to clinical phase II trials in several advanced stage solid cancer entities as well as hematological malignancies, with on average moderate response rates (Bavetsias and Linardopoulos, 2015; Löwenberg et al., 2011; Schöffski et al., 2015; Tang et al., 2017), whereby response rates tended to be stronger in hematological malignancies (Bavetsias and Linardopoulos, 2015). Whether combination treatment regimens may further increase clinical effectivity of such inhibitors, which is indicated by several pre-clinical studies (Tang et al., 2017), remains to be elucidated in future clinical trials. BIRC5 belongs to the apoptosis inhibiting and cell proliferation promoting inhibitor of apoptosis (IAP) protein family (Xiao and Li, 2015). Agents developed to impair BIRC5 function may do so via several mechanisms: inhibition of its interaction with binding partners, inhibition of BIRC5 homodimerization, inhibition of *BIRC5* transcription, induction of *BIRC5* transcript degradation, or immunotherapeutic BIRC5 targeting (Li et al., 2019). Several compounds of different molecular

mechanisms of action showed promising pre-clinical anti-cancer effects in multiple cancer entities *in vitro* and *in vivo* (Garg et al., 2016; Li et al., 2019). YM155, a suppressor of *BIRC5* transcription, went up to clinical phase II studies in non-small cell lung cancer (NSCLC), melanoma, castrate-resistant prostate cancer (CRPC), diffuse large B-cell lymphoma (DLBCL), breast cancer, and B-cell Non-Hodgkin lymphoma alone and/or in combination therapy regimens, but exhibited limited therapeutic effectiveness (Li et al., 2019). Additionally, LY2181308, a *BIRC5* antisense oligonucleotide, was tested in up to clinical phase II studies in combination with docetaxel in NSCLC and CRPC, but showed no advantages in overall survival (OS) or progression-free survival (PFS) and a higher incidence of adverse effects as compared to docetaxel mono treatment (Li et al., 2019). Furthermore, as immunotherapeutic approaches, BIRC5 peptide vaccination either with single peptides, such as survivin-2B80-88 and SurVaxM, or peptide cocktails were used in single and/or combination therapy regimens in clinical phase II studies in pancreatic adenocarcinoma (Li et al., 2019; Shima et al., 2019), glioblastoma (Ahluwalia et al., 2019; Li et al., 2019), and advanced melanoma (Becker et al., 2012; Li et al., 2019; Nitschke et al., 2017), respectively, providing, at least partly, promising results that require clinical validation in further studies (Li et al., 2019). Given the important functional and clinical role of MYBL2 in EwS (Musa et al., 2019), targeted therapy strategies directed against the major MYBL2 targets AURKB and BIRC5 may especially constitute promising new treatment options in MYBL2 high-expressing EwS. Interestingly, recent studies showed that in EwS the preferential AURKB inhibitor AZD1152 (alias Barasertib), which has been tested in clinical phase II studies in several other cancer entities, impairs growth of EwS cells *in vitro* and *in vivo* (Sánchez-Molina et al., 2020; Wang et al., 2019) and JNJ-7706621, an inhibitor of multiple CDKs and Aurora kinases, was shown to inhibit growth of EwS xenografts (Matsuhashi et al., 2012). Regarding BIRC5 targeting in EwS, tolfenamic acid has been shown to inhibit SP1 transcription factor signaling upstream of BIRC5 and thereby to suppress BIRC5 expression and EwS cell proliferation *in vitro* (Shelake et al., 2017). However, interestingly, the major MYBL2 targets AURKB and BIRC5 are both part of the chromosomal passenger complex (CPC), a central regulatory complex during mitosis, suggesting that design of new small molecule inhibitors interfering with their protein-protein interaction may be a promising strategy for impairing their function especially in MYBL2 high-expressing EwS (Carmena et al., 2012; Keen and Taylor, 2004), which remains to be elucidated in further studies. As no specific agents targeting MYBL2 are available at the current timepoint, generally two main strategies are conceivable for effectively targeting the EWSR1-FLI1-MYBL2 axis in MYBL2 high-expressing EwS: first, using targeted therapeutic strategies directed against the main downstream

targets of MYBL2 as described in this section, or second, targeting the major upstream phosphorylating and activating Cyclin-dependent kinase (CDK2) of MYBL2 (see section 'Effectivity of targeting CDK2 in EwS and other cancer entities' for details). For the experiments shown in this thesis, the strategy of targeting MYBL2 upstream via CDK2 was chosen, as inhibitors directed against CDKs are already Food-and-Drug-Administration (FDA)-approved for breast cancer treatment (Howie et al., 2019) (see section 'Effectivity of targeting CDK2 in EwS and other cancer entities' for details) while evidence from clinical trials higher than phase II studies for effectivity of specifically targeting the major MYBL2 downstream targets in solid cancers is lacking, which suggested a CDK-targeting strategy as more promising for treatment of MYBL2 high-expressing EwS. In conclusion, several compounds constituting targeted therapy approaches directed against the in EwS identified major MYBL2 targets AURKB and BIRC5 showed, depending on cancer entity and therapy regimen, more or less promising results in up to clinical phase II studies, whereby direct evidence for treatment effectivity in EwS is yet very limited. However, whether such approaches may further succeed clinically in targeted cancer treatment, and specifically in targeted treatment of MYBL2 high-expressing EwS, requires further clinical evaluation.

6.5. Effectivity of targeting CDK2 in EwS and other cancer entities

Cyclin-dependent kinases (CDKs) are serine/threonine kinases which depend in their kinase activity on binding to certain Cyclin proteins and harbor crucial roles in numerous cellular processes, such as cell cycle control, transcriptional regulation, metabolism, and differentiation (Tadesse et al., 2019). Physiologically, MYBL2 is activated by CDK2-CyclinA/E-dependent phosphorylation during late G1 and S phase during the cell cycle (Musa et al., 2017), suggesting that targeted anti-CDK2 therapy is a promising therapeutic strategy in MYBL2 high-expressing EwS and possibly in other MYBL2 high-expressing cancers. Until now, no fully specific CDK2 inhibitors are available, but inhibitors preferentially targeting CDK2 as compared to other CDKs were developed and are commercially accessible (Tadesse et al., 2019). For several cancer entities, pre-clinical effectiveness of such CDK2 targeting has already been described, whereby, except from the data presented here in EwS (Musa et al., 2019), MYBL2-dependency of their anti-cancer effects was not experimentally evaluated (Tadesse et al., 2019). Generally, in addition, several first and second generation multi-CDK inhibitors were tested in clinical trials up to phase III for multiple cancer entities (Asghar et al., 2015), but most strikingly, selective CDK4/6 inhibitors reached first FDA-approval in 2015 (Palbociclib, alias PD-0332991) for treatment of estrogen receptor (ER) positive, HER2-negative advanced breast cancer treatment in postmenopausal

women with combined anti-estrogen therapy (Howie et al., 2019; Morrison, 2015), suggesting that the general concept of targeting CDKs may possibly as well constitute an effective strategy in clinical cancer treatment beyond breast cancer. The data presented in this thesis provide pre-clinical evidence *in vitro* and *in vivo* that high MYBL2 levels sensitize EwS cells for targeted anti-CDK2 treatment (Musa et al., 2019), which may be also the case in other cancer entities. Since neither significant weight loss of treated mice, nor histological alterations of inner organs or bone marrow was observed in mice treated for maximum 14 days in a dose up to 40mg/kg (including a break of one day per four days of treatment) with the CDK2 inhibitor NU6140 (Musa et al., 2019), it is conceivable that this inhibitor might be safely applicable in possible future clinical trials. As no fully specific CDK2 inhibitors are available, at least part of the observed effect of the used CDK2 inhibitors may as well be mediated via inhibition of other CDKs or unspecific targets. In this regard, NU6140 has the special property to preferentially target CDK2, the upstream activating kinase of MYBL2, as compared to other CDKs, but also to target AURKB, one of the major downstream targets of MYBL2 identified in EwS (Musa et al., 2019), making it appear especially effective in treatment of MYBL2 high-expressing EwS by not being fully selective. However, the MYBL2-dependency of the observed effect of NU6140 on EwS growth is most probably mediated by CDK2 inhibition rather than AURKB inhibition due to the fact that both different CDK2 inhibitors used for the experiments presented in this thesis, CVT-313 and NU6140, of which CVT-313 is not known to inhibit AURKB, show comparable MYBL2-dependencies of their effects on EwS growth (Musa et al., 2019). However, NU6140 was previously also shown to downregulate BIRC5 (Pennati et al., 2005), which is as well one of the major MYBL2 downstream targets in EwS (Musa et al., 2019). Fitting to the data presented in this thesis showing that the effect of CDK2 inhibition on EwS growth depends on MYBL2 expression and that BIRC5 is one of the major MYBL2 downstream targets in EwS (Musa et al., 2019), it is conceivable that downregulation of BIRC5 by NU6140 may be indirectly mediated via MYBL2, although such dependency was not evaluated in the respective study (Pennati et al., 2005) and was not specifically investigated in experiments underlying this thesis. Whether CDK2 inhibitors may succeed clinically in EwS or other cancer entities remains to be elucidated, as no clinical trials using such inhibitors have been conducted so far. Also, in EwS, no clinical trials using multi-CDK or selective CDK inhibitors have been conducted yet, but several multi-CDK inhibitors, such as Roscovitine (alias Seliciclib), Flavopiridol (alias Alvocidib), and JNJ-7706621 among others, have been previously shown to be pre-clinically effective (some of them synergistically with other compounds) *in vitro* and/or *in vivo* (Flores et al., 2020; Iniguez et al., 2018; Li et al., 2005, 2007; Matsuhashi et al., 2012; Richter et al.,

2020; Tirado et al., 2005). Interestingly, in case of Flavopiridol, inhibition of CDK2-Cyclin E was suggested to mainly mediate the effect of Flavopiridol treatment (Li et al., 2005), which further supports the findings presented in this thesis proposing anti-CDK2 treatment as a promising therapeutic strategy in MYBL2 high-expressing EwS (Musa et al., 2019). Furthermore, inhibition of CDK 4/6 using the FDA-approved inhibitor Palbociclib shows synergistic anticancer effectivity in EwS when combined with IGF1R inhibition, as IGF1R overexpression/activation may help EwS cells to escape selective CDK4/6 inhibition (Guenther et al., 2018). As a recent study showed that after the priming CDK2-dependent phosphorylation of MYBL2 subsequent phosphorylation by PLK1 additionally plays a role in MYBL2 activation (Werwein et al., 2019), future investigations evaluating a potentially synergistic effect of combined CDK2 and PLK1 inhibitor treatment in EwS appear to be auspicious. Taken together, pre-clinical evidence suggests that inhibition of CDKs is a promising strategy in EwS treatment, and that especially that of CDK2 is promising for targeted treatment of MYBL2-high expressing EwS (Musa et al., 2019). Such CDK2 inhibition may as well be a successful targeted treatment strategy in MYBL2 high-expressing cancers of other cancer entities, but generally requires evaluation in future clinical trials for every entity.

6.6. MYBL2 as a prognostic and/or predictive biomarker in EwS and other cancer entities

High MYBL2 expression is associated with unfavorable clinical outcome in several cancer entities, indicating the potential use of MYBL2 as a prognostic biomarker (Musa et al., 2017). As for example, MYBL2 overexpression has been shown to be associated with poor overall patient survival in breast cancer (Inoue and Fry, 2016), colorectal cancer (Ren et al., 2015), esophageal squamous cell carcinoma (Qin et al., 2016), hepatocellular carcinoma (Calvisi et al., 2011), and neuroblastoma (Raschellà et al., 1999), and furthermore, high MYBL2 expression is associated with poor disease-free survival in AML (Fuster et al., 2013), breast cancer (Inoue and Fry, 2016), and colorectal cancer (Ren et al., 2015), as well as with recurrence/relapse in AML (Fuster et al., 2013) and bladder carcinoma (Nord et al., 2010). An association of MYBL2 expression with increased risk of death and higher clinical stage has for instance been described for neuroblastoma (Raschellà et al., 1999) and renal cell carcinoma (Sakai et al., 1993), respectively. These studies exemplify that high MYBL2 expression is associated with unfavorable clinical parameters and poor patient outcome in a broad range of cancer entities. In accordance with these previous studies, the results presented in this thesis demonstrate that high

MYBL2 expression is associated with unfavorable overall EwS patient survival (Musa et al., 2019), suggesting the use of MYBL2 as a potential prognostic biomarker in EwS. However, to be fully conclusive, this association shown retrospectively on mRNA level needs to be further confirmed on protein level and preferentially validated via prospective investigation of additional cohorts. Besides the potential role of MYBL2 as a prognostic biomarker in EwS, the data presented in this thesis provide evidence that high MYBL2 expression levels sensitize EwS cells for anti-CDK2 treatment, which suggests an additional potential use of MYBL2 as a predictive biomarker for targeted anti-CDK2 therapy in MYBL2 high-expressing EwS (Musa et al., 2019), and possibly as well in other MYBL2 high-expressing cancer entities (see section 'Effectivity of targeting CDK2 in EwS and other cancer entities' for details). In case of effectivity of CDK2 inhibitor treatment in future clinical trials, also the predictive value of MYBL2 requires validation on protein level in preferentially prospectively observed patient cohorts. Taking into account the numerous studies describing an association between MYBL2 expression, unfavorable clinical parameters, and poor patient outcome in a broad range of cancer entities (Musa et al., 2017), as well as the data presented in this thesis showing that high *MYBL2* levels are associated with unfavorable overall EwS patient survival (Musa et al., 2019), MYBL2 appears to have the potential to be used as a prognostic biomarker in various cancer entities including EwS. Additionally, as high MYBL2 expression levels sensitize EwS cells for anti-CDK2 treatment, MYBL2 may be furthermore of value as a predictive biomarker for anti-CDK2 treatment in MYBL2 high-expressing EwS (Musa et al., 2019) and possibly in other MYBL2 high-expressing cancer entities.

7. CONCLUSION AND PERSPECTIVES

The data presented in this thesis establish the ‘oncogenic cooperation‘ between a somatic mutation (here *EWSR1-FLI1*) and a regulatory germline variant (here a polymorphic GGAA-microsatellite (mSat)) as a major determinant of inter-tumoral heterogeneity impacting on tumor growth, clinical outcome, and drug response through modulation of a functionally important and druggable downstream target (here MYBL2) in the EwS model (Musa and Grünewald, 2019; Musa et al., 2019). These results indicate that, after identification of disease-specific regulatory variants, future approaches of ‘omics‘-based precision oncology could additionally include sequencing of non-protein-coding regulatory genomic regions in order to risk-stratify patients into subgroups according to the inter-individually variable genetic background of dominant driving alterations (Musa and Grünewald, 2019; Musa et al., 2019). Furthermore, these findings potentially reflect a general mechanism accounting for inter-individual differences in phenotypes of diseases, which is supported by recent findings from research fields beyond oncology (Musa and Grünewald, 2019; Musa et al., 2019). In conclusion, such ‘oncogenic cooperation‘ between somatic mutations and regulatory germline variants constitute a major source of inter-tumoral heterogeneity, possibly beyond the EwS model, indicating the importance of integrating the regulatory genome into future approaches of ‘omics‘-based precision oncology (Musa and Grünewald, 2019; Musa et al., 2019).

8. REFERENCES

Aggerholm-Pedersen, N., Maretty-Kongstad, K., Keller, J., Baerentzen, S., and Safwat, A. (2016). The Prognostic Value of Serum Biomarkers in Localized Bone Sarcoma. Transl. Oncol. *9*, 322–328.

Aghighi, M., Boe, J., Rosenberg, J., Von Eyben, R., Gawande, R.S., Petit, P., Sethi, T.K., Sharib, J., Marina, N.M., DuBois, S.G., et al. (2016). Three-dimensional Radiologic Assessment of Chemotherapy Response in Ewing Sarcoma Can Be Used to Predict Clinical Outcome. Radiology *280*, 905–915.

Ahlbory, D., Appl, H., Lang, D., and Klempnauer, K.-H. (2005). Disruption of B-myb in DT40 cells reveals novel function for B-Myb in the response to DNA-damage. Oncogene *24*, 7127–7134.

Ahluwalia, M.S., Reardon, D.A., Abad, A.P., Curry, W.T., Wong, E.T., Belal, A., Qiu, J., Mogensen, K., Schilero, C., Hutson, A., et al. (2019). SurVaxM with standard therapy in newly diagnosed glioblastoma: Phase II trial update. J. Clin. Oncol. *37*, 2016–2016.

Anders, S., Pyl, P.T., and Huber, W. (2015). HTSeq--a Python framework to work with high-throughput sequencing data. Bioinformatics *31*, 166–169.

Anderson, N.D., de Borja, R., Young, M.D., Fuligni, F., Rosic, A., Roberts, N.D., Hajjar, S., Layeghifard, M., Novokmet, A., Kowalski, P.E., et al. (2018). Rearrangement bursts generate canonical gene fusions in bone and soft tissue tumors. Science *361*, eaam8419.

Arsura, M., Introna, M., Passerini, F., Mantovani, A., and Golay, J. (1992). B-myb antisense oligonucleotides inhibit proliferation of human hematopoietic cell lines. Blood *79*, 2708–2716.

Arsura, M., Luchetti, M.M., Erba, E., Golay, J., Rambaldi, A., and Introna, M. (1994). Dissociation between p93B-myb and p75c-myb expression during the proliferation and differentiation of human myeloid cell lines. Blood *83*, 1778–1790.

Asghar, U., Witkiewicz, A.K., Turner, N.C., and Knudsen, E.S. (2015). The history and future of targeting cyclin-dependent kinases in cancer therapy. Nat. Rev. Drug Discov. *14*, 130–146.

Aynaud, M.-M., Mirabeau, O., Gruel, N., Grossetête, S., Boeva, V., Durand, S., Surdez, D., Saulnier, O., Zaïdi, S., Gribkova, S., et al. (2020). Transcriptional Programs Define Intratumoral Heterogeneity of Ewing Sarcoma at Single-Cell Resolution. Cell Rep. *30*, 1767-1779.e6.

Baker, S.J., Ma'ayan, A., Lieu, Y.K., John, P., Reddy, M.V.R., Chen, E.Y., Duan, Q., Snoeck, H.-W., and Reddy, E.P. (2014). B-myb is an essential regulator of hematopoietic stem cell and myeloid progenitor cell development. Proc. Natl. Acad. Sci. U. S. A. *111*, 3122–3127.

Baldauf, M.C., Orth, M.F., Dallmayer, M., Marchetto, A., Gerke, J.S., Rubio, R.A., Kiran, M.M., Musa, J., Knott, M.M.L., Ohmura, S., et al. (2017). Robust diagnosis of Ewing sarcoma by immunohistochemical detection of super-enhancer-driven EWSR1-ETS targets. Oncotarget *9*, 1587-1601.

Baldauf, M.C., Gerke, J.S., Kirschner, A., Blaeschke, F., Effenberger, M., Schober, K., Rubio, R.A., Kanaseki, T., Kiran, M.M., Dallmayer, M., et al. (2018). Systematic identification of cancer-specific MHC-binding peptides with RAVEN. Oncoimmunology *7*, e1481558.

Barnett, J.R., Gikas, P., Gerrand, C., Briggs, T.W., and Saifuddin, A. (2020). The sensitivity, specificity, and diagnostic accuracy of whole-bone MRI for identifying skip metastases in appendicular osteosarcoma and Ewing sarcoma. Skeletal Radiol. *49*, 913–919.

Bar-Shira, A., Pinthus, J.H., Rozovsky, U., Goldstein, M., Sellers, W.R., Yaron, Y., Eshhar, Z., and Orr-Urtreger, A. (2002). Multiple genes in human 20q13 chromosomal region are involved in an advanced prostate cancer xenograft. Cancer Res. *62*, 6803–6807.

Baumgart, S.J., Nevedomskaya, E., and Haendler, B. (2019). Dysregulated Transcriptional Control in Prostate Cancer. Int. J. Mol. Sci. *20*, 2883.

Bavetsias, V., and Linardopoulos, S. (2015). Aurora Kinase Inhibitors: Current Status and Outlook. Front. Oncol. *5*, 278.

Bayley, R., Blakemore, D., Cancian, L., Dumon, S., Volpe, G., Ward, C., Almaghrabi, R., Gujar, J., Reeve, N., Raghavan, M., et al. (2018). MYBL2 Supports DNA Double Strand Break Repair in Hematopoietic Stem Cells. Cancer Res. *78*, 5767–5779.

Becker, J.C., Andersen, M.H., Hofmeister-Müller, V., Wobser, M., Frey, L., Sandig, C., Walter, S., Singh-Jasuja, H., Kämpgen, E., Opitz, A., et al. (2012). Survivin-specific T-cell reactivity correlates with tumor response and patient survival: a phase-II peptide vaccination trial in metastatic melanoma. Cancer Immunol. Immunother. *61*, 2091–2103.

Ben-Porath, I., Thomson, M.W., Carey, V.J., Ge, R., Bell, G.W., Regev, A., and Weinberg, R.A. (2008). An embryonic stem cell-like gene expression signature in poorly differentiated aggressive human tumors. Nat. Genet. *40*, 499–507.

Bersini, S., Jeon, J.S., Dubini, G., Arrigoni, C., Chung, S., Charest, J.L., Moretti, M., and Kamm, R.D. (2014). A microfluidic 3D in vitro model for specificity of breast cancer metastasis to bone. Biomaterials *35*, 2454–2461.

Bies, J., and Wolff, L. (1995). Acceleration of apoptosis in transforming growth factor beta 1-treated M1 cells ectopically expressing B-myb. Cancer Res. *55*, 501–504.

Bies, J., Hoffman, B., Amanullah, A., Giese, T., and Wolff, L. (1996). B-Myb prevents growth arrest associated with terminal differentiation of monocytic cells. Oncogene *12*, 355–363.

Bilke, S., Schwentner, R., Yang, F., Kauer, M., Jug, G., Walker, R.L., Davis, S., Zhu, Y.J., Pineda, M., Meltzer, P.S., et al. (2013). Oncogenic ETS fusions deregulate E2F3 target genes in Ewing sarcoma and prostate cancer. Genome Res. *23*, 1797–1809.

Biswas, B., Rastogi, S., Khan, S.A., Shukla, N.K., Deo, S.V.S., Agarwala, S., Sharma, D.N., Thulkar, S., Vishnubhatla, S., Pathania, S., et al. (2014). Hypoalbuminaemia is an independent predictor of poor outcome in metastatic Ewing's sarcoma family of tumours: a single institutional experience of 150 cases treated with uniform chemotherapy protocol. Clin. Oncol. R. Coll. Radiol. G. B. *26*, 722–729.

Biswas, S.C., Shi, Y., Vonsattel, J.-P.G., Leung, C.L., Troy, C.M., and Greene, L.A. (2007). Bim is elevated in Alzheimer's disease neurons and is required for beta-amyloid-induced neuronal apoptosis. J. Neurosci. *27*, 893–900.

Bölling, T., Schuck, A., Paulussen, M., Dirksen, U., Ranft, A., Könemann, S., Dunst, J., Willich, N., and Jürgens, H. (2008). Whole lung irradiation in patients with exclusively pulmonary metastases of Ewing tumors. Toxicity analysis and treatment results of the EICESS-92 trial. Strahlenther. Onkol. *184*, 193–197.

Bongio, M., Lopa, S., Gilardi, M., Bersini, S., and Moretti, M. (2016). A 3D vascularized bone remodeling model combining osteoblasts and osteoclasts in a CaP nanoparticle-enriched matrix. Nanomed. *11*, 1073–1091.

Borisa, A.C., and Bhatt, H.G. (2017). A comprehensive review on Aurora kinase: Small molecule inhibitors and clinical trial studies. Eur. J. Med. Chem. *140*, 1–19.

Boulay, G., Sandoval, G.J., Riggi, N., Iyer, S., Buisson, R., Naigles, B., Awad, M.E., Rengarajan, S., Volorio, A., McBride, M.J., et al. (2017). Cancer-Specific Retargeting of BAF Complexes by a Prion-like Domain. Cell *171*, 163-178.e19.

Boulay, G., Volorio, A., Iyer, S., Broye, L.C., Stamenkovic, I., Riggi, N., and Rivera, M.N. (2018). Epigenome editing of microsatellite repeats defines tumor-specific enhancer functions and dependencies. Genes Dev. *32*, 1008–1019.

Breitegger, B., Holzer, L.A., Beham-Schmid, C., Urban, C., Liegl-Atzwanger, B., and Leithner, A. (2020). Bone marrow aspirations in Ewing sarcomas: Are they still necessary? A single-center retrospective analysis and review of the literature. J. Cancer Res. Ther. *16*, 713–717.

Briegel, K., Lim, K.C., Plank, C., Beug, H., Engel, J.D., and Zenke, M. (1993). Ectopic expression of a conditional GATA-2/estrogen receptor chimera arrests erythroid differentiation in a hormone-dependent manner. Genes Dev. *7*, 1097–1109.

Brohl, A.S., Solomon, D.A., Chang, W., Wang, J., Song, Y., Sindiri, S., Patidar, R., Hurd, L., Chen, L., Shern, J.F., et al. (2014). The genomic landscape of the Ewing Sarcoma family of tumors reveals recurrent STAG2 mutation. PLoS Genet. *10*, e1004475.

Brohl, A.S., Patidar, R., Turner, C.E., Wen, X., Song, Y.K., Wei, J.S., Calzone, K.A., and Khan, J. (2017). Frequent inactivating germline mutations in DNA repair genes in patients with Ewing sarcoma. Genet. Med. *19*, 955–958.

Brown, C.J., Lain, S., Verma, C.S., Fersht, A.R., and Lane, D.P. (2009). Awakening guardian angels: drugging the p53 pathway. Nat. Rev. Cancer *9*, 862–873.

Calvisi, D.F., Simile, M.M., Ladu, S., Frau, M., Evert, M., Tomasi, M.L., Demartis, M.I., Daino, L., Seddaiu, M.A., Brozzetti, S., et al. (2011). Activation of v-Myb avian myeloblastosis viral oncogene homolog-like2 (MYBL2)-LIN9 complex contributes to human hepatocarcinogenesis and identifies a subset of hepatocellular carcinoma with mutant p53. Hepatology *53*, 1226–1236.

Cariboni, U., De Sanctis, R., Giaretta, M., Voulaz, E., Morenghi, E., Colombo, P., Novellis, P., Bottoni, E., Errico, V., Crepaldi, A., et al. (2019). Survival Outcome and Prognostic Factors After Pulmonary Metastasectomy in Sarcoma Patients: A 18-Year Experience at a Single High-volume Referral Center. Am. J. Clin. Oncol. *42*, 6–11.

Carmena, M., and Earnshaw, W.C. (2003). The cellular geography of Aurora kinases. Nat. Rev. Mol. Cell Biol. *4*, 842–854.

Carmena, M., Wheelock, M., Funabiki, H., and Earnshaw, W.C. (2012). The chromosomal passenger complex (CPC): from easy rider to the godfather of mitosis. Nat. Rev. Mol. Cell Biol. *13*, 789–803.

Casali, P.G., Bielack, S., Abecassis, N., Aro, H.T., Bauer, S., Biagini, R., Bonvalot, S., Boukovinas, I., Bovee, J.V.M.G., Brennan, B., et al. (2018). Bone sarcomas: ESMO-PaedCan-EURACAN Clinical Practice Guidelines for diagnosis, treatment and follow-up. Ann. Oncol. *29*, iv79–iv95.

Cervellera, M., Raschella, G., Santilli, G., Tanno, B., Ventura, A., Mancini, C., Sevignani, C., Calabretta, B., and Sala, A. (2000). Direct transactivation of the anti-apoptotic gene apolipoprotein J (clusterin) by B-MYB. J. Biol. Chem. *275*, 21055–21060.

Chang, W., Brohl, A.S., Patidar, R., Sindiri, S., Shern, J.F., Wei, J.S., Song, Y.K., Yohe, M.E., Gryder, B., Zhang, S., et al. (2016). MultiDimensional ClinOmics for Precision Therapy of Children and Adolescent Young Adults with Relapsed and Refractory Cancer: A Report from the Center for Cancer Research. Clin. Cancer Res. *22*, 3810–3820.

Charan, M., Dravid, P., Cam, M., Audino, A., Gross, A.C., Arnold, M.A., Roberts, R.D., Cripe, T.P., Pertsemlidis, A., Houghton, P.J., et al. (2020). GD2-directed CAR-T cells in combination with HGF-targeted neutralizing antibody (AMG102) prevent primary tumor growth and metastasis in Ewing sarcoma. Int. J. Cancer *146*, 3184–3195.

Charrasse, S., Carena, I., Brondani, V., Klempnauer, K.H., and Ferrari, S. (2000). Degradation of B-Myb by ubiquitin-mediated proteolysis: involvement of the Cdc34-SCF(p45Skp2) pathway. Oncogene *19*, 2986–2995.

Chen, S., Deniz, K., Sung, Y.-S., Zhang, L., Dry, S., and Antonescu, C.R. (2016). Ewing sarcoma with ERG gene rearrangements: A molecular study focusing on the prevalence of FUS-ERG and common pitfalls in detecting EWSR1-ERG fusions by FISH. Genes Chromosomes Cancer *55*, 340–349.

Chen, Y., Chi, P., Rockowitz, S., Iaquinta, P.J., Shamu, T., Shukla, S., Gao, D., Sirota, I., Carver, B.S., Wongvipat, J., et al. (2013). ETS factors reprogram the androgen receptor cistrome and prime prostate tumorigenesis in response to PTEN loss. Nat. Med. *19*, 1023–1029.

Cicconi, L., and Lo-Coco, F. (2016). Current management of newly diagnosed acute promyelocytic leukemia. Ann. Oncol. *27*, 1474–1481.

Cidre-Aranaz, F., and Alonso, J. (2015). EWS/FLI1 Target Genes and Therapeutic Opportunities in Ewing Sarcoma. Front. Oncol. *5*, 162.

Costelloe, C.M., Chuang, H.H., and Daw, N.C. (2017). PET/CT of Osteosarcoma and Ewing Sarcoma. Semin. Roentgenol. *52*, 255–268.

Crompton, B.D., Stewart, C., Taylor-Weiner, A., Alexe, G., Kurek, K.C., Calicchio, M.L., Kiezun, A., Carter, S.L., Shukla, S.A., Mehta, S.S., et al. (2014). The genomic landscape of pediatric Ewing sarcoma. Cancer Discov. *4*, 1326–1341.

Dai, M., Wang, P., Boyd, A.D., Kostov, G., Athey, B., Jones, E.G., Bunney, W.E., Myers, R.M., Speed, T.P., Akil, H., et al. (2005). Evolving gene/transcript definitions significantly alter the interpretation of GeneChip data. Nucleic Acids Res. *33*, e175.

D'Angiolella, V., Esencay, M., and Pagano, M. (2013). A cyclin without cyclin-dependent kinases: cyclin F controls genome stability through ubiquitin-mediated proteolysis. Trends Cell Biol. *23*, 135–140.

Davidson, C.J., Tirouvanziam, R., Herzenberg, L.A., and Lipsick, J.S. (2005). Functional evolution of the vertebrate Myb gene family: B-Myb, but neither A-Myb nor c-Myb, complements Drosophila Myb in hemocytes. Genetics *169*, 215–229.

Delattre, O., Zucman, J., Plougastel, B., Desmaze, C., Melot, T., Peter, M., Kovar, H., Joubert, I., de Jong, P., and Rouleau, G. (1992). Gene fusion with an ETS DNA-binding domain caused by chromosome translocation in human tumours. Nature *359*, 162–165.

Delattre, O., Zucman, J., Melot, T., Garau, X.S., Zucker, J.M., Lenoir, G.M., Ambros, P.F., Sheer, D., Turc-Carel, C., and Triche, T.J. (1994). The Ewing family of tumors--a subgroup of small-round-cell tumors defined by specific chimeric transcripts. N. Engl. J. Med. *331*, 294–299.

Deng, S., Calin, G.A., Croce, C.M., Coukos, G., and Zhang, L. (2008). Mechanisms of microRNA deregulation in human cancer. Cell Cycle *7*, 2643–2646.

Dirksen, U., Brennan, B., Le Deley, M.-C., Cozic, N., van den Berg, H., Bhadri, V., Brichard, B., Claude, L., Craft, A., Amler, S., et al. (2019). High-Dose Chemotherapy Compared With Standard Chemotherapy and Lung Radiation in Ewing Sarcoma With Pulmonary Metastases: Results of the European Ewing Tumour Working Initiative of National Groups, 99 Trial and EWING 2008. J. Clin. Oncol. *37*, 3192–3202.

Ditchfield, C., Johnson, V.L., Tighe, A., Ellston, R., Haworth, C., Johnson, T., Mortlock, A., Keen, N., and Taylor, S.S. (2003). Aurora B couples chromosome alignment with anaphase by targeting BubR1, Mad2, and Cenp-E to kinetochores. J. Cell Biol. *161*, 267–280.

Ewing, J. (1921). Diffuse endothelioma of bone. Proc. N. Y. Pathol. Soc. *21*, 17–24.

Ewing, J. (1972). Classics in oncology. Diffuse endothelioma of bone. James Ewing. Proceedings of the New York Pathological Society, 1921. CA. Cancer J. Clin. *22*, 95–98.

Falchook, G.S., Bastida, C.C., and Kurzrock, R. (2015). Aurora Kinase Inhibitors in Oncology Clinical Trials: Current State of the Progress. Semin. Oncol. *42*, 832–848.

Fan, X., and Chen, J.J. (2014). Role of Cdk1 in DNA damage-induced G1 checkpoint abrogation by the human papillomavirus E7 oncogene. Cell Cycle *13*, 3249–3259.

Ferrari, S., del Prever, A.B., Palmerini, E., Staals, E., Berta, M., Balladelli, A., Picci, P., Fagioli, F., Bacci, G., and Vanel, D. (2009). Response to high-dose ifosfamide in patients with advanced/recurrent Ewing sarcoma. Pediatr. Blood Cancer *52*, 581–584.

Ferrari, S., Sundby Hall, K., Luksch, R., Tienghi, A., Wiebe, T., Fagioli, F., Alvegard, T.A., Brach Del Prever, A., Tamburini, A., Alberghini, M., et al. (2011). Nonmetastatic Ewing family tumors: high-dose chemotherapy with stem cell rescue in poor responder patients. Results of the Italian Sarcoma Group/Scandinavian Sarcoma Group III protocol. Ann. Oncol. *22*, 1221–1227.

Fischer, M., Quaas, M., Nickel, A., and Engeland, K. (2015). Indirect p53-dependent transcriptional repression of Survivin, CDC25C, and PLK1 genes requires the cyclin-dependent kinase inhibitor p21/CDKN1A and CDE/CHR promoter sites binding the DREAM complex. Oncotarget *6*, 41402–41417.

Fischer, M., Quaas, M., Steiner, L., and Engeland, K. (2016a). The p53-p21-DREAM-CDE/CHR pathway regulates G2/M cell cycle genes. Nucleic Acids Res. *44*, 164–174.

Fischer, M., Grossmann, P., Padi, M., and DeCaprio, J.A. (2016b). Integration of TP53, DREAM, MMB-FOXM1 and RB-E2F target gene analyses identifies cell cycle gene regulatory networks. Nucleic Acids Res. *44*, 6070–6086.

Fletcher, C.D.M., Bridge, J.A., Hogendoorn, P.C.W., and Mertens, F. (2013). WHO Classification of Tumours of Soft Tissue and Bone (IARC).

Flores, G., Everett, J.H., Boguslawski, E.A., Oswald, B.M., Madaj, Z.B., Beddows, I., Dikalov, S., Adams, M., Klumpp-Thomas, C.A., Kitchen-Goosen, S.M., et al. (2020). CDK9 Blockade Exploits Context-dependent Transcriptional Changes to Improve Activity and Limit Toxicity of Mithramycin for Ewing Sarcoma. Mol. Cancer Ther. *19*, 1183–1196.

Franzetti, G.-A., Laud-Duval, K., van der Ent, W., Brisac, A., Irondelle, M., Aubert, S., Dirksen, U., Bouvier, C., de Pinieux, G., Snaar-Jagalska, E., et al. (2017). Cell-to-cell heterogeneity of EWSR1-FLI1 activity determines proliferation/migration choices in Ewing sarcoma cells. Oncogene *36*, 3505–3514.

Franzius, C., Daldrup-Link, H.E., Sciuk, J., Rummeny, E.J., Bielack, S., Jürgens, H., and Schober, O. (2001). FDG-PET for detection of pulmonary metastases from malignant primary bone tumors: comparison with spiral CT. Ann. Oncol. *12*, 479–486.

Fry, E.A., Mallakin, A., and Inoue, K. (2018). Translocations involving ETS family proteins in human cancer. Integr. Cancer Sci. Ther. *5*, 10.15761/ICST.1000281.

Fu, Z., Malureanu, L., Huang, J., Wang, W., Li, H., van Deursen, J.M., Tindall, D.J., and Chen, J. (2008). Plk1-dependent phosphorylation of FoxM1 regulates a transcriptional programme required for mitotic progression. Nat. Cell Biol. *10*, 1076–1082.

Fung, S.-M., Ramsay, G., and Katzen, A.L. (2002). Mutations in Drosophila myb lead to centrosome amplification and genomic instability. Development *129*, 347–359.

Fuster, O., Llop, M., Dolz, S., García, P., Such, E., Ibáñez, M., Luna, I., Gómez, I., López, M., Cervera, J., et al. (2013). Adverse prognostic value of MYBL2 overexpression and association with microRNA-30 family in acute myeloid leukemia patients. Leuk. Res. *37*, 1690–1696.

Galper, J., Rayner, S.L., Hogan, A.L., Fifita, J.A., Lee, A., Chung, R.S., Blair, I.P., and Yang, S. (2017). Cyclin F: A component of an E3 ubiquitin ligase complex with roles in neurodegeneration and cancer. Int. J. Biochem. Cell Biol. *89*, 216–220.

Gangwal, K., Sankar, S., Hollenhorst, P.C., Kinsey, M., Haroldsen, S.C., Shah, A.A., Boucher, K.M., Watkins, W.S., Jorde, L.B., Graves, B.J., et al. (2008). Microsatellites as EWS/FLI response elements in Ewing's sarcoma. Proc. Natl. Acad. Sci. U. S. A. *105*, 10149–10154.

Garber, J.E., and Offit, K. (2005). Hereditary cancer predisposition syndromes. J. Clin. Oncol. *23*, 276–292.

García, P., and Frampton, J. (2006). The transcription factor B-Myb is essential for S-phase progression and genomic stability in diploid and polyploid megakaryocytes. J. Cell Sci. *119*, 1483–1493.

Garg, H., Suri, P., Gupta, J.C., Talwar, G.P., and Dubey, S. (2016). Survivin: a unique target for tumor therapy. Cancer Cell Int. *16*, 49.

Garraway, L.A., Verweij, J., and Ballman, K.V. (2013). Precision oncology: an overview. J. Clin. Oncol. *31*, 1803–1805.

Gaspar, N., Hawkins, D.S., Dirksen, U., Lewis, I.J., Ferrari, S., Le Deley, M.-C., Kovar, H., Grimer, R., Whelan, J., Claude, L., et al. (2015). Ewing Sarcoma: Current Management and Future Approaches Through Collaboration. J. Clin. Oncol. *33*, 3036–3046.

Genetic Modifiers of Huntington's Disease (GeM-HD) Consortium (2015). Identification of Genetic Factors that Modify Clinical Onset of Huntington's Disease. Cell *162*, 516–526.

Gerke, J.S., Orth, M.F., Tolkach, Y., Romero-Pérez, L., Wehweck, F.S., Stein, S., Musa, J., Knott, M.M.L., Hölting, T.L.B., Li, J., et al. (2019). Integrative clinical transcriptome analysis reveals TMPRSS2-ERG dependency of prognostic biomarkers in prostate adenocarcinoma. Int. J. Cancer *146*, 2036-2046.

Gerth, H.U., Juergens, K.U., Dirksen, U., Gerss, J., Schober, O., and Franzius, C. (2007). Significant benefit of multimodal imaging: PET/CT compared with PET alone in staging and follow-up of patients with Ewing tumors. J. Nucl. Med. *48*, 1932–1939.

Gilbert, L.A., Horlbeck, M.A., Adamson, B., Villalta, J.E., Chen, Y., Whitehead, E.H., Guimaraes, C., Panning, B., Ploegh, H.L., Bassik, M.C., et al. (2014). Genome-Scale CRISPR-Mediated Control of Gene Repression and Activation. Cell *159*, 647–661.

Ginsberg, J.P., de Alava, E., Ladanyi, M., Wexler, L.H., Kovar, H., Paulussen, M., Zoubek, A., Dockhorn-Dworniczak, B., Juergens, H., Wunder, J.S., et al. (1999). EWS-FLI1 and EWS-ERG gene fusions are associated with similar clinical phenotypes in Ewing's sarcoma. J. Clin. Oncol. *17*, 1809–1814.

Golay, J., Luppi, M., Songia, S., Palvarini, C., Lombardi, L., Aiello, A., Delia, D., Lam, K., Crawford, D.H., Biondi, A., et al. (1996). Expression of A-myb, but not c-myb and B-myb, is restricted to Burkitt's lymphoma, sIg+ B-acute lymphoblastic leukemia, and a subset of chronic lymphocytic leukemias. Blood *87*, 1900–1911.

Grassilli, E., Salomoni, P., Perrotti, D., Franceschi, C., and Calabretta, B. (1999). Resistance to apoptosis in CTLL-2 cells overexpressing B-Myb is associated with B-Myb-dependent bcl-2 induction. Cancer Res. *59*, 2451–2456.

Greene, L.A., Liu, D.X., Troy, C.M., and Biswas, S.C. (2007). Cell cycle molecules define a pathway required for neuron death in development and disease. Biochim. Biophys. Acta *1772*, 392–401.

Grewal, A.S., Li, Y., Grewal, S.K., Bagatell, R., Balamuth, N., Womer, R., Kurtz, G., Tochner, Z., and Hill-Kayser, C.E. (2020). Role of Metastatic Site Irradiation in Pediatric Patients With Metastatic Ewing Sarcoma. J. Pediatr. Hematol. Oncol. *42*, e305–e309.

Gröbner, S.N., Worst, B.C., Weischenfeldt, J., Buchhalter, I., Kleinheinz, K., Rudneva, V.A., Johann, P.D., Balasubramanian, G.P., Segura-Wang, M., Brabetz, S., et al. (2018). The landscape of genomic alterations across childhood cancers. Nature *555*, 321–327.

Grünewald, T.G.P., Bernard, V., Gilardi-Hebenstreit, P., Raynal, V., Surdez, D., Aynaud, M.-M., Mirabeau, O., Cidre-Aranaz, F., Tirode, F., Zaidi, S., et al. (2015). Chimeric EWSR1-FLI1 regulates the Ewing sarcoma susceptibility gene EGR2 via a GGAA microsatellite. Nat. Genet. *47*, 1073–1078.

Grünewald, T.G.P., Cidre-Aranaz, F., Surdez, D., Tomazou, E.M., de Álava, E., Kovar, H., Sorensen, P.H., Delattre, O., and Dirksen, U. (2018). Ewing sarcoma. Nat. Rev. Dis. Primer *4*, 5.

Gualdrini, F., Corvetta, D., Cantilena, S., Chayka, O., Tanno, B., Raschellà, G., and Sala, A. (2010). Addiction of MYCN amplified tumours to B-MYB underscores a reciprocal regulatory loop. Oncotarget *1*, 278–288.

Guenther, L.M., Dharia, N.V., Ross, L., Conway, A., Robichaud, A.L., Catlett, J.L., Wechsler, C.S., Frank, E.S., Goodale, A., Church, A.J., et al. (2018). A Combination CDK4/6 and IGF1R Inhibitor Strategy for Ewing Sarcoma. Clin. Cancer Res. *25*, 1343-1357.

Guillon, N., Tirode, F., Boeva, V., Zynovyev, A., Barillot, E., and Delattre, O. (2009). The oncogenic EWS-FLI1 protein binds in vivo GGAA microsatellite sequences with potential transcriptional activation function. PloS One *4*, e4932.

Haeusler, J., Ranft, A., Boelling, T., Gosheger, G., Braun-Munzinger, G., Vieth, V., Burdach, S., van den Berg, H., Juergens, H., and Dirksen, U. (2010). The value of local treatment in patients with primary, disseminated, multifocal Ewing sarcoma (PDMES). Cancer *116*, 443–450.

Harlow, M.L., Chasse, M.H., Boguslawski, E.A., Sorensen, K.M., Gedminas, J.M., Kitchen-Goosen, S.M., Rothbart, S.B., Taslim, C., Lessnick, S.L., Peck, A.S., et al. (2019). Trabectedin Inhibits EWS-FLI1 and Evicts SWI/SNF from Chromatin in a Schedule-dependent Manner. Clin. Cancer Res. *25*, 3417–3429.

Harrington, E.A., Bebbington, D., Moore, J., Rasmussen, R.K., Ajose-Adeogun, A.O., Nakayama, T., Graham, J.A., Demur, C., Hercend, T., Diu-Hercend, A., et al. (2004). VX-680, a potent and selective small-molecule inhibitor of the Aurora kinases, suppresses tumor growth in vivo. Nat. Med. *10*, 262–267.

Hattinger, C.M., Pötschger, U., Tarkkanen, M., Squire, J., Zielenska, M., Kiuru-Kuhlefelt, S., Kager, L., Thorner, P., Knuutila, S., Niggli, F.K., et al. (2002). Prognostic impact of chromosomal aberrations in Ewing tumours. Br. J. Cancer *86*, 1763–1769.

Hauf, S., Cole, R.W., LaTerra, S., Zimmer, C., Schnapp, G., Walter, R., Heckel, A., van Meel, J., Rieder, C.L., and Peters, J.-M. (2003). The small molecule Hesperadin reveals a role for Aurora B in correcting kinetochore-microtubule attachment and in maintaining the spindle assembly checkpoint. J. Cell Biol. *161*, 281–294.

Holohan, C., Van Schaeybroeck, S., Longley, D.B., and Johnston, P.G. (2013). Cancer drug resistance: an evolving paradigm. Nat. Rev. Cancer *13*, 714–726.

Hornick, J.L. (2014). Novel uses of immunohistochemistry in the diagnosis and classification of soft tissue tumors. Mod. Pathol. *27, Suppl 1*, S47-63.

Horstmann, S., Ferrari, S., and Klempnauer, K.H. (2000). Regulation of B-Myb activity by cyclin D1. Oncogene *19*, 298–306.

Howie, L.J., Singh, H., Bloomquist, E., Wedam, S., Amiri-Kordestani, L., Tang, S., Sridhara, R., Sanchez, J., Prowell, T.M., Kluetz, P.G., et al. (2019). Outcomes of Older Women With Hormone Receptor-Positive, Human Epidermal Growth Factor Receptor-Negative Metastatic Breast Cancer Treated With a CDK4/6 Inhibitor and an Aromatase Inhibitor: An FDA Pooled Analysis. J. Clin. Oncol. *37*, 3475-3483.

Huang, H.-Y., Illei, P.B., Zhao, Z., Mazumdar, M., Huvos, A.G., Healey, J.H., Wexler, L.H., Gorlick, R., Meyers, P., and Ladanyi, M. (2005). Ewing sarcomas with p53 mutation or p16/p14ARF homozygous deletion: a highly lethal subset associated with poor chemoresponse. J. Clin. Oncol. *23*, 548–558.

Huang, W., Loganantharaj, R., Schroeder, B., Fargo, D., and Li, L. (2013). PAVIS: a tool for Peak Annotation and Visualization. Bioinformatics *29*, 3097–3099.

Huang, Y., Wu, J., Li, R., Wang, P., Han, L., Zhang, Z., and Tong, T. (2011). B-MYB delays cell aging by repressing p16 (INK4α) transcription. Cell. Mol. Life Sci. *68*, 893–901.

Hunold, A., Weddeling, N., Paulussen, M., Ranft, A., Liebscher, C., and Jürgens, H. (2006). Topotecan and cyclophosphamide in patients with refractory or relapsed Ewing tumors. Pediatr. Blood Cancer *47*, 795–800.

Hutter, R.V., Francis, K.C., and Foote, F.W. (1964). Ewing's sarcoma in siblings: report of the second known occurrence. Am. J. Surg. *107*, 598–603.

Hyman, D.M., Taylor, B.S., and Baselga, J. (2017). Implementing Genome-Driven Oncology. Cell *168*, 584–599.

Ichikawa, H., Shimizu, K., Katsu, R., and Ohki, M. (1999). Dual transforming activities of the FUS (TLS)-ERG leukemia fusion protein conferred by two N-terminal domains of FUS (TLS). Mol. Cell. Biol. *19*, 7639–7650.

Iltzsche, F., Simon, K., Stopp, S., Pattschull, G., Francke, S., Wolter, P., Hauser, S., Murphy, D.J., Garcia, P., Rosenwald, A., et al. (2017). An important role for Myb-MuvB and its target gene KIF23 in a mouse model of lung adenocarcinoma. Oncogene *36*, 110–121.

Iniguez, A.B., Stolte, B., Wang, E.J., Conway, A.S., Alexe, G., Dharia, N. V, Kwiatkowski, N., Zhang, T., Abraham, B.J., Mora, J., et al. (2018). EWS/FLI Confers Tumor Cell Synthetic Lethality to CDK12 Inhibition in Ewing Sarcoma. Cancer Cell *33*, 202-216.e6.

Inoue, K., and Fry, E.A. (2016). Novel Molecular Markers for Breast Cancer. Biomark. Cancer *8*, 25–42.

Irizarry, R.A., Hobbs, B., Collin, F., Beazer-Barclay, Y.D., Antonellis, K.J., Scherf, U., and Speed, T.P. (2003). Exploration, normalization, and summaries of high density oligonucleotide array probe level data. Biostatistics *4*, 249–264.

Italiano, A., Mir, O., Mathoulin-Pelissier, S., Penel, N., Piperno-Neumann, S., Bompas, E., Chevreau, C., Duffaud, F., Entz-Werlé, N., Saada, E., et al. (2020). Cabozantinib in patients with advanced Ewing sarcoma or osteosarcoma (CABONE): a multicentre, single-arm, phase 2 trial. Lancet Oncol. *21*, 446–455.

Iwai, N., Kitajima, K., Sakai, K., Kimura, T., and Nakano, T. (2001). Alteration of cell adhesion and cell cycle properties of ES cells by an inducible dominant interfering Myb mutant. Oncogene *20*, 1425–1434.

Iwamoto, Y. (2007). Diagnosis and treatment of Ewing's sarcoma. Jpn. J. Clin. Oncol. *37*, 79–89.

Iyirhiaro, G.O., Zhang, Y., Estey, C., O'Hare, M.J., Safarpour, F., Parsanejad, M., Wang, S., Abdel-Messih, E., Callaghan, S.M., During, M.J., et al. (2014). Regulation of ischemic neuronal death by E2F4-p130 protein complexes. J. Biol. Chem. *289*, 18202–18213.

Jawad, M.U., Cheung, M.C., Min, E.S., Schneiderbauer, M.M., Koniaris, L.G., and Scully, S.P. (2009). Ewing sarcoma demonstrates racial disparities in incidence-related and sex-related differences in outcome: an analysis of 1631 cases from the SEER database, 1973-2005. Cancer *115*, 3526–3536.

Jeon, I.S., Davis, J.N., Braun, B.S., Sublett, J.E., Roussel, M.F., Denny, C.T., and Shapiro, D.N. (1995). A variant Ewing's sarcoma translocation (7;22) fuses the EWS gene to the ETS gene ETV1. Oncogene *10*, 1229–1234.

Ji, J., and Hemminki, K. (2006). Familial risk for histology-specific bone cancers: an updated study in Sweden. Eur. J. Cancer *42*, 2343–2349.

Johnson, K.M., Taslim, C., Saund, R.S., and Lessnick, S.L. (2017). Identification of two types of GGAA-microsatellites and their roles in EWS/FLI binding and gene regulation in Ewing sarcoma. PloS One *12*, e0186275.

Johnson, L.R., Johnson, T.K., Desler, M., Luster, T.A., Nowling, T., Lewis, R.E., and Rizzino, A. (2002). Effects of B-Myb on gene transcription: phosphorylation-dependent activity ans acetylation by p300. J. Biol. Chem. *277*, 4088–4097.

Johnson, T.K., Schweppe, R.E., Septer, J., and Lewis, R.E. (1999). Phosphorylation of B-Myb regulates its transactivation potential and DNA binding. J. Biol. Chem. *274*, 36741–36749.

Johnson, W.E., Li, C., and Rabinovic, A. (2007). Adjusting batch effects in microarray expression data using empirical Bayes methods. Biostatistics *8*, 118–127.

Joyce, M.J., Harmon, D.C., Mankin, H.J., Suit, H.D., Schiller, A.L., and Truman, J.T. (1984). Ewing's sarcoma in female siblings. A clinical report and review of the literature. Cancer *53*, 1959–1962.

Kalus, S., Vidoni, A., Oliveira, I., and Saifuddin, A. (2020). Image-guided core needle biopsy for Ewing sarcoma of bone: a 10-year single-institution review. Eur. Radiol. *30*, 5308–5314.

Kasalak, Ö., Overbosch, J., Adams, H.J., Dammann, A., Dierckx, R.A., Jutte, P.C., and Kwee, T.C. (2019). Diagnostic value of MRI signs in differentiating Ewing sarcoma from osteomyelitis. Acta Radiol. *60*, 204–212.

Katzen, A.L., Jackson, J., Harmon, B.P., Fung, S.M., Ramsay, G., and Bishop, J.M. (1998). Drosophila myb is required for the G2/M transition and maintenance of diploidy. Genes Dev. *12*, 831–843.

Keen, N., and Taylor, S. (2004). Aurora-kinase inhibitors as anticancer agents. Nat. Rev. Cancer *4*, 927–936.

Kim, S.K., and Park, Y.-K. (2016). Ewing sarcoma: a chronicle of molecular pathogenesis. Hum. Pathol. *55*, 91–100.

Kim, B.M., Hong, Y., Lee, S., Liu, P., Lim, J.H., Lee, Y.H., Lee, T.H., Chang, K.T., and Hong, Y. (2015). Therapeutic Implications for Overcoming Radiation Resistance in Cancer Therapy. Int. J. Mol. Sci. *16*, 26880–26913.

Knight, A.S., Notaridou, M., and Watson, R.J. (2009). A Lin-9 complex is recruited by B-Myb to activate transcription of G2/M genes in undifferentiated embryonal carcinoma cells. Oncogene *28*, 1737–1747.

Kondo, T. (2020). Current Status and Perspectives of Patient-Derived Models for Ewing's Sarcoma. Cancers (Basel) *12*, 2520.

Kopp, L.M., Hu, C., Rozo, B., White-Collins, A., Huh, W.W., Yarborough, A., Herzog, C.E., and Hingorani, P. (2015). Utility of bone marrow aspiration and biopsy in initial staging of Ewing sarcoma. Pediatr. Blood Cancer *62*, 12–15.

Koshkin, V.S., Bolejack, V., Schwartz, L.H., Wahl, R.L., Chugh, R., Reinke, D.K., Zhao, B., O, J.H., Patel, S.R., Schuetze, S.M., et al. (2016). Assessment of Imaging Modalities and Response Metrics in Ewing Sarcoma: Correlation With Survival. J. Clin. Oncol. *34*, 3680–3685.

Kovar, H. (2010). Downstream EWS/FLI1 - upstream Ewing's sarcoma. Genome Med. *2*, 8.

Kovar, H., Auinger, A., Jug, G., Aryee, D., Zoubek, A., Salzer-Kuntschik, M., and Gadner, H. (1993). Narrow spectrum of infrequent p53 mutations and absence of MDM2 amplification in Ewing tumours. Oncogene *8*, 2683–2690.

Kron, K.J., Murison, A., Zhou, S., Huang, V., Yamaguchi, T.N., Shiah, Y.-J., Fraser, M., van der Kwast, T., Boutros, P.C., Bristow, R.G., et al. (2017). TMPRSS2-ERG fusion co-opts master transcription factors and activates NOTCH signaling in primary prostate cancer. Nat. Genet. *49*, 1336–1345.

Kuleta-Bosak, E., Kluczewska, E., Machnik-Broncel, J., Madziara, W., Ciupińska-Kajor, M., Sojka, D., Rogala, W., Juszczyk, J., and Wilk, R. (2010). Suitability of imaging methods (X-ray, CT, MRI) in the diagnostics of Ewing's sarcoma in children - analysis of own material. Pol. J. Radiol. *75*, 18–28.

Lang, G., Gombert, W.M., and Gould, H.J. (2005). A transcriptional regulatory element in the coding sequence of the human Bcl-2 gene. Immunology *114*, 25–36.

Langmead, B., and Salzberg, S.L. (2012). Fast gapped-read alignment with Bowtie 2. Nat. Methods *9*, 357–359.

Lassmann, S., Weis, R., Makowiec, F., Roth, J., Danciu, M., Hopt, U., and Werner, M. (2007). Array CGH identifies distinct DNA copy number profiles of oncogenes and tumor suppressor genes in chromosomal- and microsatellite-unstable sporadic colorectal carcinomas. J. Mol. Med. *85*, 293–304.

Latham, K.E., Litvin, J., Orth, J.M., Patel, B., Mettus, R., and Reddy, E.P. (1996). Temporal patterns of A-myb and B-myb gene expression during testis development. Oncogene *13*, 1161–1168.

Levenson, V.V., Davidovich, I.A., and Roninson, I.B. (2000). Pleiotropic resistance to DNA-interactive drugs is associated with increased expression of genes involved in DNA replication, repair, and stress response. Cancer Res. *60*, 5027–5030.

von Levetzow, C., Jiang, X., Gwye, Y., von Levetzow, G., Hung, L., Cooper, A., Hsu, J.H.-R., and Lawlor, E.R. (2011). Modeling initiation of Ewing sarcoma in human neural crest cells. PloS One *6*, e19305.

Li, H., and Durbin, R. (2009). Fast and accurate short read alignment with Burrows-Wheeler transform. Bioinformatics *25*, 1754–1760.

Li, X., and McDonnell, D.P. (2002). The transcription factor B-Myb is maintained in an inhibited state in target cells through its interaction with the nuclear corepressors N-CoR and SMRT. Mol. Cell. Biol. *22*, 3663–3673.

Li, F., Aljahdali, I., and Ling, X. (2019). Cancer therapeutics using survivin BIRC5 as a target: what can we do after over two decades of study? J. Exp. Clin. Cancer Res. *38*, 368.

Li, H., Handsaker, B., Wysoker, A., Fennell, T., Ruan, J., Homer, N., Marth, G., Abecasis, G., Durbin, R., and 1000 Genome Project Data Processing Subgroup (2009). The Sequence Alignment/Map format and SAMtools. Bioinformatics *25*, 2078–2079.

Li, J., Dallmayer, M., Kirchner, T., Musa, J., and Grünewald, T.G.P. (2018). PRC1: Linking Cytokinesis, Chromosomal Instability, and Cancer Evolution. Trends Cancer *4*, 59–73.

Li, X., Tanaka, K., Nakatani, F., Matsunobu, T., Sakimura, R., Hanada, M., Okada, T., Nakamura, T., and Iwamoto, Y. (2005). Transactivation of cyclin E gene by EWS-Fli1 and antitumor effects of cyclin dependent kinase inhibitor on Ewing's family tumor cells. Int. J. Cancer *116*, 385–394.

Li, Y., Tanaka, K., Li, X., Okada, T., Nakamura, T., Takasaki, M., Yamamoto, S., Oda, Y., Tsuneyoshi, M., and Iwamoto, Y. (2007). Cyclin-dependent kinase inhibitor, flavopiridol, induces apoptosis and inhibits tumor growth in drug-resistant osteosarcoma and Ewing's family tumor cells. Int. J. Cancer *121*, 1212–1218.

Li, Y.-J., Yang, X., Zhang, W.-B., Yi, C., Wang, F., and Li, P. (2017). Clinical implications of six inflammatory biomarkers as prognostic indicators in Ewing sarcoma. Cancer Manag. Res. *9*, 443–451.

Lin, D., Fiscella, M., O'Connor, P.M., Jackman, J., Chen, M., Luo, L.L., Sala, A., Travali, S., Appella, E., and Mercer, W.E. (1994). Constitutive expression of B-myb can bypass p53-induced Waf1/Cip1-mediated G1 arrest. Proc. Natl. Acad. Sci. U. S. A. *91*, 10079–10083.

Lin, S.-H., Sampson, J.N., Grünewald, T.G.P., Surdez, D., Reynaud, S., Mirabeau, O., Karlins, E., Rubio, R.A., Zaidi, S., Grossetête-Lalami, S., et al. (2020). Low-frequency variation near common germline susceptibility loci are associated with risk of Ewing sarcoma. PLoS One *15*, e0237792.

Liu, D.X., Biswas, S.C., and Greene, L.A. (2004). B-myb and C-myb play required roles in neuronal apoptosis evoked by nerve growth factor deprivation and DNA damage. J. Neurosci. *24*, 8720–8725.

Livak, K.J., and Schmittgen, T.D. (2001). Analysis of relative gene expression data using real-time quantitative PCR and the 2(-Delta Delta C(T)) Method. Methods *25*, 402–408.

Llombart-Bosch, A., Machado, I., Navarro, S., Bertoni, F., Bacchini, P., Alberghini, M., Karzeladze, A., Savelov, N., Petrov, S., Alvarado-Cabrero, I., et al. (2009). Histological heterogeneity of Ewing's sarcoma/PNET: an immunohistochemical analysis of 415 genetically confirmed cases with clinical support. Virchows Arch. *455*, 397–411.

Lorvellec, M., Dumon, S., Maya-Mendoza, A., Jackson, D., Frampton, J., and García, P. (2010). B-Myb is critical for proper DNA duplication during an unperturbed S phase in mouse embryonic stem cells. Stem Cells *28*, 1751–1759.

Love, M.I., Huber, W., and Anders, S. (2014). Moderated estimation of fold change and dispersion for RNA-seq data with DESeq2. Genome Biol. *15*, 550.

Löwenberg, B., Muus, P., Ossenkoppele, G., Rousselot, P., Cahn, J.-Y., Ifrah, N., Martinelli, G., Amadori, S., Berman, E., Sonneveld, P., et al. (2011). Phase 1/2 study to assess the safety, efficacy, and pharmacokinetics of barasertib (AZD1152) in patients with advanced acute myeloid leukemia. Blood *118*, 6030–6036.

Lu, E., Ryan, C.W., Bassale, S., Lim, J.Y., and Davis, L.E. (2020). Feasibility of Treating Adults with Ewing or Ewing-Like Sarcoma with Interval-Compressed Vincristine, Doxorubicin, and Cyclophosphamide Alternating with Ifosfamide and Etoposide. Oncologist *25*, 150–155.

Machado, I., Yoshida, A., Morales, M.G.N., Abrahão-Machado, L.F., Navarro, S., Cruz, J., Lavernia, J., Parafioriti, A., Picci, P., and Llombart-Bosch, A. (2018). Review with novel markers facilitates precise categorization of 41 cases of diagnostically challenging, "undifferentiated small round cell tumors". A clinicopathologic, immunophenotypic and molecular analysis. Ann. Diagn. Pathol. *34*, 1–12.

Machiela, M.J., Grünewald, T.G.P., Surdez, D., Reynaud, S., Mirabeau, O., Karlins, E., Rubio, R.A., Zaidi, S., Grossetete-Lalami, S., Ballet, S., et al. (2018). Genome-wide association study identifies multiple new loci associated with Ewing sarcoma susceptibility. Nat. Commun. *9*, 3184.

Mackintosh, C., Ordóñez, J.L., García-Domínguez, D.J., Sevillano, V., Llombart-Bosch, A., Szuhai, K., Scotlandi, K., Alberghini, M., Sciot, R., Sinnaeve, F., et al. (2012). 1q gain and CDT2 overexpression underlie an aggressive and highly proliferative form of Ewing sarcoma. Oncogene *31*, 1287–1298.

Manak, J.R., Mitiku, N., and Lipsick, J.S. (2002). Mutation of the Drosophila homologue of the Myb protooncogene causes genomic instability. Proc. Natl. Acad. Sci. U. S. A. *99*, 7438–7443.

Mannefeld, M., Klassen, E., and Gaubatz, S. (2009). B-MYB is required for recovery from the DNA damage-induced G2 checkpoint in p53 mutant cells. Cancer Res. *69*, 4073–4080.

Martinelli, M., Parra, A., Scapoli, L., De Sanctis, P., Chiadini, V., Hattinger, C., Picci, P., Zucchini, C., and Scotlandi, K. (2016). CD99 polymorphisms significantly influence the probability to develop Ewing sarcoma in earlier age and patient disease progression. Oncotarget *7*, 77958–77967.

Martinez, I., and Dimaio, D. (2011). B-Myb, cancer, senescence, and microRNAs. Cancer Res. *71*, 5370–5373.

Maruyama, H., Ishitsuka, Y., Fujisawa, Y., Furuta, J., Sekido, M., and Kawachi, Y. (2014). B-Myb enhances proliferation and suppresses differentiation of keratinocytes in three-dimensional cell culture. Arch. Dermatol. Res. *306*, 375–384.

Matsuhashi, A., Ohno, T., Kimura, M., Hara, A., Saio, M., Nagano, A., Kawai, G., Saitou, M., Takigami, I., Yamada, K., et al. (2012). Growth suppression and mitotic defect induced by JNJ-7706621, an inhibitor of cyclin-dependent kinases and aurora kinases. Curr. Cancer Drug Targets *12*, 625–639.

McKenna, A., Hanna, M., Banks, E., Sivachenko, A., Cibulskis, K., Kernytsky, A., Garimella, K., Altshuler, D., Gabriel, S., Daly, M., et al. (2010). The Genome Analysis Toolkit: a MapReduce framework for analyzing next-generation DNA sequencing data. Genome Res. *20*, 1297–1303.

Minas, T.Z., Surdez, D., Javaheri, T., Tanaka, M., Howarth, M., Kang, H.-J., Han, J., Han, Z.-Y., Sax, B., Kream, B.E., et al. (2017). Combined experience of six independent laboratories attempting to create an Ewing sarcoma mouse model. Oncotarget *8*, 34141–34163.

Mita, A.C., Mita, M.M., Nawrocki, S.T., and Giles, F.J. (2008). Survivin: key regulator of mitosis and apoptosis and novel target for cancer therapeutics. Clin. Cancer Res. *14*, 5000–5005.

Mobahat, M., Narendran, A., and Riabowol, K. (2014). Survivin as a preferential target for cancer therapy. Int. J. Mol. Sci. *15*, 2494–2516.

Monument, M.J., Johnson, K.M., Grossmann, A.H., Schiffman, J.D., Randall, R.L., and Lessnick, S.L. (2012). Microsatellites with macro-influence in ewing sarcoma. Genes *3*, 444–460.

Monument, M.J., Johnson, K.M., McIlvaine, E., Abegglen, L., Watkins, W.S., Jorde, L.B., Womer, R.B., Beeler, N., Monovich, L., Lawlor, E.R., et al. (2014). Clinical and biochemical function of polymorphic NR0B1 GGAA-microsatellites in Ewing sarcoma: a report from the Children's Oncology Group. PloS One *9*, e104378.

Morita, K., He, S., Nowak. RP, Wang, J., Zimmerman, M., Fu; C, Durbin, A., Martel, M., Prutsch, N., Gray, N., et al. (2020). Allosteric Activators of Protein Phosphatase 2A Display Broad Antitumor Activity Mediated by Dephosphorylation of MYBL2. Cell *181*, 702-71.

Morrison, C. (2015). Pfizer's CDK4/6 inhibitor approved for advanced breast cancer. Nat. Biotechnol. *33*, 323–324.

Mowla, S.N., Lam, E.W.-F., and Jat, P.S. (2014). Cellular senescence and aging: the role of B-MYB. Aging Cell *13*, 773–779.

Müller, G.A., Quaas, M., Schümann, M., Krause, E., Padi, M., Fischer, M., Litovchick, L., DeCaprio, J.A., and Engeland, K. (2012). The CHR promoter element controls cell cycle-dependent gene transcription and binds the DREAM and MMB complexes. Nucleic Acids Res. *40*, 1561–1578.

Musa, J., and Grünewald, T.G.P. (2019). Interaction between somatic mutations and germline variants contributes to clinical heterogeneity in cancer. Mol. Cell. Oncol. *7*, 1682924.

Musa, J., Aynaud, M.-M., Mirabeau, O., Delattre, O., and Grünewald, T.G. (2017). MYBL2 (B-Myb): a central regulator of cell proliferation, cell survival and differentiation involved in tumorigenesis. Cell Death Dis. *8*, e2895.

Musa, J., Cidre-Aranaz, F., Aynaud, M.-M., Orth, M.F., Knott, M.M.L., Mirabeau, O., Mazor, G., Varon, M., Hölting, T.L.B., Grossetête, S., et al. (2019). Cooperation of cancer drivers with regulatory germline variants shapes clinical outcomes. Nat. Commun. *10*, 4128.

Ahead of original publication, this article was published as a Biorxiv preprint (DOI 10.1101/506659).

Nanni, P., Landuzzi, L., Manara, M.C., Righi, A., Nicoletti, G., Cristalli, C., Pasello, M., Parra, A., Carrabotta, M., Ferracin, M., et al. (2019). Bone sarcoma patient-derived xenografts are faithful and stable preclinical models for molecular and therapeutic investigations. Sci. Rep. *9*, 12174.

Ness, S.A. (2003). Myb protein specificity: evidence of a context-specific transcription factor code. Blood Cells. Mol. Dis. *31*, 192–200.

Newman, E.N., Jones, R.L., and Hawkins, D.S. (2013). An evaluation of [F-18]-fluorodeoxy-D-glucose positron emission tomography, bone scan, and bone marrow aspiration/biopsy as staging investigations in Ewing sarcoma. Pediatr. Blood Cancer *60*, 1113–1117.

Ng, T.L., O'Sullivan, M.J., Pallen, C.J., Hayes, M., Clarkson, P.W., Winstanley, M., Sorensen, P.H.B., Nielsen, T.O., and Horsman, D.E. (2007). Ewing sarcoma with novel translocation t(2;16) producing an in-frame fusion of FUS and FEV. J. Mol. Diagn. *9*, 459–463.

Niethard, F.U., Pfeil, J., and Biberthaler, P. (2009). Duale Reihe Orthopädie und Unfallchirurgie (Thieme).

Nitschke, N.J., Bjoern, J., Iversen, T.Z., Andersen, M.H., and Svane, I.M. (2017). Indoleamine 2,3-dioxygenase and survivin peptide vaccine combined with temozolomide in metastatic melanoma. Stem Cell Investig. *4*, 77.

Noort, S., Zimmermann, M., Reinhardt, D., Cuccuini, W., Pigazzi, M., Smith, J., Ries, R.E., Alonzo, T.A., Hirsch, B., Tomizawa, D., et al. (2018). Prognostic impact of t(16;21)(p11;q22) and t(16;21)(q24;q22) in pediatric AML: a retrospective study by the I-BFM Study Group. Blood *132*, 1584–1592.

Nor Rashid, N., Yusof, R., and Watson, R.J. (2011). Disruption of repressive p130-DREAM complexes by human papillomavirus 16 E6/E7 oncoproteins is required for cell-cycle progression in cervical cancer cells. J. Gen. Virol. *92*, 2620–2627.

Nord, H., Segersten, U., Sandgren, J., Wester, K., Busch, C., Menzel, U., Komorowski, J., Dumanski, J.P., Malmström, P.-U., and Díaz de Ståhl, T. (2010). Focal amplifications are associated with high grade and recurrences in stage Ta bladder carcinoma. Int. J. Cancer *126*, 1390–1402.

Okada, M., Akimaru, H., Hou, D.-X., Takahashi, T., and Ishii, S. (2002). Myb controls G(2)/M progression by inducing cyclin B expression in the Drosophila eye imaginal disc. EMBO J. *21*, 675–684.

Osterloh, L., von Eyss, B., Schmit, F., Rein, L., Hübner, D., Samans, B., Hauser, S., and Gaubatz, S. (2007). The human synMuv-like protein LIN-9 is required for transcription of G2/M genes and for entry into mitosis. EMBO J. *26*, 144–157.

Pang, C.L., Toh, S.Y., He, P., Teissier, S., Ben Khalifa, Y., Xue, Y., and Thierry, F. (2014). A functional interaction of E7 with B-Myb-MuvB complex promotes acute cooperative transcriptional activation of both S- and M-phase genes. (129 c). Oncogene *33*, 4039–4049.

Papetti, M., and Augenlicht, L.H. (2011). MYBL2, a link between proliferation and differentiation in maturing colon epithelial cells. J. Cell. Physiol. *226*, 785–791.

Parikh, N., Hilsenbeck, S., Creighton, C.J., Dayaram, T., Shuck, R., Shinbrot, E., Xi, L., Gibbs, R.A., Wheeler, D.A., and Donehower, L.A. (2014). Effects of TP53 mutational status on gene expression patterns across 10 human cancer types. J. Pathol. *232*, 522–533.

Park, H.J., Costa, R.H., Lau, L.F., Tyner, A.L., and Raychaudhuri, P. (2008). Anaphase-promoting complex/cyclosome-CDH1-mediated proteolysis of the forkhead box M1 transcription factor is critical for regulated entry into S phase. Mol. Cell. Biol. *28*, 5162–5171.

Patel, M., Simon, J.M., Iglesia, M.D., Wu, S.B., McFadden, A.W., Lieb, J.D., and Davis, I.J. (2012). Tumor-specific retargeting of an oncogenic transcription factor chimera results in dysregulation of chromatin and transcription. Genome Res. *22*, 259–270.

Patnaik, S., Yarlagadda, J., and Susarla, R. (2018). Imaging features of Ewing's sarcoma: Special reference to uncommon features and rare sites of presentation. J. Cancer Res. Ther. *14*, 1014–1022.

Pennati, M., Campbell, A.J., Curto, M., Binda, M., Cheng, Y., Wang, L.-Z., Curtin, N., Golding, B.T., Griffin, R.J., Hardcastle, I.R., et al. (2005). Potentiation of paclitaxel-induced apoptosis by the novel cyclin-dependent kinase inhibitor NU6140: a possible role for survivin down-regulation. Mol. Cancer Ther. *4*, 1328–1337.

Peter, M., Couturier, J., Pacquement, H., Michon, J., Thomas, G., Magdelenat, H., and Delattre, O. (1997). A new member of the ETS family fused to EWS in Ewing tumors. Oncogene *14*, 1159–1164.

Pfister, K., Pipka, J.L., Chiang, C., Liu, Y., Clark, R.A., Keller, R., Skoglund, P., Guertin, M.J., Hall, I.M., and Stukenberg, P.T. (2018). Identification of Drivers of Aneuploidy in Breast Tumors. Cell Rep. *23*, 2758–2769.

Pilkinton, M., Sandoval, R., and Colamonici, O.R. (2007). Mammalian Mip/LIN-9 interacts with either the p107, p130/E2F4 repressor complex or B-Myb in a cell cycle-phase-dependent context distinct from the Drosophila dREAM complex. Oncogene *26*, 7535–7543.

Postel-Vinay, S., Véron, A.S., Tirode, F., Pierron, G., Reynaud, S., Kovar, H., Oberlin, O., Lapouble, E., Ballet, S., Lucchesi, C., et al. (2012). Common variants near TARDBP and EGR2 are associated with susceptibility to Ewing sarcoma. Nat. Genet. *44*, 323–327.

Qiao, H., and Tang, T. (2018). Engineering 3D approaches to model the dynamic microenvironments of cancer bone metastasis. Bone Res. *6*, 3.

Qin, H.-D., Liao, X.-Y., Chen, Y.-B., Huang, S.-Y., Xue, W.-Q., Li, F.-F., Ge, X.-S., Liu, D.-Q., Cai, Q., Long, J., et al. (2016). Genomic Characterization of Esophageal Squamous Cell Carcinoma Reveals Critical Genes Underlying Tumorigenesis and Poor Prognosis. Am. J. Hum. Genet. *98*, 709–727.

Quaas, M., Müller, G.A., and Engeland, K. (2012). p53 can repress transcription of cell cycle genes through a p21(WAF1/CIP1)-dependent switch from MMB to DREAM protein complex binding at CHR promoter elements. Cell Cycle *11*, 4661–4672.

Raine, K.M., Van Loo, P., Wedge, D.C., Jones, D., Menzies, A., Butler, A.P., Teague, J.W., Tarpey, P., Nik-Zainal, S., and Campbell, P.J. (2016). ascatNgs: Identifying Somatically Acquired Copy-Number Alterations from Whole-Genome Sequencing Data. Curr. Protoc. Bioinformatics *56*, 15.9.1-15.9.17.

Ramsay, R.G., and Gonda, T.J. (2008). MYB function in normal and cancer cells. Nat. Rev. Cancer *8*, 523–534.

Raschellà, G., Negroni, A., Sala, A., Pucci, S., Romeo, A., and Calabretta, B. (1995). Requirement of b-myb function for survival and differentiative potential of human neuroblastoma cells. J. Biol. Chem. *270*, 8540–8545.

Raschellà, G., Tanno, B., Bonetto, F., Negroni, A., Claudio, P.P., Baldi, A., Amendola, R., Calabretta, B., Giordano, A., and Paggi, M.G. (1998). The RB-related gene Rb2/p130 in neuroblastoma differentiation and in B-myb promoter down-regulation. Cell Death Differ. *5*, 401–407.

Raschellà, G., Cesi, V., Amendola, R., Negroni, A., Tanno, B., Altavista, P., Tonini, G.P., De Bernardi, B., and Calabretta, B. (1999). Expression of B-myb in neuroblastoma tumors is a poor prognostic factor independent from MYCN amplification. Cancer Res. *59*, 3365–3368.

Remmele, W., and Stegner, H.E. (1987). [Recommendation for uniform definition of an immunoreactive score (IRS) for immunohistochemical estrogen receptor detection (ER-ICA) in breast cancer tissue]. Pathol. *8*, 138–140.

Ren, F., Wang, L., Shen, X., Xiao, X., Liu, Z., Wei, P., Wang, Y., Qi, P., Shen, C., Sheng, W., et al. (2015). MYBL2 is an independent prognostic marker that has tumor-promoting functions in colorectal cancer. Am. J. Cancer Res. *5*, 1542–1552.

Richter, G., Hensel, T., Schmidt, O., Saratov, V., von Heyking, K., Becker-Dettling, F., Prexler, C., Yen, H., Steiger, K., Fulda, S., et al. (2020). Combined Inhibition of Epigenetic Readers and Transcription Initiation Targets the EWS-ETS Transcriptional Program in Ewing Sarcoma. Cancers (Basel) *12*, 304.

Rickman, D.S., Soong, T.D., Moss, B., Mosquera, J.M., Dlabal, J., Terry, S., MacDonald, T.Y., Tripodi, J., Bunting, K., Najfeld, V., et al. (2012). Oncogene-mediated alterations in chromatin conformation. Proc. Natl. Acad. Sci. U. S. A. *109*, 9083–9088.

Riggi, N., Cironi, L., Provero, P., Suvà, M.-L., Kaloulis, K., Garcia-Echeverria, C., Hoffmann, F., Trumpp, A., and Stamenkovic, I. (2005). Development of Ewing's sarcoma from primary bone marrow-derived mesenchymal progenitor cells. Cancer Res. *65*, 11459–11468.

Riggi, N., Knoechel, B., Gillespie, S.M., Rheinbay, E., Boulay, G., Suvà, M.L., Rossetti, N.E., Boonseng, W.E., Oksuz, O., Cook, E.B., et al. (2014). EWS-FLI1 utilizes divergent chromatin remodeling mechanisms to directly activate or repress enhancer elements in Ewing sarcoma. Cancer Cell *26*, 668–681.

Rocchi, A., Manara, M.C., Sciandra, M., Zambelli, D., Nardi, F., Nicoletti, G., Garofalo, C., Meschini, S., Astolfi, A., Colombo, M.P., et al. (2010). CD99 inhibits neural differentiation of human Ewing sarcoma cells and thereby contributes to oncogenesis. J. Clin. Invest. *120*, 668–680.

Romero-Pérez, L., Surdez, D., Brunet, E., Delattre, O., and Grünewald, T.G.P. (2019). STAG Mutations in Cancer. Trends Cancer *5*, 506-520.

Roussel, M., Saule, S., Lagrou, C., Rommens, C., Beug, H., Graf, T., and Stehelin, D. (1979). Three new types of viral oncogene of cellular origin specific for haematopoietic cell transformation. Nature *281*, 452–455.

Rovani, M.K., Brachmann, C.B., Ramsay, G., and Katzen, A.L. (2012). The dREAM/Myb-MuvB complex and Grim are key regulators of the programmed death of neural precursor cells at the Drosophila posterior wing margin. Dev. Biol. *372*, 88–102.

Rutkowski, P., Kamińska, J., Kowalska, M., Ruka, W., and Steffen, J. (2003). Cytokine and cytokine receptor serum levels in adult bone sarcoma patients: correlations with local tumor extent and prognosis. J. Surg. Oncol. *84*, 151–159.

Sadasivam, S., and DeCaprio, J.A. (2013). The DREAM complex: master coordinator of cell cycle-dependent gene expression. Nat. Rev. Cancer *13*, 585–595.

Sadasivam, S., Duan, S., and DeCaprio, J.A. (2012). The MuvB complex sequentially recruits B-Myb and FoxM1 to promote mitotic gene expression. Genes Dev. *26*, 474–489.

Sakai, N., Kubota, Y., and Shuin, T. (1993). Statistically significant expression of B-myb in clinically advanced human renal-cell carcinomas. Int. J. Oncol. *2*, 419–423.

Sala, A., Kundu, M., Casella, I., Engelhard, A., Calabretta, B., Grasso, L., Paggi, M.G., Giordano, A., Watson, R.J., Khalili, K., et al. (1997). Activation of human B-MYB by cyclins. Proc. Natl. Acad. Sci. U. S. A. *94*, 532–536.

Salah, S., To, Y.H., Khozouz, O., Ismail, T., Yaser, S., Alnsour, A., Shahin, O., Sultan, I., Abuhijlih, R., Halalsheh, H., et al. (2020). Irinotecan and temozolomide chemotherapy in paediatric and adult populations with relapsed Ewing Sarcoma. Clin. Transl. Oncol. *In press*. *Online ahead of print*.

Saleh, M.M., Abdelrahman, T.M., Madney, Y., Mohamed, G., Shokry, A.M., and Moustafa, A.F. (2020). Multiparametric MRI with diffusion-weighted imaging in predicting response to chemotherapy in cases of osteosarcoma and Ewing's sarcoma. Br. J. Radiol. *93*, 20200257.

Samuel, G., Crow, J., Klein, J.B., Merchant, M.L., Nissen, E., Koestler, D.C., Laurence, K., Liang, X., Neville, K., Staggs, V., et al. (2020). Ewing sarcoma family of tumors-derived small extracellular vesicle proteomics identify potential clinical biomarkers. Oncotarget *11*, 2995–3012.

Sánchez-Molina, S., Figuerola-Bou, E., Blanco, E., Sánchez-Jiménez, M., Táboas, P., Gómez, S., Ballaré, C., García-Domínguez, D.J., Prada, E., Hontecillas-Prieto, L., et al. (2020). RING1B recruits EWSR1-FLI1 and cooperates in the remodeling of chromatin necessary for Ewing sarcoma tumorigenesis. Sci. Adv. *6*, eaba3058.

Sankar, S., and Lessnick, S.L. (2011). Promiscuous partnerships in Ewing's sarcoma. Cancer Genet. *204*, 351–365.

Sankar, S., Bell, R., Stephens, B., Zhuo, R., Sharma, S., Bearss, D.J., and Lessnick, S.L. (2013). Mechanism and relevance of EWS/FLI-mediated transcriptional repression in Ewing sarcoma. Oncogene *32*, 5089–5100.

Santilli, G., Schwab, R., Watson, R., Ebert, C., Aronow, B.J., and Sala, A. (2005). Temperature-dependent modification and activation of B-MYB: implications for cell survival. J. Biol. Chem. *280*, 15628–15634.

Savola, S., Klami, A., Myllykangas, S., Manara, C., Scotlandi, K., Picci, P., Knuutila, S., and Vakkila, J. (2011). High Expression of Complement Component 5 (C5) at Tumor Site Associates with Superior Survival in Ewing's Sarcoma Family of Tumour Patients. ISRN Oncol. *2011*, 168712.

Schindelin, J., Arganda-Carreras, I., Frise, E., Kaynig, V., Longair, M., Pietzsch, T., Preibisch, S., Rueden, C., Saalfeld, S., Schmid, B., et al. (2012). Fiji: an open-source platform for biological-image analysis. Nat. Methods *9*, 676–682.

Schneider, C.A., Rasband, W.S., and Eliceiri, K.W. (2012). NIH Image to ImageJ: 25 years of image analysis. Nat. Methods *9*, 671–675.

Schöffski, P., Besse, B., Gauler, T., de Jonge, M.J.A., Scambia, G., Santoro, A., Davite, C., Jannuzzo, M.G., Petroccione, A., and Delord, J.-P. (2015). Efficacy and safety of biweekly i.v. administrations of the Aurora kinase inhibitor danusertib hydrochloride in independent cohorts of patients with advanced or metastatic breast, ovarian, colorectal, pancreatic, small-cell and non-small-cell lung cancer: a multi-tumour, multi-institutional phase II study. Ann. Oncol. *26*, 598–607.

Schubert, S., Horstmann, S., Bartusel, T., and Klempnauer, K.-H. (2004). The cooperation of B-Myb with the coactivator p300 is orchestrated by cyclins A and D1. Oncogene *23*, 1392–1404.

Schwab, R., Caccamo, A., Bettuzzi, S., Anderson, J., and Sala, A. (2007). B-MYB is hypophosphorylated and resistant to degradation in neuroblastoma: implications for cell survival. Blood Cells. Mol. Dis. *39*, 263–271.

Scotlandi, K., Remondini, D., Castellani, G., Manara, M.C., Nardi, F., Cantiani, L., Francesconi, M., Mercuri, M., Caccuri, A.M., Serra, M., et al. (2009). Overcoming resistance to conventional drugs in Ewing sarcoma and identification of molecular predictors of outcome. J. Clin. Oncol. *27*, 2209–2216.

Selvanathan, S.P., Graham, G.T., Grego, A.R., Baker, T.M., Hogg, J.R., Simpson, M., Batish, M., Crompton, B., Stegmaier, K., Tomazou, E.M., et al. (2019). EWS-FLI1 modulated alternative splicing of ARID1A reveals novel oncogenic function through the BAF complex. Nucleic Acids Res. *47*, 9619–9636.

Senft, D., Leiserson, M.D.M., Ruppin, E., and Ronai, Z.A. (2017). Precision Oncology: The Road Ahead. Trends Mol. Med. *23*, 874–898.

Seong, H.-A., Manoharan, R., and Ha, H. (2011). B-MYB positively regulates serine-threonine kinase receptor-associated protein (STRAP) activity through direct interaction. J. Biol. Chem. *286*, 7439–7456.

Sheffield, N.C., Pierron, G., Klughammer, J., Datlinger, P., Schönegger, A., Schuster, M., Hadler, J., Surdez, D., Guillemot, D., Lapouble, E., et al. (2017). DNA methylation heterogeneity defines a disease spectrum in Ewing sarcoma. Nat. Med. *23*, 386–395.

Shelake, S., Sankpal, U.T., Paul Bowman, W., Wise, M., Ray, A., and Basha, R. (2017). Targeting specificity protein 1 transcription factor and survivin using tolfenamic acid for inhibiting Ewing sarcoma cell growth. Invest. New Drugs *35*, 158–165.

Shepard, J.L., Amatruda, J.F., Stern, H.M., Subramanian, A., Finkelstein, D., Ziai, J., Finley, K.R., Pfaff, K.L., Hersey, C., Zhou, Y., et al. (2005). A zebrafish bmyb mutation causes genome instability and increased cancer susceptibility. Proc. Natl. Acad. Sci. U. S. A. *102*, 13194–13199.

Shi, H., Bevier, M., Johansson, R., Grzybowska, E., Chen, B., Eyfjörd, J.E., Hamann, U., Manjer, J., Enquist, K., Henriksson, R., et al. (2011). Single nucleotide polymorphisms in the 20q13 amplicon genes in relation to breast cancer risk and clinical outcome. Breast Cancer Res. Treat. *130*, 905–916.

Shi, X., Zheng, Y., Jiang, L., Zhou, B., Yang, W., Li, L., Ding, L., Huang, M., Gery, S., Lin, D.-C., et al. (2020). EWS-FLI1 regulates and cooperates with core regulatory circuitry in Ewing sarcoma. Nucleic Acids Res. *48*, 11434–11451.

Shima, H., Tsurita, G., Wada, S., Hirohashi, Y., Yasui, H., Hayashi, H., Miyakoshi, T., Watanabe, K., Murai, A., Asanuma, H., et al. (2019). Randomized phase II trial of survivin 2B peptide vaccination for patients with HLA-A24-positive pancreatic adenocarcinoma. Cancer Sci. *110*, 2378–2385.

Shimizu, K., Ichikawa, H., Tojo, A., Kaneko, Y., Maseki, N., Hayashi, Y., Ohira, M., Asano, S., and Ohki, M. (1993). An ets-related gene, ERG, is rearranged in human myeloid leukemia with t(16;21) chromosomal translocation. Proc. Natl. Acad. Sci. U. S. A. *90*, 10280–10284.

Shin, D.H., Lee, H.W., Jeon, G.S., Lee, H.Y., Lee, K.H., and Cho, S.S. (2001). Constitutive expression of c-myb mRNA in the adult rat brain. Brain Res. *892*, 203–207.

Shukla, N., Schiffman, J., Reed, D., Davis, I.J., Womer, R.B., Lessnick, S.L., Lawlor, E.R., and COG Ewing Sarcoma Biology Committee (2013). Biomarkers in Ewing Sarcoma: The Promise and Challenge of Personalized Medicine. A Report from the Children's Oncology Group. Front. Oncol. *3*, 141.

Shulman, D.S., Klega, K., Imamovic-Tuco, A., Clapp, A., Nag, A., Thorner, A.R., Van Allen, E., Ha, G., Lessnick, S.L., Gorlick, R., et al. (2018). Detection of circulating tumour DNA is associated with inferior outcomes in Ewing sarcoma and osteosarcoma: a report from the Children's Oncology Group. Br. J. Cancer *119*, 615–621.

Sizemore, G.M., Pitarresi, J.R., Balakrishnan, S., and Ostrowski, M.C. (2017). The ETS family of oncogenic transcription factors in solid tumours. Nat. Rev. Cancer *17*, 337–351.

Soccio, R.E., Chen, E.R., Rajapurkar, S.R., Safabakhsh, P., Marinis, J.M., Dispirito, J.R., Emmett, M.J., Briggs, E.R., Fang, B., Everett, L.J., et al. (2015). Genetic Variation Determines PPARγ Function and Anti-diabetic Drug Response In Vivo. Cell *162*, 33–44.

Sorensen, P.H., Lessnick, S.L., Lopez-Terrada, D., Liu, X.F., Triche, T.J., and Denny, C.T. (1994). A second Ewing's sarcoma translocation, t(21;22), fuses the EWS gene to another ETS-family transcription factor, ERG. Nat. Genet. *6*, 146–151.

Sotoca, A.M., Prange, K.H.M., Reijnders, B., Mandoli, A., Nguyen, L.N., Stunnenberg, H.G., and Martens, J.H.A. (2016). The oncofusion protein FUS-ERG targets key hematopoietic regulators and modulates the all-trans retinoic acid signaling pathway in t(16;21) acute myeloid leukemia. Oncogene *35*, 1965–1976.

Stein, C.K., Qu, P., Epstein, J., Buros, A., Rosenthal, A., Crowley, J., Morgan, G., and Barlogie, B. (2015). Removing batch effects from purified plasma cell gene expression microarrays with modified ComBat. BMC Bioinformatics *16*, 63.

Stone, L. (2017). Prostate cancer: Mastering transcription: TMPRSS2-ERG and the cis-regulatory landscape. Nat. Rev. Urol. *14*, 579.

Stracquadanio, G., Wang, X., Wallace, M.D., Grawenda, A.M., Zhang, P., Hewitt, J., Zeron-Medina, J., Castro-Giner, F., Tomlinson, I.P., Goding, C.R., et al. (2016). The importance of p53 pathway genetics in inherited and somatic cancer genomes. Nat. Rev. Cancer *16*, 251–265.

Subramanian, A., Tamayo, P., Mootha, V.K., Mukherjee, S., Ebert, B.L., Gillette, M.A., Paulovich, A., Pomeroy, S.L., Golub, T.R., Lander, E.S., et al. (2005). Gene set enrichment analysis: a knowledge-based approach for interpreting genome-wide expression profiles. Proc. Natl. Acad. Sci. U. S. A. *102*, 15545–15550.

Tadesse, S., Caldon, E.C., Tilley, W., and Wang, S. (2019). Cyclin-Dependent Kinase 2 Inhibitors in Cancer Therapy: An Update. J. Med. Chem. *62*, 4233–4251.

Tal, A.L., Doshi, H., Parkar, F., Abraham, T., Love, C., Ye, K., Yang, R., Hoang, B., Loeb, D., Chou, A., et al. (2020). The Utility of 18FDG PET/CT Versus Bone Scan for Identification of Bone Metastases in a Pediatric Sarcoma Population and a Review of the Literature. J. Pediatr. Hematol. Oncol. *In press*. *Online ahead of print*.

Tanaka, M., Yamazaki, Y., Kanno, Y., Igarashi, K., Aisaki, K., Kanno, J., and Nakamura, T. (2014). Ewing's sarcoma precursors are highly enriched in embryonic osteochondrogenic progenitors. J. Clin. Invest. *124*, 3061–3074.

Tang, A., Gao, K., Chu, L., Zhang, R., Yang, J., and Zheng, J. (2017). Aurora kinases: novel therapy targets in cancers. Oncotarget *8*, 23937–23954.

Tanner, M.M., Grenman, S., Koul, A., Johannsson, O., Meltzer, P., Pejovic, T., Borg, A., and Isola, J.J. (2000). Frequent amplification of chromosomal region 20q12-q13 in ovarian cancer. Clin. Cancer Res. *6*, 1833–1839.

Tao, D., Pan, Y., Jiang, G., Lu, H., Zheng, S., Lin, H., and Cao, F. (2015). B-Myb regulates snail expression to promote epithelial-to-mesenchymal transition and invasion of breast cancer cell. Med. Oncol. *32*, 412.

Tarasov, K.V., Tarasova, Y.S., Tam, W.L., Riordon, D.R., Elliott, S.T., Kania, G., Li, J., Yamanaka, S., Crider, D.G., Testa, G., et al. (2008a). B-MYB is essential for normal cell cycle progression and chromosomal stability of embryonic stem cells. PloS One *3*, e2478.

Tarasov, K.V., Testa, G., Tarasova, Y.S., Kania, G., Riordon, D.R., Volkova, M., Anisimov, S.V., Wobus, A.M., and Boheler, K.R. (2008b). Linkage of pluripotent stem cell-associated transcripts to regulatory gene networks. Cells Tissues Organs *188*, 31–45.

Thakore, P.I., D'Ippolito, A.M., Song, L., Safi, A., Shivakumar, N.K., Kabadi, A.M., Reddy, T.E., Crawford, G.E., and Gersbach, C.A. (2015). Highly specific epigenome editing by CRISPR-Cas9 repressors for silencing of distal regulatory elements. Nat. Methods *12*, 1143–1149.

Tirado, O.M., Mateo-Lozano, S., and Notario, V. (2005). Roscovitine is an effective inducer of apoptosis of Ewing's sarcoma family tumor cells in vitro and in vivo. Cancer Res. *65*, 9320–9327.

Tirode, F., Laud-Duval, K., Prieur, A., Delorme, B., Charbord, P., and Delattre, O. (2007). Mesenchymal stem cell features of Ewing tumors. Cancer Cell *11*, 421–429.

Tirode, F., Surdez, D., Ma, X., Parker, M., Le Deley, M.C., Bahrami, A., Zhang, Z., Lapouble, E., Grossetête-Lalami, S., Rusch, M., et al. (2014). Genomic landscape of Ewing sarcoma defines an aggressive subtype with co-association of STAG2 and TP53 mutations. Cancer Discov. *4*, 1342–1353.

Tomazou, E.M., Sheffield, N.C., Schmidl, C., Schuster, M., Schönegger, A., Datlinger, P., Kubicek, S., Bock, C., and Kovar, H. (2015). Epigenome mapping reveals distinct modes of gene regulation and widespread enhancer reprogramming by the oncogenic fusion protein EWS-FLI1. Cell Rep. *10*, 1082–1095.

Tomlins, S.A., Rhodes, D.R., Perner, S., Dhanasekaran, S.M., Mehra, R., Sun, X.-W., Varambally, S., Cao, X., Tchinda, J., Kuefer, R., et al. (2005). Recurrent fusion of TMPRSS2 and ETS transcription factor genes in prostate cancer. Science *310*, 644–648.

Tomlins, S.A., Laxman, B., Dhanasekaran, S.M., Helgeson, B.E., Cao, X., Morris, D.S., Menon, A., Jing, X., Cao, Q., Han, B., et al. (2007). Distinct classes of chromosomal rearrangements create oncogenic ETS gene fusions in prostate cancer. Nature *448*, 595–599.

Toretsky, J.A., Steinberg, S.M., Thakar, M., Counts, D., Pironis, B., Parente, C., Eskenazi, A., Helman, L., and Wexler, L.H. (2001). Insulin-like growth factor type 1 (IGF-1) and IGF binding protein-3 in patients with Ewing sarcoma family of tumors. Cancer *92*, 2941–2947.

Toscani, A., Mettus, R.V., Coupland, R., Simpkins, H., Litvin, J., Orth, J., Hatton, K.S., and Reddy, E.P. (1997). Arrest of spermatogenesis and defective breast development in mice lacking A-myb. Nature *386*, 713–717.

Trapnell, C., Pachter, L., and Salzberg, S.L. (2009). TopHat: discovering splice junctions with RNA-Seq. Bioinformatics *25*, 1105–1111.

Trauth, K., Mutschler, B., Jenkins, N.A., Gilbert, D.J., Copeland, N.G., and Klempnauer, K.H. (1994). Mouse A-myb encodes a trans-activator and is expressed in mitotically active cells of the developing central nervous system, adult testis and B lymphocytes. EMBO J. *13*, 5994–6005.

Urano, F., Umezawa, A., Yabe, H., Hong, W., Yoshida, K., Fujinaga, K., and Hata, J. (1998). Molecular analysis of Ewing's sarcoma: another fusion gene, EWS-E1AF, available for diagnosis. Jpn. J. Cancer Res. *89*, 703–711.

Valery, P.C., McWhirter, W., Sleigh, A., Williams, G., and Bain, C. (2002). Farm exposures, parental occupation, and risk of Ewing's sarcoma in Australia: a national case-control study. Cancer Causes Control *13*, 263–270.

Vogelstein, B., Papadopoulos, N., Velculescu, V.E., Zhou, S., Diaz, L.A., and Kinzler, K.W. (2013). Cancer genome landscapes. Science *339*, 1546–1558.

Volchenboum, S.L., Andrade, J., Huang, L., Barkauskas, D.A., Krailo, M., Womer, R.B., Ranft, A., Potratz, J., Dirksen, U., Triche, T.J., et al. (2015). Gene Expression Profiling of Ewing Sarcoma Tumors Reveals the Prognostic Importance of Tumor-Stromal Interactions: A Report from the Children's Oncology Group. J. Pathol. Clin. Res. *1*, 83–94.

Völker, T., Denecke, T., Steffen, I., Misch, D., Schönberger, S., Plotkin, M., Ruf, J., Furth, C., Stöver, B., Hautzel, H., et al. (2007). Positron emission tomography for staging of pediatric sarcoma patients: results of a prospective multicenter trial. J. Clin. Oncol. *25*, 5435–5441.

Vrana, J.A., Decker, R.H., Johnson, C.R., Wang, Z., Jarvis, W.D., Richon, V.M., Ehinger, M., Fisher, P.B., and Grant, S. (1999). Induction of apoptosis in U937 human leukemia cells by suberoylanilide hydroxamic acid (SAHA) proceeds through pathways that are regulated by Bcl-2/Bcl-XL, c-Jun, and p21CIP1, but independent of p53. Oncogene *18*, 7016–7025.

Vu, V., Verster, A.J., Schertzberg, M., Chuluunbaatar, T., Spensley, M., Pajkic, D., Hart, G.T., Moffat, J., and Fraser, A.G. (2015). Natural Variation in Gene Expression Modulates the Severity of Mutant Phenotypes. Cell *162*, 391–402.

Wagner, L.M., McAllister, N., Goldsby, R.E., Rausen, A.R., McNall-Knapp, R.Y., McCarville, M.B., and Albritton, K. (2007). Temozolomide and intravenous irinotecan for treatment of advanced Ewing sarcoma. Pediatr. Blood Cancer *48*, 132–139.

Wang, S., Hwang, E.E., Guha, R., O'Neill, A.F., Melong, N., Veinotte, C.J., Conway Saur, A., Wuerthele, K., Shen, M., McKnight, C., et al. (2019). High-throughput Chemical Screening Identifies Focal Adhesion Kinase and Aurora Kinase B Inhibition as a Synergistic Treatment Combination in Ewing Sarcoma. Clin. Cancer Res. *25*, 4552–4566.

Wang, Z., Liu, P., Inuzuka, H., and Wei, W. (2014). Roles of F-box proteins in cancer. Nat. Rev. Cancer *14*, 233–247.

Ward, C., Volpe, G., Cauchy, P., Ptasinska, A., Almaghrabi, R., Blakemore, D., Nafria, M., Kestner, D., Frampton, J., Murphy, G., et al. (2018). Fine-Tuning Mybl2 Is Required for Proper Mesenchymal-to-Epithelial Transition during Somatic Reprogramming. Cell Rep. *24*, 1496-1511.e8.

Watson, S., Perrin, V., Guillemot, D., Reynaud, S., Coindre, J.-M., Karanian, M., Guinebretière, J.-M., Freneaux, P., Loarer, F.L., Bouvet, M., et al. (2018). Transcriptomic definition of molecular subgroups of small round cell sarcomas. J. Pathol. *245*, 29–40.

Werwein, E., Cibis, H., Hess, D., and Klempnauer, K.-H. (2019). Activation of the oncogenic transcription factor B-Myb via multisite phosphorylation and prolyl cis/trans isomerization. Nucleic Acids Res. *47*, 103–121.

Whelan, J., Le Deley, M.-C., Dirksen, U., Judson, I.R., Hawkins, D.S., Van Den Berg, H., Ladenstein, R., Kruseova, J., Ranft, A., Amler, S., et al. (2016). Efficacy of busulfan-melphalan high dose chemotherapy consolidation (BuMel) in localized high-risk Ewing sarcoma (ES): Results of EURO-EWING 99-R2 randomized trial (EE99R2Loc). J. Clin. Oncol. *34*, 11000–11000.

Whelan, J., Le Deley, M., Dirksen, U., Le Teuff, G., Brennan, B., Gaspar, N., Hawkins, D., Amler, S., Bauer, S., Bielack, S., et al. (2018). High-Dose Chemotherapy and Blood Autologous Stem-Cell Rescue Compared With Standard Chemotherapy in Localized High-Risk Ewing Sarcoma: Results of Euro-E.W.I.N.G.99 and Ewing-2008. J. Clin. Oncol. *36*, JCO2018782516.

Widhe, B., and Widhe, T. (2000). Initial symptoms and clinical features in osteosarcoma and Ewing sarcoma. J. Bone Joint Surg. Am. *82*, 667–674.

Willems, T., Zielinski, D., Yuan, J., Gordon, A., Gymrek, M., and Erlich, Y. (2017). Genome-wide profiling of heritable and de novo STR variations. Nat. Methods *14*, 590–592.

Worch, J., Cyrus, J., Goldsby, R., Matthay, K.K., Neuhaus, J., and DuBois, S.G. (2011). Racial differences in the incidence of mesenchymal tumors associated with EWSR1 translocation. Cancer Epidemiol. Biomarkers Prev. *20*, 449–453.

Wu, Q., Kirschmeier, P., Hockenberry, T., Yang, T.-Y., Brassard, D.L., Wang, L., McClanahan, T., Black, S., Rizzi, G., Musco, M.L., et al. (2002). Transcriptional regulation during p21WAF1/CIP1-induced apoptosis in human ovarian cancer cells. J. Biol. Chem. *277*, 36329–36337.

Wu, Z., Huang, X., Huang, X., Zou, Q., and Guo, Y. (2013). The inhibitory role of Mir-29 in growth of breast cancer cells. J. Exp. Clin. Cancer Res. *32*, 98.

Xiao, M., and Li, W. (2015). Recent Advances on Small-Molecule Survivin Inhibitors. Curr. Med. Chem. *22*, 1136–1146.

Xue, R., Lewis, V.O., Moon, B.S., and Lin, P.P. (2019). Local recurrence of Ewing sarcoma: Is wide excision an acceptable treatment? J. Surg. Oncol. *120*, 746–752.

Yamauchi, T., Ishidao, T., Nomura, T., Shinagawa, T., Tanaka, Y., Yonemura, S., and Ishii, S. (2008). A B-Myb complex containing clathrin and filamin is required for mitotic spindle function. EMBO J. *27*, 1852–1862.

Yang, L., Embree, L.J., and Hickstein, D.D. (2000). TLS-ERG leukemia fusion protein inhibits RNA splicing mediated by serine-arginine proteins. Mol. Cell. Biol. *20*, 3345–3354.

Yang, X., Nakao, Y., Pater, M.M., Tang, S.C., and Pater, A. (1997). Expression of cellular genes in HPV16-immortalized and cigarette smoke condensate-transformed human endocervical cells. J. Cell. Biochem. *66*, 309–321.

Yoshihara, K., Shahmoradgoli, M., Martínez, E., Vegesna, R., Kim, H., Torres-Garcia, W., Treviño, V., Shen, H., Laird, P.W., Levine, D.A., et al. (2013). Inferring tumour purity and stromal and immune cell admixture from expression data. Nat. Commun. *4*, 2612.

Yu, J., Yu, J., Mani, R.-S., Cao, Q., Brenner, C.J., Cao, X., Wang, X., Wu, L., Li, J., Hu, M., et al. (2010). An integrated network of androgen receptor, polycomb, and TMPRSS2-ERG gene fusions in prostate cancer progression. Cancer Cell *17*, 443–454.

Yu, Z., Kim, J., He, L., Creighton, C.J., Gunaratne, P.H., Hawkins, S.M., and Matzuk, M.M. (2014). Functional analysis of miR-34c as a putative tumor suppressor in high-grade serous ovarian cancer. Biol. Reprod. *91*, 113.

Yuan, J., Zhang, Y., Sheng, Y., Fu, X., Cheng, H., and Zhou, R. (2015). MYBL2 guides autophagy suppressor VDAC2 in the developing ovary to inhibit autophagy through a complex of VDAC2-BECN1-BCL2L1 in mammals. Autophagy *11*, 1081–1098.

Zauli, G., Voltan, R., di Iasio, M.G., Bosco, R., Melloni, E., Sana, M.E., and Secchiero, P. (2011). miR-34a induces the downregulation of both E2F1 and B-Myb oncogenes in leukemic cells. Clin. Cancer Res. *17*, 2712–2724.

Zerkalenkova, E., Panfyorova, A., Kazakova, A., Baryshev, P., Shelihova, L., Kalinina, I., Novichkova, G., Maschan, M., Maschan, A., and Olshanskaya, Y. (2018). Molecular characteristic of acute leukemias with t(16;21)/FUS-ERG. Ann. Hematol. *97*, 977–988.

Zhan, M., Riordon, D.R., Yan, B., Tarasova, Y.S., Bruweleit, S., Tarasov, K.V., Li, R.A., Wersto, R.P., and Boheler, K.R. (2012). The B-MYB transcriptional network guides cell cycle progression and fate decisions to sustain self-renewal and the identity of pluripotent stem cells. PloS One *7*, e42350.

Zhang, B., Chen, W., and Roman, A. (2006). The E7 proteins of low- and high-risk human papillomaviruses share the ability to target the pRB family member p130 for degradation. Proc. Natl. Acad. Sci. U. S. A. *103*, 437–442.

Zhang, P., Samuel, G., Crow, J., Godwin, A.K., and Zeng, Y. (2018). Molecular assessment of circulating exosomes toward liquid biopsy diagnosis of Ewing sarcoma family of tumors. Transl. Res. *201*, 136–153.

Zhang, Y., Liu, T., Meyer, C.A., Eeckhoute, J., Johnson, D.S., Bernstein, B.E., Nusbaum, C., Myers, R.M., Brown, M., Li, W., et al. (2008). Model-based analysis of ChIP-Seq (MACS). Genome Biol. *9*, R137.

Zhu, W., Giangrande, P.H., and Nevins, J.R. (2004). E2Fs link the control of G1/S and G2/M transcription. EMBO J. *23*, 4615–4626.

Zorbas, M., Sicurella, C., Bertoncello, I., Venter, D., Ellis, S., Mucenski, M.L., and Ramsay, R.G. (1999). c-Myb is critical for murine colon development. Oncogene *18*, 5821–5830.

Zucman, J., Melot, T., Desmaze, C., Ghysdael, J., Plougastel, B., Peter, M., Zucker, J.M., Triche, T.J., Sheer, D., and Turc-Carel, C. (1993). Combinatorial generation of variable fusion proteins in the Ewing family of tumours. EMBO J. *12*, 4481–4487.

9. APPENDIX

9.1. Supplementary figures and tables

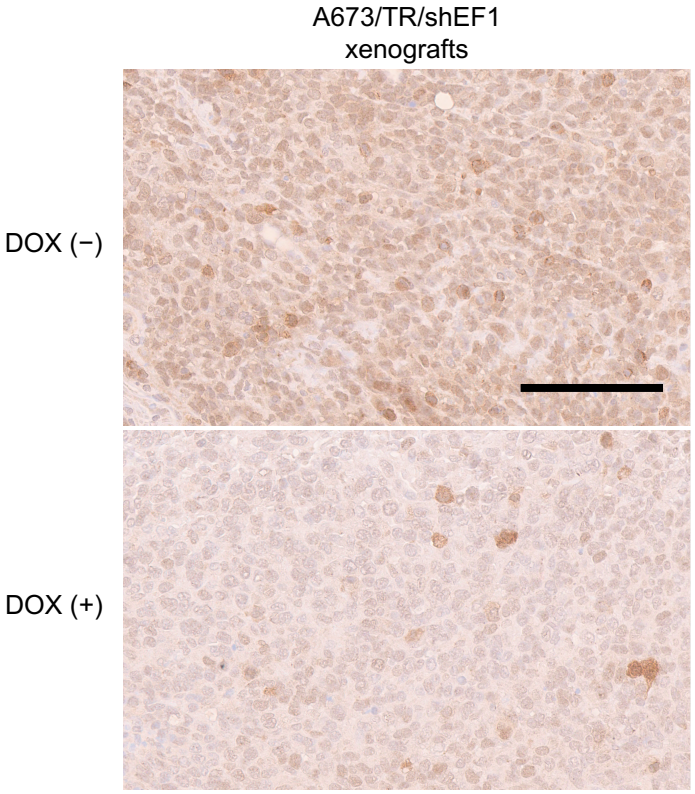

Supplementary Figure 1: Figure 13F as a larger scale histological image. Representative p-MYBL2 immunohistochemistry (IHC) micrographs of xenografts described in Figure 13 ‘(E)‘. Scale bar represents 100µm. Modified from Musa et al., 2019.

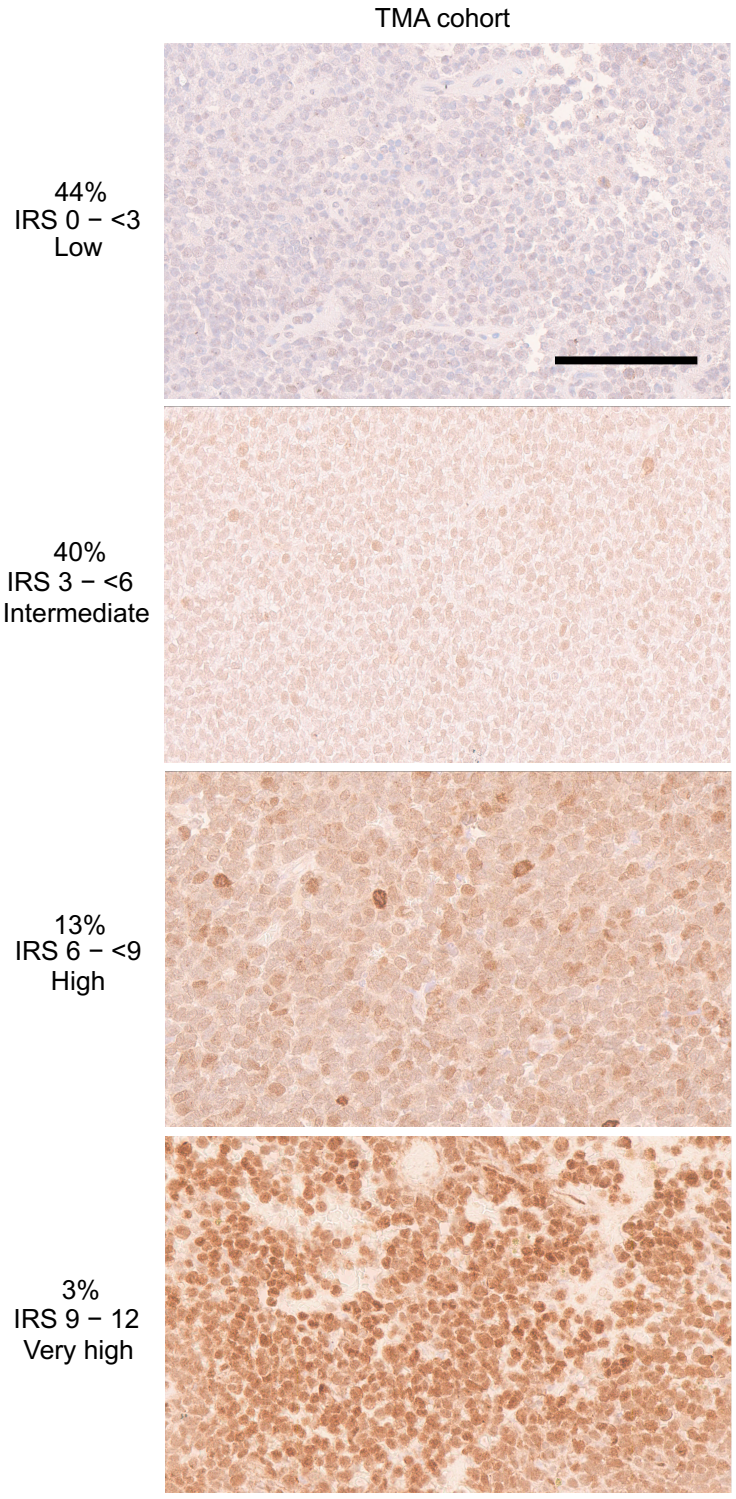

Supplementary Figure 2: Figure 15D as a larger scale histological image. Representative micrographs of p-MYBL2 immunohistochemistry (IHC) performed on a tissue microarray (TMA) including 208 primary EwS. Scale bar represents 100µm. Modified from Musa et al., 2019.

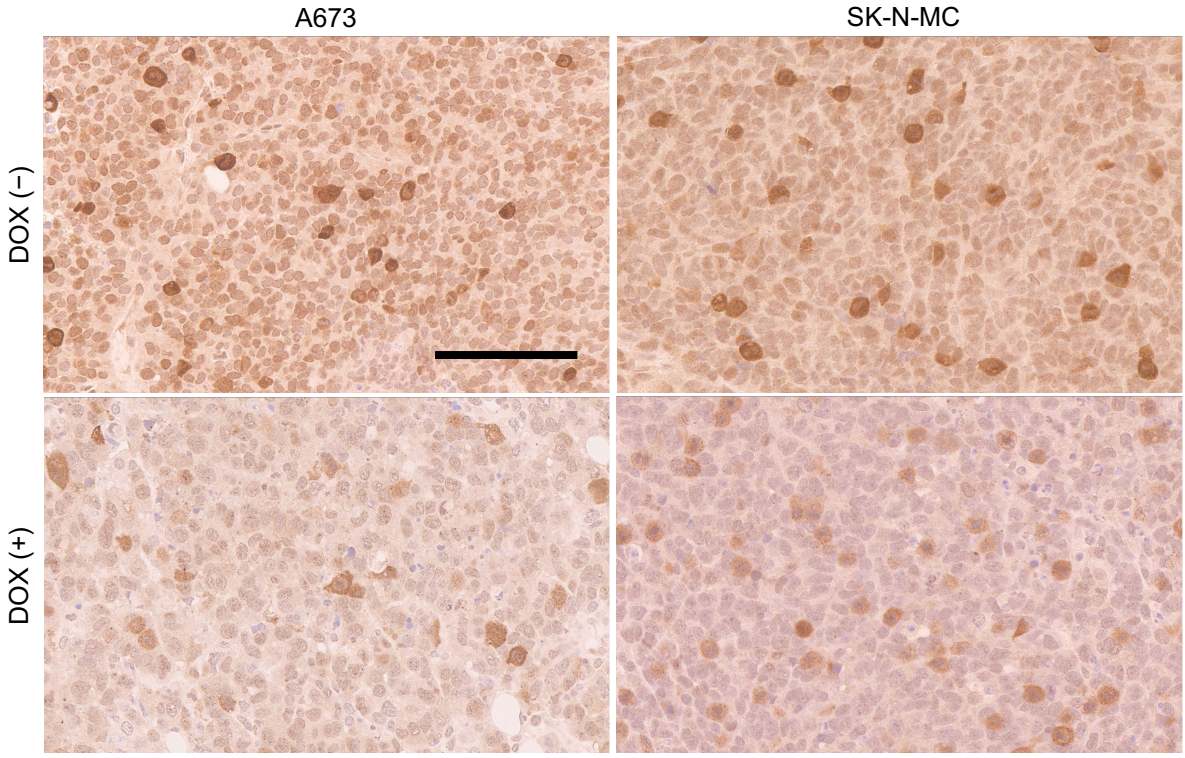

Supplementary Figure 3: Figure 17C as a larger scale histological image. Representative p-MYBL2 immunohistochemistry (IHC) micrographs of A673 and SK-N-MC xenografts containing a DOX-inducible MYBL2-targeting shRNA, whereby mice were treated either with or without DOX addition to the drinking water. Scale bar represents 100µm. Modified from Musa et al., 2019.

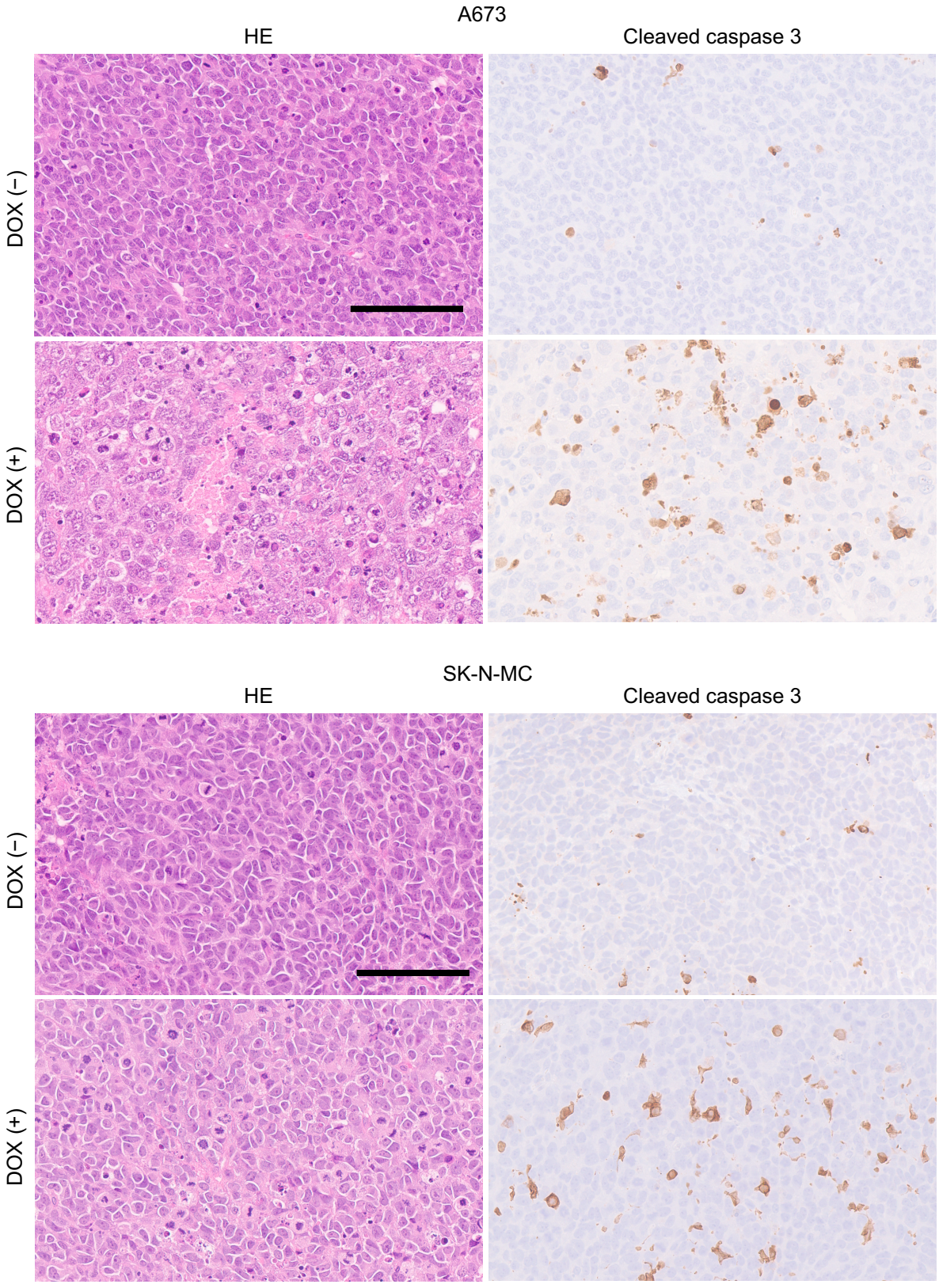

Supplementary Figure 4: Figure 17E as a larger scale histological image. Representative micrographs of hematoxylin and eosin (HE) staining and cleaved caspase 3 (CC3) immunohistochemistry (IHC) of cell line xenografts as described in Figure 17 '(C)'. Scale bar represents 100µm. Modified from Musa et al., 2019.

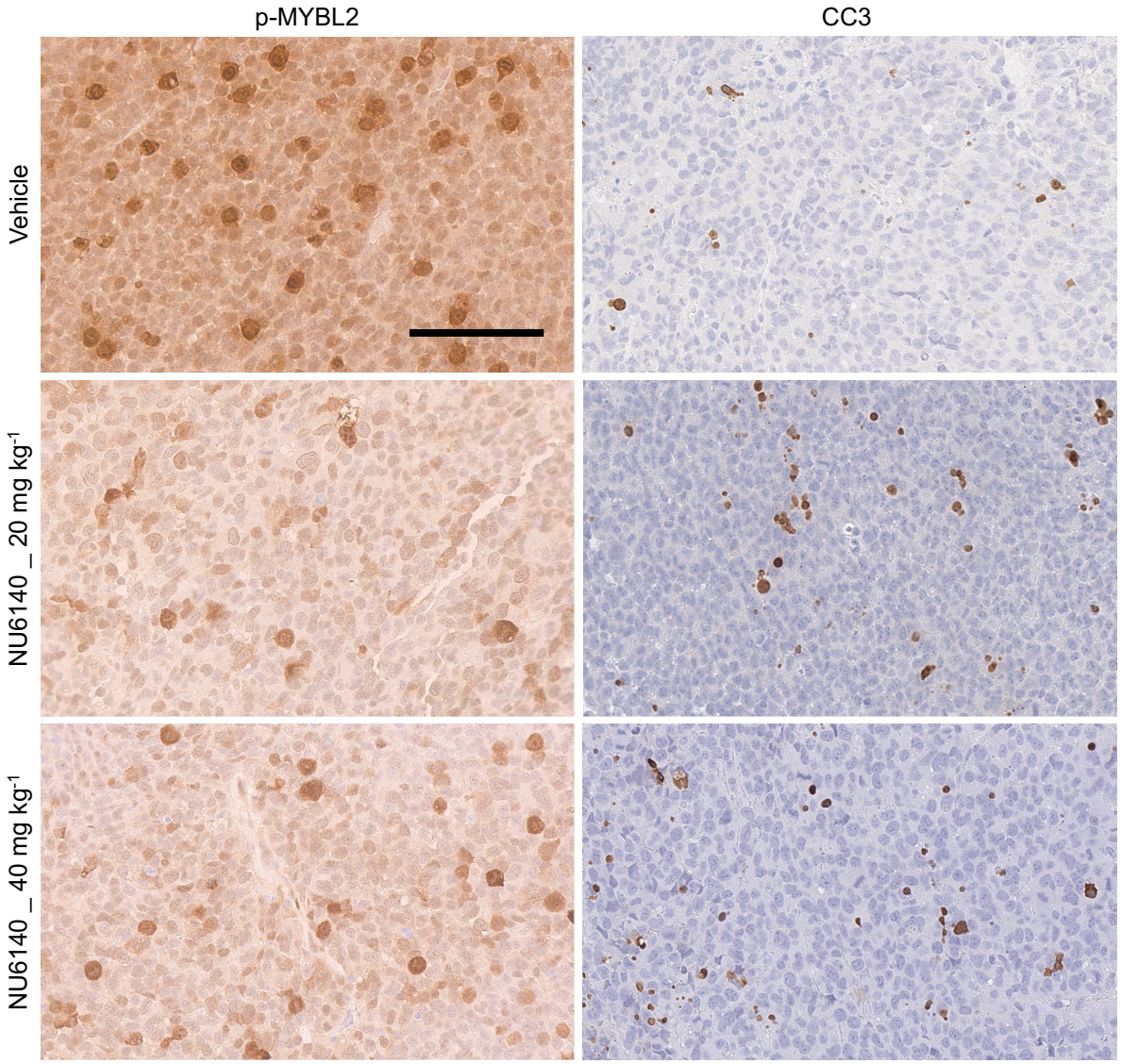

Supplementary Figure 5: Figure 21C as a larger scale histological image. Representative micrographs of p-MYBL2 and cleaved caspase 3 (CC3) immunohistochemistry (IHC) for each treatment group as described in Figure 21 '(A)'. Scale bar represents 100µm. Modified from Musa et al., 2019.

Entrez ID	Gene symbol	FC (log2)	*P* value	Bonferroni
55771	*PRR11*	-1.715	2.453E-07	1.045E-04
80119	*PIF1*	-2.415	6.591E-07	2.808E-04
NA	*CTD-2510F5.4*	-1.821	8.231E-07	3.507E-04
10787	*NCKAP1*	-1.613	8.734E-07	3.721E-04
100129482	*ZNF37BP*	1.514	1.202E-06	5.120E-04
400954	*EML6*	2.064	2.050E-06	8.733E-04
729533	*FAM72A*	-1.589	2.464E-06	0.001
1789	*DNMT3B*	-1.691	3.639E-06	0.002
84722	*PSRC1*	-1.628	4.253E-06	0.002
216	*ALDH1A1*	1.983	4.936E-06	0.002
332	*BIRC5*	-2.068	5.264E-06	0.002
25915	*NDUFAF3*	-1.780	5.299E-06	0.002
607	*BCL9*	-1.610	5.378E-06	0.002
55815	*TSNAXIP1*	1.743	5.598E-06	0.002
127933	*UHMK1*	1.840	5.767E-06	0.002
6907	*TBL1X*	-1.638	6.341E-06	0.003
150468	*CKAP2L*	-1.846	6.933E-06	0.003
7804	*LRP8*	-1.919	7.146E-06	0.003
5501	*PPP1CC*	-1.821	7.451E-06	0.003
55765	*C1orf106*	1.665	8.160E-06	0.003
1033	*CDKN3*	-1.942	8.296E-06	0.004
148534	*TMEM56*	1.598	9.019E-06	0.004
144193	*AMDHD1*	1.779	9.071E-06	0.004
653820	*FAM72B*	-1.660	1.261E-05	0.005
8804	*CREG1*	1.692	1.280E-05	0.005
192683	*SCAMP5*	2.647	1.307E-05	0.006
79745	*CLIP4*	1.695	1.383E-05	0.006
10097	*ACTR2*	-1.618	1.684E-05	0.007
94030	*LRRC4B*	-1.834	1.712E-05	0.007
220002	*CYBASC3*	1.908	1.906E-05	0.008
5873	*RAB27A*	1.566	2.190E-05	0.009
154743	*C7orf60*	1.525	2.639E-05	0.011
388963	*C2orf81*	1.548	2.711E-05	0.012
10112	*KIF20A*	-1.776	2.855E-05	0.012
80321	*CEP70*	-1.762	3.138E-05	0.013
1191	*CLU*	1.923	3.222E-05	0.014
899	*CCNF*	-1.601	3.232E-05	0.014
90139	*TSPAN18*	-1.508	3.325E-05	0.014
100131193	*KIAA1984-AS1*	2.029	3.421E-05	0.015
140609	*NEK7*	1.789	3.443E-05	0.015
64753	*CCDC136*	2.445	3.709E-05	0.016
6674	*SPAG1*	2.132	4.092E-05	0.017
54956	*PARP16*	-1.626	4.216E-05	0.018
10023	*FRAT1*	2.107	4.483E-05	0.019
3113	*HLA-DPA1*	2.028	4.705E-05	0.020
127253	*TYW3*	1.930	4.764E-05	0.020
728568	*C12orf73*	1.851	4.834E-05	0.021

54813	*KLHL28*	1.745	4.932E-05	0.021
9586	*CREB5*	2.583	4.965E-05	0.021
55819	*RNF130*	-1.704	4.989E-05	0.021
92340	*C17orf72*	1.750	5.308E-05	0.023
283987	*HID1*	2.559	5.651E-05	0.024
NA	*RP5-1180C10.2*	1.628	5.652E-05	0.024
340533	*KIAA2022*	-1.788	5.758E-05	0.025
4605	*MYBL2*	-2.629	5.891E-05	0.025
9212	*AURKB*	-1.721	5.941E-05	0.025
253558	*LCLAT1*	1.701	6.052E-05	0.026
414918	*DENND6B*	2.169	6.061E-05	0.026
4288	*MKI67*	-1.792	6.126E-05	0.026
728833	*FAM72D*	-1.548	6.506E-05	0.028
283431	*GAS2L3*	-2.057	6.507E-05	0.028
255101	*CCDC108*	5.359	6.726E-05	0.029
26258	*BLOC1S6*	1.534	7.238E-05	0.031
124976	*SPNS2*	2.380	7.334E-05	0.031
27250	*PDCD4*	2.022	7.457E-05	0.032
3679	*ITGA7*	1.877	7.581E-05	0.032
56204	*FAM214A*	1.595	7.740E-05	0.033
373	*TRIM23*	1.738	8.433E-05	0.036
55800	*SCN3B*	1.695	8.938E-05	0.038
10644	*IGF2BP2*	-1.648	9.495E-05	0.040
130612	*TMEM198*	3.294	9.500E-05	0.040
374986	*FAM73A*	2.166	9.666E-05	0.041
196500	*PIANP*	1.660	9.880E-05	0.042
114821	*SCAND3*	1.516	1.064E-04	0.045
NA	*CTD-3116E22.4*	1.654	1.128E-04	0.048
387856	*C12orf68*	1.865	1.166E-04	0.050

Supplementary Table 1: Most significant differentially expressed genes (DEGs) upon MYBL2 knockdown in A673, SK-N-MC, and RDES EwS cells as determined by RNA sequencing (RNA-seq). RNA-seq was performed with (siMYBL2_1) or without (siControl) MYBL2 knockdown in technical triplicates per cell line. Most significant DEGs were defined by a mean log2 fold change (FC) |≥1.5| and a *P* value < 0.05 (Bonferroni-corrected). Data from Musa et al., 2019.

Entrez ID	Gene Symbol	$r_{Pearson}$	*P* value	Bonferroni
4605	*MYBL2*	1.000	0.000E+00	0.000E+00
899	*CCNF*	0.790	1.039E-36	2.007E-32
332	*BIRC5*	0.776	1.237E-34	2.389E-30
9212	*AURKB*	0.747	6.825E-31	1.318E-26
4288	*MKI67*	0.672	3.501E-23	6.761E-19
55771	*PRR11*	0.649	2.983E-21	5.761E-17
10112	*KIF20A*	0.638	2.321E-20	4.483E-16
150468	*CKAP2L*	0.571	1.009E-15	1.949E-11
27250	*PDCD4*	-0.528	2.585E-13	4.992E-09
84722	*PSRC1*	0.512	1.753E-12	3.386E-08
1033	*CDKN3*	0.493	1.559E-11	3.011E-07
56204	*FAM214A*	-0.481	5.519E-11	1.066E-06
80119	*PIF1*	0.436	4.425E-09	8.546E-05
79745	*CLIP4*	-0.354	2.961E-06	0.057
374986	*FAM73A*	-0.347	4.718E-06	0.091
7804	*LRP8*	0.337	8.741E-06	0.169
414918	*DENND6B*	-0.333	1.172E-05	0.226
5501	*PPP1CC*	0.324	2.010E-05	0.388
6907	*TBL1X*	0.321	2.460E-05	0.475
54813	*KLHL28*	-0.299	8.912E-05	1.000
253558	*LCLAT1*	0.290	1.469E-04	1.000
10097	*ACTR2*	0.267	5.088E-04	1.000
728568	*C12orf73*	0.263	6.326E-04	1.000
196500	*PIANP*	0.235	0.002	1.000
100129482	*ZNF37BP*	-0.234	0.002	1.000
283431	*GAS2L3*	0.227	0.003	1.000
124976	*SPNS2*	0.196	0.011	1.000
127933	*UHMK1*	0.173	0.026	1.000
1789	*DNMT3B*	0.160	0.039	1.000
9586	*CREB5*	0.149	0.056	1.000
80321	*CEP70*	-0.137	0.078	1.000
26258	*BLOC1S6*	-0.132	0.090	1.000
10644	*IGF2BP2*	0.117	0.133	1.000
192683	*SCAMP5*	0.116	0.136	1.000
54956	*PARP16*	0.115	0.141	1.000
127253	*TYW3*	0.112	0.150	1.000
10787	*NCKAP1*	-0.112	0.151	1.000
90139	*TSPAN18*	-0.104	0.183	1.000
55819	*RNF130*	-0.087	0.266	1.000
607	*BCL9*	0.086	0.270	1.000
140609	*NEK7*	-0.084	0.282	1.000
8804	*CREG1*	-0.083	0.290	1.000
64753	*CCDC136*	0.078	0.320	1.000
148534	*TMEM56*	0.061	0.435	1.000
1191	*CLU*	-0.037	0.640	1.000
400954	*EML6*	0.013	0.867	1.000

Supplementary Table 2: Correlation of expression of genes in **Suppl.Tab.1** exhibiting MYBL2 promoter binding with *MYBL2* expression in microarray data of 166 primary EwS. Data from Musa et al., 2019.

Entrez ID	Gene symbol	*P* value
27250	*PDCD4*	2.057E-04
899	*CCNF*	4.009E-04
4605	*MYBL2*	0.001
55771	*PRR11*	0.002
54813	*KLHL28*	0.002
56204	*FAM214A*	0.005
192683	*SCAMP5*	0.006
332	*BIRC5*	0.008
84722	*PSRC1*	0.016
374986	*FAM73A*	0.016
9212	*AURKB*	0.024
9586	*CREB5*	0.026
10112	*KIF20A*	0.033
6907	*TBL1X*	0.035
79745	*CLIP4*	0.042
124976	*SPNS2*	0.046
4288	*MKI67*	0.048
414918	*DENND6B*	0.061
80119	*PIF1*	0.065
1191	*CLU*	0.070
10787	*NCKAP1*	0.081
7804	*LRP8*	0.092
150468	*CKAP2L*	0.097
5501	*PPP1CC*	0.102
10097	*ACTR2*	0.116
54956	*PARP16*	0.120
10644	*IGF2BP2*	0.169
55819	*RNF130*	0.213
8804	*CREG1*	0.284
90139	*TSPAN18*	0.307
196500	*PIANP*	0.347
607	*BCL9*	0.396
100129482	*ZNF37BP*	0.507
1033	*CDKN3*	0.556
127253	*TYW3*	0.583
400954	*EML6*	0.593
140609	*NEK7*	0.595
728568	*c12orf73*	0.644
253558	*LCLAT1*	0.672
80321	*CEP70*	0.690
283431	*GAS2L3*	0.703
26258	*BLOC1S6*	0.724
148534	*TMEM56*	0.817
127933	*UHMK1*	0.828
64753	*CCDC136*	0.841
1789	*DNMT3B*	0.865

Supplementary Table 3: Association of genes in **Suppl.Tab.2** with overall survival using the described dataset with matched clinical data (stratification: median gene expression). Data from Musa et al., 2019.

9.2. List of figures and tables

9.3. List of abbreviations

^{18}F-FDG-PET	^{18}F-fluorodeoxyglucose positron-emission tomography
AML	Acute myeloid leukemia
AP	Alkaline phosphatase
ATCC	American Type Culture Collection
ATP	Adenosine triphosphate
ATRA	All-trans retinoic acid
AYA	Adolescents and young adults
BAF (complex)	BRG1- or HBRM-associated factors chromatin remodeling complex
BCS	Body Condition Score
bp	Base pair(s)
CC3	Cleaved caspase 3
CDF	Chip description file
CDK	Cyclin-dependent kinase
cDNA	Complementary DNA
C. elegans	Caenorhabditis elegans
CFA	Colony formation assay
ChIP-seq	Chromatin immunoprecipitation and DNA sequencing
CHR	Cell cycle genes homology region
CNA	Copy-number alteration
COG	Children’s Oncology Group
CPC	Chromosomal passenger complex
CRISPR	Clustered regularly interspaced short palindromic repeats
CRISPRi	Clustered regularly interspaced short palindromic repeats interference
CRP	C-reactive protein
CRPC	Castrate-resistant prostate cancer
CT	Computed tomography
dCas9	DNAse-dead Cas9
DEG	Differentially expressed genes
DLBCL	Diffuse large B-cell lymphoma
DMSO	Dimethyl sulfoxide
DNA	Deoxyribonucleic acid
DNAse-seq	DNase I hypersensitive sites sequencing
dNTP	Deoxynucleoside triphosphate
dTTP	Deoxythymidine triphosphate
dUTP	Deoxyuridine triphosphate

DOX	Doxycycline
DREAM (complex)	Dimerization partner, RB-like proteins, E2F, and Multi-vulval class B complex
DSMZ	German Collection of Microorganisms and Cell lines
EDTA	Ethylenediaminetetraacetic acid
EGA	European Genome-phenome Archive
EMBL	European Molecular Biology Laboratory
EMT	Epithelial-to-mesenchymal transition
ER	Estrogen receptor
ESC	Embryonic stem cell(s)
ESR	Erythrocyte sedimentation rate
EtBr	Ethidium bromide
EwS	Ewing sarcoma
eQTL	Expression quantitative trait loci
FAB (classification)	French-American-British (classification)
FBS	FOXM1 binding site
FC	Fold change
FCS	Fetal calf serum
FDR	False discovery rate
FFPE	Formalin-fixed and paraffin-embedded
FISH	Fluorescence in-situ hybridization
FITC	Fluorescein isothiocyanate
FSC	Forward scatter
FSC-A	Forward scatter area
FSC-H	Forward scatter height
GEO	Gene expression omnibus
gRNA	Guide RNA
GSE	Genetic suppressor element
GSEA	Gene set enrichment analysis
GWAS	Genome-wide association study
HDAC	Histone deacetylase
HE	Hematoxylin and eosin
hg19	Human (reference) genome 19
HipSTR	Haplotype inference and phasing for Short Tandem Repeats
HPF	High-power field
HPLC	High performance liquid chromatography
HPV	Human papillomavirus
HRP	Horseradish peroxidase

HSC	Hematopoietic stem cell(s)
ICGC	International Cancer Genome Consortium
IAP (protein family)	Inhibitor of apoptosis (protein family)
IC50	Half maximal inhibitory concentration
IHC	Immunohistochemistry
IRS	Immune Reactive Score
IL-2	Interleukin 2
i.p.	Intraperitoneal
kb	Kilobase(s)
KRAB	Krüppel associated box
LB (medium)	Lysogeny broth (medium)
LDEV	Lactate dehydrogenase elevating virus
LDH	Lactate dehydrogenase
MBS	MYB binding site
MEM	Minimum Essential Medium
miRNA	Micro RNA
MRI	Magnet resonance imaging
mRNA	Messenger RNA
mSat	Microsatellite
MSC	Mesenchymal stem cell(s)
NA	Not available/applicable
NES	Normalized Enrichment Score
NGF	Nerve growth factor
NGS	Next-generation sequencing
NIH	National Institutes of Health
NSCLC	Non-small cell lung cancer
NSG	NOD scid gamma
NuRD	Nucleosome remodeling and deacetylase complex
OS	Overall survival
PAS	Periodic acid-Schiff
PBS	Phosphate-buffered saline
PCR	Polymerase chain reaction
PDX	Patient-derived xenograft
PET	Positron-emission tomography
PFS	Progression-free survival
PI	Propidium iodide
PI-A	Propidium iodide area

PI-H	Propidium iodide height
PNET	Primitive neuroectodermal tumor
pPNET	Peripheral primitive neuroectodermal tumor
pRL (vector)	pGL3-Rluc (vector)
qRT-PCR	Quantitative real-time polymerase chain reaction
REB	Research Ethics Board
RGB	Red-green-blue
RIPA (buffer)	Radioimmunoprecipitation assay (buffer)
RMA	Robust Multi-array Average
RNA	Ribonucleic acid
RNAi	RNA interference
rpm	Rotations per minute
RPMI (medium)	Roswell Park Memorial Institute (medium)
s.c.	Subcutaneous
SEM	Standard error of the mean
SOC (medium)	Super Optimal broth with Catabolite repression (medium)
SSC	Side scatter
SSC-A	Side scatter area
siRNA	Small interfering RNA
shRNA	Short hairpin RNA
shCtr	shControl
shMY_4	shMYBL2_4
shMY_6	shMYBL2_6
SNP	Single nucleotide polymorphism(s)
STR	Short tandem repeat
TAE (buffer)	TRIS, acetic acid, and EDTA (buffer)
TB	Trypan blue
TCGA	The Cancer Genome Atlas
TMA	Tissue microarray(s)
TRIS	Tris(hydroxymethyl)aminomethane
UCSC	University of California Santa Cruz
UDG	Uracil-DNA Glycosylase
UV	Ultraviolet
WCE	Whole-cell extract
WGS	Whole genome sequencing
WHO	World Health Organization
WLI	Whole-lung irradiation

10. ACKNOWLEDGEMENTS

I would like to express my deepest and sincere gratitude to my supervisor and mentor Prof. Thomas Grünewald, principal investigator of the Max-Eder Research Group for Pediatric Sarcoma Biology at the Institute of Pathology of the LMU Munich, for guidance and support throughout the years I spent in his laboratory to accomplish this work. His tireless passion for science has been a great inspiration for me, and without his support, it would have not been possible to reach many of the achievements of the recent years.

I want to thank Prof. Thomas Kirchner, director of the Institute of Pathology of the LMU Munich, for giving me the possibility and infrastructure to perform my work in his institute.

I would like to thank the Kind Philipp Foundation and the Rudolf und Brigitte Zenner Foundation for financial support.

I am very grateful for the scientific input and all contributions from every collaborator during the process of conducting and publishing the study mainly underlying this thesis.

I thank all my colleagues from our group for their continuous scientific and social support over the last years. In this regard, I especially thank Dr. Martin Orth, Dr. Maximilian Knott, and Tilman Hölting for their sincerity and friendship.

Finally, I want to thank my family to whom this thesis is dedicated: My mother, Ulrike Musa, my sister, Livia Musa, my grandmother Anna Elisabeth Müller, my grandaunt Margard Emma Lason, for every encouraging word and their love throughout the ups and downs of especially the recent years, and my father, Dr. Khalil Musa, who sadly cannot witness my graduation anymore, for having been a father that helped me to understand who I am and what I want to become.

11. PUBLICATIONS UNDERLYING THIS THESIS

11.1. Articles (peer-reviewed)

11.1.1. Original article

Musa, J., Cidre-Aranaz, F., Aynaud, M.-M., Orth, M.F., Knott, M.M.L., Mirabeau, O., Mazor, G., Varon, M., Hölting, T.L.B., Grossetête, S., Gartlgruber, M., Surdez, D., Gerke, J.S., Ohmura, S., Marchetto, A., Dallmayer, M., Baldauf, M.C., Stein, S., Sannino, G., Li, J., Romero-Pérez, L., Westermann, F., Hartmann, W., Dirksen, U., Gymrek, M., Anderson, N.D., Shlien, A., Rotblat, B., Kirchner, T., Delattre, O., Grünewald, T.G.P. Cooperation of cancer drivers with regulatory germline variants shapes clinical outcomes. **Nature Communications** 2019; 10, 4128.

Ahead of original publication, this article was published as a BioRxiv preprint (DOI 10.1101/506659).

11.1.2. Commentary article

Musa, J., and Grünewald, T.G.P. Interaction between somatic mutations and germline variants contributes to clinical heterogeneity in cancer. **Molecular & Cellular Oncology** 2019; 7, 1682924.

11.1.3. Review article

Musa, J., Aynaud, M.-M., Mirabeau, O., Delattre, O., Grünewald, T.G. MYBL2 (B-Myb): a central regulator of cell proliferation, cell survival and differentiation involved in tumorigenesis. **Cell Death & Disease** 2017; 8, e2895.

11.2. Conference presentations

11.2.1. Oral presentations

93th Annual Scientific Meeting of the Society for Paediatric Oncology and Haematology (GPOH), Frankfurt, Germany, 11/2019

3rd Crete Conference on Genes, Cell Biology, Cancer and Beyond, Heraklion, Crete, Greece, 10/2019

Hopp Children`s Cancer Center (KiTZ) Retreat, Asselheim, Heidelberg, Germany, 07/2019

EuSARC, Benediktbeuern, Munich, Germany, 06/2019

2nd Crete Conference on Genes, Cell Biology, Cancer and Beyond, Heraklion, Crete, Greece, 10/2018

1st Crete Conference on Genes, Cell Biology, Cancer and Beyond, Heraklion, Crete, Greece, 10/2017

2nd International Retreat on Cell Biology and Cancer, Civita, Italy, 10/2016

11.2.2. Poster presentations

2nd Hopp Children`s Cancer Center (KiTZ) Symposium, German Cancer Research Center (DKFZ), Heidelberg, Germany, 01/2019

Sohn Conference: Accelerating Translation of Pediatric Cancer Research, London, UK, 02/2018

8th Mildred Scheel Cancer Conference, German Cancer Aid, Bonn, Germany, 06/2017

1st Hopp Children`s Cancer Center (KiTZ) Symposium, German Cancer Research Center (DKFZ), Heidelberg, Germany, 01/2017

4th Annual Scientific Retreat of the German Cancer Consortium (DKTK), German Cancer Research Center (DKFZ), Heidelberg, Germany, 10/2016

3rd Munich Cancer Retreat of the German Cancer Consortium (DKTK), Munich, Germany, 06/2016

100th Annual Meeting of the German Society of Pathology (DGP), Berlin, Germany, 05/2016

12. PUBLICATIONS (ALL)

Status as of January 2021

Musa, J., and Cidre-Aranaz, F. Drug Screening by Resazurin Colorimetry in Ewing Sarcoma. **Methods Mol. Biol.** 2021; 2226, 159–166.

Funk, C.M., and **Musa, J.** Proliferation Assessment by Trypan Blue Exclusion in Ewing Sarcoma. **Methods Mol. Biol.** 2021; 2226, 151–158.

Grünewald, T.G., Alonso, M., Avnet, S., Banito, A., Burdach, S., Cidre-Aranaz, F., Di Pompo, G., Distel, M., Dorado-Garcia, H., Garcia-Castro, J., González-González, L., Grigoriadis, A.E., Kasan, M., Koelsche, C., Krumbholz, M., Lecanda, F., Lemma, S., Longo, D.L., Madrigal-Esquivel, C., Morales-Molina, Á., **Musa, J.**, Ohmura, S., Ory, B., Pereira-Silva, M., Perut, F., Rodriguez, R., Seeling, C., Al Shaaili, N., Shaabani, S., Shiavone, K., Sinha, S., Tomazou, E.M., Trautmann, M., Vela, M., Versleijen-Jonkers, Y.M., Visgauss, J., Zalacain, M., Schober, S.J., Lissat, A., English, W.R., Baldini, N., Heymann, D. Sarcoma treatment in the era of molecular medicine. **EMBO Mol. Med.** 2020; 12, e11131.

Marchetto, A., Ohmura, S., Orth, M.F., Knott, M.M.L. , Colombo M.V., Arrigoni, C., Bardinet, V., Saucier, D., Wehweck, F. S., Li, J., Stein, S., Gerke, J. S., Baldauf, M. C., **Musa, J.**, Dallmayer, M., Romero-Pérez, L., Hölting T. L. B., Amatruda, J.F., Cossarizza, A., Henssen, A. G., Kirchner, T., Moretti, M., Cidre-Aranaz, F., Sannino, G., Grünewald, T.G.P. Oncogenic hijacking of a developmental transcription factor evokes vulnerability toward oxidative stress in Ewing sarcoma. **Nat. Commun.** 2020; 11, 2423.

Orth, M. F., Hölting T. L. B., Dallmayer, M., Wehweck F. S., Paul, T., **Musa, J.**, Baldauf, M.C. Surdez, D., Delattre, O., Knott, M. M. L., Romero-Pérez, L., Kasan, M., Cidre-Aranaz, F., Gerke, J. S., Ohmura, S., Li, J., Marchetto, A., Henseen, A. G., Ölzem, Ö., Sugita, S., Hasegawa, T., Kanaseke, T., Betram, S., Dirksen, U., Hartmann, W., Kirchner, T., Grünewald, T.G.P., 2020. High Specificity of BCL11B and GLG1 for EWSR1-FLI1 and EWSR1-ERG Positive Ewing Sarcoma. **Cancers (Basel)** 2020; 12, 644.

Gerke, J.S., Orth, M.F., Tolkach, Y., Romero-Pérez, L., Wehweck, F.S., Stein, S., **Musa, J.**, Knott, M.M.L., Hölting, T.L.B., Li, J., Sannino, G., Marchetto, A., Ohmura, S., Cidre-Aranaz, F., Müller-Nurasyid, M., Strauch, K., Stief, C., Kristiansen, G., Kirchner, T., Buchner, A., Grünewald, T.G.P. Integrative clinical transcriptome analysis reveals TMPRSS2-ERG dependency of prognostic biomarkers in prostate adenocarcinoma. **Int. J. Cancer** 2020; 146, 2036–2046.

Musa, J., and Grünewald, T.G.P. Interaction between somatic mutations and germline variants contributes to clinical heterogeneity in cancer. **Mol. Cell. Oncol.** 2019; 7, 1682924.

Musa, J., Cidre-Aranaz, F., Aynaud, M.-M., Orth, M.F., Knott, M.M.L., Mirabeau, O., Mazor, G., Varon, M., Hölting, T.L.B., Grossetête, S., Gartlgruber, M., Surdez, D., Gerke, J.S., Ohmura, S., Marchetto, A., Dallmayer, M., Baldauf, M.C., Stein, S., Sannino, G., Li, J., Romero-Pérez, L., Westermann, F., Hartmann, W., Dirksen, U., Gymrek, M., Anderson, N.D., Shlien, A., Rotblat, B., Kirchner, T., Delattre, O., Grünewald, T.G.P. Cooperation of cancer drivers with regulatory germline variants shapes clinical outcomes. **Nat. Commun.** 2019; 10, 4128.

Sannino, G., Marchetto, A., Ranft, A., Jabar, S., Zacherl, C., Alba-Rubio, R., Stein, S., Wehweck, F.S., Kiran, M.M., Hölting, T.L.B., **Musa, J.**, Romero-Pérez, L., Cidre-Aranaz, F., Knott, M.M.L., Li, J., Jürgens, H., Sastre, A., Alonso, J., Da Silveira, W., Hardiman, G., Gerke, J.S., Orth, M.F., Hartmann, W., Kirchner, T., Ohmura, S., Dirksen, U., Grünewald, T.G.P. Gene expression and immunohistochemical analyses identify SOX2 as major risk factor for overall survival and relapse in Ewing sarcoma patients. **EBioMedicine** 2019; 47, 156–162.

Orth, M.F., Gerke, J.S., Knösel, T., Altendorf-Hofmann, A., **Musa, J.**, Alba-Rubio, R., Stein, S., Hölting, T.L.B., Cidre-Aranaz, F., Romero-Pérez, L., Dallmayer, M., Baldauf, M.C., Marchetto, A., Sannino, G., Knott, M.M.L., Wehweck, F., Ohmura, S., Li, J., Hakozaki, M., Kirchner, T., Dandekar, T., Butt, E., Grünewald, T.G.P. Functional genomics identifies AMPD2 as a new prognostic marker for undifferentiated pleomorphic sarcoma. **Int. J. Cancer** 2019; 144, 859–867.

Dallmayer, M., Li, J., Ohmura, S., Alba Rubio, R., Baldauf, M.C., Hölting, T.L.B., **Musa, J.**, Knott, M.M.L., Stein, S., Cidre-Aranaz, F., Wehweck, F.S., Romero-Pérez, L., Gerke, J.S., Orth, M.F., Marchetto, A., Kirchner, T., Bach, H., Sannino, G., Grünewald, T.G.P. Targeting the CALCB/RAMP1 axis inhibits growth of Ewing sarcoma. **Cell Death Dis.** 2019; 10, 116.

Musa, J., Li, J., Grünewald, T.G. Hepatitis B virus large surface protein is priming for hepatocellular carcinoma development via induction of cytokinesis failure. **J. Pathol.** 2019; 247, 6–8.

Baldauf, M.C., Gerke, J.S., Kirschner, A., Blaeschke, F., Effenberger, M., Schober, K., Rubio, R.A., Kanaseki, T., Kiran, M.M., Dallmayer, M., **Musa, J.**, Akpolat, N., Akatli, A.N., Rosman, F.C., Özen, Ö., Sugita, S., Hasegawa, T., Sugimura, H., Baumhoer, D., Knott, M.M.L., Sannino, G., Marchetto, A., Li, J., Busch, D.H., Feuchtinger, T., Ohmura, S., Orth, M.F., Thiel, U., Kirchner, T., Grünewald, T.G.P. Systematic identification of cancer-specific MHC-binding peptides with RAVEN. **Oncoimmunology** 2018; 7, e1481558.

Li, J., Dallmayer, M., Kirchner, T., **Musa, J.**, Grünewald, T.G.P. PRC1: Linking Cytokinesis, Chromosomal Instability, and Cancer Evolution. **Trends Cancer** 2018; 4, 59–73.

Baldauf, M.C., Orth, M.F., Dallmayer, M., Marchetto, A., Gerke, J.S., Rubio, R.A., Kiran, M.M., **Musa, J.**, Knott, M.M.L., Ohmura, S., Li, J., Akpolat, N., Akatli, A.N., Özen, Ö., Dirksen, U., Hartmann, W., de Alava, E., Baumhoer, D., Sannino, G., Kirchner, T., Grünewald, T.G.P. Robust diagnosis of Ewing sarcoma by immunohistochemical detection of super-enhancer-driven EWSR1-ETS targets. **Oncotarget** 2018; 9, 1587–1601.

Musa, J., Aynaud, M.-M., Mirabeau, O., Delattre, O., Grünewald, T.G. MYBL2 (B-Myb): a central regulator of cell proliferation, cell survival and differentiation involved in tumorigenesis. **Cell Death Dis.** 2017; 8, e2895.

Musa, J., Orth, M.F., Dallmayer, M., Baldauf, M., Pardo, C., Rotblat, B., Kirchner, T., Leprivier, G., Grünewald, T.G.P. Eukaryotic initiation factor 4E-binding protein 1 (4E-BP1): a master regulator of mRNA translation involved in tumorigenesis. **Oncogene** 2016; 35, 4675–4688.

13. CURRICULUM VITAE

This section has been removed in the public version of this thesis.

14. AFFIDAVIT

Musa, Julian

Surname, first name

I hereby declare, that the submitted thesis entitled

‘Integrative characterization of the cooperation between EWSR1-FLI1 and regulatory germline variants in tumor progression of Ewing sarcoma‘

is my own work. I have only used the sources indicated and have not made unauthorized use of services of a third party. Where the work of others has been quoted or reproduced, the source is always given.

I further declare that the submitted thesis or parts thereof have not been presented as part of an examination degree to any other university.

Heidelberg, 20.12.2021
Place, Date

Julian Musa
Signature doctoral candidate